Single–column model analysis of available NIWA observations to determine the self–cleaning capacity of the atmosphere

A thesis submitted in partial fulfilment
of the requirements for the Degree of
Doctor of Philosophy in Chemistry
in the University of Canterbury by

LAURA LÓPEZ COMÍ

National Institute of Water and Atmosphere Research
Lauder, New Zealand

Department of Chemistry, College of Science
University of Canterbury, Christchurch, New Zealand

Supervisors:
Dr. Olaf Morgenstern
Dr. Sarah Masters

2016

Abstract

Because of the complexity constraining the hydroxyl radical (OH) in global models, a single–column model has been constructed to investigate how chemistry–climate model data biases affect OH concentrations. By using a single–column model, only the fast photochemical processes of the overhead column are considered, hence neglecting the interaction with circulation dynamics present in chemistry–climate models. As a starting point to this work, the single–column model has been set up for Lauder, a research station located in New Zealand representative of the background conditions of the southern mid–latitudes. By using long–term observations and other available data (e.g. re–analysis data), a bias–correction was applied to a few factors that are mostly driving the OH chemistry at this site, i.e. O_3, H_2O, CO, CH_4, and temperature, inferring the concentrations of OH and other short–lived species.

For testing purposes, a tropospheric steady–state model for Lauder has been developed to be compared with the single–column model. The result of this comparison shows that OH concentrations obtained from the single–column model are mostly consistent with those of the steady–state model, meaning that the single–column model passes a basic plausibility test of its functionality.

In the sensitivity analyses using the single–column model, the contribution of O_3, H_2O, CO, CH_4, and temperature to the budget of tropospheric OH at Lauder has been assessed, individually and in combination. Results indicate that OH responds approximately linearly to

correcting biases in O_3, H_2O, CO, and CH_4, except for temperature. The individual sensitivity coefficients show directly related OH responses to relative changes in O_3 and photolysis [$jO(^1D)$], which range from around 0 % to 25 %, and between 20 % and 50 % respectively. The response of OH is also directly related to the applied relative changes in H_2O, varying from around 5 – 10 % to 50 %. The OH sensitivity to correcting CH_4 and CO biases is inversely related to the relative changes applied to these two chemical species, which range from about –17 % to –35 %, and between –30 % and –50 % respectively. The assessment of the effects of temperature in OH indicates a non–linear response of OH to temperature biases, but these effects are found to be small. Furthermore, the modelled OH obtained from driving the major forcings simultaneously shows an approximately linear relationship with the combination of the individual linear contributions. Therefore, the quantification of the individual contributions of biases in the major trace gases and temperature to OH chemistry allows for a bias–corrected calculation of OH in the troposphere at Lauder, especially for H_2O and O_3, which are the dominating factors controlling the OH abundance at this site. Additional analyses of long–term time series of OH at Lauder under clear–sky conditions provide evidence of short–term variations of OH but a significant long–term trend (5.4 ± 2.7 % at the 95 % confidence interval) was only found at 5 – 7.5 km in the troposphere. This trend in OH is mainly caused by an increase in humidity in the re–analysis data at these altitudes.

Sensitivity simulations taking the effect of clouds into account were also conducted using the single–column model. Results indicate that OH responds approximately linearly to changes in photolysis rates due to the presence of clouds. The impacts of liquid water and ice clouds were studied separately and in combination. The modelled OH responds plausibly to the presence of clouds corresponding to proportional changes in $jO(^1D)$ that vary between 0 % – 10 %, 0 % – 12 %, and 0 % – 20 % due to ice, liquid water, and the combination of ice + liquid water clouds respectively. Moreover, the vertical distribution of clouds seems to have more influence on photolysis and OH, rather than the change in cloud water content.

Because of the large uncertainty of the impact of clouds on photolysis and OH in global models, and the lack of suitable observations for clouds at Lauder to constrain the single–column model, their impact on OH has been quantified separately from the effect of bias–correcting the major forcings. By using a single–column model, only instantaneous changes in the chemistry of the overhead column caused by correcting biases in the major species to OH chemistry have been considered. The advantage is that it allows straight forward control of all impact parameters and enables separation of long– and short–lived effects. The single–column model could also be applied to other clean environments using the same methods conducted in this work. However, its applicability would need to be reassessed for regions where tropospheric chemical conditions become more complex, i.e. organic compounds and NO_x that play a key role in the chemistry of O_3 and OH.

Acknowledgements

I am taking this opportunity to express gratitude to my PhD supervisors, Dr. Olaf Morgenstern and Dr. Sarah Masters, for giving me the opportunity to undertake a PhD in atmospheric sciences, and for their unconditional guidance, help and support over the last three years. I am grateful to Dr. Guang Zeng, for providing me with tropospheric chemistry feedback and for her support during my PhD on several occasions. I would also like to thank Dr. Richard McKenzie and Ben Liley for their help and training on atmospheric measurements analysis, especially at the beginning of my PhD. My sincere thanks also goes to Dan Smale, who introduced me to IDL programming and took some time out of his busy schedule to help me. Thanks also to Mike Kotkamp for teaching me how to calibrate MOPI1 and run the Dutch and Japanese Lidars. Dr. Richard Querel, John Robinson, Paul Johnston, and Alan Thomas for feedback about Lauder instrumentation and other things.

Special thanks to Dr. Ayoe Buus Hansen for her help, support, and patience especially throughout the end of my PhD. I will never forget our lunch time at the hostel, tea breaks, and beer times. Wills Dobson for his daily visits to my office and his funny loud voice. Dr. Stefanie Kremser for listening to me on several occasions and for our tramping trips. My gratitude also goes to Dr. Karin Kreher and Dr. Greg Bodeker for their support and dinner invitations.

Last but not the least, I would like to express my love and sincere gratitude to my family for supporting me throughout my academic trajectory. Also a huge thanks to my friends back home and to Mauricio Veloso Coronado for his company, love, and patience.

Abbreviations and Acronyms

ACCMIP	**A**tmospheric **C**hemistry **C**limate **M**odel **I**ntercomparison **P**roject
ASAD	**A** **S**elf–contained **A**tmospheric chemistry co**D**e
BB	**B**iomass **B**urning
CCM	**C**hemistry–**C**limate **M**odel
CCN	**C**loud **C**ondensation **N**uclei
CFC	**C**hloro**F**luoro**C**arbon
CTM	**C**hemical **T**ransport **M**odel
CLaMS	**C**hemical **La**grangian **M**odel of the **S**tratosphere
DIAL	**DI**fferential **A**bsorption **L**idar
DU	**D**obson **U**nits
ECC	**E**lectrochemical **C**oncentration **C**ell
ECMWF	**E**uropean **C**entre for **M**edium–Range **W**eather **F**orecasts
ENSO	**E**l **N**iño **S**outhern **O**scillation
ERAI	**E**CMWF **R**e–**A**nalyses **I**nterim
FAGE	**F**luorescence **A**ssay by **G**as **E**xpansion
FPH	**F**rost **P**oint **H**ygrometer

FTS	**F**ourier **T**ransform **S**pectrometer
FTIR	**F**ourier **T**ransform **I**nfrared **S**pectrometer
GCM	**G**eneral **C**irculation **M**odel
GHG	**G**reen**H**ouse **G**as
GLOMAP	**GLO**bal **M**odel of **A**erosol **P**rocesses
HadGEM	**Had**ley Centre **G**lobal **E**nvironment **M**odel
HC	**H**ydro**C**arbon
HCFC	**H**ydro**C**hloro**F**luoro**C**arbon
HFC	**H**ydro**F**luoro**C**arbon
IC	**I**ce **C**loud
INTEX–NA	**INTE**rcontinental Chemical Transport E**X**periment – **N**orth **A**merica
IR	**I**nfra**R**ed
LIC	**L**iquid – **I**ce **C**loud
LIDAR	**LI**ght **D**etection **A**nd **R**anging
LT	**L**ower **T**roposphere
LWC	**L**iquid **W**ater **C**loud
MACC	**M**onitoring **A**tmospheric **C**omposition and **C**limate
MetUM	**M**et **O**ffice's **U**nified **M**odel
MIR	**M**id–**I**nfra**R**ed
MOPI1	**M**icrowave **O**zone **P**rofiling **I**nstrument **1**
NASA	**N**ational **A**eronautics and **S**pace **A**dministration

NDACC	**N**etwork for the **D**etection of **A**tmospheric **C**omposition **C**hange
NH	**N**orthern **H**emisphere
NIR	**N**ear–**I**nfra**R**ed
NIWA	**N**ational **I**nstitute of **W**ater and **A**tmosphere
NMVOC	**N**on–**M**ethane **V**olatile **O**rganic **C**ompound
NOAA	**N**ational **O**ceanic and **A**tmospheric **A**dministration
NZAC	**N**ew **Z**ealand **A**tmospheric **C**hemistry
ODE	**O**rdinary **D**ifferential **E**quation
ODS	**O**zone–**D**epleting **S**ubstances
***o*–VOC**	**o**xygenated–**V**olatile **O**rganic **C**ompound
PFC	**P**er**F**luoro**C**arbon
PSC	**P**olar**S**tratospheric**C**loud
RH	**R**elative **H**umidity
RIVM	**R**ijks **I**nstituut voor **V**olksgezondheid en **M**ilieu
RMSE	**R**oot–**M**ean–**S**quare **E**rror
SCM	**S**ingle–**C**olumn **M**odel
SCO	**S**lant **C**olumn **O**zone
SH	**S**outhern **H**emisphere
SSM	**S**teady–**S**tate **M**odel
SST	**S**ea **S**urface **T**emperature
STE	**S**tratosphere–**T**roposphere **E**xchange

SZA	**S**olar **Z**enith **A**ngle
TCC	**T**otal **C**loud **C**over
TCCON	**T**otal **C**arbon **C**olumn **O**bserving **N**etwork
TCO	**T**otal **C**olumn **O**zone
TEI	**T**hermo **E**nvironmental **I**nstrument
p–TOMCAT	(**p**arallel)–**T**oulouse **O**ff–line **M**odel of **C**hemistry **A**nd **T**ransport
UKCA	**U**nited **K**ingdom **C**hemistry and **A**erosols
UMIST	**U**niversity of **M**anchester **I**nstitute of **S**cience and **T**echnology
UT	**U**pper **T**roposphere
UV	**U**ltra**V**iolet
UVA	**U**ltra**V**iolet **A**
UVB	**U**ltra**V**iolet **B**
UVC	**U**ltra**V**iolet **C**
UVL	**U**ltra**V**iolet **L**auder
VOC	**V**olatile **O**rganic **C**ompound
WAOSE	**W**eybourne **A**tmospheric **O**bservatory **S**ummer **E**xperiment

Chemical Abbreviations

$BrO_x = Br + BrO$	Bromine family
$ClO_x = Cl + ClO + ClO_2 + 2Cl_2O_2$	Chlorine family
$HO_x = H + OH + HO_2$	Family of hydrogen oxide radicals
$HO_y = H + OH + HO_2 + 2H_2O_2$	Extended family of hydrogen oxide radicals
$NO_x = NO + NO_2$	Family of nitrogen oxide radicals
$O_x = O_3 + O(^1D) + O(^3P)$	Odd oxygen family
R, R′, R″	Organic radicals
R′R″CO	Ketones
R″CHO	Aldehydes

Contents

Abstract **ii**

Acknowledgements **v**

Abbreviations and Acronyms **vi**

Chemical Abbreviations **x**

1 Introduction **1**

2 General background **7**

2.1 Troposphere and stratosphere: Composition 8

2.2 Radiation 11

2.3 O_3 photochemistry and its link to OH 14

3 Models and methods of analysis **23**

3.1 UKCA chemistry–climate model 23

3.2 NZAC single–column model 27

3.2.1 FAST–JX photolysis scheme 28

3.2.2 Chemical integration package 30

3.3 Steady–state model 33

3.4 Methodology 39

4 Observational data **48**

4.1 Analysis of the NO_2 and O_3 photolysis rates 49

4.2 Construction of O_3 profiles 53

4.2.1 Instrumentation 53

4.2.2 Time series of O_3 profiles 55
4.3 Construction of H_2O profiles 67
4.3.1 Instrumentation 68
4.3.2 Time series of H_2O profiles 70
4.4 Construction of CO profiles 74
4.5 Construction of CH_4 profiles 78
4.6 Construction of temperature profiles 81

5 Sensitivity of OH to key forcings 85
5.1 Validation of FAST–JX 86
5.2 Comparison of the NZAC SCM to the SSM 94
5.3 Sensitivity of OH to O_3 biases 102
5.4 Sensitivity of OH to H_2O biases 111
5.5 Sensitivity of OH to CH_4 biases 113
5.6 Sensitivity of OH to CO biases 115
5.7 Sensitivity of OH to temperature biases 117
5.8 Sensitivity of OH to biases in all forcings 120
5.9 Comparison of modelled OH to observations 123
5.10 Variability and trends of OH 125

6 Impact of clouds on OH 130
6.1 Introduction 130
6.2 Results and Discussion 132
6.2.1 Impact of ICs on $jO(^1D)$ and OH 137
6.2.2 Impact of LWCs on $jO(^1D)$ and OH 139
6.2.3 Impact of LICs on $jO(^1D)$ and OH 141
6.3 Conclusions 143

7 Summary, conclusions, and outlook 147

Bibliography 156

A NZAC SCM chemical abbreviations 182

B FAST–JX photolysis reactions 183

C NZAC SCM chemical mechanism **185**

D Instruments & other data sources **194**

List of Figures

2.1 US standard atmosphere 9
2.2 Electromagnetic radiation spectrum 12
2.3 Reduced daytime tropospheric photochemical process 17

3.1 Flow diagram of ASAD being called from a CCM 30
3.2 Flow chart of the NZAC SCM code 40

4.1 Time series of ratios of clear–sky UV spectrometer values compared with values from ancillary instruments 51
4.2 Time series of observed local solar noon $j\mathrm{NO_2}$ and $j\mathrm{O}(^1\mathrm{D})$ . . 52
4.3 Ozonesonde $\mathrm{O_3}$ mean annual cycle 56
4.4 Comparison between the TEI and ozonesonde surface $\mathrm{O_3}$ measurements 57
4.5 Comparison of the $\mathrm{O_3}$ mean annual cycle between a pair of instruments between 20 and 30 km 60
4.6 Scatter plots between pairs of instruments from 20 and 30 km 62
4.7 Constructed time series of $\mathrm{O_3}$ profiles 64
4.8 Comparison of Dobson $\mathrm{O_3}$ columns versus vertical integrated $\mathrm{O_3}$ profiles measurements 66
4.9 Comparison of the mean annual cycle of $\mathrm{H_2O}$ measured with the frost point hygrometer to three different datasets 72
4.10 Constructed time series of $\mathrm{H_2O}$ profiles 73
4.11 Time series of CO column measured by the FTIR spectrometer. Ratio of fitted CO columns. Percentage difference of CO columns 76
4.12 Constructed time series of CO profiles 77

4.13 (A) Cape Grim and UKCA CCM CH_4 surface data. (B) Time series of the percentage difference between surface UKCA CCM and Cape Grim CH_4. (C) Multi–annual and monthly–mean percentage difference between UKCA total column and FTIR total column CH_4 79
4.14 Constructed time series of CH_4 profiles 81
4.15 Constructed time series of temperature profiles 82

5.1 Validation of FAST–JX jNO_2 and $jO(^1D)$ at the surface . . . 88
5.2 Validation of FAST–JX jNO_2 and $jO(^1D)$ at 20 km 89
5.3 Vertical profiles of $jO(^1D)$ calculated with FAST–JX. Comparison with the study by Liu *et al.* (2006) 90
5.4 Vertical profiles of $jO(^1D)$, jNO_2, and jNO_3 calculated with FAST–JX. Comparison with the study by Wild *et al.* (2000) . 92
5.5 Surface jNO_2 and $jO(^1D)$ calculated with FAST–JX. Comparison with the study by Voulgarakis *et al.* (2009) . . . 93
5.6 Density plot of OH concentrations between the single–column model and the steady–state model 96
5.7 Comparison of differences in OH due to differences in the key forcings between the NZAC SCM and the SSM 99
5.8 Seasonal percentage differences between perturbation simulations and the reference simulation for OH and $jO(^1D)$ 104
5.9 Multi–annual and monthly–mean OH responses to O_3 biases relative to the reference simulation 106
5.10 Scatter plots of the relationships of $jO(^1D)$ with the slant O_3 column, OH with $jO(^1D)$, and OH with the slant O_3 column 108
5.11 Sensitivity coefficients between OH and each perturbation variable 110
5.12 Multi–annual and monthly–mean OH responses to H_2O biases relative to the reference simulation 112
5.13 Multi–annual and monthly–mean OH responses to CH_4 biases relative to the reference simulation 114
5.14 Multi–annual and monthly–mean OH responses to CO biases relative to the reference simulation 116

5.15 Multi–annual and monthly–mean OH responses to temperature biases relative to the reference simulation 118
5.16 Multi–annual and monthly–mean OH responses to all forcings combined. Scatter plot of the response of OH to the combination of all forcings versus the sum of the OH response to individual forcings 122
5.17 Comparison between modelled and measured OH 124
5.18 Variability and trends of OH 126
5.19 Annual–mean anomalies and trends of OH and ERAI – UKCA CCM H_2O at 5 – 7.5 km of altitude 127

6.1 Comparison between the UKCA CCM and the observed total cloud covers 133
6.2 Comparison of the cloud effects on photolysis rates between the UKCA CCM and the NZAC SCM 136
6.3 Multi–annual and monthly mean response of $j\mathrm{O}(^1\mathrm{D})$ and OH to the presence of ICs 138
6.4 Multi–annual and monthly mean response of $j\mathrm{O}(^1\mathrm{D})$ and OH to the presence of LWCs 140
6.5 Multi–annual and monthly mean response of $j\mathrm{O}(^1\mathrm{D})$ and OH to the presence of LICs 142

List of Tables

3.1 Sensitivity simulations performed with the NZAC SCM under clear–sky conditions to assess the OH sensitivity to biases in several forcings 42

3.2 Simulations performed with the NZAC SCM under clear–sky conditions to assess OH variability and trends 43

3.3 Simulations performed with the NZAC SCM under cloudy conditions 44

3.4 Sensitivity simulations performed with the SSM under clear–sky conditions 46

B.1 FAST–JX photolysis reactions 183

C.1 NZAC SCM heterogeneous reactions 185

C.2 NZAC SCM bimolecular reactions 186

C.3 NZAC SCM unimolecular and termolecular reactions 193

D.1 Instrumentation and other data sources 195

Chapter 1

Introduction

The hydroxyl radical (OH) is one of the most important chemical species present in the atmosphere. It is the major atmospheric oxidant and has been called the "detergent of the atmosphere" because it cleanses the atmosphere through a series of chemical reactions involving oxidation and removal of a large amount of pollutants (Levy, 1971; Logan *et al.*, 1981; Thompson, 1992; Naik *et al.*, 2013), including methane (CH_4) and carbon monoxide (CO). The primary source of OH radicals is tropospheric ozone (O_3), an air pollutant and a greenhouse gas (GHG). Although tropospheric O_3 only accounts for 10 % of the total atmospheric O_3 abundance, it plays an essential role in photochemical processes controlling the atmospheric oxidising capacity, which is mainly determined by the abundance of OH radicals. Furthermore, stratospheric O_3 depletion and predicted recovery, and general climate change have had/will have an impact on the evolution of tropospheric composition. Ozone–depleting substances (ODS), e.g. chlorofluorocarbons (CFCs), methyl chloride (CH_3Cl), and nitrous oxide (N_2O) are transported to the stratosphere where they yield the ClO_x and the NO_x radicals that destroy stratospheric O_3. Likewise, CH_4 is a source of HO_x that also destroys stratospheric O_3. Changes in stratospheric O_3 moderate the O_3 photolysis rate [$jO(^1D)$], and thus impact tropospheric O_3 and OH abundances.

Modelling global atmospheric composition and processes are key to

understanding how anthropogenic activities will impact the composition of the atmosphere. Atmospheric modelling has made great advances so that the state–of–the–art chemistry–climate models (CCMs) are highly comprehensive. Nonetheless, many challenges still remain. CCMs differ in their representations of physical and chemical processes, i.e. transport, dispersion, deposition, and chemical mechanisms employed which affect the calculated concentrations of short–lived species. The sensitivity of short–lived species (e.g. OH radical) to these processes are often obscure in a global model in which the effects from each process can not be easily separated.

Due to its short lifetime [$\sim$ 1 second (Prinn, 2001; Elshorbany *et al.*, 2012)], OH is highly variable and difficult to measure. It also responds to numerous factors (e.g. cloudiness and humidity), of which implementation is model dependent. Thus, there is considerable disagreement amongst models regarding its abundance (e.g. as expressed by the CH_4 lifetime). One cause for such disagreement is the underlying chemical mechanisms. *In–situ* measurements of OH concentrations have been performed in the past two decades in order to understand the chemical mechanisms that explain the evolution of the OH radical [see review by Heard and Pilling (2003)]. The most commonly used technique for field measurements of OH is called the "Fluorescence Assay by Gas Expansion" (FAGE) and is based on the detection of species such as OH, as well as formaldehyde (HCHO), and nitrogen dioxide (NO_2), both in the laboratory and in the free atmosphere through laser–induced fluorescence spectroscopy (Clemitshaw, 2004). Ground and air based field campaigns using the FAGE technique for field OH measurements have been carried out in a wide variety of environments ranging from urban regions in the Northern Hemisphere (NH) [e.g. in New York (USA): Ren *et al.* (2003), in the Mexico City Metropolitan Area (Mexico): Dusanter *et al.* (2009)] to clean–air marine atmospheres of the Southern Hemisphere (SH) [e.g. at the Cape Grim Baseline Air Pollution Station (Tasmania): Creasey *et al.* (2003), and at the British Antarctic Survey's Halley Research Station (coastal Antarctica): Bloss *et al.* (2007)].

Likewise, in order to understand the long–term, global OH variations and trends, a useful method is to track the long–term behaviour of the concentration of long–lived chemicals at a global scale. Such tracking is an indirect measurement of OH and is based on monitoring atmospheric chemical species oxidised by OH, of which sources are relatively well established and for which their OH–oxidation is believed to be their dominant removal mechanism. The most widely used example for tracking OH is an man–made solvent (ODS) called methyl chloroform (CH_3CCl_3), due to its relatively well–known source strength (industrial releases) and well–mixed nature (Prinn *et al.*, 2005; Montzka *et al.*, 2011). The dominant tropospheric removal process for CH_3CCl_3 is by reaction with OH. Hence, global daytime OH concentrations have been inferred using these measurement techniques, e.g. a small inter–annual variation in OH between 1998 – 2007 was inferred using CH_3CCl_3 measurements (Montzka *et al.*, 2011).

But how do models compare with present–day observations? They simulate diverse present–day OH concentrations/CH_4 lifetimes which tend to differ from observational estimates. These differences with respect to observations are indicative of the different physical and chemical mechanisms present in the models. Currently, efforts to improve the underlying understanding of OH involve studying how the precursors to O_3 interact with each other and performing detailed measurements of climate drivers affecting atmospheric composition. Nevertheless, despite the recent advances in OH measurements and in the understanding of OH chemistry, it remains a challenge to constrain OH in global models due to the sparsity and difficulty of its measurements, and hence they are only somewhat useful to assess the quality of the chemical mechanisms included in global models.

Therefore, a step forward to address the problem of modelling OH is to complement global chemistry models with local–scale models (box models or single–column models) constrained as much as possible by observations

and incorporating only fast photochemical processes, hence neglecting transport and other physical processes. In a forward sense, a bias correction is applied to the forcings that play a major role in the OH chemistry at the site considered, inferring OH concentrations that may better agree with observations. The use of local models allows sensitivity studies for OH at different sites of the globe – where long–term measurements are available (e.g. O_3) – to assess how biases in long–lived constituents commonly found in chemistry–climate model data affect OH.

In the past, Grenfell *et al.* (1999) and Emmerson *et al.* (2005, 2007) employed box models to simulate OH and HO_2 and compared them to observations. In particular, Emmerson *et al.* (2005) studied the sensitivity of OH and HO_2 to increases in nitrogen oxide (NO), nitrogen dioxide (NO_2), and nitrous acid (HONO). In this PhD project, a single–column model (SCM) constrained with available long–term observations was constructed [New Zealand Atmospheric Chemistry single–column model (NZAC SCM)], yielding a continuous record of the OH radical. The use of the NZAC SCM provides a useful tool which aims at studying how biases in other constituents and temperature affect the abundance of OH. As a starting point to this work, the model was set up for Lauder, New Zealand (45.04°S, 169.69°E, 370 metres above sea level), a clean–air research site representative of SH midlatitudes operated by the National Institute of Water and Atmospheric Research (NIWA).

Most trace gas observations at Lauder have been in operation for decades. Some of these long–term records were used to constrain the NZAC SCM. To supplement, re–analysis meteorological data and data from the Cape Grim Station (Tasmania) were also used to constrain the model. Therefore, long–term observations of the major forcings that play a major role in the OH chemistry at Lauder (i.e. O_3, H_2O, CH_4, CO, and temperature) were used to assess OH concentration changes due to correcting chemistry–climate model biases in the mentioned forcings. Furthermore, long–term time series of OH provided by the NZAC SCM were used to analyse variability and trends of OH at Lauder.

The present thesis is organised as follows: Following the introduction and description of the aims behind this work, some fundamental background of important relevance to this thesis is described in Chapter 2.

In Chapter 3, a general overview of the models employed in this work is discussed; (1) the United Kingdom Chemistry Aerosol chemistry–climate model (UKCA CCM) used for the construction of the (2) NZAC SCM from which the results of this thesis were obtained; (3) the steady–state model (SSM) developed for the troposphere to assess the accuracy of the NZAC SCM.

Chapter 4 describes the procedure to turn available observed surface, total column, and profile measurements into time series of the key forcings that are central to the OH photochemistry, of a common format suitable for running the NZAC SCM. In addition, Chapter 4 provides a detailed description of the analysis of the photolysis rates of NO_2 and O_3 [$j\mathrm{NO}_2$ and $j\mathrm{O}(^1\mathrm{D})$] measurements that were used to validate the photolysis scheme of the NZAC SCM (FAST–JX).

Chapter 5 describes and illustrates the results of the response of OH to model biases of the key forcings under clear–sky conditions (no clouds and aerosols were considered). Trends and variability in OH are also assessed in Chapter 5, along with the validation of FAST–JX of the NZAC SCM, and the comparison between the NZAC SCM and the SSM.

Chapter 6 examines the response of OH to the presence of clouds, and how the photolysis rates are affected by these changes in comparison with the clear–sky conditions.

Finally, the results that are presented in Chapters 5 and 6 are summarised, and conclusions drawn in Chapter 7. Suggestions are also made for future research in atmospheric modelling in Chapter 7, based on the results presented in this thesis.

Chapter 2

General background

Over the last century, human activities have led to disturbances in atmospheric composition by changing the concentration of GHGs and aerosols. GHGs and aerosols affect climate by altering incoming radiation and outgoing infrared radiation that are part of the Earth's energy balance. Short–lived species, and OH in particular, play a key role in oxidising a large number of these anthropogenic pollutants. Oxidation processes that occur in the troposphere are of key importance because the troposphere contains the bulk of atmospheric mass and because GHGs and other pollutants are generally emitted at the Earth's surface. The stratosphere, where most of the atmospheric O_3 is found, is crucial in determining tropospheric composition, since absorption of solar radiation by the overhead O_3 column controls much of the radiation flux reaching the troposphere.

This chapter introduces some general background that is relevant to the subject of this thesis. Section 2.1 describes the structures of the troposphere and the stratosphere, and their composition. Radiation, which plays an important role in driving photolysis reactions, and thus affecting atmospheric composition is introduced in Section 2.2. A general overview of the photochemistry of tropospheric and stratospheric O_3 and its link to the OH radical is outlined in Section 2.3.

2.1 The troposphere and stratosphere: Composition

The Earth's atmosphere is a thin layer of gases that surrounds the Earth. It is mostly composed of nitrogen (N_2) (78 % by mole fraction or volume), oxygen (O_2) (21 % by mole fraction or volume), argon (Ar) (0.9 % by mole fraction or volume), carbon dioxide (CO_2) (0.03 % by mole fraction or volume), and trace amounts of other gases. It insulates the Earth from extreme temperatures; it keeps heat inside the atmosphere and it also shields the Earth from much of the Sun's incoming ultraviolet (UV) radiation. The distinctive temperature gradients of the atmosphere lead to differences in behaviour, which make convenient to characterise four different regions along the temperature profile, i.e. the troposphere, the stratosphere, the mesosphere, and the thermosphere (Brasseur and Solomon, 1986; Brasseur *et al.*, 1999), of which points of inflection mark the boundaries that separate the four layers. The name of these boundaries are the tropopause, the stratopause and the mesopause. Figure 2.1 shows the temperature profile of the atmosphere. This section focuses on describing the troposphere and stratosphere, where O_3 and other trace gases have a direct or an indirect impact on the production of OH radicals.

The troposphere is the region from the surface of the Earth to approximately 17 km in the tropics and around 10 km in the extratropics. Its lowest part is called the planetary boundary layer (up to 2 km above the Earth's surface) where surface effects are important. The troposphere is characterized by a decrease in temperature with altitude from an average of 15°C at sea level to about –55°C at the top of the troposphere. This temperature difference occurs because convective overturning processes dominate over radiation whereby parcels of warm air rise adiabatically and expand to the tropopause, carrying water vapour (H_2O) and forming clouds as they condense due to the low temperatures. The troposphere is weakly stratified and relatively well mixed, thus yielding a decrease in temperature with height. The location of the tropopause varies with latitude and season since temperature is dominated by this radiative

and convective exchange. The tropopause is the boundary between the troposphere and the following layer called the stratosphere.

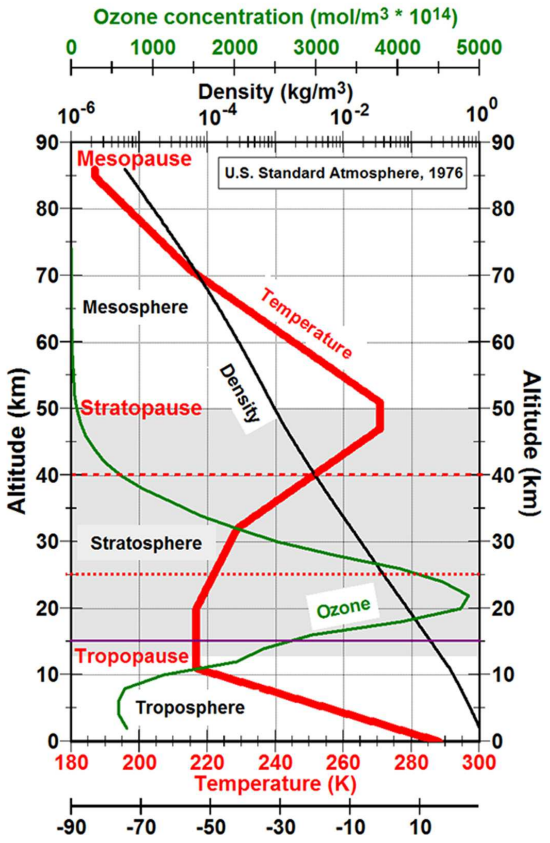

Figure 2.1: *US standard atmosphere. Atmospheric temperature (red), O_3 (green) and density (black) profiles. This figure has only been used for illustration. Source: [Standard Atmosphere, US (1976)].*

The troposphere contains at least 75 % of the total mass of the atmosphere approximately, since pressure decreases exponentially with height (Peixoto and Oort, 1992). Both natural and anthropogenic molecules are found in the troposphere. Among them are N_2 (78 % by

mole fraction or volume) and O_2 (21 % by mole fraction or volume) (dry air) which account for approximately 99 % of the total volume of the atmosphere. The rest are minor constituents such as O_3, H_2O, CO_2, CH_4, CO, hydrocarbons (HCs), CFCs and halons (bromine–containing compounds), nitrogen and sulphur compounds, which account for the remaining 1 % of the total. Within the 1 % of tropospheric composition, H_2O is the most abundant, followed by CO_2, CH_4, O_3 and the remaining chemical compounds mentioned above.

The troposphere contains most of the pollutants, e.g. GHGs, which have been emitted into the atmosphere from either natural (e.g. volcanoes eruptions, BB which is mostly natural) or anthropogenic sources (e.g. industrial activities, agriculture, fossil–fuel usage). Pollutants emitted into the atmosphere are removed by dry and wet depositions, and by chemical conversion into species such as H_2O and CO_2. Some short–lived chemical species (e.g. OH), nitrate (NO_3), organic peroxy and hydroperoxyl radicals (HO_2 and RO_2) are capable of oxidizing a large number of mostly organic pollutants. The radical that contributes most to the cleaning of the atmosphere is the OH radical, discovered by Levy (1971).

Above the troposphere lies the stratosphere, located between 9 km (higher in the tropics) and $\sim$ 50 km. The stratosphere is divided into the lower stratosphere, which is relatively weakly stratified, and the more strongly middle and upper stratified stratosphere. The temperature profile is largely determined by absorption of ultraviolet (UV) radiation by O_3 which forms the O_3 layer (Dessler, 2000) (Figure 2.1 green line). In the stratosphere there is a progressive increase in temperature with altitude, as shown in Figure 2.1 (red line), producing a vertical stratification. 99 % of the mass of the atmosphere is located within the lower 30 km above the surface of the Earth.

The minor constituents in the stratosphere mainly consist of O_3 ($\sim$ 90 % of the total atmospheric O_3), as well as other trace gases, e.g. H_2O, odd hydrogen (HO_x), odd nitrogen (NO_x) and odd chlorine (ClO_x) families,

carbon–oxide compounds (CO, CO_2), and CH_4 (Hudson, 1979; Solomon, 1983).

In the classification used in Figure 2.1, the regions of the atmosphere are divided according to temperature (red line), in particular whether it increases or decreases with altitude. The principal energy source for the Earth's atmosphere is solar radiation, which causes a series of physical and chemical processes, that determine not only the temperature profile shown in Figure 2.1, but also the atmospheric composition. The next section introduces fundamental concepts relating to radiation, and of particular relevance to the subject of this thesis.

2.2 Radiation

Since the Earth's atmosphere is determined by complex chemical reactions, the assessment of the rates at which these chemical reactions occur becomes crucial in order to quantify each of the chemical constituents, ultimately predicting future changes in the atmospheric composition by means of chemical models. Thus, radiation is one of the most important factors controlling the rates at which the photochemical reactions occur in the atmosphere.

Electromagnetic radiation interacts with matter in different ways across the spectrum. These types of interaction are so different that, even though the electromagnetic radiation is a continuous spectrum of frequencies and wavelengths, the spectrum is divided into several regions for practical reasons related to these qualitative interaction differences (Figure 2.2). These regions extend from gamma (γ) and X–rays at the highest frequencies to radio–waves at the lowest. Furthermore, the extraterrestrial solar spectrum, as part of the electromagnetic spectrum, is divided into various spectral windows: infrared (IR) (700 nm – 1 mm), visible (400 – 700 nm) and a small fraction of the UV region (100 – 400 nm) (Brasseur and Solomon, 1986).

UV radiation is subdivided into three bands: UVA radiation (315 – 400 nm), UVB radiation (280 – 315 nm), and UVC radiation (100 – 290 nm). UVC accounts only for 0.6 % of the incident solar spectrum at the top of the atmosphere, and is detrimental to human health and the biosphere, but is largely absorbed by O_2 below $\sim$ 240 nm and by O_3 below 280 nm (McKenzie and Madronich, 2003).

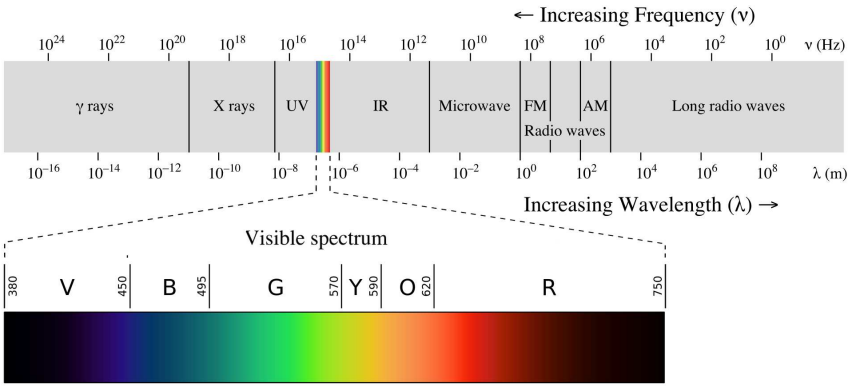

Figure 2.2: *Electromagnetic radiation spectrum.*
Source: http://blogs.unimelb.edu.au/

UVB radiation is absorbed by stratospheric O_3 (the O_3 layer). The UVB radiation is highly variable and dependent on solar zenith angle (SZA) and stratospheric O_3. Only a small unabsorbed part of UVB radiation reaches the ground; this is responsible for the production of vitamin D in humans (McKenzie *et al.*, 2009). Nevertheless, the UVB radiation can also have a negative environmental impact on Earth's system. Because of the depletion of the O_3 layer during the 20^{th} century, there has been an increase in the amount of UVB radiation reaching the Earth's surface which is sufficient to damage DNA molecules in both plants and animals, and cause sunburn in humans (and consequently skin cancer in the long term) and eye diseases (McKenzie and Madronich, 2003).

UVA radiation is less absorbed by O_3; thus a larger percentage of it reaches the Earth's surface year–round, but it is supposed to be weakly carcinogenic, unlike the UVB radiation (Matsumura and Ananthaswamy, 2004). Likewise, IR radiation is emitted by the Earth's surface and the atmosphere, but also absorbed by GHGs in the atmosphere (Brasseur and Solomon, 1986). Conversely, radiation in the visible range is essential for the biosphere and it is the portion of the electromagnetic spectrum that can produce a sensation of sight.

In order to assess the importance of an atmospheric photochemical reaction, it is important to calculate the rate at which atmospheric molecules react. For this, it is necessary to determine the radiation at various altitudes in the atmosphere, as well as how this radiation is attenuated as it penetrates the Earth's atmosphere (Brasseur and Solomon, 1986). Any excited species can undergo different photochemical processes, i.e. quenching, photodissociation, reaction with a collision partner, and ionization. The probability of any of these processes occurring is called the quantum yield. Photolysis rates (j–values) of a certain molecule X and at altitude z in the atmosphere are determined not only by the quantum yield, but also by the actinic flux (cm^{-2} s^{-1} nm^{-1}), and the absorption cross–section (cm^2) which is the ability of the molecule to absorb these photons (Equation 2.1):

$$j(X;z) = \int_{\lambda} \sigma_a(X;\lambda;T;P)\ \phi(X;\lambda;T;P)\ F(\lambda)\ d\lambda \tag{2.1}$$

where F is the actinic flux at a given wavelength (λ), and σ_a and ϕ are the absorption cross–section and quantum yield for species X at a given wavelength (λ), temperature (T), and pressure (P).

The actinic flux is the radiation at a particular point in the atmosphere available to molecules from all directions, whereas the spectral irradiance refers to flow of energy crossing flat surfaces having fixed spatial orientation

(J m^{-2} nm^{-1}) (Madronich, 1987). The actinic flux and the irradiance are calculated by integrating the spectral radiance $L(\lambda;\, \alpha;\, \beta)$ (cm^{-2} s^{-1} nm^{-1} sr^{-1}) over all angles (Equations 2.2 and 2.3 respectively) in the atmosphere:

$$F(\lambda) = \int_0^{2\pi} \int_0^{\pi} L(\lambda; \alpha; \beta)\ \sin\alpha\ d\alpha\ d\beta \tag{2.2}$$

$$E(\lambda) = \int_0^{2\pi} \int_0^{\pi} L(\lambda; \alpha; \beta)\ \cos\alpha\ \sin\alpha\ d\alpha\ d\beta \tag{2.3}$$

where F and E are the actinic flux and irradiance respectively at a given wavelength (λ), and α, β are the spherical coordinates.

2.3 O_3 photochemistry and its link to OH

O_3 is of central importance in both tropospheric and stratospheric chemistry. Stratospheric O_3 shields the Earth's surface from UV radiation. However, O_3 near the surface is toxic to human health and plants (Houghton *et al.*, 2001). The tropospheric O_3 burden has increased considerably due to enhanced emissions of NO_x (NO + NO_2), CH_4, CO and other volatile organic compounds (VOCs) (Volz and Kley, 1988; Marenco *et al.*, 1994). Although tropospheric O_3 only accounts for 10 % of the total atmospheric O_3 abundance, it plays an essential role in photochemical processes controlling the atmospheric oxidising capacity through the production of OH radicals. Thus, O_3 plays an essential role in affecting tropospheric composition; it is the primary source of OH through photolysis and the photolysis rates are affected by the amount of O_3 column.

Daytime oxidation in the troposphere is mainly driven by free–radical reactions and intermediate oxidation products. OH and HO_2 radicals (collectively known as HO_x along with H) are key to the photochemistry of the troposphere. The oxidation chain by radicals is initialised by the OH formation which involves O_3 photolysis at a wavelength of less than

310 nm to yield $O(^1D)$, and the subsequent reaction of $O(^1D)$ with H_2O to form two molecules of OH (Levy, 1971):

$$O_3 + h\nu \longrightarrow O(^1D) + O_2 \qquad \lambda \lesssim 310 \text{ nm} \tag{R 2.1}$$

$$O(^1D) + H_2O \longrightarrow 2\,OH \tag{R 2.2}$$

The tropospheric chemistry of O_3 is mainly tied to NO_x by the photolysis of nitrogen dioxide (NO_2):

$$NO_2 + h\nu \longrightarrow O(^3P) + NO \tag{R 2.3}$$

$$O(^3P) + O_2 + M \longrightarrow O_3 + M \tag{R 2.4}$$

O_3 formed in Reaction R 2.4 will react with NO to yield NO_2:

$$NO + O_3 \longrightarrow NO_2 + O_2 \tag{R 2.5}$$

Additionally, HC compounds undergo oxidation reactions which are mainly initiated by the OH radical and by direct photodissociation during the day time. OH plays a key role in tropospheric oxidation chemistry through its reactions with CO, CH_4 and higher HCs (RH):

$$OH + CO \longrightarrow H + CO_2 \tag{R 2.6}$$

$$OH + CH_4 \longrightarrow CH_3 + H_2O \tag{R 2.7}$$

$$OH + RH \longrightarrow R + H_2O \tag{R 2.8}$$

Peroxy radicals are formed by addition of O_2 to the radicals H, methyl (CH_3) and R generated in the primary step:

$$H + O_2 + M \longrightarrow HO_2 + M \tag{R 2.9}$$

$$CH_3 + O_2 + M \longrightarrow CH_3O_2 + M \tag{R 2.10}$$

$$R + O_2 + M \longrightarrow RO_2 + M \quad (R\,2.11)$$

If NO_x is present in the atmosphere, as it is in urban areas, peroxy radicals are removed by the following reactions, leading to O_3 production via NO_2 photolysis:

$$HO_2 + NO \longrightarrow OH + NO_2 \quad (R\,2.12)$$

$$CH_3O_2 + NO \longrightarrow CH_3O + NO_2 \quad (R\,2.13)$$

$$RO_2 + NO \longrightarrow RO + NO_2 \quad (R\,2.14)$$

OH is thus regenerated, and CH_3O and RO are formed. These in turn react with O_2, isomerise or decompose, disturbing the O_3–NO–NO_2 cycle:

$$CH_3O + O_2 \longrightarrow HCHO + HO_2 \quad (R\,2.15)$$

$$RO + O_2 \longrightarrow R'R''CO + HO_2 \quad (R\,2.16)$$

$$RO \longrightarrow R' + R''CHO \quad (R\,2.17)$$

The above reactions yield formaldehyde (HCHO), ketones ($R'R''CO$), or aldehydes ($R''CHO$). These products are either re–oxidised or photolysed leading to a chain mechanism (but they can also be lost through dry and wet depositions), with the peroxy radicals acting as important intermediate species. In this case, the O_3 production is dominated by the oxidation of CO, CH_4, and higher HCs in the presence of NO_x (Crutzen, 1973; Wennberg *et al.*, 1998; Lelieveld and Dentener, 2000), whereby the peroxy radicals formed in Reactions R 2.9, R 2.10, and R 2.11 react with NO to form NO_2, which is then photolysed to form an atom of ground state oxygen (O^3P), that with addition of O_2 produces O_3.

Conversely, in the background troposphere, where concentrations of NO_x are relatively low, O_3 is mainly subjected to chemical destruction, and the peroxy radicals mainly go through the following reactions:

$$HO_2 + HO_2 \longrightarrow H_2O_2 + O_2 \quad \text{(R 2.18)}$$

$$CH_3O_2 + HO_2 \longrightarrow CH_3OOH + O_2 \quad \text{(R 2.19)}$$

$$RO_2 + HO_2 \longrightarrow ROOH + O_2 \quad \text{(R 2.20)}$$

In remote regions, downward transport of O_3 from the stratosphere is the main tropospheric O_3 source. O_3 can also be transported from regions where it is chemically produced, due to its relatively long lifetime (from days to weeks). In general, fewer organic compounds are involved in O_3 chemical production in the SH.

Daytime tropospheric photochemical process in rich and poor NO_x environments is illustrated in Figure 2.3.

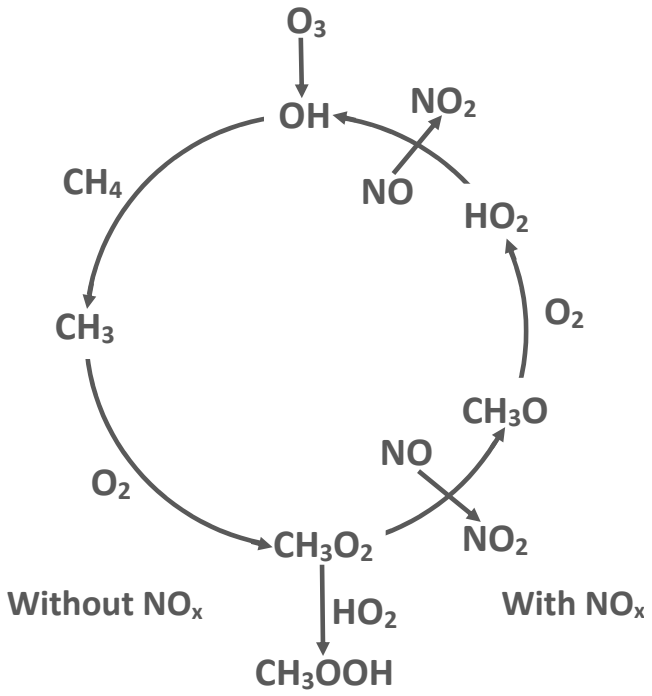

Figure 2.3: *Reduced daytime tropospheric photochemical process.*
Source: http://www.atmosp.physics.utoronto.ca/people/loic/Image34.jpg

In the stratosphere, O_3 absorbs UV radiation between wavelengths of about 200 to 315 nm (UVB and UVC radiation) as mentioned in the previous section. Average column densities of O_3 vary with season and latitude. The largest amounts of O_3 are found at polar latitudes in boreal spring in the NH, whereas the austral spring maximum occurs at mid–latitudes in the SH.

A series of reactions explain the production and destruction of atmospheric O_3, known as the Chapman cycle (Chapman, 1930). The cycle begins with the production of O_3 through O_2 photolysis (Reaction R 2.21) and the subsequent three–body reaction of the atomic oxygen formed in Reaction R 2.21 with O_2 (Reaction R 2.22):

$$O_2 + h\nu \longrightarrow O + O \qquad \text{(R 2.21)}$$

$$O + O_2 + M \longrightarrow O_3 + M \qquad \text{(R 2.22)}$$

Reaction R 2.22 is the dominant process for O_3 production in the stratosphere. Besides, direct loss of odd oxygen ($O_x = O + O_3$) is defined by Reactions R 2.23 and R 2.24, albeit not much in the lower stratosphere:

$$O + O_3 \longrightarrow 2\,O_2 \qquad \text{(R 2.23)}$$

$$O + O + M \longrightarrow O_2 + M \qquad \text{(R 2.24)}$$

However, reactions with trace constituents appear to be the major cause for the loss of stratospheric O_3, as they participate in catalytic processes that remove O_x (Crutzen, 1970; Johnston, 1971; Molina and Rowland, 1974; Stolarski and Cicerone, 1974). Catalytic destruction of stratospheric O_3 is a more efficient route of O_3 loss (Reactions R 2.25 and R 2.26). Here, 'X' denotes free–radical catalytic species, e.g. OH, Cl, Br, NO, etc. (The following reactions also apply to tropospheric O_3 loss):

$$X + O_3 \longrightarrow XO + O_2 \qquad \text{(R 2.25)}$$

$$XO + O \longrightarrow X + O_2 \qquad \text{(R 2.26)}$$

or

$$XO + O_3 \longrightarrow X + 2\,O_2$$

$$\text{Net:} \quad O + O_3 \longrightarrow O_2 + O_2 \qquad \text{(R 2.27)}$$

These catalytic reactions are responsible for the stratospheric O_3 loss or O_3 depletion. In particular, the "O_3 hole" that occurs over Antarctica in late winter/early spring owes its existence to stratospheric O_3 depletion by catalytic species (ODS). By the 1970s, halocarbons [common ones are CFCs, hydrochlorofluorocarbons (HCFCs), and bromofluorocarbons (halons)] were in broad industrial use as refrigerants, propellants, and solvents. These low–toxic and low–reactive chemicals were developed to replace HCs which were considered unsafe. However, they are transported to the stratosphere where they can undergo photolysis (due to increasing UV) despite their low reactivity, leading to an accelerated destruction of the O_3 layer (Reactions R 2.25 and R 2.26) (Chan and Chu, 2007). Therefore, increased UV penetration to the troposphere through stratospheric O_3 depletion increases the photolysis rate of O_3 [$jO(^1D)$], meaning that changes in $jO(^1D)$ have direct implications on tropospheric photochemistry via Reaction R 2.1 and the subsequent Reaction R 2.2. In the troposphere, increased $jO(^1D)$ leads to a more rapid destruction of O_3, and thus an enhancement of the OH concentration (Solomon *et al.*, 2003; Tang *et al.*, 2011; Madronich *et al.*, 2015).

The "O_3 hole" and the whole of the extratropical O_3 layer is predicted to recover during this century, largely as a result of the application of the Montreal Protocol, signed in 1987 (Newman *et al.*, 2006; Morgenstern *et al.*, 2008). The O_3 recovery implies the modification of j–rates affecting tropospheric composition.

Throughout Chapter 2, fundamental concepts relevant to the cleaning capacity of the atmosphere have been introduced. Section 2.1 has focused

on describing the parts of the atmosphere (troposphere and stratosphere) where O_3 and other trace gases have a direct or an indirect impact on the production of OH radicals. Radiation, which is responsible for driving photolysis reactions, and thus affecting tropospheric composition is introduced in Section 2.2. Finally, section 2.3 has outlined the photochemistry of O_3 and its link to the OH radical.

In this sense, tropospheric and stratospheric O_3 play an essential role in controlling the oxidising capacity of the atmosphere. Tropospheric O_3, largely because it is the *in–situ* primary source of OH radicals through photolysis and reaction with H_2O (Reactions R 2.1 and R 2.2). Likewise, stratospheric O_3 controls the production of OH radicals in the troposphere because of its impact on O_3 photolysis through absorption of UV radiation. The link between O_3 and OH is plausible: Reaction R 2.1 shows that a small amount of tropospheric O_3 and its photolysis controlled by the overhead O_3 column are essential to produce OH radicals. However, not only atmospheric O_3 is responsible for controlling the tropospheric oxidising capacity. Clouds also play a critical role in influencing tropospheric photochemistry through modification of solar radiation that determines j–rates (Thompson, 1984; Crawford *et al.*, 1999); j–rates values are enhanced above and in the upper levels of clouds, while they are decreased below optically thick clouds (Lefer *et al.*, 2003; Neu *et al.*, 2007). Since photolytical processes are the sources of free radicals such as OH, clouds also play an important role in determining the oxidation capacity of the atmosphere.

The high reactivity of OH associated with a very short lifetime explains the important cleansing role of this short–lived species compared to other oxidants. It controls the lifetime of many trace gases containing any H–C bond (e.g. CH_4) and initiates the oxidation of VOCs, which in the presence of NO_x, leads to tropospheric O_3 and smog formation. Nevertheless, only a few species are mostly driving the oxidising capacity of the atmosphere at Lauder, i.e. O_3, H_2O, CH_4, and CO (along with temperature), which will be the key forcings in the study presented here. An overview of the geographic

and atmospheric vertical distribution of these species is given as follows:

- **O_3** is found in low and high amounts in the troposphere and stratosphere (O_3 layer) respectively. Its geographical distribution is inhomogeneous, i.e. surface O_3 is higher in the NH than in the SH. At Lauder, O_3 is made up by stratosphere–troposphere exchange, from source regions where it is chemically produced, or through *in–situ* production from CH_4 oxidation (as stated previously in this section).

- **H_2O** is found in large quantities in the lower and middle troposphere, and decreases in the upper troposphere and stratosphere by orders of magnitude. In the tropics, H_2O concentrations are higher than in the extratropics, following somehow the temperature profile.

- **CH_4** is a very long–lived species (its lifetime is $\sim$ 9 years). Thus, it is vertically well mixed decreasing slightly with altitude. Its well–mixed nature means that there are also small variations on CH_4 concentrations across locations, with only a small inter–hemispheric gradient.

- **CO** has industrial (mainly fossil fuels), biomass burning, and biogenic sources. Its relatively long lifetime ($\sim$ 2 months) means that CO can be transported to Lauder through inter–hemispheric and hemispheric transport. There is also a vertical gradient, in which CO decreases from the surface to the upper troposphere.

Currently, efforts to improve the understanding of OH chemistry involves studying how the precursors to O_3 interact with each other and performing detailed measurements of trace gases in the atmosphere, such as those described above. Additionally, the use of atmospheric climate models has proven to be a valuable tool for the study of tropospheric O_3 and OH chemistry. Here, a single–column model has been constructed in order to assess how these key chemical species, i.e. O_3, H_2O, CH_4, CO (and also temperature), affect OH at one site, Lauder (Chapter 3).

Chapter 3

Models and methods of analysis

In order to assess how modelled OH is influenced by the processes that control its concentrations, here a simple chemistry model that mainly represents the fast aspects of tropospheric and stratospheric chemistry is presented. This chapter describes the construction of a SCM in order to assess the oxidising capacity of the atmosphere at the remote SH location, Lauder (Section 3.2). This chapter also introduces and describes a CCM used to build the SCM and a SSM for comparison with the SCM. They are presented in Sections 3.1 and 3.3 respectively.

3.1 The UKCA chemistry–climate model

In recent years, coupled CCMs have been developed in order to quantitatively describe how atmospheric temperature, air pressure, winds, H_2O, clouds, and precipitation all respond to solar heating of the Earth's surface and atmosphere. These responses are based on physical parameterisations such as convection, radiation, dry and wet depositions along with transport and the temporal evolution of the trace gases composition (Eyring *et al.*, 2005). CCMs represent the thermodynamics and chemistry of the atmosphere as a fully coupled system. Nevertheless,

the interpretation of results in CCMs can be more difficult than if processes are treated individually, as in the case of chemistry–transport models (CTMs) for chemistry, and global climate models (GCMs) for dynamical processes (Morgenstern *et al.*, 2010). Challenges in the development of CCMs include:

1. Dynamics:
   The core of most CCMs is a set of hydrostatic dynamical differential equations called either the primitive or the governing equations, which are the momentum, the continuity, and the thermodynamic energy equations (Holton, 2004).

   Although CCMs used by the international community are principally hydrostatic, non–hydrostatic CCMs have also been developed such as the UKCA CCM (Telford *et al.*, 2008), based on the dynamical core by Davies *et al.* (2005). Both hydrostatic and non–hydrostatic CCMs also use parameterisations to describe processes that are unresolved at the grid scale. (e.g. convection, boundary–layer processes, cloud physics).

2. Radiation:
   Photolysis reactions play a major role in driving the chemistry of the atmosphere by dissociating molecules that initiate the oxidation of many trace gases and drive radical chemistry (refer to Chapter 2.2). Therefore, modelling photolysis processes accurately becomes crucial in order to understand the chemistry of the atmosphere. There are usually two types of methods used to calculate photolysis rates in CCMs. One is the so–called off–line method which involves interpolation of photolysis rates using a pre–calculated table of photolysis rates as functions of e.g. pressure, SZA, overhead column for O_3, solar output, and often temperature (Lary and Pyle, 1991). The content is then read, interpolated with respect to the dimensions of the table, and used in the CCM. By contrast, in the online method the photolysis rate calculation is integrated into a GCM so that the

radiative transfer equation is calculated at the time of simulation accounting for variations in albedo, cloudiness, aerosols, and solar output unlike the off–line method, which considers the above parameters to be invariant during the simulation [e.g. Rasch *et al.* (1995); Chipperfield (1999)].

3. Chemistry and composition:
   Reactions between chemical compounds are described by a series of first–order ordinary differential equations, making the atmospheric chemical kinetics predictable compared to atmospheric dynamics which introduce chaos into the climate system (see Chapter 2.3 for details in tropospheric reactions). The number of chemical species typically used varies considerably in CCMs, but is always much smaller than the actual number of chemical compounds found in the atmosphere.

   Since the cost of computation of CCMs is very high (the cost is usually dominated by chemistry), some models aim to either simplify the chemistry of the troposphere or even to fully prescribe tropospheric constituents, i.e. stratospheric CTMs which represent stratospheric O_3 (Chipperfield, 1999; McLinden *et al.*, 2000) as the coupling between dynamics and O_3 chemistry in the troposphere is weaker than in the stratosphere. By contrast, other CCMs evaluate the tropospheric composition as part of the total calculation, e.g. UKCA CCM (O'Connor *et al.*, 2014). Despite the high cost of the computation of CCMs they are an essential tool to provide information on the global evolution of the atmospheric composition.

The UKCA CCM[1] runs within the Met Office's Unified Model (MetUM) (Swinbank *et al.*, 1998; Telford *et al.*, 2008; Dixon *et al.*, 2009) and has been coupled to the HadGEM1 (Johns *et al.*, 2006; Martin *et al.*, 2006), HadGEM2 (Collins *et al.*, 2011; Jones *et al.*, 2011; Martin *et al.*,

[1] http://www.ukca.ac.uk

2011), and HadGEM3 (Hewitt *et al.*, 2011) models. It is a comprehensive chemistry and aerosol model capable of reproducing the troposphere and stratosphere. Therefore, it has various configurations which are described in several papers: Morgenstern *et al.* (2009) evaluate the chemical composition of the stratosphere. O'Connor *et al.* (2014) evaluate tropospheric chemistry, and Mann *et al.* (2010) evaluate the GLOMAP–mode aerosol scheme which now forms part of the UKCA CCM. Moreover, Telford *et al.* (2013) implemented the FAST–JX photolysis scheme (as described in Subsection 3.2.1 of Section 3.2) into the UKCA CCM.

The tropospheric scheme by O'Connor *et al.* (2014) performs well for global and zonal mean distributions of CO, CH_4, and NO_x relative to observations. It also produces O_3 concentrations that are consistent with other models and with ozonesonde observations for the mid– and upper–troposphere. However, it does less well in reproducing surface O_3 concentrations maybe due to incomplete NMVOC chemistry (e.g. isoprene chemistry). This suggests that the tropospheric scheme of the UKCA CCM by (O'Connor *et al.*, 2014) is suitable from a climate perspective but unsuitable for air quality purposes. The stratospheric scheme in the UKCA CCM (Morgenstern *et al.*, 2009) is a comprehensive description of stratospheric chemistry, including bromine and chlorine chemistry, heterogeneous processes on Polar Stratospheric Clouds (PSCs), and liquid sulfate aerosols. The model reproduces the mean meteorological state of the stratosphere almost everywhere except for the tropical tropopause. Likewise, stratospheric chemistry resembles observations.

The UKCA CCM is a non–hydrostatic CCM, configured with 60 levels from the surface up to 84 km, and a horizontal resolution of 3.75^{o} x 2.5^{o} in longitude and latitude (Hardiman *et al.*, 2010). The dynamical core is that of Davies *et al.* (2005) and the vertical coordinate system in the model is hybrid–height. The UKCA CCM version used here is 7.3 and is similar to that by Morgenstern *et al.* (2013) and Telford *et al.* (2013). Its tropospheric configuration is "standard" tropospheric chemistry including

the isoprene chemistry by Pöschl *et al.* (2000). NMVOCs source gases include ethane (C_2H_6), propane (C_3H_6), acetone (CH_3COCH_3), HCHO, acetaldehyde (CH_3CHO), and isoprene (C_5H_8). Other source gases are CO and NO_x. CH_4 is largely prescribed at the surface (i.e. CH_4 emissions are not used) (Morgenstern *et al.*, 2013). In the stratosphere, it includes the comprehensive stratospheric chemistry as described in Morgenstern *et al.* (2009). By contrast to Morgenstern *et al.* (2009), it includes an online photolysis scheme (FAST–JX) (Neu *et al.*, 2007; Telford *et al.*, 2013) which is described in detail in the next section. Telford *et al.* (2013) states that photolysis rate values improve from those of the off–line methods used in the previous versions in comparison with observations and other models. However, the model now produces too much global OH, which itself affects CO concentrations and CH_4 lifetime. This is believed to be a result of a previous cancellation of errors in the off–line method, which now has been removed in FAST–JX.

For the analyses of the OH sensitivity to biases in the key forcings, archived run information from the UKCA CCM was used. Throughout all the thesis, there are well supported statements regarding the performance of the UKCA CCM version used in this thesis, where comparisons of UKCA fields in O_3, H_2O, CH_4, CO, and temperature were compared to observations (Chapters 4 and 5).

3.2 The NZAC single–column model

SCMs (or 1–D models) simulate the time evolution of a single atmospheric column. They differ from CCMs, since the interactions with the circulation dynamics are neglected. This simplification and the use of only one column in the simulations make SCMs economic to run, since they allow the study of hypotheses and processes that would be far more costly to explore if a CCM was employed. Modelling the atmospheric boundary layer with SCMs is commonly used (Mihailovic *et al.*, 2005; Cuxart *et al.*, 2006), as well as the development and evaluation of diabatic processes (Randall

et al., 2003; Bergman and Sardeshmukh, 2004), the impact of GHG emissions on climate change (Vupputuri *et al.*, 1995), cloud processes (Kylling *et al.*, 2005), and the chemistry of halogen compounds (Piot and von Glasow, 2008; Joyce *et al.*, 2014).

The NZAC SCM developed in this thesis is a simplified version of the UKCA CCM in which only photolysis and chemical kinetics are included. The NZAC SCM configuration is that of the UKCA CCM with a 60–σ–level vertical coordinate and a maximum altitude level of around 84 km in the upper atmosphere. The forcing data for the SCM consists of long–term profile series of temperature, pressure, clouds (if prescribed) and 86 chemical compounds (e.g. O_3). The work carried out in this thesis aims to simulate the short–lived OH radical in the troposphere with a lifetime of $\sim$ 1 second (Prinn, 2001; Elshorbany *et al.*, 2012), much shorter than the chemical step of 1 hour typically used in the UKCA CCM. Thus, the time step used in the NZAC model is 20 minutes which is sufficient to numerically solve differential equations of the chemical reactions involving the OH radical. Several runs have been carried out according to the number of forcings that are directly or indirectly involved in the OH oxidation. A detailed description of the results obtained from the NZAC SCM is given in Chapters 5 and 6.

The NZAC SCM includes the FAST–JX photolysis scheme and a chemical integration package, which are described in the following subsections (3.2.1 and 3.2.2) respectively.

3.2.1 FAST–JX photolysis scheme

The FAST–JX interactive photolysis scheme[2] is an updated version of the FAST–J code by Wild *et al.* (2000) which efficiently estimates tropospheric photolysis rates under clear–sky, cloudy and aerosol conditions. Wild *et al.* (2000) designed 7 wavelength bins between 289 – 850 nm to discretise the

[2]Code available in http://www.ess.uci.edu/∼prather

solar spectrum (wavelengths shorter than 289 nm are assumed to be attenuated above the tropopause) that allowed calculations to be performed faster. A second approach developed by Bian and Prather (2002), FAST–J2, is an 11–bin extension of the FAST–J scheme into the stratosphere and lower mesosphere (up to 60 km) encompassing wavelengths between 177 and 291 nm. FAST–JX is a further development on FAST–J2, providing the full scattering calculations for the total 18 wavelength bins (Neu *et al.*, 2007) (stratospheric scattering had been ignored in FAST–J2). FAST–JX is much more economic than other radiative models that usually employ more than 170 wavelength bins.

FAST–JX introduces several improvements with respect to FAST–J2. One is the addition of a new and more efficient algorithm (cloud overlap scheme) that adds in more levels in order to solve the radiative transfer problem in optically dense clouds. In this scheme, for each column affected by clouds, a set of random distributions of clouds is generated and the radiative transfer is calculated for every member of the set. The resulting actinic fluxes are then averaged for the photolysis rate calculation. Moreover, solar fluxes and cross sections have been updated in FAST–JX. The photolysis scheme returns the photolysis rates of 59 chemical species (Table B.1 of Appendix B).

FAST–JX has been compared to observations in the past. Voulgarakis *et al.* (2009) assessed surface $j\mathrm{NO_2}$ and $j\mathrm{O}(^1\mathrm{D})$ obtained from FAST–JX and compared them to WAOSE'95 observations. Telford *et al.* (2013) compared both FAST–JX $j\mathrm{NO_2}$ and $j\mathrm{O}(^1\mathrm{D})$ to observations collected during a flight in the INTEX–NA campaign. FAST–JX has been implemented in a few models like p–TOMCAT CTM (Voulgarakis *et al.*, 2009), UKCA CCM (Telford *et al.*, 2013), and Polair3D CTM (Real and Sartelet, 2011).

3.2.2 Chemical integration package

The NZAC SCM uses a chemical integration package which contains: A chemical mechanism comprising chemical species and gas–phase reactions to be defined as input tables, the 'A self–contained atmospheric chemistry code' (ASAD) package[3], and the Newton–Raphson solver.

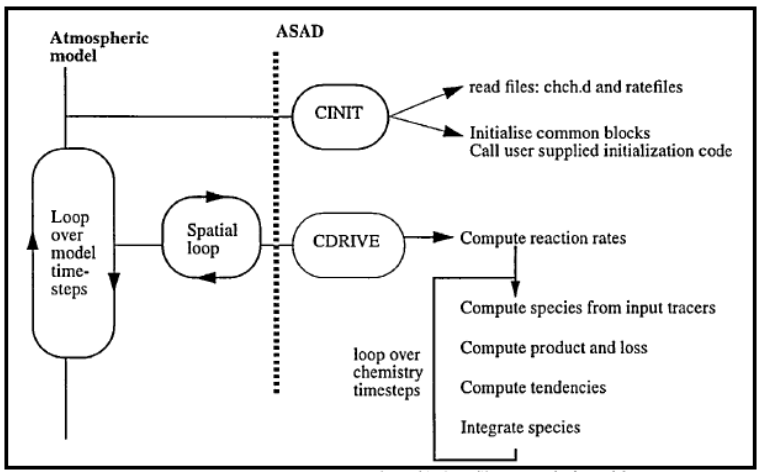

Figure 3.1: *Flow diagram of ASAD being called from a CCM. Source: [Carver* et al. *(1997)].*

ASAD (Carver *et al.*, 1997) was originally developed based on the DELOAD program (Nejad, 1986) and the UMIST database (Millar *et al.*, 1991). It is responsible for computing and integrating forward in time the production and loss chemical rates of change by using information from the chemical reactions defined in the input tables, and also from ground emission and deposition schemes. Since ASAD uses these input tables of chemical reactions, very little programming is required, programming errors are less likely to occur and times of development are reduced. Thus, it is easy to be implemented in box models, 1–D, 2–D and 3–D models. For example, ASAD has been implemented in some CCMs like the CLaMS

[3]http://www.atm.ch.cam.ac.uk/acmsu/asad/

modular CTM (McKenna *et al.*, 2002) and the UKCA CCM [e.g. Morgenstern *et al.* (2009)].

The calling model calls the subroutine CINIT to initialise ASAD by reading in the input tables and producing constants and common variables. In the model's time loop, the main subroutine CDRIVE is called and computes the reaction rates, controlling the chemical substeps and solution of the chemistry kinetic equations. The solution obtained from ASAD is passed back to the main code of the calling model (Figure 3.1).

The local rate of change of a species eventually computed by the CCM is described as per Equation 3.1:

$$\frac{\partial y}{\partial t} = \frac{dy}{dt} - \vec{u}\vec{\nabla}y \tag{3.1}$$

where y is the chemical species, t is the time, and $\vec{u}$ is the velocity vector. The first term ($\frac{dy}{dt}$) is the sum of the rates of change of a species due to chemistry, surface emission and depositions, where emissions and depositions are only evaluated by ASAD if the information is supplied (surface emissions and depositions are not considered in the NZAC SCM). The second term ($\vec{u}\vec{\nabla}y$) accounts for the rate of change of a species due to transport which is provided by the CCM; this is also ignored in the NZAC SCM.

Additionally, it uses approximations for one steady–state species [O(^{1}D)] and fractional products when complex reactions are present. Chemical reactions are tabulated in four different tables representing bimolecular, termolecular, photolysis, and heterogeneous reactions, in which the respective reaction rates are calculated as shown below:

1. Bimolecular reactions:

$$k = k_0 \left(\frac{T}{300}\right)^{\alpha} exp\left(\frac{-\beta}{T}\right) \tag{3.2}$$

where k is the rate coefficient in cm^{-3} s^{-1}, T is the temperature in Kelvin (°K), k_0 is the pre–exponential factor in cm^{-3} s^{-1}, and α, β are constants that define the dependence of the reactions rates (k) on temperature. k_0, α, and β are specified in the input table.

2. Termolecular and unimolecular reactions:

$$k = \left(\frac{k_0[\mathrm{M}]}{1 + k_0[\mathrm{M}]/k_\infty} \right) F_c^{(1+(log k_0[\mathrm{M}]/k_\infty)^2)^{-1}} \tag{3.3a}$$

where k is the rate coefficient in cm^{-3} s^{-1}, [M] is the concentration of the third body (molec/cm^3), and F_c is usually a constant value. However, F_c can present a certain temperature dependence and then the expression that defines it is Equation 3.3 b:

$$F_c = exp(-T/f) \tag{3.3b}$$

where f is a parameter that defines the dependence of F_c on temperature and is specified in the rate table. k_0 and k_∞ are the low and high pressure rate constants, described by Equations 3.3 c and 3.3 d as follows:

$$k_0 = k_1 \left(\frac{T}{300} \right)^{\alpha_1} exp\left(\frac{-\beta_1}{T} \right) \tag{3.3c}$$

$$k_\infty = k_2 \left(\frac{T}{300} \right)^{\alpha_2} exp\left(\frac{-\beta_2}{T} \right) \tag{3.3d}$$

where k_1, k_2 are pre–exponential factors, and α_1, β_1, α_2, β_2 are constants that define the dependence of the low and high pressure rate constants (k_0 and k_∞) on temperature. These parameters are specified in the rate table.

3. Photolysis rates are calculated online by FAST–JX, which uses tabulated information on cross sections and a listing of photolysis reactions.

4. Heterogeneous reaction rates are not tabulated but rather are hard–coded in both the UKCA CCM and the NZAC SCM.

For detailed technical information of the ASAD package, refer to Carver *et al.* (1997).

The NZAC SCM also uses the Newton–Raphson solver for chemistry once the reaction rates have been provided by ASAD. For this, the discretized system of chemical kinetics equations $[x^{i+1} = F(x^i)]$ is reformulated into a form $\Phi(x^{i+1}) = 0$. Let $\mathbf{D}$ be its Jacobian matrix $[(\mathbf{D} = (\partial\Phi_i/\partial x_j)]$, then the solution to the next timestep is obtained through the following iterative expression until convergence is achieved:

$$x_{n+1} = x_n - \mathbf{D}^{-1}(x_n)\Phi(x_n) \tag{3.4}$$

If the expression above does not converge, the process is repeated but with a halved timestep, i.e. the model uses adaptive timestep adjustment. The solution of Equation 3.4 is the final concentration of the chemical species.

The NZAC SCM contains 232 different chemical reactions (Tables C.1, C.2, and C.3 in Appendix C) to be used by ASAD, and uses the photolysis rates provided by the FAST–JX photolysis scheme (Table B.1 in Appendix B). The information of the kinetic rates are then passed to the Newton–Raphson solver for chemistry.

3.3 Steady–state model

The steady–state or stationary–state approximation is a method that is based on the assumption that the source and sink terms of a species are equal. In this work, the SSM was used to verify that the NZAC SCM produces reasonable results for OH. The steady–state assumption simply means that production equals loss for a species, i.e. the rate of change equals zero. This applies to short–lived species such as OH, since the lifetime for

the loss of these species is shorter than the timescale on which the sources are varying (Brasseur *et al.*, 1999; Brown *et al.*, 2003). Therefore, it is assumed that the first step of the reaction is relatively slow and it is the one that determines the rate of the total reaction (Reaction R 3.1). Reactions R 3.1 describe the simplified process in two steps:

$$\begin{aligned} \mathrm{A} &\xrightarrow{k'} \mathrm{X} \quad \textit{slow step 1} \\ \mathrm{X} &\xrightarrow{k''} \mathrm{B} \quad \textit{fast step 2} \end{aligned} \tag{R 3.1}$$

where A and B are the reactants and the product species respectively, X is the intermediate species, and k' and k'' are the rate coefficients.

Because of the complexity and variability of reactions that are carried out in the atmosphere, steady–state approximations for the troposphere have been made to convert its complexity into a simple chemical model system which can be solved analytically. This section outlines the development of a SSM for the troposphere, which aims to fulfill the steady–state approximations that describe the oxidising capacity of the atmosphere. Several studies have developed steady–state approximations to determine the concentration of different species such as the nitrate radical (NO_3) and dinitrogen pentoxide (N_2O_5) (Martínez *et al.*, 2000; Brown *et al.*, 2003), to evaluate the production of O_3 to changes in NO and HCs (Kleinman *et al.*, 1997), or to assess the uncertainty of the measured peroxy radicals with those from the steady–state calculations (Cantrell *et al.*, 1997). The application of the steady–state assumption to OH is described step by step as follows:

The OH and HO_2 radicals are central to the photochemistry of the atmosphere as part of the HO_x family (Chapter 2). Therefore, the reactions of importance that have been taken into account in the steady–state model are only those which dominate the production and loss of HO_x in the troposphere. The rest of the reactions become negligible for simplification in order to avoid the formation of complex algebraic expressions. A reduced reaction scheme for HO_x in the troposphere

includes:

- **Breakdown of main source reactions for HO_x**

$$CH_3OO + NO \xrightarrow[+\,O_2]{k_1} HO_2 + HCHO + NO_2 \qquad (R\,3.2)$$

$$O(^1D) + H_2O \xrightarrow{k_2} 2\,OH \qquad (R\,3.3)$$

$$H_2O_2 + h\nu \xrightarrow{j_1} 2\,OH \qquad (R\,3.4)$$

$$HCHO + h\nu \xrightarrow[+\,2\,O_2]{j_2} 2\,HO_2 + CO \qquad (R\,3.5)$$

Reaction R 3.3 is the same as Reaction R 2.2.

- **Breakdown of main sink reactions for HO_x**

$$2\,HO_2 \xrightarrow{k_3} H_2O_2 + O_2 \qquad (R\,3.6)$$

$$HO_2 + CH_3O_2 \xrightarrow{k_4} CH_3OOH + O_2 \qquad (R\,3.7)$$

$$HO_2 + CH_3O_2 \xrightarrow{k_5} HCHO + H_2O + O_2 \qquad (R\,3.8)$$

$$OH + CH_4 \xrightarrow[+\,O_2]{k_6} H_2O + CH_3O_2 \qquad (R\,3.9)$$

$$OH + HO_2 \xrightarrow{k_7} H_2O + O_2 \qquad (R\,3.10)$$

$$HO_2 + NO_2 + M \xrightarrow{k_8} HO_2NO_2 + M \qquad (R\,3.11)$$

$$2\,HO_2 + M \xrightarrow{k_9} H_2O_2 + O_2 + M \qquad (R\,3.12)$$

Reactions R 3.6, R 3.7, and R 3.9 are the same as Reactions R 2.18, R 2.19, and R 2.7 respectively.

Likewise, the OH and HO_2 radicals can be treated separately like individual members of the family with their source and sink reactions:

- **Breakdown of main source reactions for HO_2**

$$H + O_2 + M \xrightarrow{k_{10}} HO_2 + M \qquad (R\,3.13)$$

$$O_3 + OH \xrightarrow{k_{11}} HO_2 + O_2 \qquad (R\,3.14)$$

Reaction R 3.13 is the same as Reaction R 2.9.

- **Breakdown of main sink reactions for HO_2**

$$NO + HO_2 \xrightarrow{k_{12}} OH + NO_2 \quad \text{(R 3.15)}$$

$$HO_2 + O_3 \xrightarrow{k_{13}} OH + 2\,O_2 \quad \text{(R 3.16)}$$

Reaction R 3.15 is the same as Reaction R 2.12.

- **Breakdown of main source reactions for OH**

$$O(^1D) + H_2O \xrightarrow{k_2} 2\,OH \quad \text{(R 3.17)}$$

$$HO_2 + NO \xrightarrow{k_{12}} OH + NO_2 \quad \text{(R 3.18)}$$

$$HO_2 + O_3 \xrightarrow{k_{13}} OH + 2\,O_2 \quad \text{(R 3.19)}$$

$$H + O_3 \xrightarrow{k_{14}} OH + O_2 \quad \text{(R 3.20)}$$

Reactions R 3.17, R 3.18, and R 3.19 are the same as Reactions R 3.3, R 3.15, and R 3.16 respectively.

- **Breakdown of main sink reactions for OH**

$$OH + CH_4 \xrightarrow[+\,O_2]{k_6} H_2O + CH_3O_2 \quad \text{(R 3.21)}$$

$$OH + CO \xrightarrow{k_{15}} H + CO_2 \quad \text{(R 3.22)}$$

$$OH + HCHO \xrightarrow[+\,O_2]{k_{16}} H_2O + HO_2 + CO \quad \text{(R 3.23)}$$

$$OH + O_3 \xrightarrow{k_{11}} HO_2 + O_2 \quad \text{(R 3.24)}$$

Reactions R 3.21 and R 3.24 are the same as Reactions R 3.9 and R 3.14 respectively. Likewise, Reaction R 3.22 is the same as Reaction R 2.6.

H, as part of the HO_x family should be treated accordingly. Thus, H from Reactions R 3.13 and R 3.20 can be replaced by the main source and sink reactions for H (Reactions R 3.25 and R 3.26) respectively,

- **Main source reaction for H**

$$OH + CO \xrightarrow{k_{15}} H + CO_2 \quad \text{(R 3.25)}$$

- **Main sink reaction for H**

$$H + O_2 + M \xrightarrow{k_{10}} HO_2 + M \qquad (R\,3.26)$$

Reaction R 3.25 and R 3.26 are the same as Reactions R 3.22 and R 3.13 respectively.

If a steady–state is assumed in OH, HO_2, and HO_x, the production (P) and loss (L) for the former species are approximately equal due to the equilibrium with the intermediate species. Therefore, the concentrations of OH, HO_2, and HO_x in the troposphere can be established according to the following steady–state approximations in which P = L for HO_x (Equations 3.5 a and b),

$$\begin{aligned} P_{HO_x} = {} & k_1[CH_3OO][NO] + 2k_2[O(^1D)][H_2O] + 2j_1[H_2O_2] \\ & + 2j_2[HCHO] \end{aligned} \qquad (3.5a)$$

$$\begin{aligned} L_{HO_x} = {} & 2k_3[HO_2]^2 + k_4[HO_2][CH_3OO] + k_5[HO_2][CH_3OO] \\ & + k_6[OH][CH_4] + 2k_7[OH][HO_2] + k_8[HO_2][NO_2][M] \\ & + 2k_9[HO_2]^2[M] \end{aligned} \qquad (3.5b)$$

for the HO_2 radical (Equations 3.6 a and b),

$$P_{HO_2} = k_{15}[OH][CO] + k_{11}[O_3][OH] \qquad (3.6a)$$

$$L_{HO_2} = k_{12}[NO][HO_2] + k_{13}[HO_2][O_3] \qquad (3.6b)$$

and for the OH radical (Equations 3.7 a and b),

$$\begin{aligned} P_{OH} = {} & 2k_2[O(^1D)][H_2O] \; + k_{12}[HO_2][NO] + k_{13}[HO_2][O_3] \\ & + k_{14}\frac{k_{15}[OH][CO]}{k_{10}[O_2][M]}[O_3] \end{aligned} \qquad (3.7a)$$

$$\begin{aligned} L_{OH} = {} & k_6[CH_4][OH] + k_{15}[CO][OH] + k_{16}[HCHO][OH] \\ & + k_{11}[O_3][OH] \end{aligned} \qquad (3.7b)$$

where k_i is the rate coefficient for each reation.

By setting the ratio of the family members (R) in the expressions 3.5 and 3.6 to be equal, where R is $[OH]/[HO_2]$, the concentration of HO_2 can be deduced from a resulting quadratic equation expressed by,

$$\begin{aligned} Y = &(Zk_7 + 2k_9[M] + 2k_3)[HO_2]^2 \\ &+ (Zk_6[CH_4] + k_8[NO_2][M] + (k_4 + k_5)[CH_3OO])[HO_2] \end{aligned} \tag{3.8a}$$

where Z is,

$$Z = \frac{k_{12}[NO] + k_{13}[O_3]}{k_{15}[CO] + k_{11}[O_3]} \tag{3.8b}$$

and Y is,

$$\begin{aligned} Y = &k_1[CH_3OO][NO] + 2k_2[O(^1D)][H_2O] + 2j_1[H_2O_2] \\ &+ 2j_2[HCHO] \end{aligned} \tag{3.8c}$$

Likewise, the OH concentration is derived by setting Equations 3.6 a and b to be equal, where HO_2 is substituted by the HO_2 concentration obtained through the quadratic equation 3.8a. The expression for OH is then described by Equation 3.9. Note that the procedure to obtain both HO_2 and OH concentrations is equivalent to also using expressions 3.5 and 3.7.

$$[OH] = \frac{k_{12}[NO][HO_2] + k_{13}[O_3][HO_2]}{k_{15}[CO] + k_{11}[O_3]} \tag{3.9}$$

The target of the construction of a simple SSM for the troposphere was to test the accuracy of the NZAC SCM to a steady–state approximation. Hence, the sensitivity of the OH radical to varying different fields was also evaluated by the SSM through Equation 3.10, where X are the species O_3, H_2O, CH_4, and CO, but also temperature.

$$\frac{d[OH]}{d[X]} = \frac{\partial[OH]}{\partial[X]} + \frac{\partial[HO_2]}{\partial[X]}\frac{\partial[OH]}{\partial[HO_2]} + \frac{\partial[H]}{\partial[X]}\frac{\partial[OH]}{\partial[H]} \tag{3.10}$$

More terms could be added to expression 3.10 since other species play a role in the sensitivity of the OH radical to X. Given that the NZAC SCM was run with data from a very clean–air site (Lauder), and there were no additional observational data to constrain other species, Equation 3.10 was considered sufficient to represent the sensitivity of OH to X. A clear example would be the sensitivity of OH to O_3 variations, since the photochemical production of O_3 in the troposphere is mainly tied to the NO_x family by the photolysis of NO_2 (Reaction R 2.3) (Farrow and Graedel, 1977). Nevertheless, in urban areas, the only significant chemical sources of O_3 in the troposphere are from the reactions of peroxy radicals with NO producing NO_2 (Reactions R 2.12, R 2.13, R 2.14) (Kleinman *et al.*, 1997). In this case the sensitivity of OH to O_3 is expressed by Equation 3.11, but for the reasons stated above, the last term of Equation 3.11 was neglected from calculations.

$$\frac{d[\mathrm{OH}]}{d[\mathrm{O_3}]} = \frac{\partial[\mathrm{OH}]}{\partial[\mathrm{O_3}]} + \frac{\partial[\mathrm{HO_2}]}{\partial[\mathrm{O_3}]}\frac{\partial[\mathrm{OH}]}{\partial[\mathrm{HO_2}]} + \frac{\partial[\mathrm{H}]}{\partial[\mathrm{O_3}]}\frac{\partial[\mathrm{OH}]}{\partial[\mathrm{H}]} + \frac{\partial[\mathrm{OH}]}{\partial[\mathrm{NO_2}]}\frac{\partial[\mathrm{NO_2}]}{\partial[\mathrm{O_3}]} \quad (3.11)$$

Comparisons of the sensitivity of OH to X solved by the SSM have been made to those obtained by the NZAC SCM. The results of these comparisons are fully explained in Chapter 5.

3.4 Methodology

Within the context of this work, a SCM for Lauder was developed (NZAC SCM) using the interactive FAST–JX photolysis scheme (Neu *et al.*, 2007; Telford *et al.*, 2013) and the chemical integration package as provided by the UKCA CCM (Morgenstern *et al.*, 2013) (refer to Subsections 3.2.1 and 3.2.2). In this case, the interaction with circulation dynamics is neglected and thus, only the fast photochemical processes of one single column are considered. The NZAC SCM construction process entailed adapting the UKCA CCM code by Morgenstern *et al.* (2013) [including FAST–JX by

Neu *et al.* (2007) and Telford *et al.* (2013)], to a wrapper program[4] written in FORTRAN90 which calls the UKCA CCM main module. An executable was thus created to perform simulations with the NZAC SCM. An schematic representing how the NZAC SCM code operates is displayed in Figure 3.2.

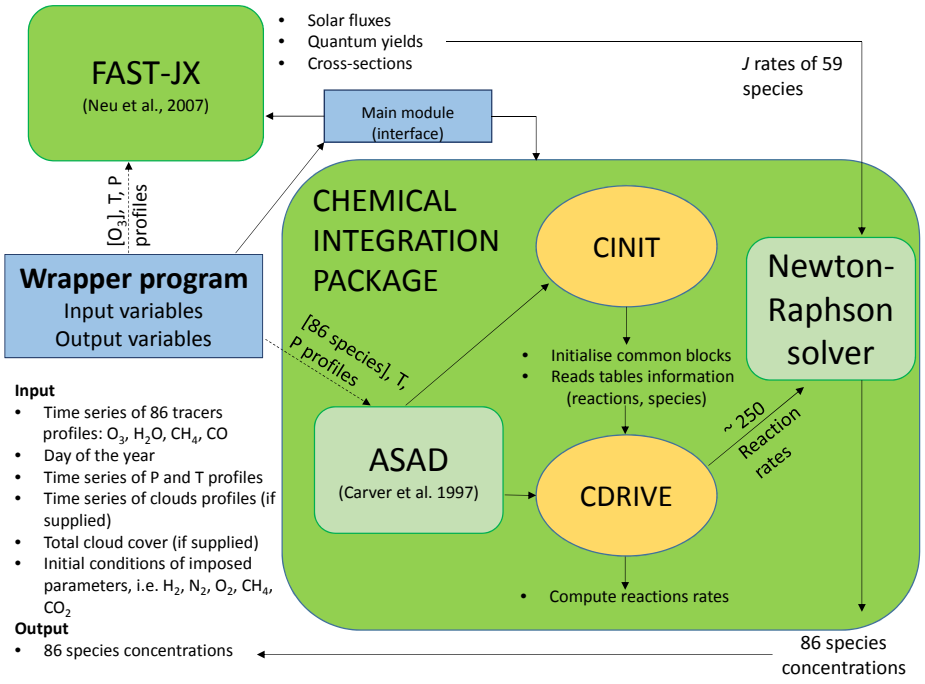

Figure 3.2: *Flow chart illustrating how the NZAC SCM code operates.*

The wrapper program includes constant values for imposed parameters in the model (e.g. N_2), and information on profile time series of all the input data, i.e. temperature, pressure, altitude levels, initial concentrations of 86 species, ice and liquid clouds (if supplied), and total cloud cover (if supplied). The information provided by the wrapper program is passed onto the main module of the UKCA CCM. As per Figure 3.2, FAST–JX requires O_3, clouds (if supplied), temperature, and pressure profiles as

[4]A wrapper program is a program that runs the standard program.

provided by the wrapper program, in order to calculate the photolysis rates of 59 species (Table B.1 of Appendix B). The wrapper program also provides the chemistry integration package with information on 86 species initial concentrations, temperature, and pressure profiles. The chemistry integration package includes tabulated information on chemical species and 232 chemical reactions (Tables C.1, C.2, and C.3 in Appendix C), the ASAD package which calculates the reaction rates of these chemical reactions, and the Newton–Raphson solver for the calculation of the 86 chemical species final concentrations (refer to Subsection 3.2.2), which are finally stored by the wrapper program.

For the forcings relevant to the study conducted in this thesis (O_3, H_2O, CH_4, CO, and temperature), long–term profile time series were produced by using measurements from Lauder (e.g. ozonesondes), the Cape Grim station (Tasmania), and data from the European Centre for Medium–Range Weather Forecasts (ECMWF) Re–analyses–Interim (hereafter ERAI)[5], described in Chapter 4. UKCA CCM output data were used for the rest of the forcings required by the NZAC SCM and to complement some of the measurements profiles.

Several simulations (single– and multiple–perturbation runs) were performed using the prescribed forcings for the study of the OH sensitivity to chemistry–climate model biases under clear–sky conditions. For that, long–time series of measurements encompassing the period between 1994 and 2010 were used to constrain the NZAC SCM. A reference simulation was also produced using only output data from the UKCA CCM. The information of the different NZAC SCM runs performed under clear–sky conditions in order to assess the OH sensitivity to correcting biases in the key forcings is summarised in Table 3.1.

[5]http://ecmwf.int/products/data/

NZAC SCM : Clear-sky conditions (1994 – 2010)	
Forcings	**Data used**
O_3	**1. Kinetics effect:** O_3 changes → ozonesondes (0-25 km) + MOPI1 (26-84 km). UKCA data for other species and temperature. **2. Photolysis effect:** jO(^{1}D) changes according to O_3 changes. UKCA data for all species and temperature. **3. Kinetics + photolysis effects:** O_3 changes → ozonesondes + MOPI1. jO(^{1}D) changes according to O_3 changes. UKCA data for other species and temperature.
H_2O	**1.** Changes in H_2O → radiosondes (0-8 km) + UKCA H_2O (9-84 km). UKCA data for other species and temperature. **2.** Changes in H_2O → ERAI (0-8 km) + UKCA H_2O (9-84 km). UKCA data for other species and temperature.
CH_4	Changes in CH_4 → rescaled UKCA CH_4 to Cape Grim surface CH_4. UKCA data for other species and temperature.
CO	Changes in CO → rescaled UKCA CO to FTIR CO. UKCA data for other species and temperature.
Temperature	**1. Kinetics effect:** T changes → radiosondes (0-25 km) + MOPI1 (26-84 km). UKCA data for all species. **2. Photolysis effect:** jO(^{1}D) changes according to T changes. UKCA data for all species and temperature. **3. Kinetics + photolysis effects:** T changes → radiosondes + MOPI1. jO(^{1}D) changes according to T changes. UKCA data for all species.
O_3, H_2O, CH_4, CO, Temperature	**1.** Changes in O_3, H_2O, CH_4, CO, and temperature using observations mentioned above. For H_2O, radiosonde (0-8 km) + UKCA (9-84 km) data are used. **2.** Changes in O_3, H_2O, CH_4, CO, and temperature using observations mentioned above. For H_2O, ERAI (0-8 km) + UKCA (9-84 km) data are used.
Reference	UKCA data for all species and temperature.

Table 3.1: *Sensitivity simulations performed with the NZAC SCM to assess the contribution of changes in the key forcings to OH chemistry at Lauder under clear–sky conditions. The table includes the type of measurement / data set used to prescribe the key forcings. The time period of simulation encompasses the time frame between 1994 and 2010.*

An additional analysis entailed assessing the OH variations and trends under clear–sky conditions. Thus, two multiple–perturbation runs were conducted in addition to the reference run (Table 3.2). The constraining time period spans the time frame from 1986 to 2012.

NZAC SCM : Clear-sky conditions (1986 – 2012)	
Forcings	**Data used**
O_3, H_2O, CH_4, CO, Temperature	Changes in O_3, H_2O, CH_4, CO, and temperature using observations (see Table 3.1). For H_2O, radiosonde (0-8 km) + UKCA (9-84 km) data are used.
O_3, H_2O, CH_4, CO, Temperature	Changes in O_3, H_2O, CH_4, CO, and temperature using observations (see Table 3.1). For H_2O, ERAI (0-8 km) + UKCA (9-84 km) data are used.
Reference	UKCA data for all species and temperature.

Table 3.2: *Simulations performed with the NZAC SCM to assess the variability and trends of OH at Lauder under clear–sky conditions. The time period of simulation encompasses the time frame between 1986 and 2012.*

Furthermore, a separate study was conducted to assess how photolysis rates and OH are affected by the the presence of clouds. To do this, the NZAC SCM was constrained with UKCA CCM output data for ice and liquid water clouds profiles, and total cloud cover. A cloud–free simulation was also produced to be compared with the simulations considering cloud effects (Table 3.3). For all the sensitivity simulations conducted in this thesis (including the simulations performed in cloudy conditions), the input data were read in at the time of the ozonesonde measurements

(approximately once per week). Therefore, the constraining measurements / data sets and UKCA output data were adjusted to follow ozonesonde observations. The results of the analyses conducted under clear–sky conditions are given in Chapter 5, whereas the results of the simulations run under cloudy conditions are given in Chapter 6.

NZAC SCM : Cloudy conditions (1986 – 2012)	
Forcings	**Data used**
Ice clouds	Ice clouds → UKCA data. Liquid clouds are set to 0. UKCA data for all species and temperature.
Liquid clouds	Liquid clouds → UKCA data. Ice clouds are set to 0. UKCA data for all species and temperature.
Ice + Liquid clouds	Ice + liquid clouds → UKCA data. UKCA data for all species and temperature.
Reference	Ice + liquid clouds set to 0 → cloud-free situation. UKCA data for all species and temperature.

Table 3.3: *Simulations performed with the NZAC SCM to assess the impact of clouds on photolysis rates and OH. The table includes the type of data set used to constrain the NZAC SCM. The time period of simulation encompasses the time frame between 1986 and 2012.*

Additionally, as part of the work undertaken for this thesis, a SSM for OH, HO_2, and HO_x was developed to provide a plausibility test for the NZAC SCM. A global budget of reaction throughputs for all reaction

channels considered by the UKCA CCM was used to establish the steady–state reactions for OH, HO_2, and HO_x to be considered in the SSM. The SSM uses the steady–state approximations, as described in the previous section, to infer the steady–state OH concentrations. Rate constants for each reaction included in the SSM were calculated based on the rate coefficients used by the NZAC SCM chemical mechanism (input tables). Photolysis rates were taken from the FAST–JX photolysis scheme. The SSM is run along 60 vertical levels (the same levels used in the NZAC SCM) and the constraining time period is that of the NZAC SCM (1994 – 2010) – the input data are read in at the time of the ozonesonde measurements.

Nine simulations were run with the SSM under clear–sky conditions and results compared to those of the NZAC SCM (Table 3.1). One simulation consisted of comparing the OH concentrations obtained from the two models, of which input data are those of the reference forcings (using UKCA CCM output data). Other eight simulations (amongst the eight perturbation simulations there are two single– and two multiple–perturbation runs using different H_2O data sets) were performed to compare the OH sensitivity to varying the key forcings (O_3, H_2O, CH_4, CO, and temperature) between the two models. For these simulations, observations were used to prescribe the previous parameters and UKCA CCM output data were used for the rest of the species considered in the SSM (see Table 3.4 for details of the SSM simulations). In the simulations performed with the SSM, the steady–state assumption was assumed for each reaction that takes part in the tropospheric HO_x chemistry. This approach also neglects circulation, and details around the steady–state assumption for HO_x have a small effect on the chemistry investigated here. The results of the comparison of the NZAC SCM to the SSM for HO_x are also given in Chapter 5.

SSM : Clear-sky conditions (1994 – 2010)	
Forcings	**Data used**
Reference (OH comparison)	UKCA data for all species and temperature.
O_3	Changes in O_3 → ozonesondes + MOPI1. (kinetics + photolysis effects) $jO(^1D)$ changes according to O_3 changes. UKCA data for other species and temperature.
H_2O	**1.** Changes in H_2O → radiosondes (0-8 km) + UKCA H_2O (9-84 km). UKCA data for other species and temperature. **2.** Changes in H_2O → ERAI (0-8 km) + UKCA H_2O (9-84 km). UKCA data for other species and temperature.
CH_4	Changes in CH_4 → rescaled UKCA CH_4 to Cape Grim surface CH_4. UKCA data for other species and temperature.
CO	Changes in CO → rescaled UKCA CO to FTIR CO. UKCA data for other species and temperature.
Temperature	Changes in T → radiosondes + MOPI1. (kinetics + photolysis effects) $jO(^1D)$ changes according to T changes. UKCA data for all species
O_3, H_2O, CH_4, CO, Temperature	**1.** Changes in O_3, H_2O, CH_4, CO, and temperature using observations mentioned above. For H_2O, radiosonde (0-8 km) + UKCA (9-84 km) data are used. **2.** Changes in O_3, H_2O, CH_4, CO, and temperature using observations mentioned above. For H_2O, ERAI (0-8 km) + UKCA (9-84 km) data are used.

Table 3.4: *Simulations performed with the SSM to evaluate the performance of the NZAC SCM. The table includes the type of measurement / data set used to prescribe the key forcings. The time period of simulation encompasses the time frame between 1994 and 2010.*

Chapter 4

Observational data

Lauder research station (hereafter Lauder) has a wide range of world–class instruments dedicated to international O_3 and climate research which mainly measure O_3, associated trace gases like NO_2, GHGs, and UV radiation.

To analyse the sensitivity of the OH radical to different species, data from Lauder, Cape Grim (Tasmania), ERAI, and UKCA CCM output data have been used as forcing data for constraining the NZAC SCM. The NZAC SCM input encompasses multi–year time series of 86 tracers profiles, as well as temperature and pressure profiles, as stated in Chapter 3. Amongst the 86 tracers, some key species such as O_3, H_2O, CH_4, and CO are measured at Lauder along with temperature, and have been used in the NZAC SCM. H_2O and CH_4 have also been prescribed using ERAI and data from the Cape Grim station (Tasmania), respectively. Besides, the UKCA CCM output data were employed as a complement to prescribe the former species along with other measurements (Lauder, Cape Grim, and ERAI). The UKCA CCM output data were also used for other input species included in the model.

This chapter describes the procedure to turn available observed surface, total column, and profile measurements into time series for O_3, H_2O, CH_4, CO, temperature and pressure profiles (Sections 4.2 to 4.6) into a common

format suitable for running the NZAC SCM. Section 4.1 describes the analysis of the photolysis rates of NO_2 and O_3 [hereafter jNO$_2$ and jO(^{1}D)] measured at Lauder that were used to validate FAST–JX from the NZAC SCM. A description of the validation of FAST–JX is given in Chapter 5 Section 5.1. The construction of time series of O_3, H_2O, CH_4, CO, and temperature profiles are described in subsequent sections.

4.1 Measurements of the NO_2 and O_3 photolysis rates at Lauder

jNO$_2$ has been measured by two radiometers operating at Lauder since late 1993. The radiometers measure actinic fluxes across the UV spectrum. The top (upper) radiometer measures the downwelling actinic flux, whereas the bottom (lower) radiometer measures the upwelling actinic flux reflected by the ground.

The first step was to analyse the raw data and identify any instrumental drift present in the data. To do this, the data of the upper radiometer was compared to other instruments operating at Lauder. The measurements from the lower radiometer were discarded due to the low values of jNO$_2$ measured if compared to the upper radiometer. (Note that if there is snow cover, the two signals become comparable. The lower instrument is therefore useful as a snow–cover detector). The instruments that were used to derive any drift from the radiometers were the UVM spectrometer[1], the Eppley UVA and the Yankee UVB radiometers, which are designed to measure erythemally–weighted UV (Refer to Appendix D for further technical information on the instruments). The irradiance measurements obtained by the UVM spectrometer were converted into solar actinic fluxes using an algorithm by McKenzie *et al.* (2002). By obtaining the actinic fluxes, jNO$_2$ was calculated through Equation 2.1.

[1]The UVM spectrometer started to operate at Lauder after the UVL instrument. The M is the following letter of the alphabet after the L which stands for Lauder.

Drifts on both the lower radiometer and the UVM spectrometer data prior to 2000 needed to be corrected. Therefore, the irradiances measured by both the Eppley UVA and the Yankee UVB radiometers were compared to that of the UVM. Preliminary analyses of the data showed some discontinuities in both the radiometer and the UVM spectrometer that were more likely due to instrument issues than an atmospheric effect. The upper radiometer has episodically suffered from rain penetration into the system. Conversely, the UVM spectrometer showed a discontinuity that was caused by a change from an integrating sphere to a diffuser. Both the integrating sphere and the diffuser are designed to give a cosine weighting of incident light (they both measure irradiance). The diffuser achieves this by transmitting a small fraction of the incident light (less than 1 %), whereas the integrating sphere has a highly reflecting inner surface, so the light is reflected inside many times before a small fraction enters the spectrometer through the entrance slit.

Additionally, it was necessary to consider the variability in radiation due to daily and seasonal variation of the SZA, and the variability due to cloud conditions. Clouds can either enhance or decrease the actinic fluxes at the surface (Madronich, 1987; Wild *et al.*, 2000; Kylling *et al.*, 2005; Neu *et al.*, 2007). Therefore, the data analysis was restricted to only clear–sky conditions for simplicity (Note that aerosol–related extinction and scattering, although likely small, would have affected the measurements). To do this, a mathematical expression (Equation 4.1), – which only works for clear–sky conditions – was used to fit the data for each day:

$$F(x) = \mathrm{A}[\cos(x)]^{\mathrm{B}} \tag{4.1}$$

where x is the SZA, A is an amplitude factor, and B governs the width of the envelope, a parameter that indirectly measures diffusion. All the data from the instruments were fitted by Equation 4.1, obtaining the entire time series of only clear–sky days.

In order to infer any possible drift between the instruments, the ratios of clear–sky UV spectrometer values (UVM data) compared with values from the upper, the Eppley UVA and the Yankee UVB radiometers at different SZA were calculated (Figure 4.1 A, B, and C).

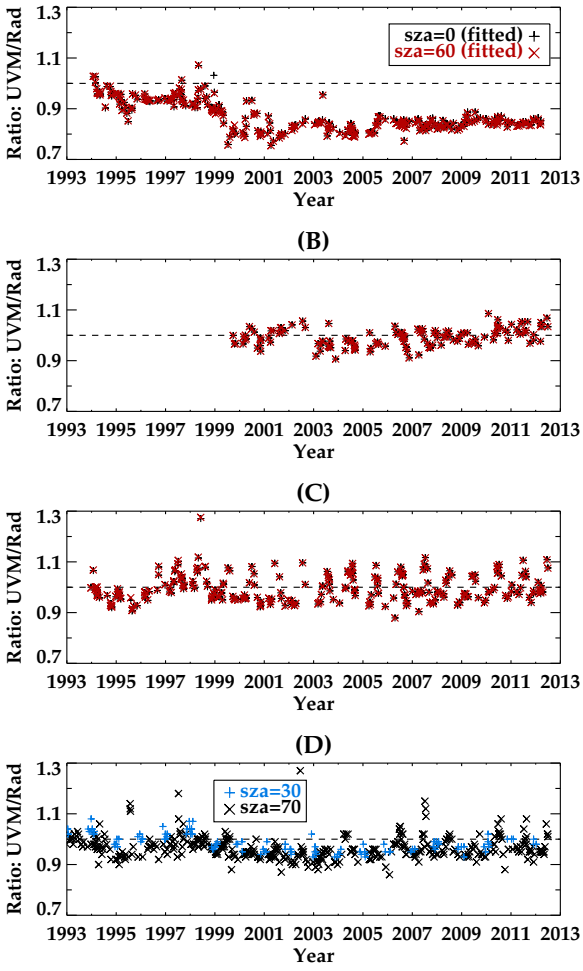

Figure 4.1: *Time series of ratios of clear–sky UV spectrometer (UVM) values compared with values from ancillary instruments: (A) upper radiometer, (B) Eppley UVA radiometer, (C) Yankee UVB radiometer. (D) The lowest panel shows ratios with respect to a clear–sky model. Panel A illustrates the jNO_2 ratio. Panels B, C, and D show the ratio of irradiances.*

Additionally, Figure 4.1 D shows the ratio of the UVA radiation to a clear–sky radiative transfer model. The model calculates the UVA under clear–sky conditions, fixed clean air conditions and fixed surface albedo. Thus, measured values are expected to be higher than the model if there is snow cover, or lower than the model if there are clouds or aerosols present. Discontinuities in data common to all would be due to calibration errors in the UVM spectrometer. Other discontinuities, such as the large reduction in $j\mathrm{NO}_2$ ratios which do not occur for other instruments, show that the problem is with the upper radiometer.

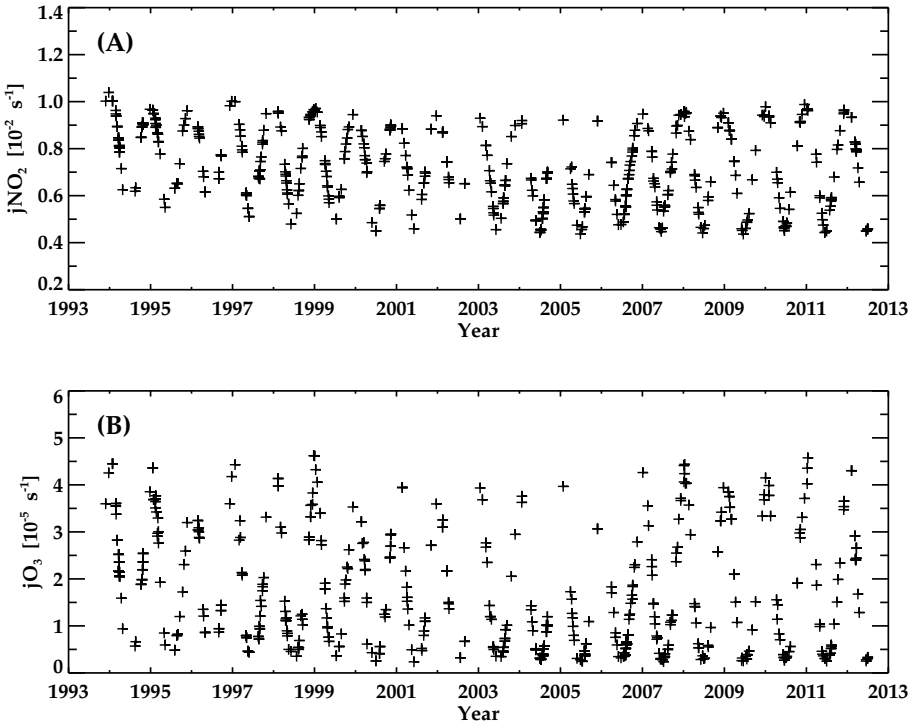

Figure 4.2: *Time series of corrected local solar noon (A) jNO_2 and (B) $jO(^1D)$ observed from the UVM spectrometer.*

From the ratios of clear–sky UVM spectrometer values compared with values of other instruments, the stability of the UVM spectrometer with

respect to the other instruments is confirmed for the periods before and after the change of the entrance optics. Thus, a correction factor was applied to $j\mathrm{NO_2}$ obtained from the upper radiometer based on the annually–averaged ratios (Figure 4.2 A). $j\mathrm{O}(^1\mathrm{D})$ was also obtained from the UVM spectrometer (Figure 4.2 B).

4.2 Construction of O_3 profiles

4.2.1 Instrumentation

Lauder has several instruments which measure O_3 in different ways: vertical profiles, total column or surface concentration. The instruments of which data have been used in this thesis are described as follows (for detailed information refer to Appendix D):

1. The Electrochemical Concentration Cell (ECC) ozonesondes:
   The ECC type ozonesonde balloons are launched weekly at Lauder. The O_3 profile data are submitted to the database of the Network for the Detection of Atmospheric Composition Change (NDACC). The balloons carry a sensor with them that measures high–resolution profiles of O_3 to an altitude of up to 35 km, where they burst and the instrument parachutes back to the ground. O_3 is estimated by an electrochemical process that generates electrical current in proportion to O_3 concentrations. This process, described in detail by Komhyr (1969), Stübi *et al.* (2008), and Vömel and Diaz (2010), is based on the fast reaction of O_3 and iodide (I^-) to give iodine (I_2) in an aqueous solution (Reaction R 4.1).

$$2\,\mathrm{KI} + \mathrm{O_3} + \mathrm{H_2O} \longrightarrow 2\,\mathrm{KOH} + \mathrm{I_2} + \mathrm{O_2} \qquad \text{(R 4.1)}$$

   Additional sensors are added to the ozonesonde, such as a barometer, a thermometer, and a hygrometer, to measure *in–situ* pressure, temperature, and H_2O mixing ratios respectively. The ozonesonde

transmits the information on O_3 and the meteorological variables by radio to a ground receiver station. Lauder has long ozonesonde records of O_3 profiles covering 1986 to the present, as part of an international effort to understand stratospheric O_3. The ozonesonde records have been used as a reference time period in the construction of the time series for O_3 and for the species discussed in the next sections.

2. 'Light Detection And Ranging' instrument (LIDAR):
   The ozonesonde balloons are complemented by a ground–based LIDAR instrument installed by the Dutch Rijks Instituut voor Volksgezondheid Milieu (RIVM) research group as part of the NDACC network. The instrument operates only in clear–sky nights and emits a pulse of laser light into the sky at two wavelengths (308 and 353 nm). The signals at these wavelengths are scattered back by air molecules and measured versus travel time of the beam (Swart *et al.*, 1995; Meijer *et al.*, 2003). O_3 profiles are derived by using the 'DIfferential Absorption Lidar method' (DIAL) (Measures, 1984; Brinksma *et al.*, 2000) at high vertical resolution (2 – 5 km), covering the height range of 8 to 50 km.

3. 'Microwave Ozone Profiling Instrument 1' (MOPI1):
   In a similar manner, the ground–base MOPI1 provides continuous O_3 profiles from altitudes of 20 to 75 km and has been operating since 1994. The instrument consists of a heterodyne receiver and a 120 channel spectrometer to detect the radiation by O_3 molecules every 30 min at 110.836 GHz (Parrish *et al.*, 1992; Parrish, 1994). The O_3 mixing ratio is derived from the shape of the excited O_3 spectral emission line as a function of pressure. A description of the method employed to estimate the O_3 mixing ratio is given by Rodgers (1976).

4. O_3 spectrophotometer (Dobson):
   The Dobson instrument is an O_3 spectrophotometer that measures the total column O_3 (TCO) expressed in Dobson Units (DU) (1 DU = 2.69 x 10^{16} molec/cm^2) by using direct sunlight (Dobson, 1957;

Komhyr, 1980). The instrument splits the incoming light into the spectrum wavelengths. Since O_3 absorbs UV radiation at the 305.5 nm wavelength (UVB), the amount of O_3 in the atmosphere is a function of the relative intensity of UVB at 305.5 nm which reaches the Earth's surface, relative to that at 325.4 nm wavelength at which O_3 does not absorb (UVA). Additionally, the Dobson data can be used to derive the amount of O_3 in the atmosphere by using the ratio of zenith sky intensities of the UVB and the UVA radiation as function of SZA, known as the Umkehr method (Götz, 1931; Dobson, 1957).

5. 'Thermo Environmental Instrument' (TEI):
   The TEI instrument is a continuous UV photometric O_3 analyser and is part of the National Oceanic and Atmospheric Administration's (NOAA) global *in–situ* O_3 network.[2] It measures the concentration of surface O_3 by the absorption of UV radiation at 254 nm wavelength (Oltmans *et al.*, 2006). The degree of absorption is directly proportional to the amount of O_3. The raw data is processed to produce a 1 hour calibrated O_3 concentration data set.

4.2.2 Time series of O_3 profiles

This subsection presents the procedure performed for constructing the time series of O_3 profiles. The period of reference is 1986 – 2012, the period covered by the ozonesondes data. Given the fact that the LIDAR and the MOPI1 began to operate in 1994, two different time series of O_3 profiles (and thus the rest of the forcings used in this study) that covered different periods were considered in the analysis. The longer time series covers the period between 1986 and 2012 and it was used to run simulations in order to analyse the variability and trends of OH. A shorter period (1994 – 2010) was used to run the different simulations in order to assess the sensitivity of OH to changes in the key forcings. For O_3, the first and longer time series of O_3 profiles contains ozonesonde data complemented above 25 km with O_3 from the UKCA CCM output. The second and shorter time series

[2] http://www.noaa.gov/

includes ozonesonde data and MOPI1 data above 25 km of altitude.

Ozonesondes were used to cover the whole troposphere and the lower stratosphere, since they are considered to provide accurate *in–situ* measurements of O_3 at higher vertical resolution ($\sim$ 0.2 km) compared to other instruments. Figure 4.3 depicts the mean annual cycle of O_3 measured by the ozonesondes at Lauder. The O_3 layer has a maximum O_3 concentration in late winter/early spring for the lower stratospheric layer due to the Brewer–Dobson circulation which transports O_3–rich air from the tropics to midlatitudes (Newell, 1963; Butchart, 2014).

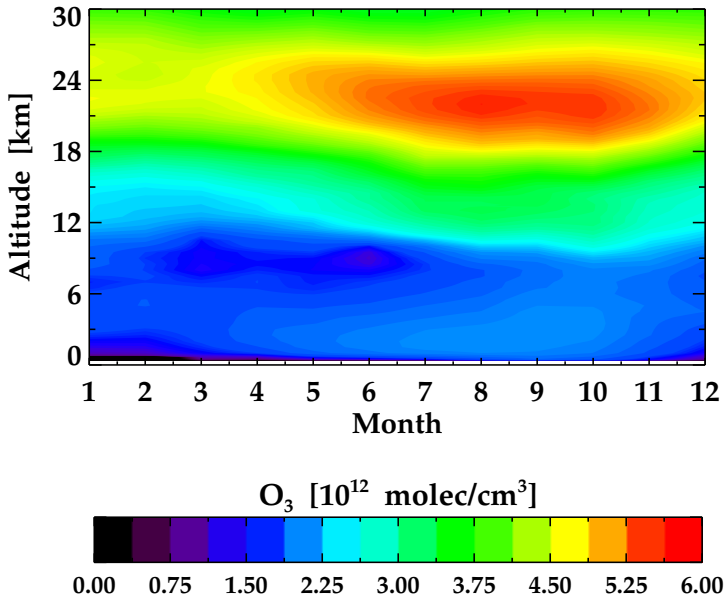

Figure 4.3: *O_3 mean annual cycle obtained from the ozonesonde from the surface up to 30 km of altitude.*

In order to establish the accuracy of the ozonesonde measurements at the surface, a comparison of the surface O_3 between the ozonesonde and the TEI instrument was made, showing a good agreement between them (Figure 4.4 A). Figure 4.4 B displays the relative difference between the instruments

computed through Equation 4.2:

$$\Delta \mathrm{O_3}(i,j) = \frac{x(i,j) - x_{ref}(i,j)}{x_{ref}(i,j)} \tag{4.2}$$

where x is the surface O_3 measured by the ozonesonde, x_{ref} is the TEI measurement, j is the altitude [$j = 0$ (surface)], and i is the time.

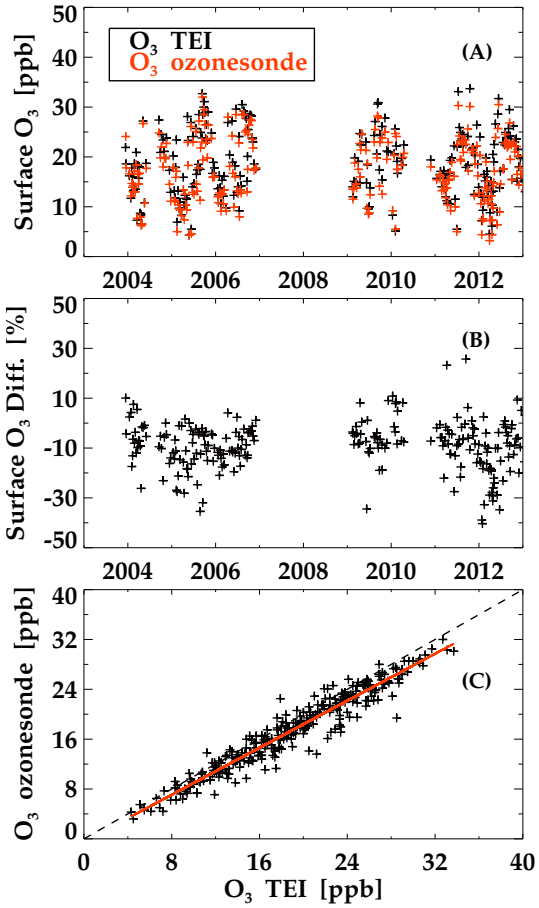

Figure 4.4: *Comparison between the TEI and ozonesonde surface O_3 measurements. (A) Time series of surface O_3 from TEI (black) and ozonesonde (red) in ppb. (B) Percentage difference of the ozonesonde relative to TEI. (C) Scatter plot of the comparison between TEI and ozonesonde surface O_3 in ppb.*

The percentage difference between the two measurements can be explained by a few factors, i.e. the temporal variability of O_3 (the ozonesondes data are 30 second average and the TEI data are 1 hour average), the ozonesonde response to different concentrations of KI solutions (Johnson *et al.*, 2002), and the local variations (e.g. sonde background settlement).

Also, low surface O_3 (of the order of 10 – 30 ppb) mean that small changes in the O_3 concentration are inherently translated into large percentage differences. In spite of this, a mean relative bias of –8.6 % computed through Equation 4.3, and a high degree of correlation (r = 0.97) were found for the whole period, except for the years 2007 and 2008 which were discarded for comparison due to TEI instrumental issues.

$$\overline{\Delta O_3(j)} = \frac{\sum_i \Delta O_3(i,j)}{N(i)} \tag{4.3}$$

where j is the altitude [$j = 0$ (surface)], $N(i)$ the number of measurements (equivalent to time i), and $\overline{\Delta O_3(j)}$ is the mean surface O_3 relative bias. Furthermore, the relationship between the instruments at the surface is linear (Figure 4.4 C), with only a 5.5 % deviation from the slope 1. Therefore, it is adequate to use surface O_3 from the ozonesondes measurements in the NZAC SCM simulations.

The ozonesonde profiles do not usually reach above 35 km of altitude, thus O_3 profiles from either LIDAR or MOPI1 were adopted. Therefore, comparisons of the MOPI1 and the LIDAR to the ozonesonde were made in order to establish the accuracy of the instruments with respect to the ozonesonde and between each other. Considering that measurements from each instrument are not similarly spaced throughout the year and that the altitude ranges covered by each instrument are different, simultaneous or quasi–simultaneous measurements within 24 hours (LIDAR) were applied

for comparison and the O_3 profiles were linearly interpolated onto an uniform 100–metre altitude grid. The altitude range chosen for comparison was a common altitude range between 20 and 30 km in the stratosphere, as MOPI1 does not cover the region below 20 km and data from ozonesondes typically do not provide accurate measurements above 30 km of altitude (Brinksma *et al.*, 2002; Smit *et al.*, 2007). Furthermore, larger differences between instruments were observed below 18 km due to the large O_3 variability in the lower stratosphere related to e.g. variability of the tropopause height (Nair *et al.*, 2012).

Figure 4.5 displays the mean annual cycle percentage difference of instrument pairs between 20 and 30 km calculated by Equation 4.2 (panels 1a, 2a, and 3a), and their respective mean biases (panels 1b, 2b, and 3b) expressed by Equation 4.3, where these differences were averaged over the monthly averaged period (i) equivalent to the number of measurements $N(i)$. In both Equations 4.2 and 4.3, j is the altitude between 20 and 30 km.

In Figure 4.5 1a and 2a, ozonesonde is the reference instrument for the comparisons between LIDAR and ozonesonde, and between MOPI1 and ozonesonde respectively. For Figure 4.5 3a, LIDAR is the reference instrument for the comparison between MOPI1 and LIDAR. A good agreement between the pairs of instruments can be established from Figure 4.5. The difference between the ozonesonde and the LIDAR shown in the top left panel (1a) of Figure 4.5 only ranges between –4 % and 4 % and is similar to the results by Brinksma *et al.* (2000). The middle left panel (2a) shows a percentage relative difference between the ozonesonde and the MOPI1 which ranges between –2 % and 6 %, showing a better overall agreement between the instruments than the comparison in panel (1a), despite the 6 % discrepancy at 20 and 28 km. In the case of the LIDAR and the MOPI1, the relative difference shown in the bottom left panel (3a) ranges between 1 % and 6 % and largely agrees with the 1 % and 5 % range found by Brinksma *et al.* (2000). Although the latter is a small discrepancy, it must be taken into account that Brinksma *et al.* (2000)

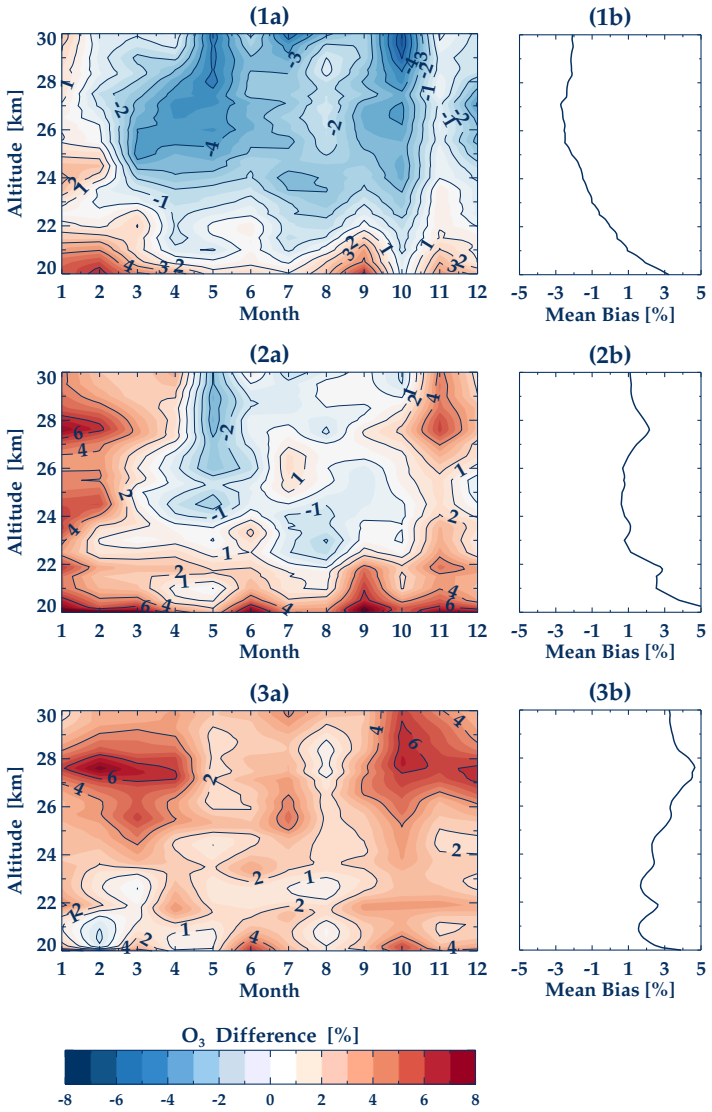

Figure 4.5: *Comparison of the O_3 mean annual cycle between a pair of instruments between 20 and 30 km. Panels 1a, 2a, and 3a are the percentage differences in O_3 between pairs of instruments and Panels 1b, 2b, and 3b are the mean biases of the percentage differences. (1) LIDAR relative to the ozonesonde (reference). (2) MOPI1 and ozonesonde (reference). (3) MOPI1 and LIDAR (reference).*

compared short periods up to 4 years, whereas this comparison accounts for the full time period of measurements.

Differences between measurements by various instruments could be caused in part by different altitude resolutions. Additionally, LIDAR measurements are carried out during clear nights, whereas ozonesonde launches occur near midday (around 1:00 pm local time). Hence, the nonsimultaneity in the ozonesonde and the LIDAR measurements introduces a further inconsistency compared to that in the MOPI1 and the ozonesonde profiles comparison, since the measurements of these instruments coincide much better in time. Despite small discrepancies, the mean relative bias of the 3 comparisons (right panels 1b, 2b, and 3b) is less than ± 5 %, similar to the results found by Nair *et al.* (2012), for the comparisons of LIDAR – ozonesonde and of LIDAR – satellites.

To set a maximum altitude for the ozonesonde profiles, linear fits between pairs of instruments were produced between altitudes of 20 and 30 km (Figure 4.6). A good linear fit between the instruments was obtained at all altitude ranges (A, B, C, and D) with a high degree of correlation, and almost all data close to the slope of 1. Therefore, this comparison did not provide a clear guidance for defining an optimal transition altitude for the merged O_3 dataset.

Given the fact that some ozonesondes do not reach 30 km of altitude, the altitude of transition was set to be 25 km. Even though both instruments show a good correspondance with the ozonesonde data between 20 and 30 km of altitude that does not exceed ± 5 % inaccuracy, MOPI1 data were chosen to complete the time series of O_3 profiles above 25 km from 1994 until 2010, taking into account the low temporal resolution of the LIDAR measurements, and the nonsimultaneity in the ozonesonde and LIDAR measurements (as stated previously).

When dealing with long–term records of measurements, gaps often occur due to instrument failures or measurement limitations. Consequently, the

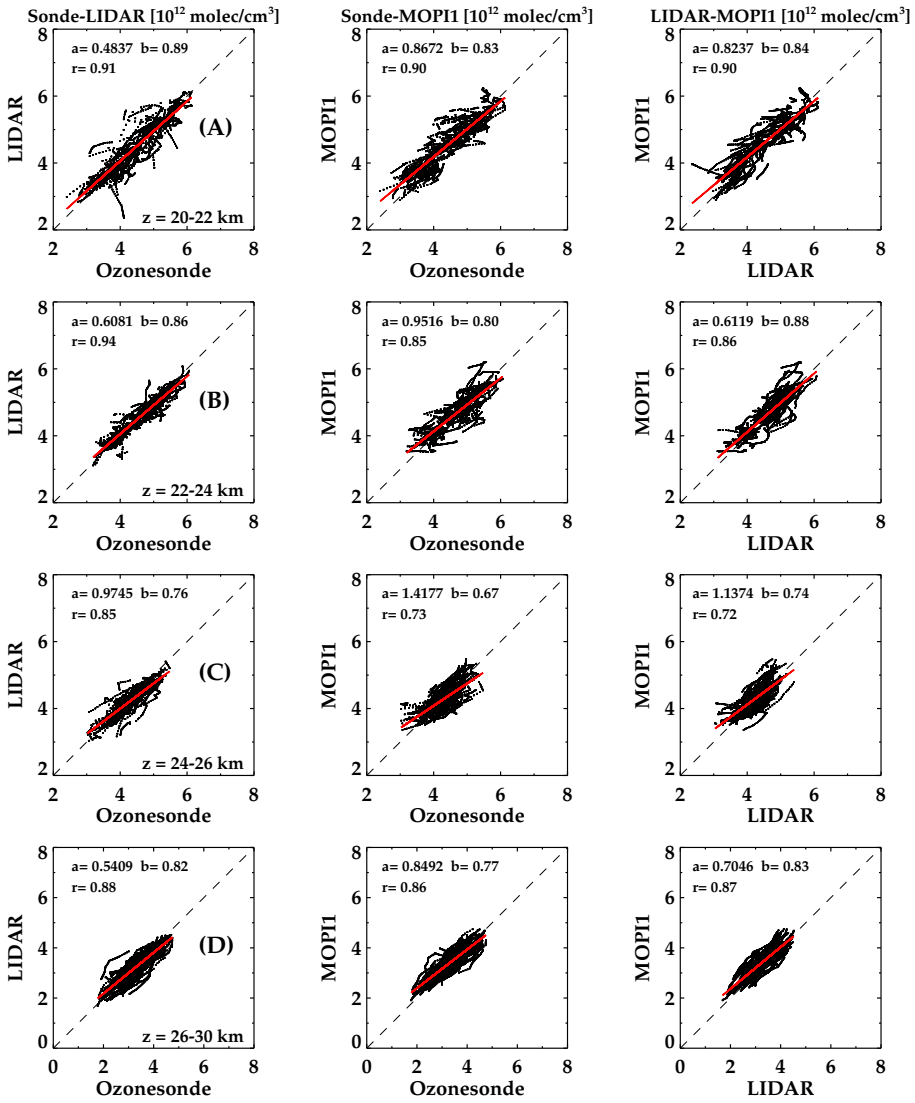

Figure 4.6: *Scatter plots between pairs of instruments. Left panels are the comparisons between the ozonesonde and the LIDAR. Middle panels show the comparisons between the ozonesonde and the MOPI1 and the right panels between the LIDAR and the MOPI1. A) 20 – 22 km B) 22 – 24 km C) 24 – 26 km and D) 26 – 30 km. The scatter plots include the coefficients for the linear fit: 'a' is the constant offset, 'b' is the slope, and 'r' is the Pearson correlation coefficient.*

resultant gaps in the time series of measurements limit the use of these data and hamper inter–comparisons with other instruments. This is the case of the MOPI1 instrument which presented long gaps (i.e. longer than one month) between October 1994 and March 1995, and between October 2003 and April 2004, which were caused by instrument failure. Therefore, it was necessary to use a suitable gap–filling method to generate a complete MOPI1 O_3 time series that covered the ozonesonde measurements period. The method employed to fill the gaps was a Fourier series model which was applied to the MOPI1 time series of O_3:

$$\begin{aligned} Y(t) = A_0 + A_1\cos(2\pi t) + A_2\sin(2\pi t) + A_3\cos(4\pi t) \\ + A_4\sin(4\pi t) + A_5\cos(6\pi t) + A_6\sin(6\pi t) \end{aligned} \tag{4.4}$$

where parameters A_1 to A_6 describe the O_3 annual cycle, A_0 is the constant offset, and t is the time in years since 1994.

The resulting time series of completed O_3 profiles with ozonesonde and MOPI1 measurements is depicted in Figure 4.7 A, with a well–defined O_3 layer between $\sim$ 20 km and $\sim$ 30 km in summer and between $\sim$ 15 km and $\sim$ 30 km in winter. Likewise, a time series of O_3 profiles was also constructed using the O_3 output data from the UKCA CCM. This time series, displayed in Figure 4.7 B, was used as an O_3 reference time series in the analyses performed for the purpose of this thesis.

On the dates when ozonesonde and MOPI1 measurements were made quasi–simultaneously with the Dobson spectrophotometer, measurements could be compared to the TCO measured by the Dobson spectrophotometer, which is often used to calibrate data measured by other methods. O_3 columns densities were determined by integrating the measured ozonesonde and MOPI1 O_3 profiles. The anomalies of the integrated O_3 profiles and the Dobson TCO were obtained by removing their annual cycles (calculated through Equation 4.4). The anomalies of TCO were interpolated onto a regular time grid, and a one–year moving–average filter was applied to the new regular time series. The

comparison of the O_3 column anomalies is displayed in Figure 4.8 A, where an interannual variability of up to about 3 % of the average O_3 column is seen.

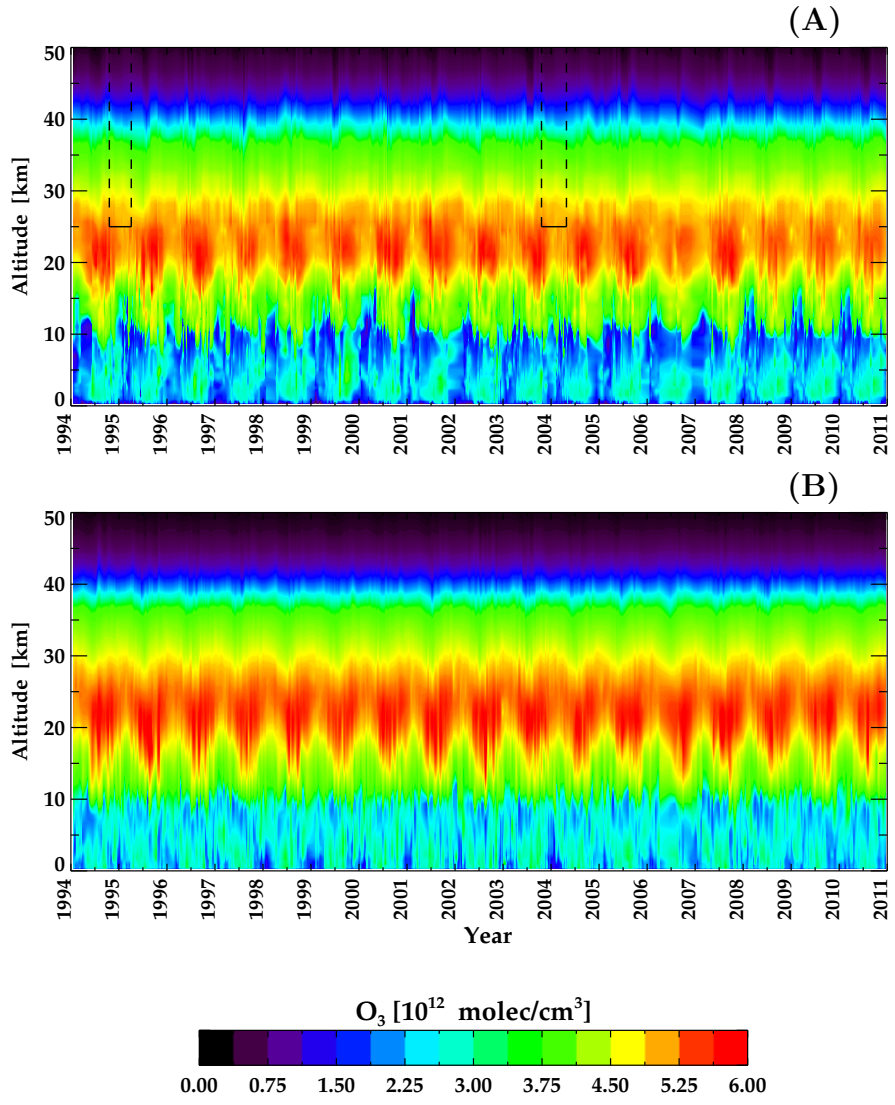

Figure 4.7: *(A) Time series of O_3 profiles constructed by ozonesonde measurements spliced with MOPI1 measurements. The areas within the black boxes were filled using Equation 4.4. (B) Time series of UKCA O_3 profiles.*

The overall agreement between the O_3 total column densities is shown to be good in Figure 4.8 B which shows the scatter plot of the TCO from Dobson and the integrated ozonesonde and MOPI1 O_3 profiles. The root–mean–square error (RMSE) of the differences in O_3 column densities calculated through Equation 4.5 is 15 DU, corresponding to about 5 % of the average O_3 column density.

$$\mathrm{RMSE} = \sqrt{\frac{\sum_{i=1}^{N}(\hat{Y}_i - Y_i)^2}{N}} \tag{4.5}$$

where $\hat{Y}_i$ is the integrated measured O_3 profile, Y_i is the Dobson measurement, and N is the total number of measurements.

Previous comparisons of integrated profiles of ozonesonde and LIDAR data with Dobson measurements from Lauder were carried out by Brinksma *et al.* (2000), who obtained a 3 % RMSE, which is slightly smaller compared to the 5 % obtained for the comparison of the integrated spliced O_3 profiles of the ozonesonde and MOPI1 here. This might be due to an inadvertent error compensation (e.g. the night–time bias of LIDAR measurements compensating for a possible underestimation of O_3 by the ozonesondes). Furthermore, the slope of the linear fit of this comparison (Figure 4.8 B) is 0.93. According to Brinksma *et al.* (2000), the Dobson spectrophotomer assumes fixed temperature values, altitude average of the O_3 cross section (Komhyr *et al.*, 1989), relative O_3 distributions, and SZA [the latter assumption to revert from slant column O_3 (SCO) to TCO] for the retrieval of the TCO, which could explain this deviation of the slope from 1.

Regardless of the small discrepancies found with other studies that also compared O_3 column densities at Lauder, Rinsland *et al.* (1996) found a 3 % RMSE between the Fourier–Transform InfraRed (FTIR) and the Dobson total columns. Both instruments are standard methods for measuring TCO densities, which suggests that a 5 % RMSE between the Dobson and the integrated profiles is reasonable.

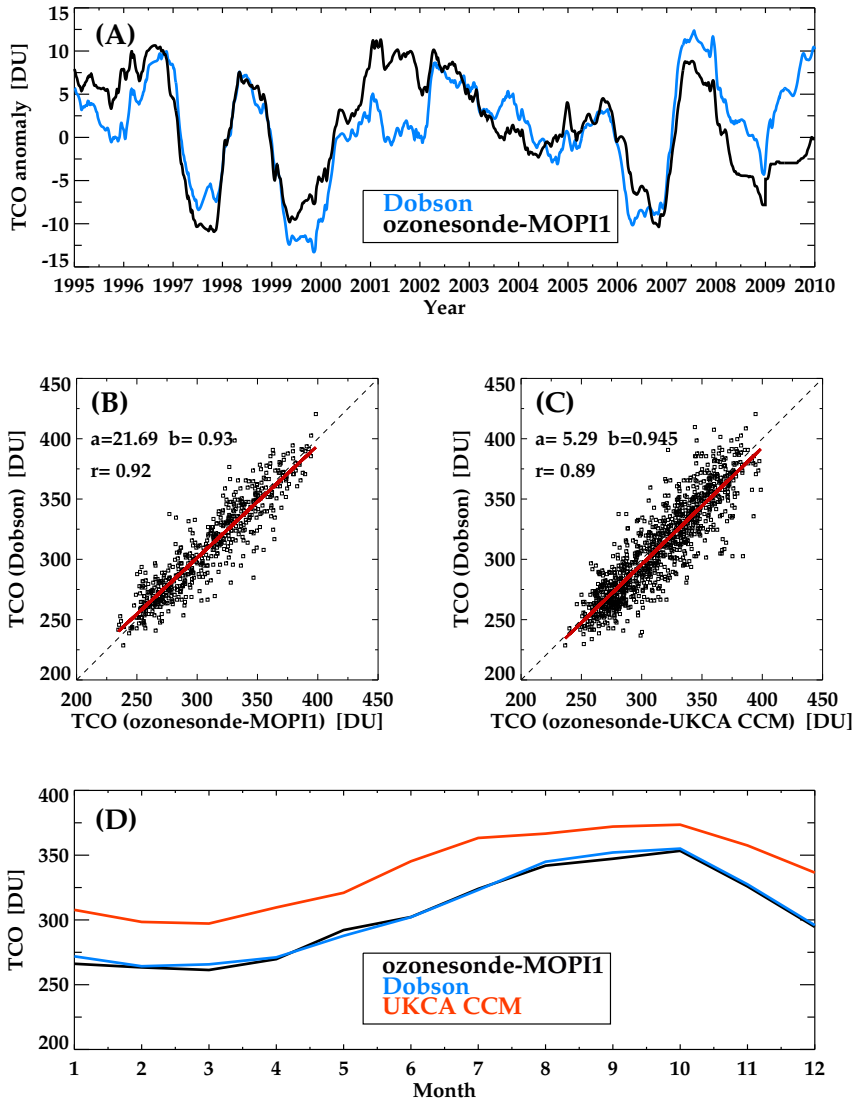

Figure 4.8: *(A) Anomalies of total column O_3 (TCO) in DU. Blue line: Dobson measurements. Black line: vertical integration of merged ozonesonde and MOPI O_3 measurements. (B) Scatter plot of O_3 column densities in DU: altitude integration of ozonesonde and MOPI1 O_3 profile measurements (horizontal axis) and Dobson measurements (vertical axis). (C) Scatter plot of O_3 column densities in DU: altitude integration of ozonesonde and UKCA CCM O_3 profile measurements (horizontal axis) and Dobson measurements (vertical axis). (D) Mean annual cycle of UKCA CCM (red line), Dobson (blue line), and ozonesonde–MOPI1 (black line) TOCs in DU.*

The second time series of O_3 profiles covers the whole period of ozonesonde launches between 1986 and 2012. Ozonesonde profiles and UKCA CCM O_3 output data are merged, with 25 km chosen as the transition altitude between the two datasets. A linear fit was also performed between the Dobson measurements and the integration of the merged ozonesonde and UKCA CCM columns (Figure 4.8 C). The deviation of the slope is 5.5 % from the slope 1 for the linear fit, which shows a slightly smaller deviation from the slope 1 compared to the slope of the linear fit between the Dobson and the ozonesonde – MOPI1 columns. However, the integration of profiles using ozonesonde spliced with UKCA CCM data introduces a further $\sim$ 1 % RMSE in the comparison with the Dobson measurements. This might be due to that the UKCA CCM does not capture the day–to–day variation of the weather condition as the model is not forced by re–analysis meteorological data. Furthermore, the UKCA CCM overestimates stratospheric O_3 density by 20 DU (in spring) to 40 DU year–round (Figure 4.8 D) in comparison to observations (Dobson and integration of the merged ozonesonde – MOPI1 columns). This overstimation of O_3 by the UKCA CCM is also reflected in Figure 4.7 B.

Once both time series of O_3 profiles were constructed, they were converted into a suitable common format for running the NZAC SCM. O_3 profiles were linearly interpolated onto the model's σ–vertical grid. Likewise, UKCA CCM output data that covered the ozonesonde period were used to establish a reference time series of O_3 profiles that were used for the analyses explained in the following chapter. Similarly, the UKCA CCM O_3 data were linearly interpolated onto the NZAC SCM altitudes.

4.3 Construction of H_2O profiles

Radiosonde measurements, ERAI, and UKCA CCM output data were employed to construct two different time series of H_2O profiles which also

covered the ozonesonde period. The description of the instruments and the database used are summarised in the following subsections. Refer also to Appendix D for technical details.

4.3.1 Instrumentation

1. Radiosondes:
   Radiosondes have been launched since 1986 from Lauder. They consist of a small package that is attached to the ozonesonde and measures vertical profiles of relative humidity (RH), temperature, atmospheric pressure and wind velocity (also described in Subsection 4.2.1 for the description of the ozonesondes). Radiosondes consist of a thin polymer moisture capacitor, which contains twin sensors, called HUMICAPS, to prevent the deposition of ice by heating one sensor while the other takes measurements (Vömel *et al.*, 2007).

   Since H_2O is highly variable in space and time (Elliott and Gaffen, 1991; Luers and Eskridge, 1998), radiosonde measurement accuracy is variable for different sensors (Moradi *et al.*, 2013). Furthermore, drifts in datasets are being introduced due to changes in the design and features of the radiosondes (Elliott and Gaffen, 1991). Despite attempts to homogenize data records from different sources, such as statistical approaches (Turner *et al.*, 2003; Vömel *et al.*, 2007), humidity climatologies constructed using radiosonde measurements are still subject to significant uncertainty due to geographically and temporally sensor–dependent errors (Wang *et al.*, 2013).

2. Frost Point Hygrometer (FPH):
   The saturation vapour pressure of water is strictly a function of the air temperature. If the air cools down, H_2O condenses, decreasing the amount of H_2O. The temperature at which H_2O begins to condense is known as the dewpoint, and it depends on how much H_2O is in the air. Dewpoints below 0°C, where H_2O condenses to solid ice instead of liquid water, are instead known as frost points. FPH instruments are based on this equilibrium thermodynamics principle. They contain a mirror on which a thin layer of frost is

mantained by monitoring the thin frost layer with a small infrared beam coupled to a microprocessor–controlled feedback loop (Hurst *et al.*, 2014) that regulates the mirror temperature. The frost point temperature is achieved when the thin frost layer stabilizes and it is indicative of how much H_2O is in the air.

To derive the RH or the mixing ratios of H_2O, the partial pressure of H_2O needs to be determined through, e.g. the formulation by Goff and Gratch (1946) of the Clausius–Clapeyron equation. For a plane surface of pure water the expression is Equation 4.6a:

$$\begin{aligned}\log_{10} e_{sw} = &-7.90298\left(\frac{T_s}{T}-1\right)+5.02808\log_{10}\left(\frac{T_s}{T}\right)\\ &-1.3816\text{ x }10^{-7}\left[10^{11.344\left(1-\frac{T}{T_s}\right)}-1\right]\\ &+8.1328\text{ x }10^{-3}\left[10^{3.49149\left(\frac{T_s}{T}-1\right)}-1\right]\\ &+\log_{10} e_{ws}\end{aligned} \tag{4.6a}$$

where T is the absolute temperature, $T_s = 373.16$ K, and $e_{ws} = 1013.246$ hPa. Conversely, for a plane surface of pure ice the expression is Equation 4.6b:

$$\begin{aligned}\log_{10} e_{si} = &-9.09718\left(\frac{T_0}{T}-1\right)-3.56654\log_{10}\left(\frac{T_0}{T}\right)\\ &+0.876793\left(1-\frac{T}{T_0}\right)+\log_{10} e_{i0}\end{aligned} \tag{4.6b}$$

where T is the absolute temperature, $T_0 = 273.16$ K, and $e_{i0} = 6.1071$ hPa. The mixing ratio is then calculated by dividing the H_2O partial pressure by the pressure of dry air. Likewise, the RH is determined by using H_2O pressure over liquid formulation (Hyland and Wexler, 1983).

FPHs measure H_2O profiles at a very high vertical resolution (5 – 10 m) but at very coarse temporal resolution (once per month). Despite this, FPHs have become a valuable instrument to monitor long–term H_2O profiles, since only the thermistor requires to be calibrated, and the measurement principle has not undergone any modification (Oltmans *et al.*, 2000). At Lauder, FPH measurements started in 2003. Together with the low sampling frequency, this means that here, FPH data were used for comparison purposes only.

3. The ERAI database:
   ERAI gives a numerical description of the recent climate, produced by assimilating observations into a model simulation of climate. It contains estimates of atmospheric parameters such as air temperature, pressure, humidity, aerosol content and wind velocity at different altitudes, and surface fields such as rainfall, soil moisture content, and sea–surface temperature (SST). The estimates are produced globally at 00, 06, 12 and 18 UTC every day, and cover the period of 1979 until present (1979 marks the onset of relatively abundant satellite observations of meteorological parameters). The spatial resolution is approximately 80 km with 60 vertical levels from the surface up to 0.1 hPa (Graham *et al.*, 2005). Here, the data interpolated to a 2.5° grid was used.

4.3.2 Time series of H_2O profiles

This subsection describes the procedure to construct the time series of H_2O profiles. Lauder radiosonde H_2O data and ERAI humidity data were used to construct the H_2O timeseries, complemented by those from the UKCA CCM to constrain H_2O profiles from a transition altitude up to the top level of the NZAC SCM. Data from the FPH were only used for comparison with those from the radiosonde, ERAI, and the UKCA CCM, since the instrument has taken measurements only once per month since 2003.

Figure 4.9 displays the mean annual cycle of the percentage differences of the radiosonde, ERAI, and UKCA CCM humidity with the FPH from the surface up to 12 km in the troposphere. Figure 4.9 panel A shows the percentage difference of the H_2O concentration between the radiosonde and the FPH to be under $\pm$ 5 % in the lower and middle troposphere but with larger differences in the tropopause region ($\sim$ 11 km). These larger differences are produced because radiosondes are not as accurate as FPHs at measuring low values of H_2O, because the inaccuracy of the measurements exceeds the low humidity values (Schmidlin and Ivanov, 1998; Miloshevich *et al.*, 2001). Therefore, small variations in the H_2O concentration are translated into larger percentage differences around these altitudes (tropopause region) compared to the lower and middle troposphere.

Figure 4.9 panel B depicts larger percentage differences of ERAI H_2O compared to the FPH values that ranges from –10 % to more than 60 % in the upper troposphere. This may reflect the sparse density of measurements (which do not include Lauder data) used to constrain the ERAI simulation. In addition, the ERAI humidity fields come in 256 discrete values spanning the range of minimum to maximum H_2O mixing ratio (e.g. a 1–byte data precision). Considering a maximum mixing ratio of about 2 % in the tropics, this yields a precision of roughly 100 ppm; inadequate for representing stratospheric and upper–tropospheric H_2O. This explains the larger differences above 10 km in Figure 4.9 panel B. Figure 4.9 Panel C shows the percentage difference between the UKCA CCM H_2O and the FPH. As can be expected from a low–resolution model unconstrained by observations and subject to problems with modelling H_2O (these are common to GCMs), larger differences are found throughout the whole troposphere.

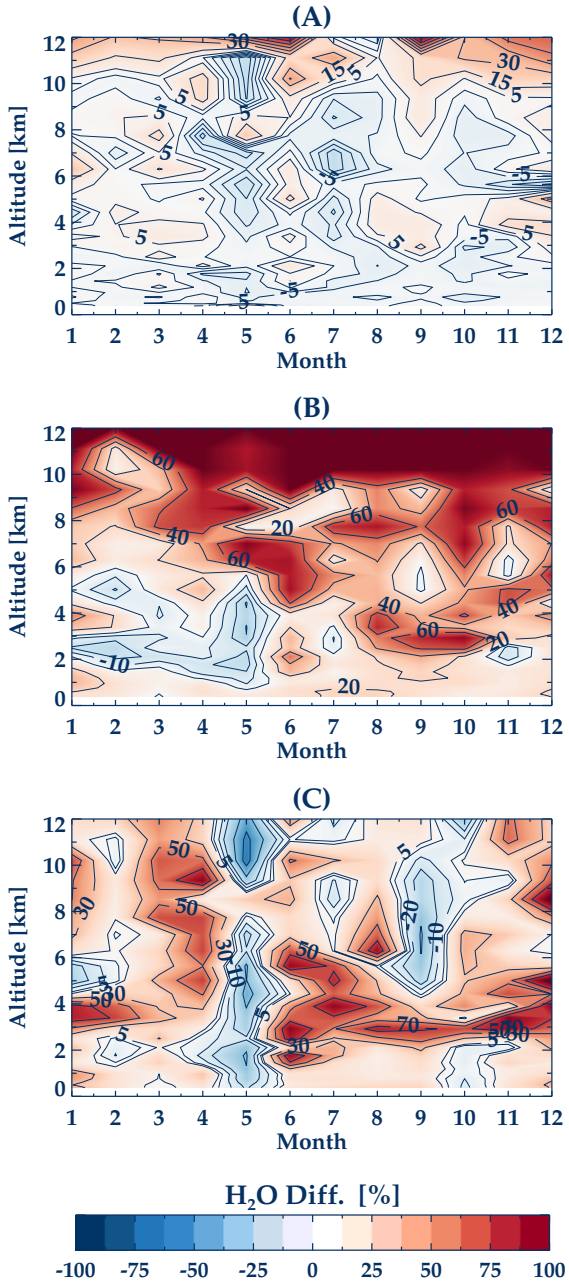

Figure 4.9: *Comparison of the mean annual cycle of H_2O measured with the frost point hygrometer to three different datasets. (A) Percentage differences between the radiosonde and the FPH H_2O measurements. (B) Percentage differences between ERAI H_2O data and the FPH H_2O measurements. (C) Percentage differences between the UKCA CCM H_2O and the FPH H_2O measurements.*

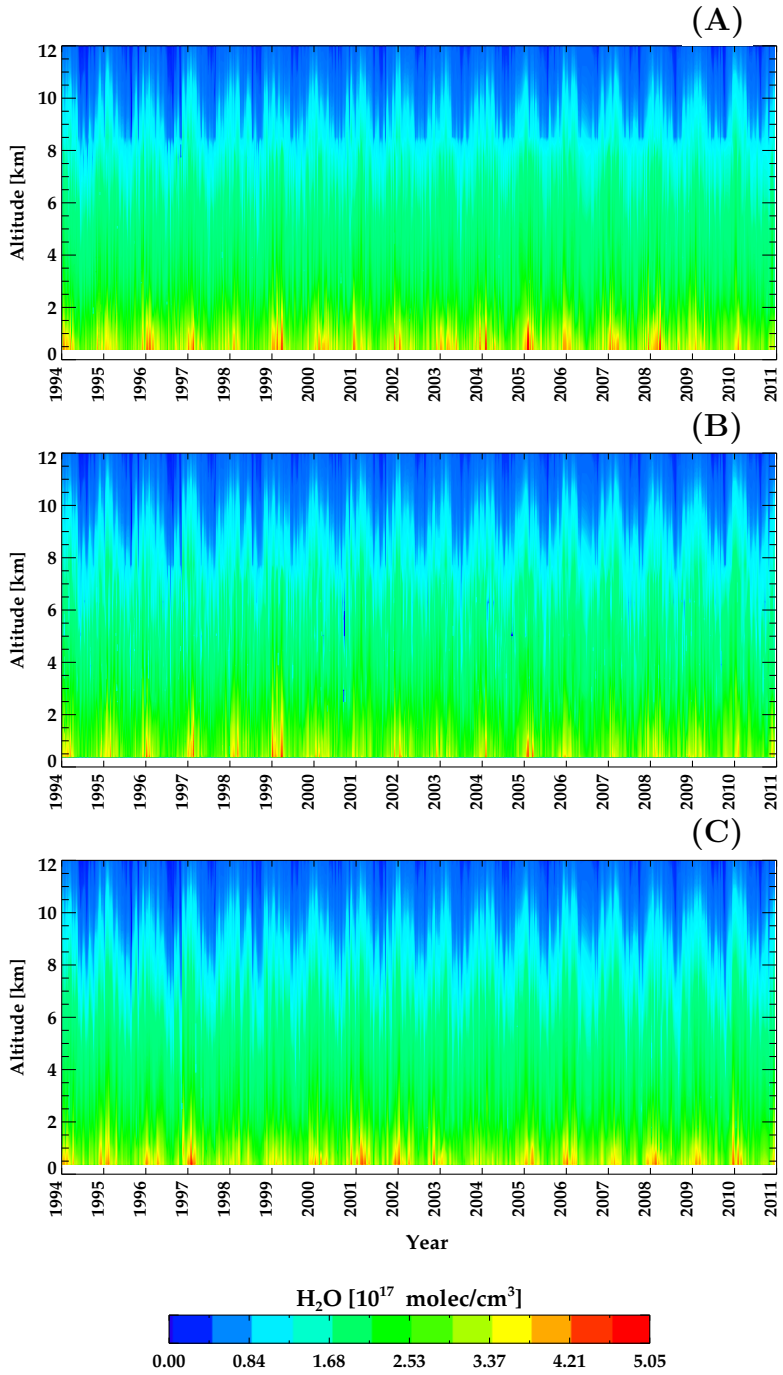

Figure 4.10: *(A) Time series of H_2O profiles constructed by radiosonde measurements spliced with UKCA CCM H_2O. (B) Time series of H_2O profiles constructed by ERAI data spliced with UKCA CCM H_2O. (C) Time series of UKCA H_2O profiles.*

To avoid including spurious H_2O data in the time series of H_2O profiles – due to the discontinuities that both datasets (radiosonde and ERAI) present in the upper troposphere –, the radiosonde and ERAI H_2O data were used independently to construct two different time series of H_2O profiles from the surface up to 8 km of altitude. Both datasets of H_2O profiles were merged with UKCA CCM H_2O output above 8 km up to the upper atmosphere. The time series of radiosonde H_2O merged with UKCA CCM is depicted in Figure 4.10 A from the surface up to 12 km of altitude, since stratospheric H_2O concentrations decrease considerably if compared to those of the troposphere. Likewise, the time series of ERAI spliced with UKCA CCM H_2O and the time series of UKCA CCM H_2O are displayed in Figure 4.10 B and C respectively. Once the profiles of H_2O from the time series were constructed, they were interpolated onto the model altitudes to be able to run the NZAC SCM.

4.4 Construction of CO profiles

CO column measurements by the FTIR spectrometer (Bruker 120HR), which operates within the NDACC network, have been conducted at Lauder since 1994. The Bruker 120HR is a type of Michelson interferometer that uses absorption spectroscopy in the mid–IR (MIR) region to remotely measure trace gases in the atmosphere. However, since 2009, a further spectrometer (Bruker 125HR) was purchased and dedicated to taking measurements of atmospheric trace gases in the near–IR (NIR) (Refer to Appendix D for detailed technical information). This is part of the Total Carbon Column Observing Network (TCCON), a ground–based network of Fourier transform spectrometers (Saad *et al.*, 2014). However, a longer time series of CO measurements that covered the ozonesonde period needed to be prescribed. FTIR provides limited profile information. Therefore CO profiles from the UKCA CCM were scaled up based on the available FTIR measurements.

In Figure 4.11 A, a complete time series of FTIR CO column from 1994

to 2010 is displayed. Several time series of observed CO at Lauder have been reported previously for shorter periods (Rinsland *et al.*, 1998, 2002; Jones *et al.*, 2001; de Laat *et al.*, 2010), showing no significant trends in CO; but these periods were too short to establish any significant trends. In comparison, a more recent study by Zeng *et al.* (2012) found a significant negative trend from 1997 to 2009 (–0.94 ± 0.47 % yr^{-1}) that was mainly attributed to a decline in the anthropogenic, NH emissions of CO.

The first step to rescale the UKCA CCM CO profiles to the FTIR CO column measurements involved fitting the time series of the CO column displayed in Figure 4.11 A to a Fourier series (Equation 4.4). An annual trend term, $A_7 t$, was added in Equation 4.4 based on the results of the multi–annual CO trend obtained by Zeng *et al.* (2012). The UKCA CCM CO profiles were integrated vertically, and the Fourier fit was also performed through the time series of the derived UKCA CCM CO column.

The second step consisted of scaling up the UKCA CO profiles by applying a factor derived from the ratio of the fitted CO data of integrated profiles and the fitted FTIR CO column. For the period between 1996 and 2011 (the years 1994 and 1995 were not considered due to the substantial gaps found in the record of the FTIR measurements), the UKCA CCM CO profiles were rescaled by the ratio of the fitted periodic CO time series for those years. The ratio of the fitted periodic time series was extrapolated back to 1986 in order to rescale the UKCA CCM CO profiles. To do this, the mean annual cycle of both fitted series was calculated for the corresponding period of 1996 – 1999. The factor derived from the ratio of the mean annual cycles was then applied to the the UKCA CCM CO profiles from 1986 to 1996. The same procedure was conducted to cover the years 2011 and 2012, during which FTIR measurements were not available. The ratio of the mean annual cycle of the fitted series for the period 2008 – 2010 was also applied to the UKCA CCM CO profiles for the last 2 years of the ozonesonde record (2011 – 2012).

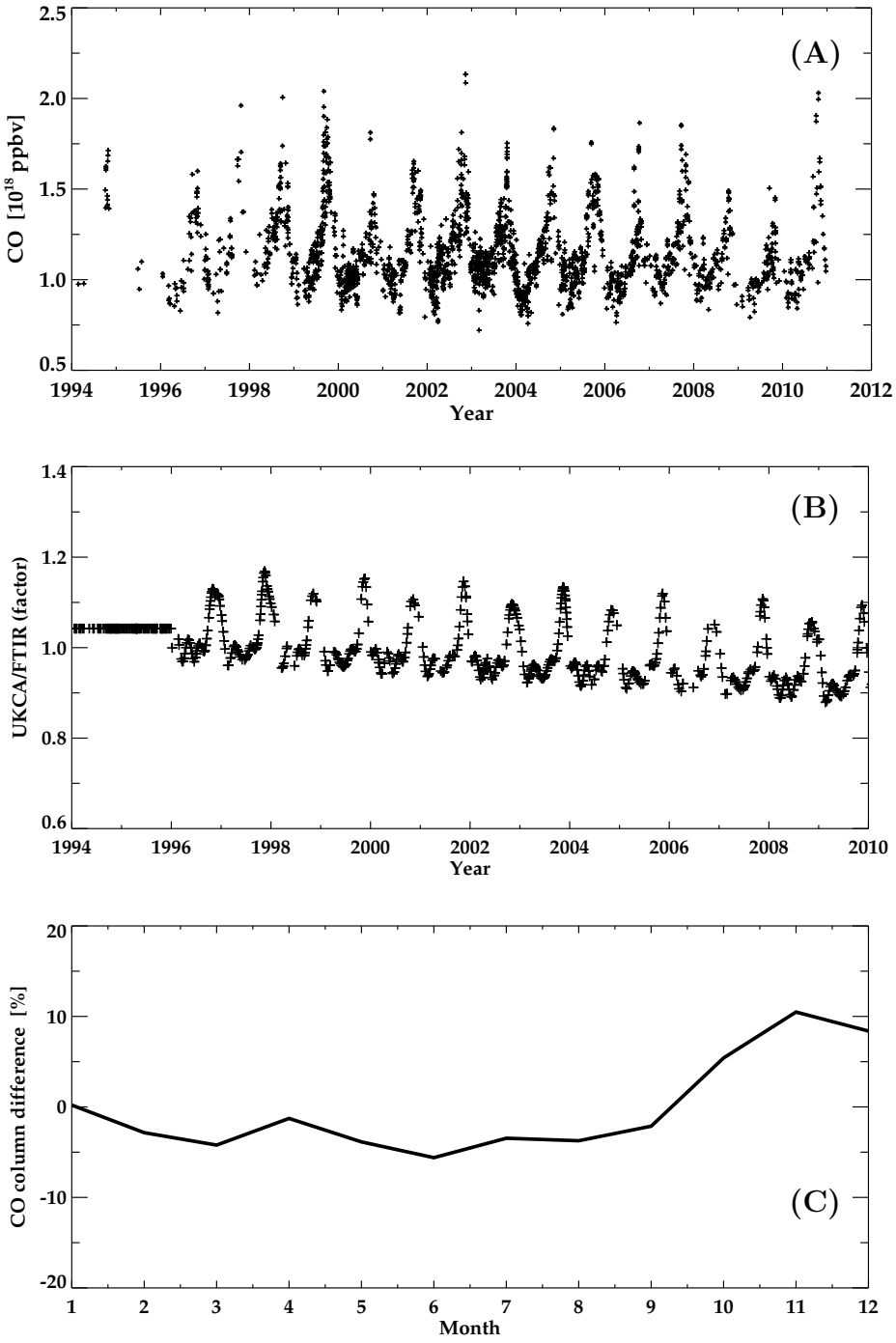

Figure 4.11: *(A) Time series of CO column measured by the FTIR spectrometer between 1994 and 2010. (B) Ratio of the fitted UKCA CO data of integrated profiles and the fitted FTIR CO column between 1994 and 2010. (C) Multi–annual and monthly–mean percentage difference between UKCA CCM and FTIR total column CO.*

The ratio of the whole time series employed to rescale the UKCA CCM CO profiles is displayed in Figure 4.11 B, where an uniform ratio value of 1.05 corresponding to the mean annual cycle of the period 1996 – 1999 is extrapolated back to 1994.

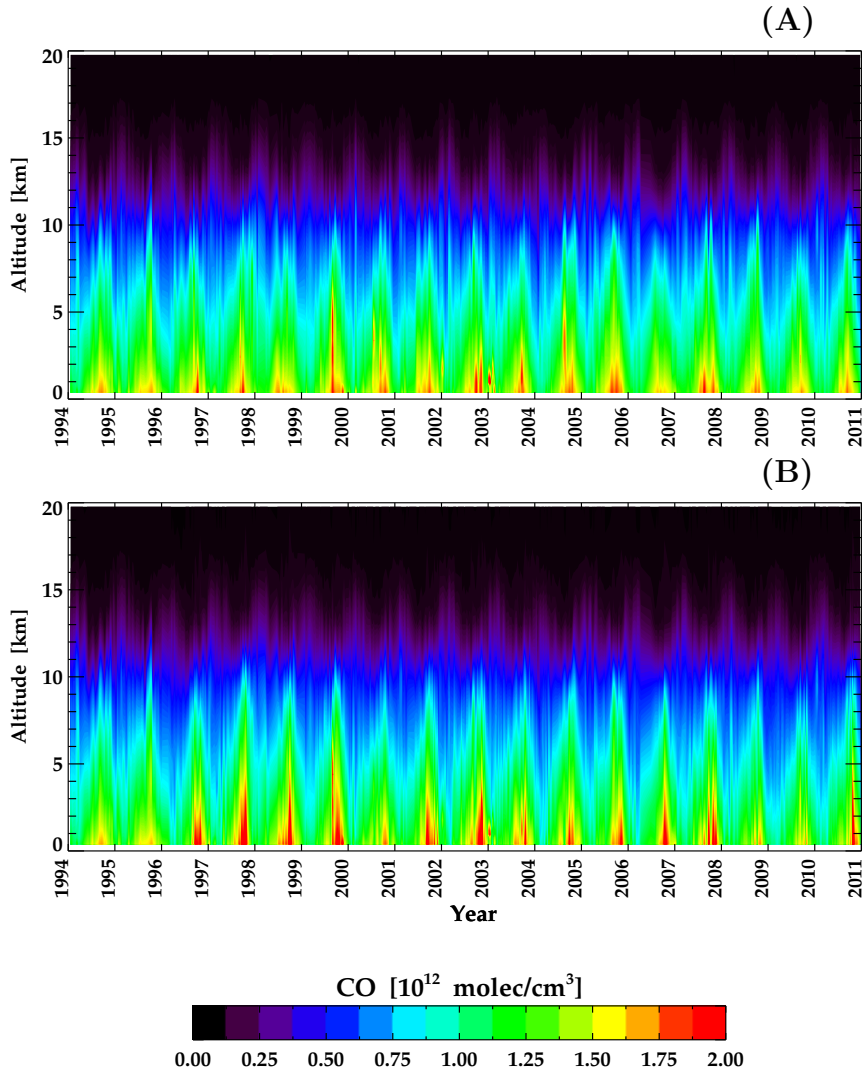

Figure 4.12: *(A) Time series of CO profiles constructed by rescaling the UKCA CCM CO to CO measurements from the FTIR spectrometer. (B) Time series of UKCA CO profiles.*

Figure 4.12 A depicts the time series of the constructed profiles for the period 1994 – 2010 from the surface up to 20 km of altitude. For comparison, the time series of UKCA CCM CO profiles for the same period is also displayed in Figure 4.12 B. The UKCA CCM underestimates total–column CO by around 5 % throughout the whole year except for late spring and summer when CO is overestimated (Figure 4.11 C). The time series of UKCA CCM CO profiles was used as a reference time series in the sensitivity analyses, the results of which are described in the next chapter.

4.5 Construction of CH_4 profiles

To construct the long–term series of CH_4 profiles, a combination of the UKCA CCM output data and surface CH_4 measurements from the Cape Grim Observatory (Tasmania – 40°S, 144.7°E) was used. The modelled CH_4 profiles were adjusted, so that the surface values matched the Cape Grim observations. This approach is based on the fact that CH_4 is well mixed and any differences in CH_4 between different sites in the SH can be ignored.

The Cape Grim station provides comprehensive *in–situ* monitoring of atmospheric composition in the SH. Among the measurements are GHGs, including CO_2, CH_4, N_2O, synthetic GHGs such as hydrofluorocarbons (HFCs), perfluorocarbons (PFCs), sulfur hexafluoride (SF_6) (Langenfelds *et al.*, 2014), ODS such as CFCs and halons (Krummel *et al.*, 2014), and radon (Zahorowski *et al.*, 2004).

The Cape Grim station is representative of the background SH condition, with the measurements at Cape Grim only taking clean air samples that are not influenced by the polluted air from the main land Australia, and the long–lived gases can be considered well–mixed.

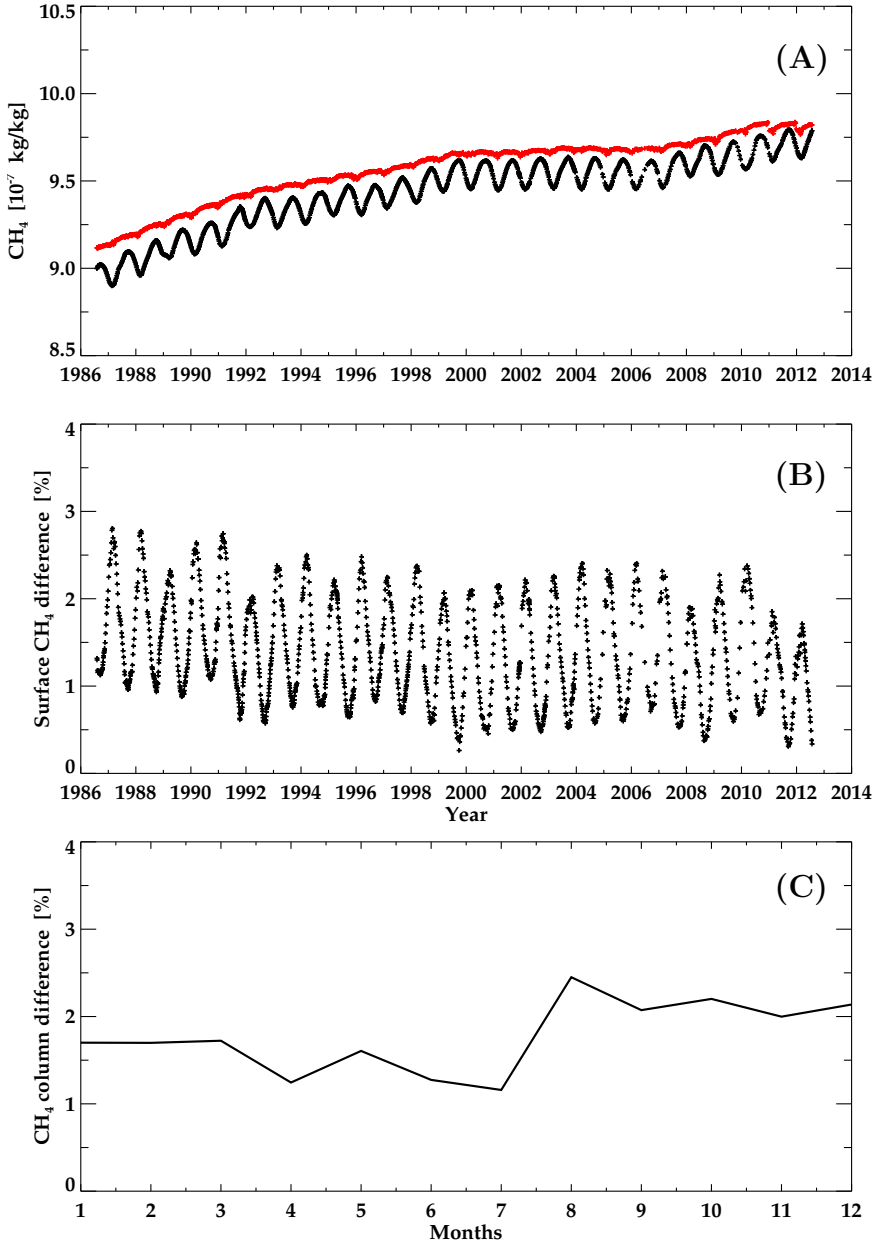

Figure 4.13: *(A) Time series of Cape Grim (black) and UKCA CCM (red) CH_4 surface measurements between 1986 and 2012. (B) Time series of the percentage difference between surface UKCA CCM and Cape Grim CH_4. (C) Multi–annual and monthly–mean percentage difference between UKCA CCM and FTIR total column CH_4.*

CH_4, as one of the GHGs measured at Cape Grim (see Appendix D for detailed information on the CH_4 measurements at Cape Grim), has been measured since 1984, showing a $\sim$ 10 % increase at the surface over the period covered by the ozonesondes (Figure 4.13 A black solid line). This pattern is also reflected by the UKCA CCM surface CH_4 (red solid line). As displayed in Figure 4.13 A, surface UKCA CCM CH_4 is overestimated with respect to Cape Grim measurements, with only a $\sim$ 2 % mean bias for the period 1986 – 2012 (Figure 4.13 B). Additionally, UKCA CCM and FTIR CH_4 total columns at Lauder were compared (Figure 4.13 C). The result also shows a $\sim$ 2 % positive mean bias of the UKCA CCM total column CH_4 relative to observations.

Although total columns of CH_4 are measured at Lauder since 2001 by the Fourier Transform infrared Spectrometer (FTS or FTIR), the measurements do not cover the full time period of the ozonesondes. Therefore, only Cape Grim surface CH_4 data were used to rescale the CH_4 profiles from the UKCA CCM output. The resulting time–series of CH_4 profiles is displayed in Figure 4.14 A, along with the UKCA CCM CH_4 profiles in Figure 4.14 B. CH_4 data above altitudes of 20 km are not represented due to the low values of CH_4 compared to those in the troposphere. As observed in Figure 4.14, the vertical gradient of CH_4 is small in the troposphere, since CH_4 is well–mixed as mentioned previously; above the tropopause, CH_4 values drop off sharply with height. The seasonal cycle of the tropopause height contributes to a seasonal cycle of the total column CH_4 (Zander *et al.*, 1989), although this seasonality is not considered in the UKCA CCM simulations. By rescaling the UKCA CCM CH_4 to Cape Grim surface CH_4, UKCA CCM data for Lauder now have realistic seasonality, but variability due to day–to–day weather is still not adequately represented. A 1.7 % RMSE and a 0.36 % mean bias were obtained between the vertical integrated rescaled CH_4 profiles and the FTIR total columns; These small discrepancies are indicative of the small variability of CH_4 across locations throughout the troposphere. The CH_4 profiles were also interpolated onto the model altitudes.

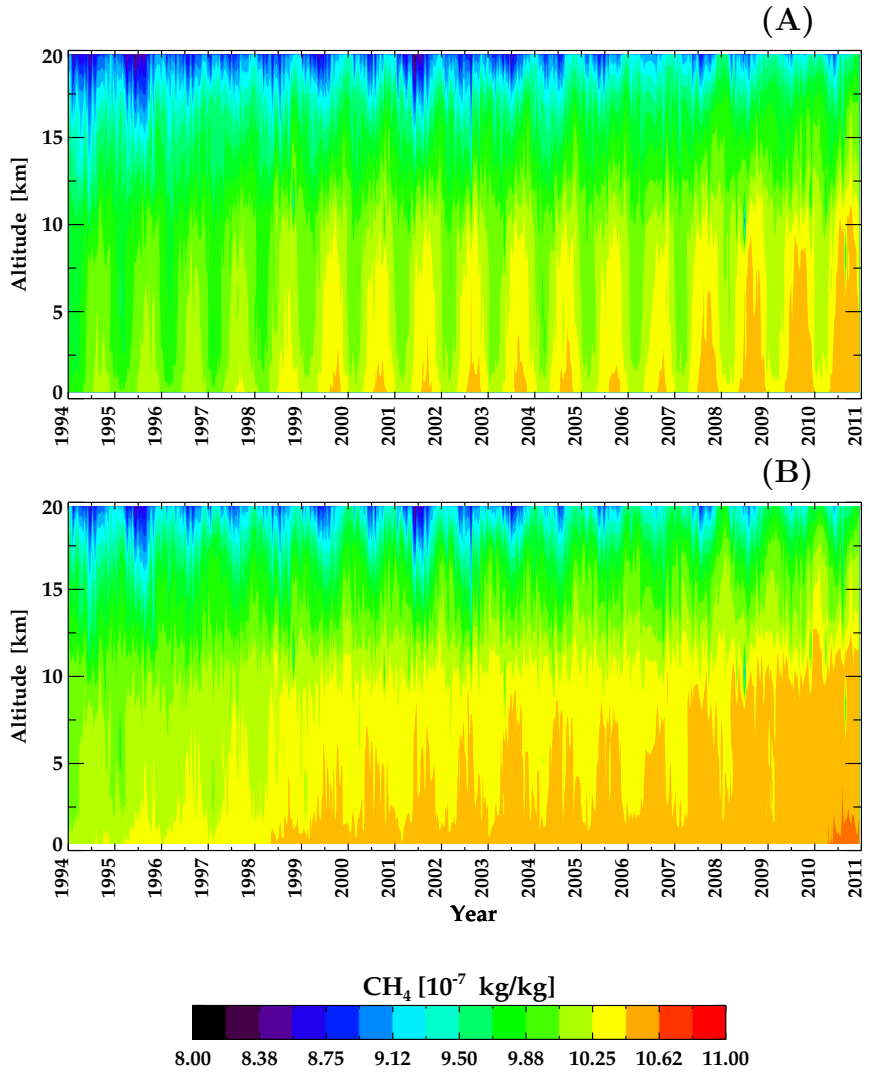

Figure 4.14: *(A) Time series of CH_4 profiles constructed by rescaling the UKCA CCM CH_4 to surface CH_4 measurements from Cape Grim (Tasmania). (B) Time series of UKCA CCM CH_4 profiles.*

4.6 Construction of temperature profiles

This section shows the construction of temperature profiles, following the same procedure as for the construction of O_3 profiles (see Section 4.2). The

first time series (1994 – 2010) comprised radiosonde temperature merged with MOPI1 temperature. The second time series (1986 – 2012) consisted of radiosonde temperature and temperature from the UKCA CCM.

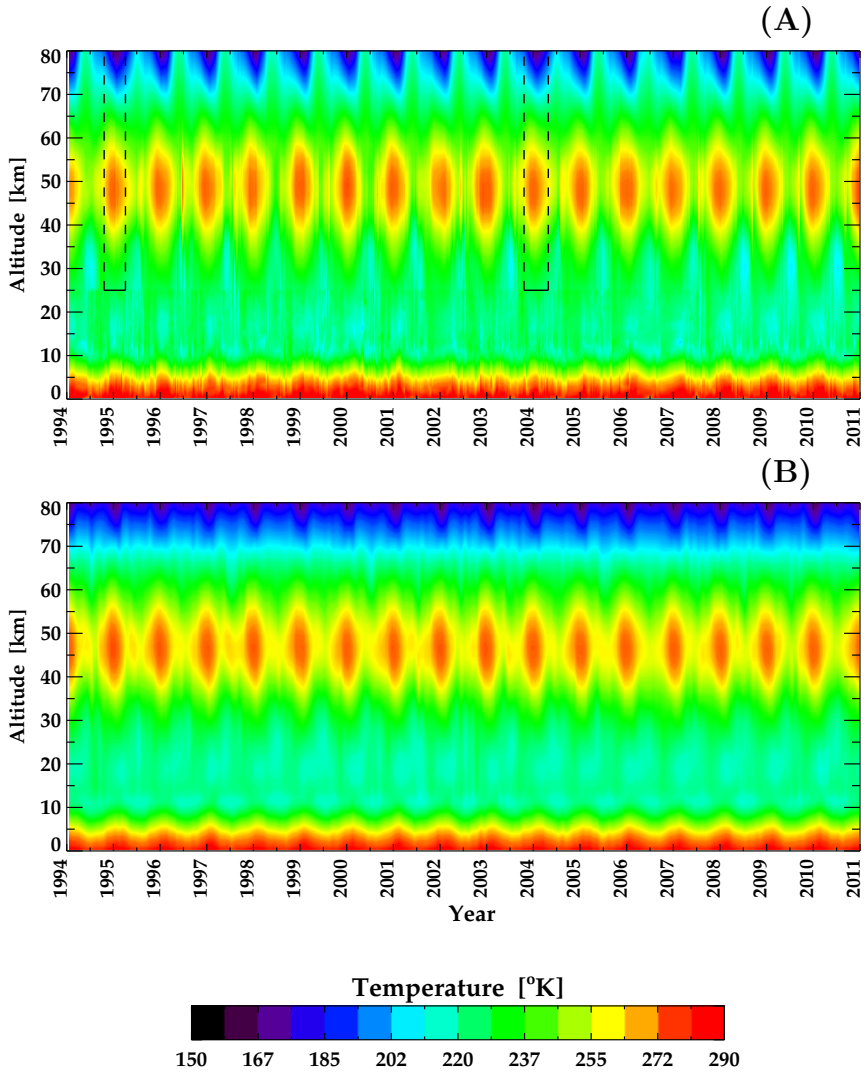

Figure 4.15: *(A) Time series of temperature profiles constructed by radiosonde measurements merged with MOPI1 measurements. The areas within black boxes were filled using Equation 4.4. (B) Time series of UKCA CCM temperature profiles.*

Figure 4.15 A shows the time series of temperature profiles constructed for the period 1994 – 2010. MOPI1 temperature gaps were filled by applying Equation 4.4 to the time series. The long time series of temperature is not displayed as it does not provide any additional information with respect to the short period. Figure 4.15 B depicts the time series of UKCA CCM temperature profiles for the same period.

The time series of temperature profiles compare well with the typical temperature structure of the atmosphere shown in Brasseur and Solomon (1986) and Brasseur *et al.* (1999), that was described in Chapter 2.

This chapter has focused on describing the procedure to turn available surface, total column, and profile measurements into time series for O_3, H_2O, CH_4, CO, temperature and pressure profiles into a common format suitable for running the NZAC SCM. The first section of this chapter is a description of the analysis of $j\mathrm{NO}_2$ and $j\mathrm{O}(^1\mathrm{D})$ measured at Lauder. These measurements were used to validate the FAST–JX photolysis scheme (Chapter 5). The subsequent sections of this chapter have focused on describing the construction of the time series of O_3, H_2O, CH_4, CO, and temperature profiles used to run the NZAC SCM. The results of the sensitivity of OH to correcting chemistry–climate model biases in these forcings are also given in Chapter 5.

Chapter 5

Sensitivity of OH due to different forcings under clear sky conditions

Several simulations were performed with the NZAC SCM in order to elucidate the contribution of biases in the key factors affecting OH photochemistry at Lauder, i.e. O_3, H_2O, CH_4, CO, and temperature, as stated in previous chapters. These key prescribed fields were used to perform individual simulations under clear–sky (cloudless and no aerosols) conditions, and a simulation with all forcings combined.

The work presented in this chapter is devoted to describing and illustrating the results of the sensitivity of the OH radical to these individual forcings (Sections 5.3 to 5.7), and the sensitivity of OH to all the species combined (Section 5.8) under clear–sky conditions. Likewise, long–term trends and the variability of OH are discussed in Section 5.10. The validation of the FAST–JX photolysis scheme results with Lauder observations, and comparisons with other published studies are presented in Section 5.1. Furthermore, a comparison of the NZAC SCM to the SSM is presented in Section 5.2.

5.1 Validation of the FAST–JX photolysis scheme

Two key photolysis rates control much of tropospheric chemistry: $j\mathrm{O}(^1\mathrm{D})$ through Reaction R 2.1 to produce $\mathrm{O}(^1\mathrm{D})$ which is the main source of OH, and $j\mathrm{NO_2}$ through Reaction R 2.3 which controls the photochemical production of $\mathrm{O_3}$ and the concentration of peroxy radicals, as reported previously in Chapter 2.3. To test the performance of the FAST–JX photolysis scheme, surface $j\mathrm{NO_2}$ and $j\mathrm{O}(^1\mathrm{D})$ obtained from FAST–JX under clear–sky conditions were compared to Lauder observations for cloudless conditions and to those of the UKCA CCM for the closest geographical position (Figure 5.1) under all–sky conditions.

In Figure 5.1 the mean annual cycle (as a function of the day of the year[1]), of surface $j\mathrm{NO_2}$ is depicted in the left panels 1a, 2a, and 3a. The right panels 1b, 2b, and 3b show surface $j\mathrm{O}(^1\mathrm{D})$ for a SZA corresponding to a local solar noon and a fixed surface albedo of 0.25 representative of Lauder. The comparison of $j\mathrm{NO_2}$ and $j\mathrm{O}(^1\mathrm{D})$ obtained from the NZAC SCM to observations and the UKCA CCM was made for three different scenarios to allow systematic comparisons between the photolysis rates. The first scenario used the UKCA CCM $\mathrm{O_3}$ which is displayed in Figure 5.1 1a and 1b; the second scenario with the merged ozonesonde and MOPI1 $\mathrm{O_3}$ as per Figure 5.1 2a and 2b; finally the third scenario used the merged ozonesonde and UKCA CCM $\mathrm{O_3}$ shown in Figure 5.1 3a and 3b to run the FAST–JX photolysis scheme.

For the $j\mathrm{NO_2}$ values obtained from the FAST–JX of the NZAC SCM (Figure 5.1 1a, 2a, and 3a), a systematic relative mean bias of about 30 % (ranging from 14 % to 39 %) with observations for the 3 scenarios was found. This difference with respect to observations is more likely to be attributable to discontinuities found in the $j\mathrm{NO_2}$ measurements (as reported in Chapter 4.1) than fluctuations in $\mathrm{O_3}$ and surface albedo. The

[1]The day of the year goes from 1 to 360 days instead of 365, since the UKCA CCM uses 360 days to allow simplification in some calculations, e.g. when calculating annual mean cycles.

sensitivity of $j\mathrm{NO_2}$ to the previous effects is very small, and it can only be attributed to the scattering by the presence of clouds and aerosols (Krol and Weele, 1997; Vuilleumier *et al.*, 2001; Balis *et al.*, 2002). Although $j\mathrm{NO_2}$ and $j\mathrm{O(^1D)}$ observations were restricted to only clear–sky data, the effect of Mie scattering by aerosols cannot be excluded in the time series of $j\mathrm{NO_2}$ and $j\mathrm{O(^1D)}$. Nevertheless, the effect of aerosols on photolysis rates is considered to be small in Lauder. For $j\mathrm{NO_2}$ in particular, changes in the aerosol optical depth produces slight changes in $j\mathrm{NO_2}$ (Balis *et al.*, 2002).

Furthermore, the UKCA CCM $j\mathrm{NO_2}$ and $j\mathrm{O(^1D)}$ are affected by clouds and aerosols as shown in Figure 5.1 (a and b panels). However, $j\mathrm{NO_2}$ (which is barely affected by the $\mathrm{O_3}$ column) from the UKCA CCM is highly correlated with that of the NZAC SCM for clear–sky situations. The abnormaly large values in winter shown in the UKCA CCM data correspond to a sharp increase in the surface albedo due to individual snow events typical of the winter season in the model, visible in both $j\mathrm{NO_2}$ and $j\mathrm{O(^1D)}$.

For the $j\mathrm{O(^1D)}$ values (Figure 5.1 1b, 2b, and 3b), variable systematic differences with respect to observations are seen for each scenario. For the first scenario, a mean relative bias of 12 % relative to observations is obtained (panel 1b). For the second and third scenario, higher mean relative biases of 33.4 % and 24.74 % that vary with season are obtained respectively (panels 2b and 3b). These differences are solely attributed to the strong dependence of $j\mathrm{O(^1D)}$ on the stratospheric $\mathrm{O_3}$ column (Thompson *et al.*, 1989; Krol and Weele, 1997) and also its vertical distribution (Forster, 1995), due to the small effect that aerosols produce on photolysis rates at Lauder.

The better agreement of $j\mathrm{O(^1D)}$ with observations in panel 1b may be misleading, because the UKCA CCM overestimates TCO by $\sim$ 20 DU in spring and by as much as 40 DU year–round (as reported in Chapter 4). The overestimated TCO leads to decreased UVB radiation and consequently decreased $j\mathrm{O(^1D)}$ values. Conversely, the higher mean relative biases of 33.4

% and 24.74 % with respect to observations are attributed to the lower TCO values in both scenarios relative to the first scenario where UKCA CCM O_3 was considered.

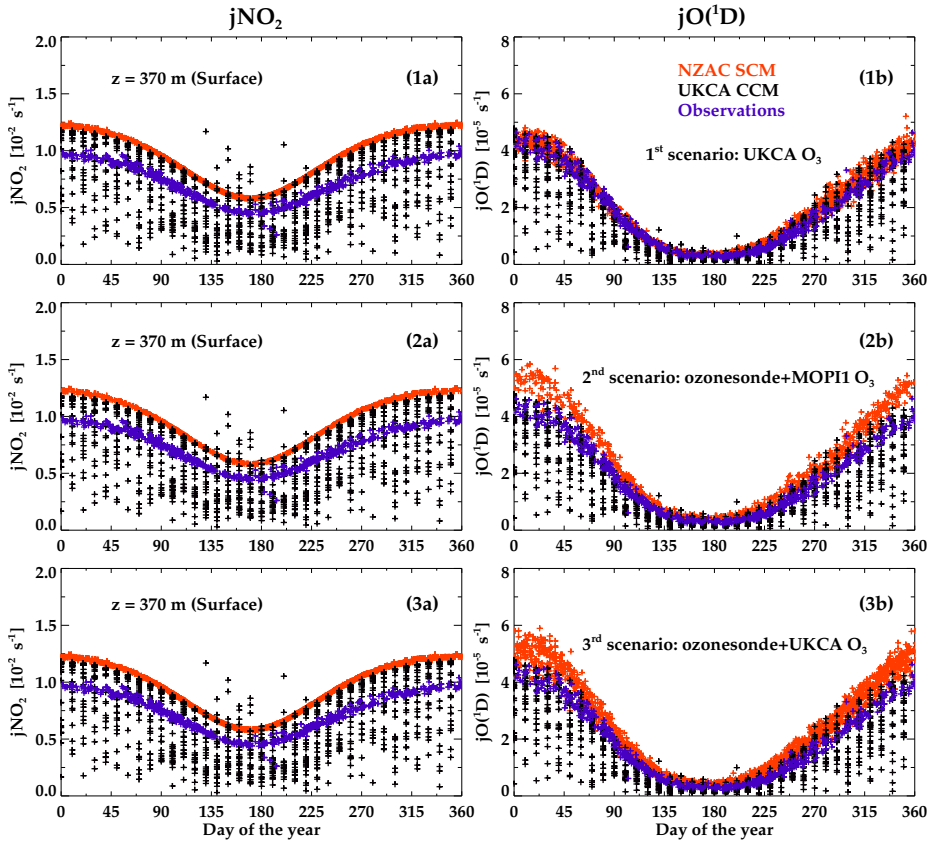

Figure 5.1: *Comparisons of the mean annual cycle of the surface jNO_2 (Panels 1a, 2a, and 3a) and $jO(^1D)$ (Panels 1b, 2b, and 3b) obtained from the NZAC SCM (red), with observations (blue) (corrected jNO_2 measured by the upper radiometer and $jO(^1D)$ by the UVM spectrometer) and those of the UKCA CCM (black). (1) Photolysis rates obtained by running the NZAC SCM with the UKCA CCM O_3. (2) The same as (1) but with spliced ozonesonde and MOPI1 O_3. (3) The same as (1) but with spliced ozonesonde and UKCA CCM O_3.*

A comparison of $j\mathrm{NO}_2$ and $j\mathrm{O}(^1\mathrm{D})$ from the NZAC SCM and from the UKCA CCM was also made at 20 km of altitude (Figure 5.2). For

clear–sky days, the jNO_2 and $jO(^1D)$ values obtained from the NZAC SCM are similar to those of the UKCA CCM. As expected, under cloudy conditions there is an increase of jNO_2 and $jO(^1D)$ in the UKCA CCM at 20 km, relative to the NZAC SCM; this is attributed to the increased effective surface albedo associated with clouds compared to the clear–sky condition (Thompson *et al.*, 1989; Wild *et al.*, 2000).

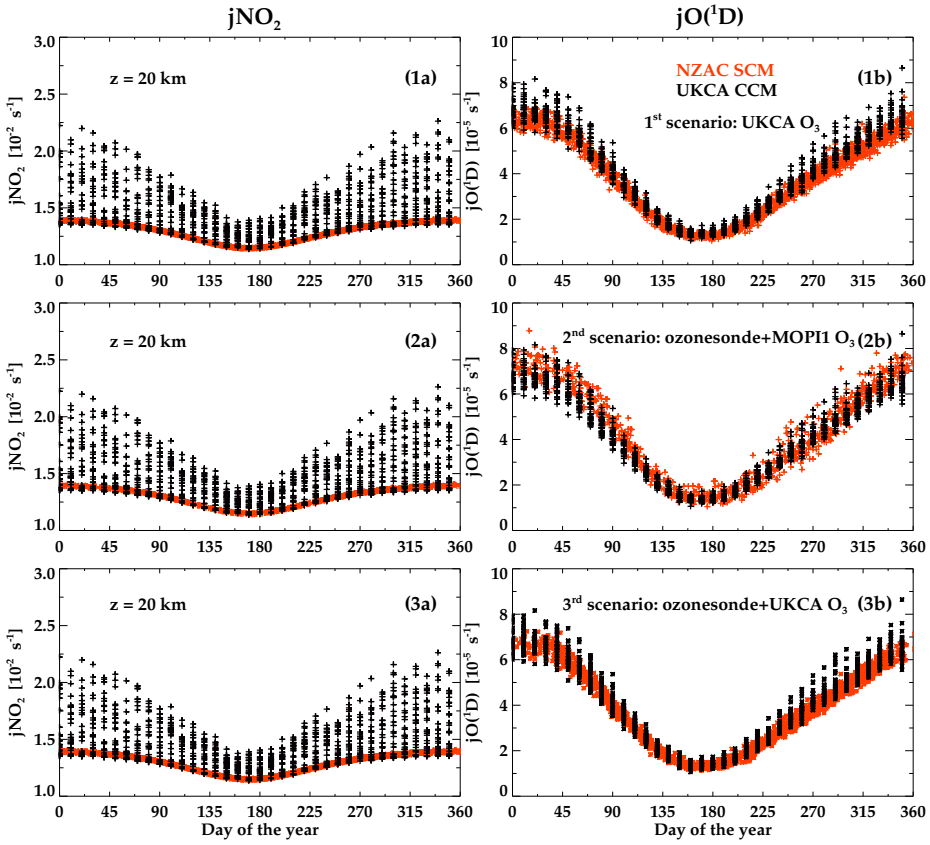

Figure 5.2: *Comparisons of the mean annual cycle of the jNO_2 at 20 km (Panels 1a, 2a, and 3a) and $jO(^1D)$ (Panels 1b, 2b, and 3b) obtained from the NZAC SCM (red) with those of the UKCA CCM (black). (1) Photolysis rates obtained by running the NZAC SCM with the UKCA CCM O_3. (2) The same as (1) but with spliced ozonesonde and MOPI1 O_3. (3) The same as (1) but with spliced ozonesonde and UKCA CCM O_3.*

Despite the good agreement between the NZAC SCM and the UKCA CCM at the surface and at 20 km of altitude, the differences with surface observations are considerable for $j\mathrm{NO_2}$ and $j\mathrm{O}(^1\mathrm{D})$ as displayed in Figure 5.1. Because of the discontinuities found in the observational data due to instrumental issues, the quality of the $j\mathrm{NO_2}$ and $j\mathrm{O}(^1\mathrm{D})$ measurements was difficult to ascertain, causing a large uncertainty when comparing it with the NZAC SCM. Therefore, the comparison with observations does not suffice as validation of the NZAC SCM, and requires further comparisons with other studies that previously validated FAST–J or FAST–JX; for instance, a study by Liu *et al.* (2006) who uses FAST–J to study the impact of clouds on $j\mathrm{O}(^1\mathrm{D})$ and compares it to clear–sky conditions (Figure 5.3).

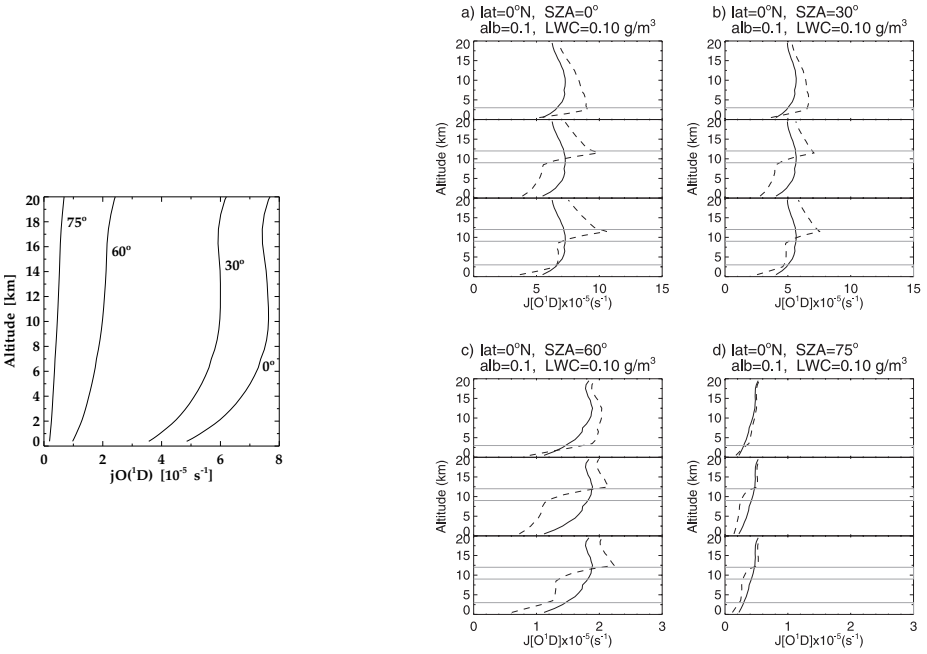

(a) **FAST–JX (NZAC)** (b) **Liu *et al.* (2006)**

Figure 5.3: *(a) Vertical profiles of $jO(^1D)$ at SZAs of 0°, 30°, 60°, and 75°, surface albedo of 0.1, and 0°N latitude in clear–sky conditions obtained from FAST–JX of the NZAC SCM. Comparison with (b) the study by Liu* et al. *(2006) calculated with FAST–J (solid line). The dashed and horizontal lines denote the influence of clouds on $jO(^1D)$ and cloud layers respectively [not represented in FAST–JX (a)].*

To compare FAST–JX results with those of Liu *et al.* (2006), the same conditions of Liu *et al.* (2006) were applied in FAST–JX calculations. These assumed a latitude of 0°N, 0.1 surface albedo, and SZAs = 0°, 30°, 60°, and 75°. The results on $j\mathrm{O}(^1\mathrm{D})$ (Figure 5.3 left panel) compare well with those of Liu *et al.* (2006) (Figure 5.3 middle and right panels) from the surface up to 20 km of altitude for clear–sky conditions. Small differences could be attributed to differences in O_3 concentration used to run these two photolysis schemes (FAST–JX was run with UKCA CCM O_3).

A comparison of FAST–JX $j\mathrm{NO}_2$, $j\mathrm{NO}_3$, and $j\mathrm{O}(^1\mathrm{D})$ (Figure 5.4 left panels) was also made with the FAST–J results by Wild *et al.* (2000) (Figure 5.4 right panels), using the same initial conditions of mid–latitude summer at SZAs of 0°, 60°, and 80° under clear–sky conditions. Figure 5.4 shows a good agreement between the two photolysis schemes. A small discrepancy that increases with altitude is observed for $j\mathrm{O}(^1\mathrm{D})$ at a SZA of 0° (Figure 5.4 top panels), which may be caused by the differences in O_3 concentration used in each photolysis scheme (as stated above), or most likely due to updates in the O_3 absorption cross–sections and quantum yields since the original study by Wild *et al.* (2000). Nevertheless, $j\mathrm{O}(^1\mathrm{D})$ at SZAs of 60° and 80° from FAST–JX correspond well with $j\mathrm{O}(^1\mathrm{D})$ from FAST–J by Wild *et al.* (2000), as well as $j\mathrm{NO}_2$ and $j\mathrm{NO}_3$ at all SZAs (Figure 5.4 middle and bottom panels).

Voulgarakis *et al.* (2009) also ran FAST–JX and compared the results with surface observations measured at Weybourne (52.9°N, 1.1°E) for a whole month (June 1995) which showed a good agreement between the modelled and the observed photolysis rates of $j\mathrm{NO}_2$ and $j\mathrm{O}(^1\mathrm{D})$. The $j\mathrm{NO}_2$ and $j\mathrm{O}(^1\mathrm{D})$ from FAST–JX of the NZAC SCM (Figure 5.5 top panels) under clear–sky conditions are compared with those calculated by Voulgarakis *et al.* (2009) (Figure 5.5 bottom panels) under cloudy conditions. A surface albedo of 0.05 was considered and aerosols were not included.

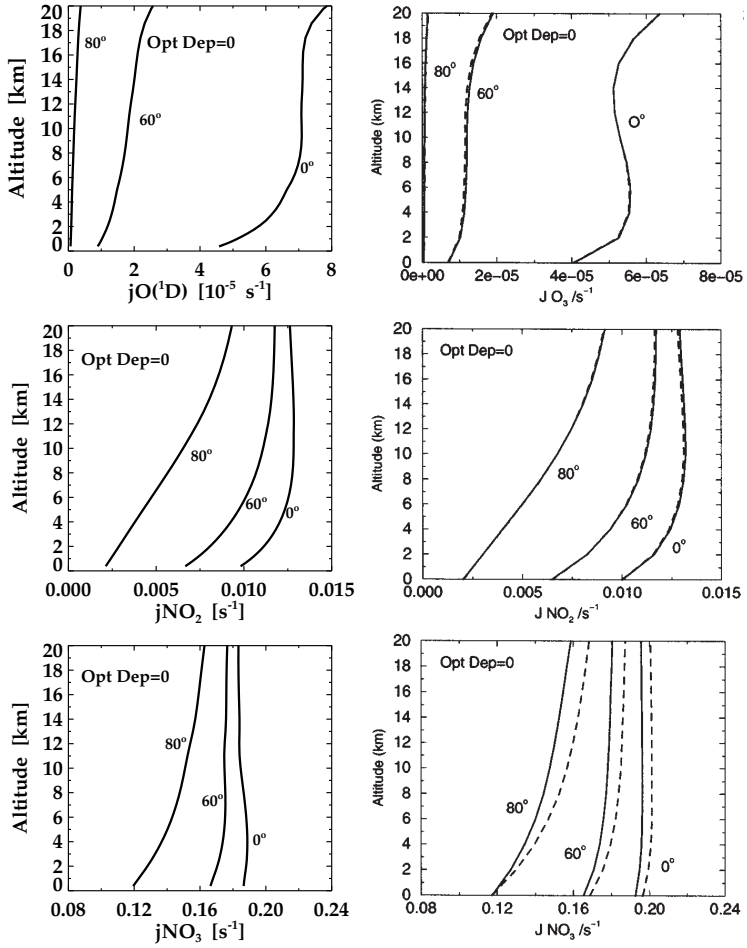

(a) **FAST–JX (NZAC)** (b) **Wild *et al.* (2000)**

Figure 5.4: *(a) Vertical profiles of $jO(^1D)$ (top), jNO_2 (middle), and jNO_3 (bottom) at SZAs of 0°, 60°, and 80° for mid–latitude summer and clear–sky conditions calculated with FAST–JX. Comparison with (b) the study by Wild* et al. *(2000) calculated with FAST–J (solid line). The dashed lines in the right panels display the results from the calculations using the standard UCI code [Wild* et al. *(2000)], which is not assessed here.*

While not considering aerosols, Voulgarakis *et al.* (2009) ran FAST–JX taking into account the effect of clouds in order to compare the results with observations for the whole month. As expected, discrepancies exist between j rates calculated here and those from Voulgarakis *et al.* (2009), due to the

fact that the NZAC SCM only runs under clear–sky conditions and the O_3 input is different from that of Voulgarakis *et al.* (2009).

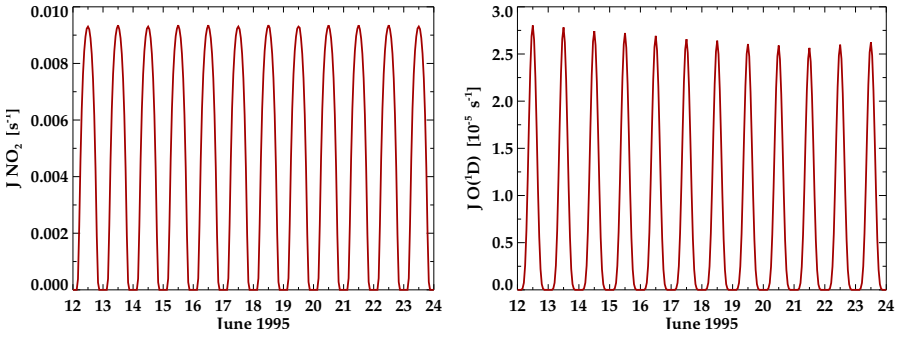

(a) **FAST–JX (NZAC)**

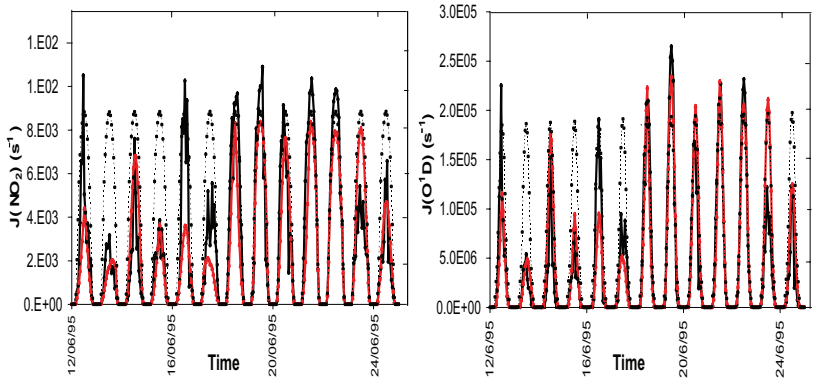

(b) **Voulgarakis *et al.* (2009)**

Figure 5.5: (a) *Surface jNO_2 (left) and $jO(^1D)$ (right) under clear–sky conditions with a surface albedo of 0.05, obtained from FAST–JX of the NZAC SCM. (b) Surface jNO_2 (left) and $jO(^1D)$ (right) under cloudy conditions with a surface albedo of 0.05, obtained from FAST–JX of Voulgarakis* et al. *(2009). The red solid line denotes the calculated jNO_2 and $jO(^1D)$ by FAST–JX of the NZAC SCM and of Voulgarakis* et al. *(2009). Measurements of jNO_2 and $jO(^1D)$ in Voulgarakis* et al. *(2009) are displayed in black solid line in the bottom panels. Also, in the bottom panels, the dashed line displays the calculations using a standard scheme (STD scheme) in Voulgarakis* et al. *(2009) which is not assessed here.*

For simulations on the days when clear sky is assumed [higher $j\mathrm{NO_2}$ and $j\mathrm{O}(^1\mathrm{D})$ values are observed], FAST–JX of the NZAC SCM is in good

agreement with FAST–JX used by Voulgarakis *et al.* (2009) with $j\mathrm{NO_2}$ values close to 9 x 10^{-3} $\mathrm{s^{-1}}$ and $j\mathrm{O(^1D)}$ values that range between 2.5 x 10^{-5} and 2.75 x 10^{-5} $\mathrm{s^{-1}}$. Small differences in $j\mathrm{NO_2}$ and $j\mathrm{O(^1D)}$ between FAST–JX of the NZAC SCM and FAST–JX by Voulgarakis *et al.* (2009) may be due to the different $\mathrm{O_3}$ used in these two schemes in which $j\mathrm{O(^1D)}$ is more affected. Another inconsistency between the the two schemes is that the NZAC SCM assumes clear–sky conditions, whereas the study by Voulgarakis *et al.* (2009) is based on cloudy conditions.

Overall, the performance of FAST–JX of the NZAC SCM relative to these three studies is good, with small discrepancies attributed to either differences in the supplied $\mathrm{O_3}$ or differences regarding sky conditions (FAST–JX of the NZAC SCM is based on clear–sky days whereas FAST–JX by Voulgarakis *et al.* (2009) is based on cloudy conditions). $j\mathrm{NO_2}$ and $j\mathrm{O(^1D)}$ calculated using the FAST–JX of the NZAC SCM were shown to compare well with those of the UKCA CCM and calculations from other studies for clear–sky conditions. While not all photolysis rates used in NZAC SCM have been assessed here (there are 59 in total), $j\mathrm{NO_2}$ and $j\mathrm{O(^1D)}$ are sensitive to actinic fluxes in different wavelengths regions, therefore it is likely that other photolysis rates are also correctly calculated. Good agreement in $j\mathrm{NO_2}$ and $j\mathrm{O(^1D)}$ with these studies, and assuming a correct implementation of cross–section information for other photolysed species, imply that other photolysis reactions are also adequately captured. Therefore, FAST–JX of the NZAC SCM is satisfactory in calculating the photolysis rates that will be the key in the study of OH chemistry presented in the following sections of Chapter 5.

5.2 Comparison of the NZAC SCM to the SSM

This section outlines the description and discussion of the results obtained from the comparison of the NZAC SCM to the SSM for OH which has already been described in Chapter 3. The advantage of using a SSM is that it is essentially an analytical calculation which provides a plausibility

test for the NZAC SCM. Also using the SSM, the response of OH to varying external parameters can be compared to this analytical model. However, it should be noted that assumptions that were made here would limit the applicability of the SSM under other conditions, i.e. the reduced mechanism will not be applicable in polluted regions due to the different chemical regime there compared to that in the clean region. Furthermore, the steady–state assumption as such, or details of the formulation such as which species to include in the chemical family, may come in for scrutiny. This is explored in this section.

In this section, it is separately assessed how the SSM and the NZAC SCM compare for the reference forcings (using UKCA CCM data), and how the responses of OH to changes in the key forcings (O_3, H_2O, CH_4, CO, and temperature) compare between the two models. For that, the steady–state calculations were performed using the trace gas concentrations and temperature constrained in the NZAC SCM as input, using observational data for the key parameters and UKCA CCM output (see Chapter 4). The comparison with the SSM was only performed for the troposphere (surface up to 10 km of altitude).

OH concentrations obtained from both models are compared for the reference forcings in Figure 5.6 for the troposphere. In clean–air sites such as Lauder, the chemistry of OH is expected to be dominated by O_3 photolysis (Reaction R 2.1), the subsequent reaction of $O(^1D)$ with H_2O (Reaction R 2.2), and its removal by reactions with CO and CH_4 (Reactions R 2.6 and R 2.7 respectively) (Smith *et al.*, 2006), which have been included in the SSM. Therefore, OH from the NZAC SCM should show a good agreement with that of the SSM, as clearly shown in Figure 5.6; it shows that most data are near the 1:1 diagonal, with some deviation from the linearity in the SSM as OH concentration increases during summer.

In Figure 5.6, H_2O_2 was not treated as member of the HO_x family which is assumed to be in steady state. However, it could be argued that

formation and loss of H_2O_2 from HO_x is fast enough for H_2O_2 to be treated as in steady–state with the rest of the family (which becomes HO_y if H_2O_2 is included), since HO_x is strongly linked to H_2O_2 production and destruction. The globally averaged lifetime of H_2O_2 is a few hours as reported by Hua *et al.* (2008) and Allen *et al.* (2013). For testing purposes, H_2O_2 was assumed to be in steady state in a separate simulation, with only the daytime situation being considered, near the local solar noon, when H_2O_2 minimizes.

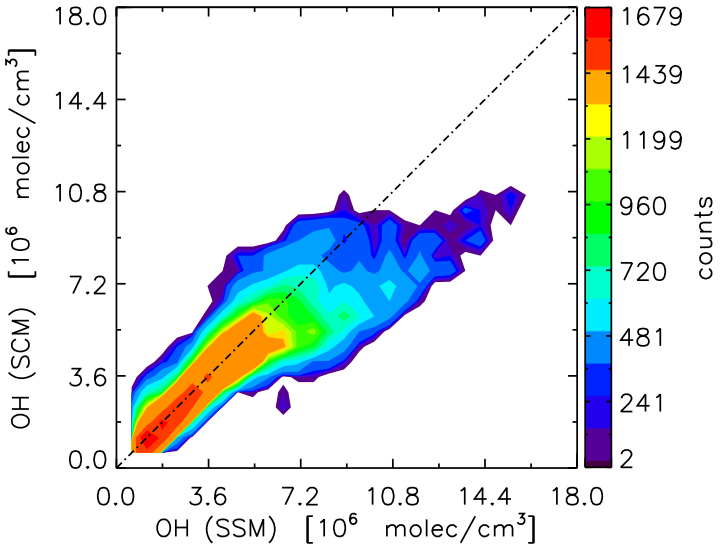

Figure 5.6: *Density plot of OH concentrations in the SSM versus OH concentrations in the NZAC SCM for the reference simulation (UKCA CCM data). The displayed concentration range has been divided, for both axes, into 36 subintervals and the number of occurrences of OH in each resulting grid box is displayed here. Only levels below 10 km are considered.*

Consequently, the steady–state assumption for HO_x was extended to incorporate H_2O_2 into the family (HO_y), using an iterative calculation. For that, the main reactions for H_2O_2 in the troposphere which dominate

the production and loss of HO_y in clean environments are the HO_2 radical recombination (Reactions R 3.6 and R 3.12), and its dependence on photolysis (Reaction R 3.4) along with its reaction with the OH radical (Reaction R 5.1) respectively:

$$OH + H_2O_2 \xrightarrow{k_{17}} H_2O + HO_2 \qquad \text{(R 5.1)}$$

The steady–state expression for H_2O_2 results in Equation 5.1:

$$[H_2O_2] = \frac{(k_3 + k_9[M])[HO_2]^2}{j_1 + k_{17}[OH]} \qquad (5.1)$$

The comparison of OH concentrations between the NZAC SCM and the SSM which includes H_2O_2 to be in steady state as part of HO_y, showed a only slight improvement with respect to the results shown in Figure 5.6, and therefore it is not displayed here. This result suggests that assumptions made in formulating the SSM used here may have limitations. In principle, the inclusion of additional OH sources and sinks in the SSM would make the steady–state prediction more realistic, but this is not pursued here for simplicity.

The response of OH to changes in the most important forcings adopted in the NZCA SCM and SSM are examined. Values of those forcings from observations and from UKCA CCM simulations are used to drive the two models for the sensitivity test. For that, differences in OH to varying the most important forcings were calculated for both models (NZAC SCM and SSM) as per Equation 5.2:

$$\Delta[OH] = [OH]_{x+\Delta x} - [OH]_x \qquad (5.2)$$

where $[OH]_{x+\Delta x}$ is the OH concentration calculated using observed forcings assuming correcting 'x' with its bias Δx, $[OH]_x$ is the OH concentration calculated using UKCA CCM output, and $\Delta[OH]$ is the absolute difference of OH between the two simulations. The sensitivity of OH to forcings is expressed as $\frac{\Delta[OH]}{\Delta[x]}$, which will be discussed in the next

section. Figure 5.7 shows OH differences calculated using Equation 5.2 for both simulations (NZAC SCM and SSM) displayed as scatter plots. If the two models were identical, the data would lie on the 1:1 diagonals. Deviations from that result are due to differences in the formulations, i.e. the simpler mechanism in the SSM and the steady–state assumption itself.

OH differences due to O_3 forcing are shown in Figure 5.7 A. The deviation of the slope from 1 by 31 % indicates the difference between the models. Omission of odd nitrogen chemistry in the SSM is one of these differences. O_3 controls OH via $O(^1D)$ production through photolysis of O_3 (Reaction R 2.1), in which, for very low NO abundances, the OH concentration is enhanced when the O_3 concentration increases (Poppe *et al.*, 1993). By contrast, in a high NO_x environment the dominant process is the sink of HO_x radicals through oxidation of NO_2 by OH (Elshorbany *et al.*, 2012) which suppresses OH formation:

$$NO_2 + OH + M \longrightarrow HNO_3 + M \qquad \text{(R 5.2)}$$

In the SSM, this reaction was neglected in the steady–state equation for HO_x. Although NO_x abundance is generally low at Lauder, NO_x could still affect HO_x in the comparison of the two models. Reaction R 5.2 might explain the 31 % deviation of the slope from the slope 1 observed in Figure 5.7 A. In contrast, for low NO_x values, the sink reaction for HO_x to form H_2O_2 (Reaction R 3.6) becomes more relevant than Reaction R 5.2. For that reason, the comparison of differences in OH to varying O_3 between the two models assuming H_2O_2 to be in steady state was also performed. The results obtained[2] show similar OH differences with a 35 % deviation from the slope 1. While these differences remain unexplained, the correlation between the models is good in both steady–state assumptions for HO_x with a high degree of correlation ($r = 0.89$), and with the OH differences produced by the two models generally within 10 % of each other.

[2]The comparison of the NZAC SCM with the SSM when including H_2O_2 as member of the family HO_y are not displayed here. Only the orthogonal fit parameters are discussed.

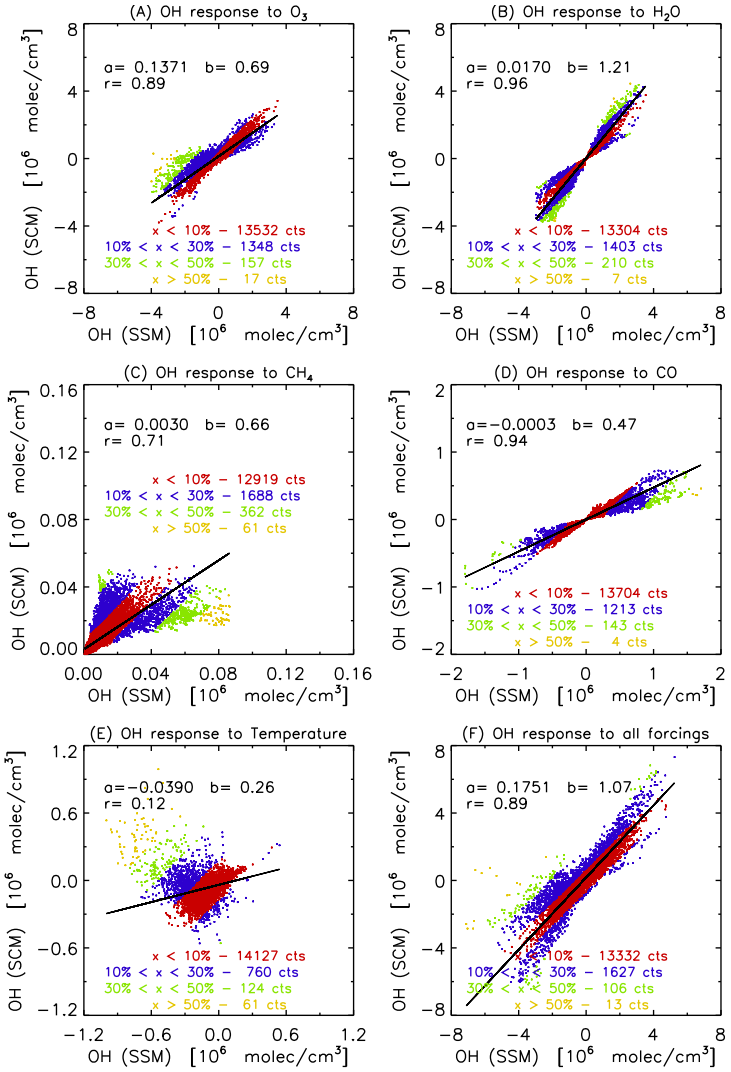

Figure 5.7: *(A) Comparison of differences in OH due to different O_3 forcings (observed and UKCA CCM) between the NZAC SCM and the SSM. (B) The same as (A) but using H_2O as forcing. (C) The same as (A) but using CH_4. (D) The same as (A) but using CO. (E) The same as (A) but using temperature. (F) The same as (A) but using all forcings combined. Differences between models are depicted as percentages within the ranges 0 – 10 % (red), 10 – 30 % (blue), 30 – 50 % (green), and > 50 % (yellow), and the number of data within these ranges (e.g. 0 – 10 % in red colour is the range of data that sits closer to the 1:1 diagonal); Each plot includes the coefficients for the orthogonal regression: 'a' is the constant offset, 'b' is the slope, and 'r' is the Pearson correlation coefficient.*

The comparison of the OH differences between the NZAC SCM and the SSM to changing H_2O is performed in Figure 5.7 B[3]. The comparison between the two models is reasonable, with a 21 % deviation of the slope from the slope 1. The deviation might be explained in terms of missing reactions in the SSM, e.g. oxidation of several non–methane volatile organic compounds (NMVOCs), and the formation of H_2O_2 by self–reaction of HO_2 (Reaction R 3.6). This ties up HO_x, affects OH, but is ignored in the SSM as formulated before (Reaction R 5.1). By experimentally considering H_2O_2 to be in steady state as part of HO_y, the comparison between models improves, obtaining only a 8 % deviation from the slope 1. Likewise, both models are highly correlated ($r = 0.96$ and $r = 0.97$ for the case in which H_2O_2 is considered to be in steady state).

For CH_4, Figure 5.7 C shows a discrepancy between the models of 34 % deviation of the slope 1. The possible explanation might also be due to missing oxidation reactions of NMVOCs in the SSM. The correlation between the models is fairly high ($r = 0.71$). The results of the response of OH to varying CH_4 considering H_2O_2 as part of HO_y show similar agreement with the previous case (38 % deviation and $r = 0.78$), suggesting that H_2O_2 has little effect on the CH_4 chemistry. Despite the discrepancy between the models, the impact of differences in CH_4 between observations and the reference simulation (driven with UKCA CCM data) on OH is small, in agreement with the small differences in CH_4 between the two simulations.

In the SH, direct CO emissions into the atmosphere are principally due to BB, maximizing in austral spring, and biogenic production (Swinnerton *et al.*, 1970; Watson *et al.*, 1990; Fishman *et al.*, 1991). CO and associated pollutants (some NMVOCs) due to BB are transported to clean remote areas such as Lauder (Edwards *et al.*, 2006). The 53 % deviation of the slope from the slope 1 observed in Figure 5.7 D when comparing the

[3]Here, radiosonde H_2O was used for the comparison of the NZAC SCM to the SSM. ERAI H_2O produced similar results in the comparison as for the previous case. Therefore, the results are not displayed here.

differences in OH to CO changes between the two models, may be attributable, for instance, to the missing reactions for OH loss in the SSM through reactions with some NMVOCs, as for the case of OH differences due to changes in CH_4. When assuming H_2O_2 as part of the HO_y family, the slope of the sensitivity of OH between both models improves by 15 %. This suggests that the inclusion of H_2O_2 into the family influences the final response of OH to changes in CO. Regardless of the discrepancies observed between models, the correlation is 0.94 for the case in which HO_x is assumed to be in steady state, and 0.89 for the case in which H_2O_2 becomes a member of the family (HO_y).

The comparison of the differences in OH to perturbing temperature between the NZAC SCM and the SSM is depicted in Figure 5.7 E. The agreement between models is poor. For the case in which H_2O_2 was in steady state as part of HO_y, the comparison of the differences in OH does not improve. However, the dependence of OH to errors in temperature are very small, compared to the dependence of OH to O_3 and H_2O biases. This is in agreement with O'Connor *et al.* (2009) who also find a small dependence of OH on temperature biases in the UKCA CCM.

In Figure 5.7 F the differences in OH to changes in all perturbations combined is depicted. The orthogonal regression almost follows the 1:1 line (with a slope of 1.07) and the correlation is high ($r = 0.89$). Nevertheless, this result might be due to a partial cancellation of errors, since the OH responses to the major contributors to OH chemistry in the troposphere (O_3 and H_2O) are biased in opposite directions. When H_2O_2 is included in the HO_y family, the correlation between models stay practically the same ($r = 0.93$), but the deviation of the slope from the slope 1 increases by 15 %.

Overall, from the results presented in this section, both models compare reasonably well. It is obvious that a necessary condition for the SSM to be useful is that all significant source and sink terms need to be included in the formulation. Essentially, the results confirm that the

NZAC SCM plausibly simulates OH, as compared to the analytical and intentionally simple SSM. This builds confidence in the NZAC SCM. However, it must be taken into account that the assumptions used in designing the SSM make it unsuitable under more complex atmospheric conditions, and hence it is not a good benchmark for the more complete NZAC SCM.

5.3 Sensitivity of OH to O_3 biases

Several sensitivity studies were conducted to assess the contribution of biases in known factors (O_3, H_2O, CH_4, CO, and temperature) affecting OH photochemistry at Lauder. For that, sensitivity simulations were performed to assess the response of OH to changes in each forcing individually and to all the forcings combined. Observational data were used to prescribe the key forcings (already described in Chapter 4), along with UKCA CCM data for the rest of the input species required by the model to run the different simulations. A simulation with only UKCA CCM data was also performed that was used as the reference simulation (Chapter 4).

For O_3 in particular, the major in situ source of OH in the troposphere is through the photolysis of O_3 (Reaction R 2.1) and the subsequent reaction of $O(^1D)$ with H_2O (Reaction R 2.2). The efficiency of the recycling by OH merely depends on NO_x levels; in high NO_x conditions, the reaction of NO with HO_2 (Reaction R 2.12) plays a key role in the production of a large fraction of O_3 in the troposphere, thereby producing OH. By contrast, in clean–air regions such as Lauder, the production of O_3 is mainly attributed to the oxidation of CH_4 (Reaction R 2.7) and CO (Reaction R 2.6). Under the low NO_x condition, tropospheric chemistry leads to a loss of O_3 (Crutzen, 1973; Zellner, 1999), and consequently a loss of OH. This section is devoted to describing the results of the analysis of the sensitivity of the OH radical to O_3 biases (defined as differences between observed O_3 and UKCA CCM simulated O_3) at Lauder.

Several sensitivity simulations were conducted to elucidate the response of OH to correcting O_3 biases in the troposphere at Lauder. The first sensitivity test was to assess the vertical and seasonal response of calculated OH to O_3 changes relative to the reference run which uses UKCA CCM data, i.e. replacing UKCA CCM O_3 with the observed O_3 values. Figure 5.8 shows the relative percentage differences in OH (panels a) and $j\mathrm{O}(^1\mathrm{D})$ (panels b) as the result of perturbating O_3, and other forcings (H_2O, CH_4, CO, and temperature) that will be discussed in sections 5.4 to 5.8. The results are for the period 1994 – 2010 and are displayed from 0 to 10 km of altitude.

As would be expected, from the simulation constrained with observed O_3, depicted in a solid light blue line, $j\mathrm{O}(^1\mathrm{D})$ is sensitive to the integrated O_3 absorption and scattering of photons that occur in the overhead column. Thus, the magnitude of $j\mathrm{O}(^1\mathrm{D})$ decreases markedly from the upper troposphere (UT) (not shown) to the lower troposphere (LT) for all seasons [Figure 5.8 panels b (solid light blue line)]. The simulation constrained with observed O_3 introduced 20 – 28 % differences compared to the reference simulation throughout the vertical domain for autumn and summer seasons (1b and 2b), and 14 – 20 % for spring and winter (3b and 4b). These differences are the result of the overestimation of TCO in the UKCA CCM simulation, which is seasonally varying (Chapter 4). Consequently, changes in OH in response to changes in O_3 are mainly positive (up to 7 %) for all seasons. It should be noted that the largest changes in OH occur in the free troposphere where the combined effect of changes in O_3 and $j\mathrm{O}(^1\mathrm{D})$ are probably the largest.

A second analysis was to quantify the contribution of O_3 biases to OH chemistry at Lauder, for which three sensitivity simulations were conducted in addition to the reference run. For simplicity in the analyses, an annually periodic time series was constructed for all chemical compounds in the NZAC SCM, including O_3, by fitting the time series of each chemical species to a Fourier series through Equation 4.4 (note that this was also applied to all

the forcings used in the following sections).

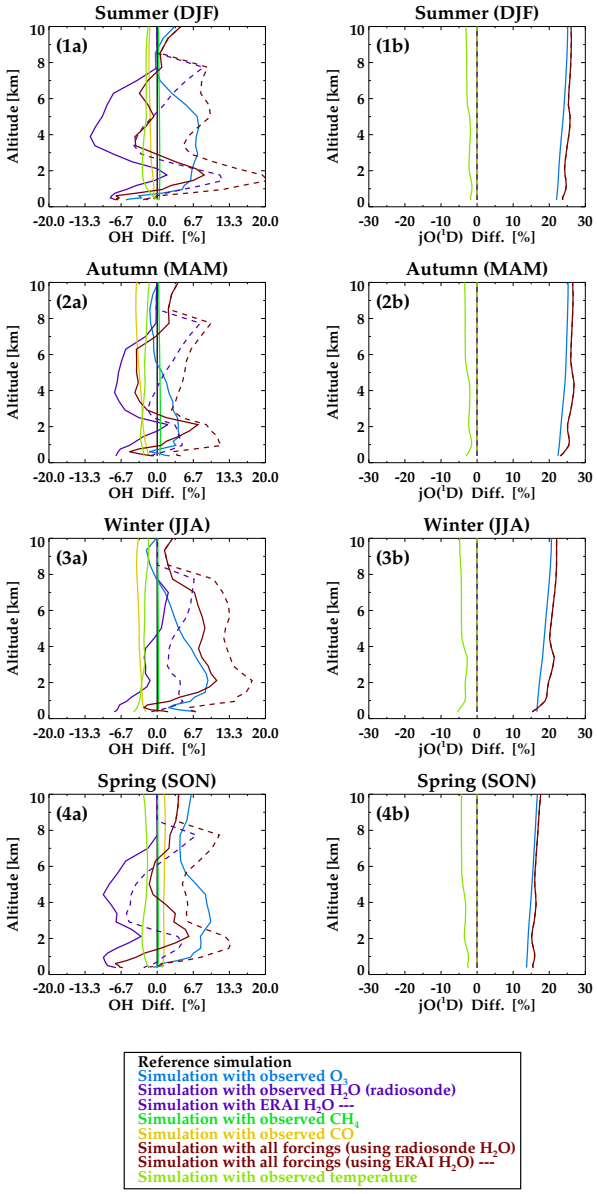

Figure 5.8: *Seasonal percentage differences between perturbation simulations and the reference simulation for OH (panel a) and $jO(^1D)$ (panel b). As per legend: Reference simulation (black solid line); simulations with observed O_3 (ozonesonde – MOPI1) (solid light blue), H_2O (radiosonde – UKCA CCM) (solid purple), H_2O (ERAI – UKCA CCM) (dashed purple), CH_4 (solid dark green), CO (solid yellow), all forcings combined using radiosonde H_2O (solid red), all forcings combined using ERAI H_2O (dashed red), and temperature (solid light green).*

For O_3, OH responses to correcting O_3 biases between observations and the reference simulation were decomposed into the effects of gas–phase kinetics excluding photolysis (hereafter kinetics effects) and the effects due to photolysis (hereafter photolysis effects) on OH caused by changing O_3.

The first simulation (kinetics effects) consisted of applying changes in O_3 concentrations but keeping $j\mathrm{O}(^1\mathrm{D})$ and the rest of the photolysis rates unchanged (using the photolysis rates from the reference simulation). A second simulation involved applying changes in $j\mathrm{O}(^1\mathrm{D})$ according to changes in O_3 (keeping the rest of photolysis rates unchanged), but considering a fixed O_3 concentration, i.e. using the O_3 concentrations of the reference simulation. A third simulation was run considering both previous effects simultaneously (kinetics + photolysis effects)[4].

The results of the three sensitivity runs are displayed in Figure 5.9. The top panels (1a and 1b) refer to the sensitivity simulation considering the kinetics effects on OH, where the difference in OH (Figure 5.9 1b) relative to the reference shows a similar positive pattern to the difference in O_3 (Figure 5.9 1a), and the largest differences are in the free troposphere where these differences vary with altitude. In summer and autumn, O_3 differences range between –5 % and –45 %, meaning that UKCA CCM O_3 is overestimated with respect to observations. This pattern translates into negative differences of the OH concentration obtained from the NZAC SCM for these seasons which range between –2 % and –20 %. In spring, observed O_3 is larger than in the reference simulation by only around 5 % and therefore OH is, in turn, increased by also around 5 %.

The results of the sensitivity simulation considering the photolysis effects are displayed in the middle panels of Figure 5.9 (2a and 2b). $j\mathrm{O}(^1\mathrm{D})$, which decreases with increasing TCO (Figure 5.9 2a), shows differences relative to the reference simulation that range between $\sim$ 14 % and $\sim$ 28 % with some altitude dependence.

[4]The third simulation is the same simulation used in the analysis of the seasonal response of OH to O_3 biases shown in Figure 5.8.

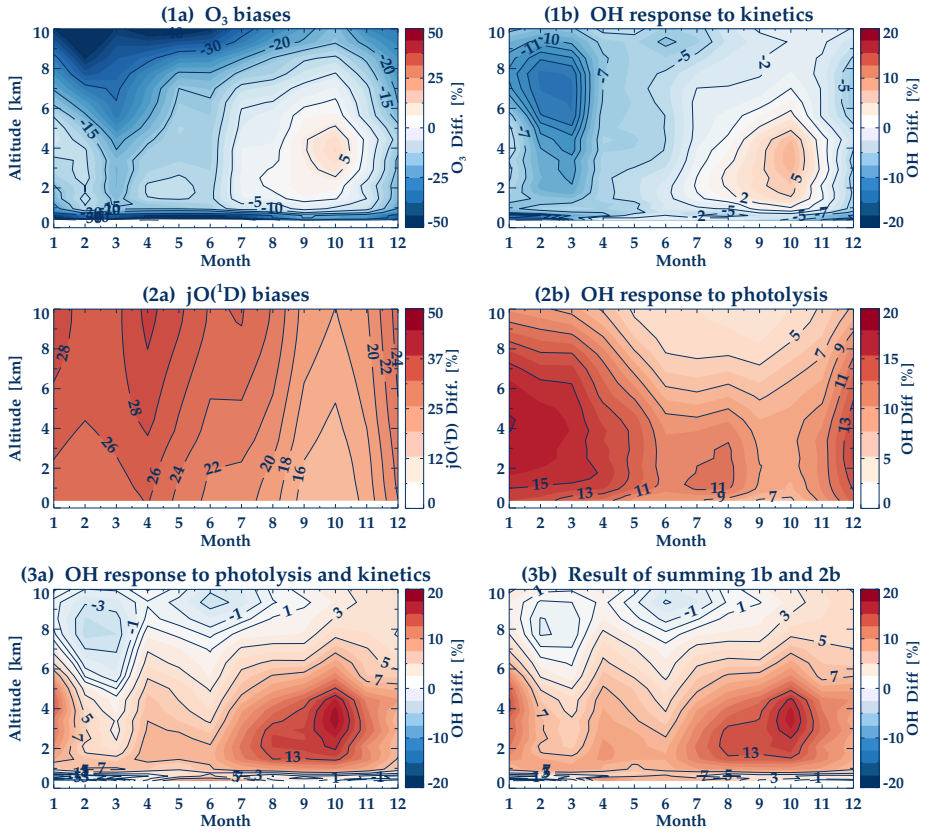

Figure 5.9: *Multi–annual and monthly–mean OH responses to O_3 biases between observations and the reference simulation. (1a) Difference in O_3 (%) relative to the reference simulation. (1b) OH difference (%) relative to the reference simulation accounting only for the kinetics effects of O_3 differences (e.g. with $jO(^1D)$ unchanged). (2a) Difference in $jO(^1D)$ (%) relative to the reference simulation. (2b) OH difference (%) relative to the reference simulation accounting only for $jO(^1D)$ differences (e.g. with O_3 unchanged). (3a) OH differences relative to the reference simulation considering the combined kinetics and photolysis effects. (3b) Sum of 1b and 2b.*

Furthermore, $j\mathrm{O}(^1\mathrm{D})$ is positive biased, in accordance with the overestimation of TCO in the UKCA CCM with respect to observations (Chapter 4). Production of OH depends on O_3 photolysis, meaning that

variations in the TCO density, which is mostly dominated by the stratospheric contribution, can induce changes in $j\mathrm{O}(^1\mathrm{D})$ in the UV region, thus affecting the O_3 loss rate via its photolysis rate (Reaction R 2.1) and the production rate of the OH radical through $\mathrm{O}(^1\mathrm{D}) + \mathrm{H_2O}$ (Reaction R 2.2), and consequently the concentrations of trace gases in the troposphere and tropospheric O_3 (Liu and Trainer, 1988; Thompson *et al.*, 1989; Madronich and Granier, 1992; Fuglestvedt *et al.*, 1994).

Therefore, the OH increases in Figure 5.9 2b are the result of increases in $j\mathrm{O}(^1\mathrm{D})$ (Figure 5.9 2a). The relative OH response is approximately half the size of the $j\mathrm{O}(^1\mathrm{D})$ relative difference, meaning that the relative changes in $j\mathrm{O}(^1\mathrm{D})$ are larger than the relative OH responses. However, Figure 5.9 1b and 2b suggest that the magnitudes of the kinetics and the photolysis effects, for the O_3 bias found at Lauder, are comparable, and that increases in O_3 and $j\mathrm{O}(^1\mathrm{D})$ lead to increases in OH and vice versa.

The relationship between these factors [TCO, $j\mathrm{O}(^1\mathrm{D})$, and OH] is confirmed in Figure 5.10, where a similar relationship of the SCO[5], and thereby $j\mathrm{O}(^1\mathrm{D})$, with OH is observed. Figure 5.10 A indicates an exponential relationship between $j\mathrm{O}(^1\mathrm{D})$ and the SCO at 6 km of altitude (Note that this effect is also visible at other altitudes); for decreasing SCO there is an increase in $j\mathrm{O}(^1\mathrm{D})$ due to the increased UV radiation that reaches the troposphere. The small curvature may be the result of ignoring the curvature of the Earth, i.e. the SCO is calculated assuming a plane–parallel atmosphere. Another reason could be that the cross section of O_3 is wavelength dependent and the actinic flux moves towards longer wavelengths with increasing SCO.

Similarly, the relationship between the $j\mathrm{O}(^1\mathrm{D})$ calculated from the effects of the overlying SCO and the OH concentration is shown in Figure 5.10 B at 6 km of altitude, with an approximately linear relationship between them. For an increasing SCO, a decrease in the $j\mathrm{O}(^1\mathrm{D})$ is expected, and thus a

[5]Unlike the TCO, the SCO depends on the SZA.

decrease in the OH concentration (Figure 5.10 C).

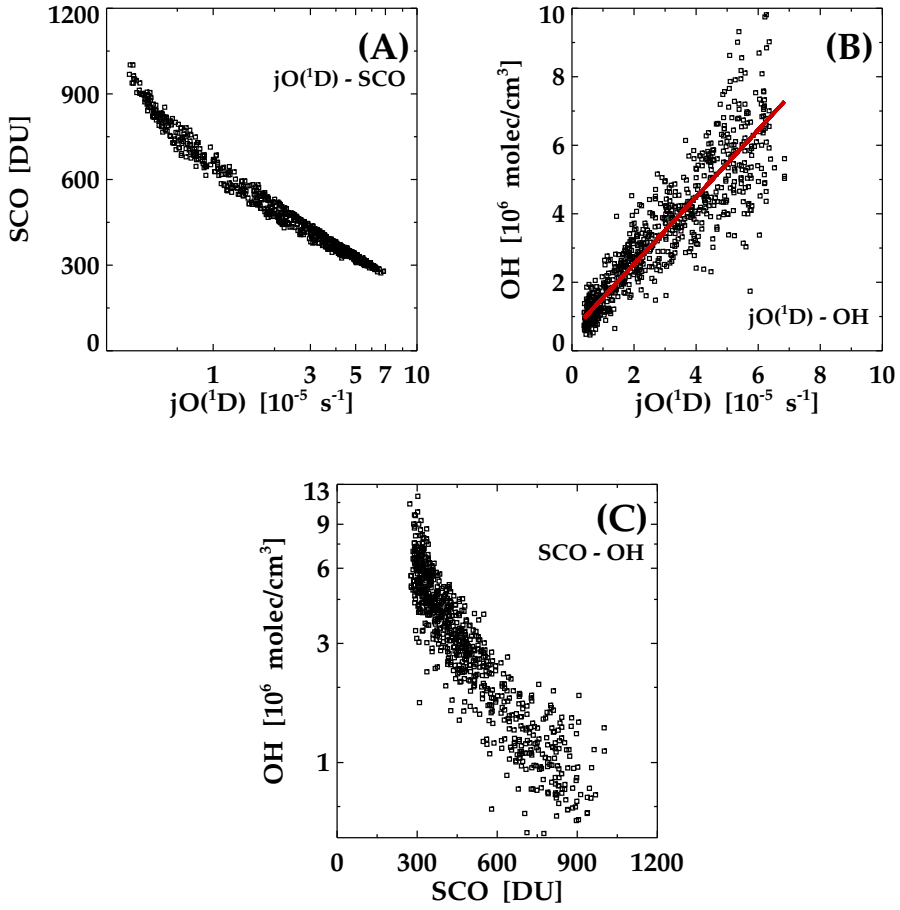

Figure 5.10: *(A) Scatter plots of the approximately exponential relationship of $jO(^1D)$ with the SCO. (B) Linear relationship of $jO(^1D)$ and the OH concentration. The red solid line denotes the linear fit between them. (C) Exponential relationship of the SCO with the OH concentration. The results shown in this figure are those obtained from the combined simulation (kinetics and photolysis effects).*

OH resulting from the combined kinetics and photolysis effects is displayed in Figure 5.9 3a, similar to Figure 5.9 3b, where the sum of both effects (1b and 2b) is displayed. Some small differences between Figure 5.9

3a from 3b are found, which are due to other factors (non–linearities) that contribute to the OH chemistry. The two model runs, considering the kinetics and the photolysis effects separately, were useful to study the impacts of changing O_3 on the OH radical. From Figure 5.9 3a and 3b, it is inferred that O_3 effects on OH can be linearly decomposed into the effects of kinetics and photolysis effects.

In an effort to determine a simple coefficient that describes the quantitative contribution of O_3 to OH, a linear regression between differences in OH and O_3 relative to the reference was conducted through the following expression[6]:

$$\frac{\Delta[\mathrm{OH}]}{[\mathrm{OH}]_{\mathrm{ref}}} = \mathrm{A_i}\frac{\Delta[\mathrm{X}]}{[\mathrm{X}]_{\mathrm{ref}}} \tag{5.3}$$

where X is the perturbation variable (in this case O_3), A_i is the slope of the linear regression, Δ[OH] is the absolute difference between the OH concentrations in the reference and perturbation simulations, Δ[X] is the absolute difference between the concentrations of the perturbation variable X and the reference variable, $[\mathrm{OH}]_{\mathrm{ref}}$ is the OH concentration obtained from the reference simulation, and $[\mathrm{X}]_{\mathrm{ref}}$ is the concentration of the reference variable. $\frac{\Delta[\mathrm{OH}]}{[\mathrm{OH}]_{\mathrm{ref}}}$ and $\frac{\Delta[\mathrm{X}]}{[\mathrm{X}]_{\mathrm{ref}}}$ denote the relative difference of the OH and X concentrations relative to the reference. The different slopes $\mathrm{A_i}$ (linear coefficients) obtained from the linear regressions are used as indicators of the OH sensitivity due to changes in each individual variable for the troposphere at Lauder. The slopes or linear coefficients are depicted in Figure 5.11 as a function of altitude from the surface up to 10 km of altitude.

For the case of O_3, the response in OH decomposed into the kinetics and photolysis effects of O_3 is shown in Figure 5.11 A. Coefficient A_1 (solid line), which denotes the response of OH to the kinetics effect of O_3, the

[6]This equation is also used to derive the linear contributions of the other key species to OH. This is described in the following sections of this chapter (Sections 5.4 to 5.7).

relative OH response is 0 – 0.25 times the relative local ozone perturbation. Likewise, OH is approximately linearly related to $jO(^1D)$ (which depends exponentially on SCO as per Figure 5.10). In this case, the response of OH is 0.5 – 0.7 times the relative change in $jO(^1D)$ (A_1" dashed line).

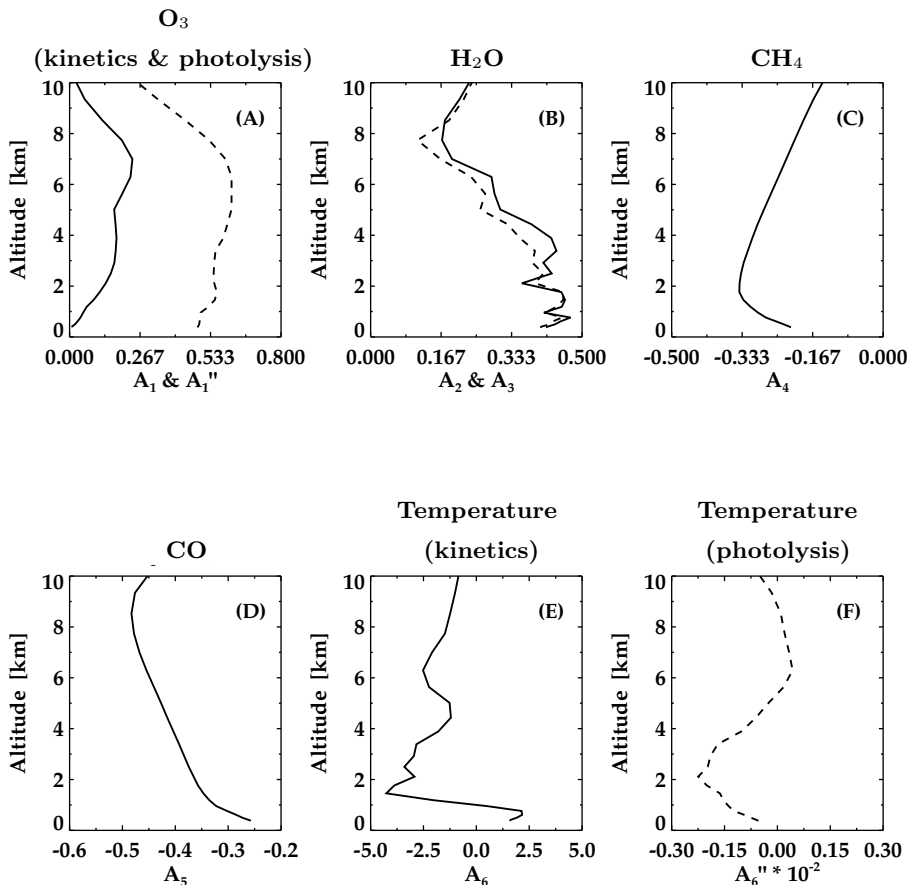

Figure 5.11: *Sensitivity coefficients 'A_i' between OH and each perturbation variable: In the calculation, multi–annual mean relative differences in OH and in the forcing are ratioed. Sensitivity of OH to changes in: (A) O_3 levels (kinetics effect) denoted by A_1 (solid line) and $jO(^1D)$ due to changes in O_3 (photolysis effect) denoted by A_1" (dashed line); (B) radiosonde – UKCA CCM H_2O (A_2 solid line) and ERAI – UKCA CCM H_2O (A_3 dashed line); (C) CH_4 (A_4); (D) CO (A_5); (E) temperature (kinetics effect) denoted by A_6; (F) $jO(^1D)$ due to changes in temperature (photolysis effect) denoted by A_6".*

5.4 Sensitivity of OH to H_2O biases

H_2O has a residence time of a few days in the atmosphere and is the main GHG of the atmosphere (Chahine, 1992). It plays a key role in tropospheric chemistry and it is involved in the formation of aerosols and clouds. It decreases rapidly with decreasing pressure, with more than 99 % of its abundance confined to the troposphere (Chapter 2 and 4). The hydrological cycle is a major factor in the H_2O budget. However, it is also formed through the oxidation of CH_4 (Reaction R 2.7), HCHO (Reaction R 3.23), some NMVOCs (Reaction R 2.8), and through the combination of OH and HO_2 (Reaction R 3.10) to a lesser extent. It is involved in OH formation through the reaction with $O(^1D)$ (Reaction R 2.2). H_2O is one of the principal ingredients for the formation of the OH radical.

To study the effects of changes in H_2O levels, two runs with the NZAC SCM were perfomed with prescribed H_2O. One run was performed using combined radiosonde and UKCA CCM H_2O. A second simulation was performed using combined ERAI and UKCA CCM H_2O (Chapter 4). Differences in OH and $jO(^1D)$ due to changes in H_2O, i.e. replacing reference H_2O with respective radiosonde and ERAI H_2O, are shown in Figure 5.8 (displayed in solid and dashed purple lines respectively). As $jO(^1D)$ is not directly affected by changes in H_2O, there is no change in $jO(^1D)$ shown here. The simulation using radiosonde combined with UKCA CCM H_2O resulted in mostly negative OH changes (up to –7 %) for most seasons except winter when H_2O levels are relatively low. The simulation using ERAI combined with UKCA CCM H_2O data leads to a systematic shift to less negative changes in OH, implying the difference in radiosonde and ERAI H_2O data. Furthermore, OH responses to H_2O biases in both runs show a similar vertical variability pattern in the vertical.

Figure 5.12 illustrates the OH response to H_2O differences with respect to the reference simulation. For both simulations, OH responses to H_2O indicate an approximately linear relationship with respect to changes in

H_2O. i.e. increases in H_2O would lead to an enhancement of OH concentrations through the reaction of $O(^1D)$ + H_2O in low NO_x regions (Reaction R 2.2), and vice versa for decreases in H_2O (Watts, 1997). The ratios of changes in OH to changes in H_2O for both simulations are similar in both magnitude and distribution (Figures 5.12 3a and 3b). This result is also reflected in Figure 5.11 B for both runs (A_2 and A_3). In general, the response of changes in OH to H_2O changes is approximately 10 to 50 %,

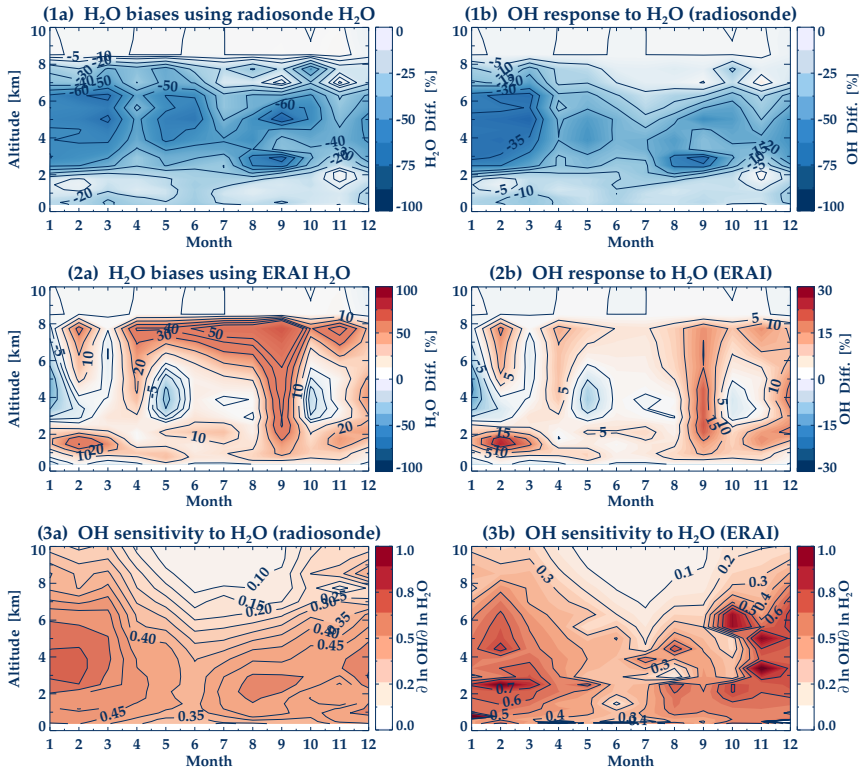

Figure 5.12: *Multi–annual and monthly–mean OH responses to H_2O between perturbation simulations and the reference simulation. (1a) Difference in radiosonde – UKCA CCM H_2O (%) relative to the reference simulation. (1b) OH difference (%) relative to the reference simulation using radiosonde – UKCA CCM H_2O. (2a) Difference in ERAI – UKCA CCM H_2O (%) relative to the reference simulation. (2b) OH difference (%) relative to the reference simulation using ERAI – UKCA CCM H_2O. (3a) Ratio of OH changes to changes in H_2O expressed as $\frac{\partial\, ln\, OH}{\partial\, ln\, H_2O}$ (1b over 1a). (3b) Ratio of OH changes to changes in H_2O expressed as $\frac{\partial\, ln\, OH}{\partial\, ln\, H_2O}$ (2b over 2a). Above 8 km UKCA CCM H_2O was used in both cases. Therefore, differences with respect to the reference simulation are close to 0.*

and the changes decrease with altitude.

5.5 Sensitivity of OH to CH_4 biases

CH_4 is the most abundant HC compound in the atmosphere and the second most important anthropogenic GHG after CO_2. It is considered a long–lived species with a lifetime of about 9 years under present–day conditions (Stevenson *et al.*, 2006). The CH_4 lifetime is often used as a global measure of OH abundance because CH_4 is removed from the atmosphere mainly through reaction with OH radicals in the troposphere (Reaction R 2.7) which is also an important sink for OH globally. At present, CH_4 is increasing in the atmosphere (see CH_4 time series in Chapter 4), meaning that increases in CH_4 emissions over time reduce the concentration of the OH radical in the atmosphere. This results in a feedback loop, whereby with less OH to react with, the lifetime of CH_4 increases as the concentration of CH_4 increases. (Prather *et al.*, 2001; Morgenstern *et al.*, 2013). The chemistry of clean environments such as Lauder is dominated by CH_4 and CO oxidations (refer also to the following section for CO) unlike other regions in the NH where chemistry is more complex due to significant anthropogenic emissions of other VOCs. This section will be focused on assessing the sensitivity of the OH radical to changes in CH_4 representative of Lauder and, to some extent, of the SH.

As a result of $\sim$ 2 % changes in CH_4 (i.e. observed – reference simulation), OH increases by up to $\sim$ 0.7 % in summer and autumn (Figure 5.8), but there are no visible changes during winter and spring. The reduction in CH_4 means that less OH is lost via CH_4 oxidation (Reaction R 2.7).

The effect of CH_4 changes on OH is displayed in Figure 5.13. CH_4 changes are small, and are vertically uniform, with some seasonal variations. Decreases in CH_4 lead to increases in OH due to reduced loss of OH by CH_4 + OH (Reaction R 2.7). The sensitivity of OH to CH_4 changes maximizes

in May / June Figure 5.13 (2), with an OH change of up to 35 % of the relative change in CH_4. By contrast, the relative change of OH maximizes in March / April, coinciding with a maximum difference in CH_4 (Figure 5.13 1a and 1b). A simplification of the ratio is performed by Figure 5.11 C, where a linear coefficient (A_4) describes the sensitivity of OH to CH_4 changes throughout the troposphere, ranging from –0.17 at the surface to –0.35 at $\sim$ 2 km of altitude, to decrease up to –0.15 at 10 km of altitude.

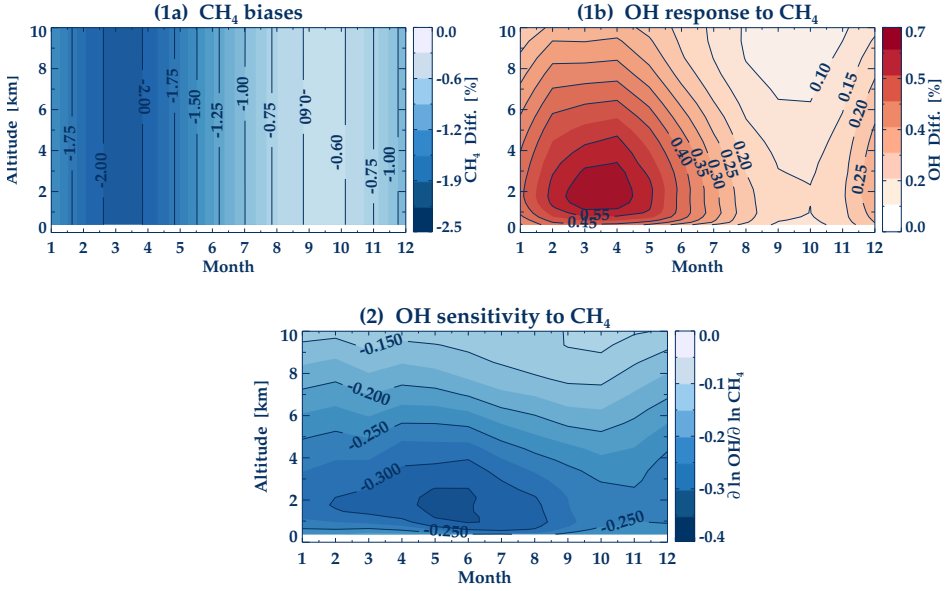

Figure 5.13: *Multi–annual and monthly–mean OH responses to CH_4 biases between observations and the reference simulation. (1a)Difference in CH_4 (%) relative to the reference simulation. (1b) OH difference (%) relative to the reference simulation. (2) Ratio of OH changes to changes in CH_4 expressed as $\frac{\partial\, ln\, OH}{\partial\, ln\, CH_4}$ (1b over 1a).*

CH_4 + OH (Reaction R 2.7) is the principal OH reaction sink along with the oxidation of CO (which will be fully described in next section). Furthermore, further oxidation of CH_4 oxidation products including CO, contribute also to the OH loss, even though some of them are also OH sources.

5.6 Sensitivity of OH to CO biases

CO is formed as a product of the oxidation of CH_4 and most NMVOCs via photolysis and oxidation of HCHO (Reactions R 3.5 and R 3.23 respectively) (Atkinson, 2000). Moreover, direct sources of CO into the atmosphere are mainly BB which maximize in spring in the SH, and on a lesser scale, biogenic processes. Therefore, anthropogenic activity is relatively unimportant in the SH (Swinnerton *et al.*, 1970; Watson *et al.*, 1990; Fishman *et al.*, 1991). Because of its long lifetime ($\sim$ 2 months), CO can be transported across large distances from the southern continents, impacting on clean–air areas such as Lauder (Edwards *et al.*, 2006; Zeng *et al.*, 2012).

In Figure 5.8, the percentage difference of OH with respect to the reference simulation for CO (yellow solid line) is less than $\pm$ 5 % for all seasons. This is confirmed by the results obtained in Figure 5.14 where the response of OH to CO biases (Figure 5.14 1b) along with changes in CO (Figure 5.14 1a) are displayed. Decreases in CO normally lead to increases in OH through the reduced loss of OH through OH + CO (Reaction R 2.6). For very low NO_x concentrations, the OH concentration varies in inverse proportion to the CO concentration (Poppe *et al.*, 1993) as is clearly seen in Figure 5.14. During the spring season, when much of the CO originates in Africa due to BB, the UKCA CCM seems to overestimate CO. This is reflected in the CO biases (Figure 5.14 1b) in spring and also in Figure 5.8.

The ratio of Figures 5.14 (1b over 1a) illustrates the sensitivity of OH to changes in CO [Figure 5.14 (2)] (the white band shown in October is the result of changes in CO forcing being close to zero), showing a dependence on altitude (also observed in Figure 5.14 1b). The sensitivity of OH due to changes in CO is always of the same negative sign (and generally of the order 0.3 – 0.5), regardless of whether CO is over– or underestimated by the UKCA CCM. Based on the ratio of the differences between OH and CO, Figure 5.11 D is suitable to establish the quantitative response of OH to CO (A_5) representative of Lauder. As per latter plots, OH shows a dependence

on CO that varies from –30 % to –50 %, in analogy to the results for CH_4 at the surface.

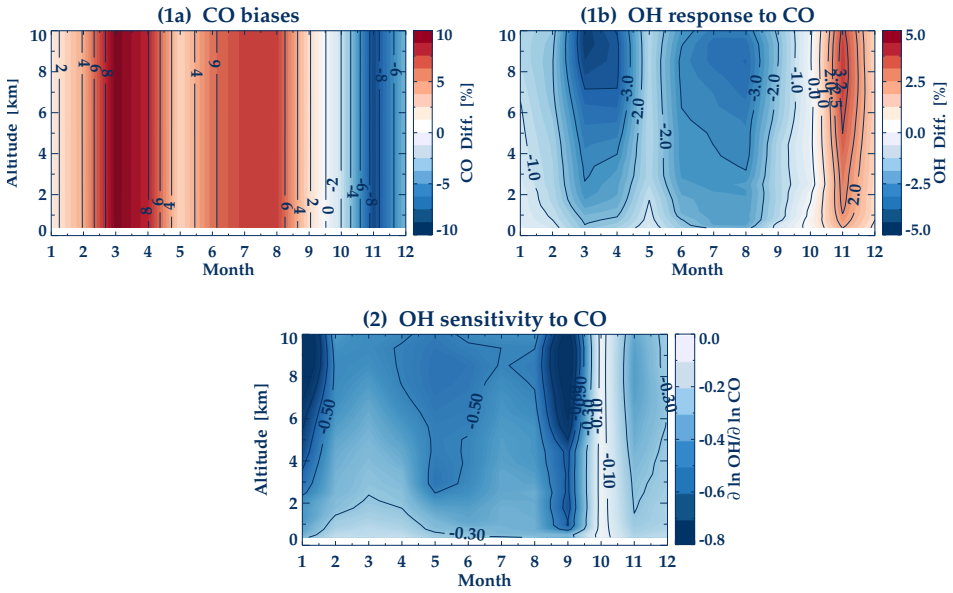

Figure 5.14: *Multi–annual and monthly–mean OH responses to CO biases between observations and the reference simulation. (1a) Difference in CO (%) relative to the reference simulation. (1b) OH difference (%) relative to the reference simulation. (2) Ratio of OH changes to changes in CO expressed as* $\frac{\partial\, ln\, OH}{\partial\, ln\, CO}$ *(1b over 1a).*

From the results obtained from CH_4 and CO, it can be established that OH is more sensitive to relative changes in CO than CH_4, if both are of the same magnitude. However, according to Naik *et al.* (2013), who also considered the effect of changes in oxidation products of CH_4 (which are not considered here), the actual OH response to CO changes may be smaller than that for CH_4, because CO lacks oxidation products that also deplete OH, unlike CH_4. This is particularly the case in the SH where other NMVOCs that also compete for OH play a lesser role (Spivakovsky *et al.*, 2000).

5.7 Sensitivity of OH to temperature biases

To study the effects of changes in temperature on OH, the same procedure as for O_3 was applied, for which the effects of temperature were decomposed into the kinetics and photolysis effects. For that, three simulations were run. In the first simulation, temperature changes were only applied to chemical kinetics, keeping all photolysis rates fixed. Note that the majority of the uni–, bi–, and termolecular reaction rates are temperature dependent. In the second simulation, only the photolysis effects were considered, which take into account changes in the photolysis rate of O_3, linked to the production rate of $O(^1D)$, which are associated to changes in temperature.

The impacts of temperature on OH via photolysis are twofold: the non–local changes in $jO(^1D)$ that are related to changes in the optical thickness of the atmosphere which depends on temperature, and the local changes of $jO(^1D)$, for which their cross–sections and quantum yields are affected by changes in temperature. Only the combined photolysis effect was evaluated in the second simulation. Finally, a third simulation was done by applying the kinetics and the photolysis effects simultaneously. The results of the three simulations are depicted in Figure 5.15.

The impact of the kinetics effects of temperature on OH is within the $\pm$ 5% range (Figure 5.15 1b) for temperature differences that range between 0°K and +5°K (Figure 5.15 1a). Likewise, the –5 % difference in $jO(^1D)$ obtained according to changes in temperature (Figure 5.15 2a) is reflected in slightly smaller OH changes (Figure 5.15 2b) that range between –3 and 3 % as for the kinetics effect. The response of OH to the kinetics and photolysis effects combined (Figure 5.15 3a) returns similar differences as for the impact of the individual effects (less than $\pm$ 5 %), as also reflected in Figure 5.8 (light green solid line). However, the sensitivity of OH to changes in temperature does not respond linearly to the combined effects as the result inferred from summing the OH responses displayed in 1b and 2b (Figure 5.15 3b). A strong non–linear response of

OH to the combined effects is clearly seen when comparing Figures 5.15 3a and 3b, where the magnitude of response in 3b is generally larger. This OH response to changes in temperature is more likely due to the non–linear dependence of most of the reaction rate coefficients on temperature.

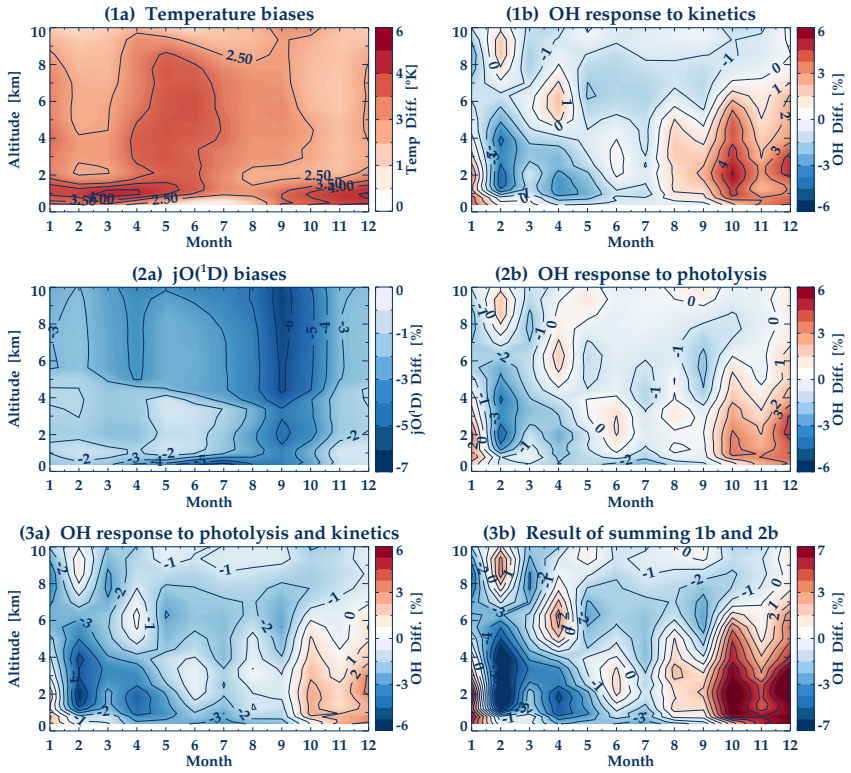

Figure 5.15: *Multi–annual and monthly–mean OH responses to temperature biases between observations (radiosonde – MOPI1 temperature) and the reference simulation. (1a) Difference in radiosonde – MOPI1 temperature in Kelvin (°K) relative to the reference temperature. (1b) OH difference (%) relative to the reference simulation accounting only for the kinetics effects of temperature differences (e.g. with $jO(^1D)$ unchanged). (2a) Difference in $jO(^1D)$ (%) relative to the reference simulation. (2b) OH difference (%) relative to the reference simulation accounting only for $jO(^1D)$ differences (i.e. with temperature unchanged). (3a) OH differences relative to the reference simulation considering the combined kinetics and photolysis effects. (3b) Sum of 1b and 2b.*

Sensitivity coefficients that define the OH response to both effects of temperature were also calculated [Figures 5.11 E (A_6) and F (A_7)], which

vary with altitude from negative to positive and vice versa, since some reactions increase with temperature whereas other decrease. From the sensitivity coefficient in Figure 5.11 E (A_6), a non–linear response of OH to the chemical kinetics of temperature can be established due to the high coefficient values, in which case the combined effect is hence perturbed. Therefore, as inferred from Figure 5.15 3a and 3b, and Figure 5.11 E (A_6), the impact of temperature biases on the OH chemistry is therefore non–linear, and is attributable, in principle, to the non–linear dependence of the reaction rate constants on temperature (kinetics effect). Therefore, the response of OH will depend on both the reference temperature (UKCA CCM temperature) and the changes in temperature applied as previously reported by Fuglestvedt *et al.* (1995).

Several sensitivity studies were conducted previously in order to elucidate the impact of temperature on OH (Stevenson *et al.*, 2000; Wild, 2007; O'Connor *et al.*, 2009). Nevertheless, none of these studies separately assessed the impacts of the kinetics and the photolysis effects of temperature on OH, but only the effects of temperature biases as a combined effect. For instance, Stevenson *et al.* (2000) noted the influence of the uncertainty in temperature (temperature increases) on CH_4 lifetime, and thereby on OH loss. Another study by Wild (2007) applied a globally uniform temperature rise of 5°K that led to a larger OH abundance and a reduction of the CH_4 lifetime of around 10 %. However, O'Connor *et al.* (2009) showed a small impact in OH abundances due to temperature changes. The disagreement of O'Connor *et al.* (2009) with Wild (2007) is likely due to the differences in temperature changes applied in both sensitivity studies. Wild (2007) applied a uniform change in temperature whereas O'Connor *et al.* (2009) applied actual climate model temperature biases, which are of different signs in different regions.

In this work, bias–correcting temperature is shown to have only a small impact on OH abundance (Figure 5.15 3a). This result broadly corroborates that of O'Connor *et al.* (2009), even though a rigorous comparison of this study to the work presented here has not been

undertaken. Moreover, applying an uniform temperature rise of 5°K to the reference temperature as in Wild (2007) (results not shown here), the results obtained do not show an enhancement of the OH abundance as stated by Wild (2007).

5.8 Sensitivity of OH to biases in all forcings combined

This section is conducted to evaluate the sensitivity of OH to all forcings combined. For that, the contribution of changing each forcing simultaneously was analysed.

Figures 5.16 A and B show the responses of OH to changing all forcings with different prescribed H_2O climatologies: (A) with radiosonde and UKCA CCM H_2O and (B) with ERAI and UKCA CCM H_2O. Of all forcings, the effect of H_2O on OH seems to be the dominating forcing (to a lesser degree O_3) in contribution to overall OH changes (due to all forcings). This is also shown in Figure 5.8 (solid and dashed dark red lines).

In general, a linear relationship can be established between OH responses to changes in major forcings that play an important role in OH chemistry, despite some non–linearities involving HO_x. As stated in the previous section, the response of OH to temperature is subjected to non–linearities but this effect is much smaller than the effects of O_3 and H_2O.

To check the linearity of OH responses to simultaneous changes in the key forcings, the combination of all individual contributions, i.e. O_3 (kinetic and photolysis effects), H_2O, CH_4, and CO to OH (Section 5.3 to 5.6), was compared to the results for OH of the NZAC SCM, using all the key forcings combined through Equation 5.4:

$$\frac{\Delta[\mathrm{OH}]}{[\mathrm{OH}]_{\mathrm{ref}}} \approx \mathrm{A}_1 \frac{\Delta[\mathrm{O_3}]}{[\mathrm{O_3}]_{\mathrm{ref}}} + \mathrm{A}_1\text{"} \frac{\Delta j\mathrm{O}(^1\mathrm{D})}{j\mathrm{O}(^1\mathrm{D})_{\mathrm{ref}}} + \mathrm{A}_2 \frac{\Delta[\mathrm{H_2O}]}{[\mathrm{H_2O}]_{\mathrm{ref}}} + \mathrm{A}_4 \frac{\Delta[\mathrm{CH_4}]}{[\mathrm{CH_4}]_{\mathrm{ref}}} + \mathrm{A}_5 \frac{\Delta[\mathrm{CO}]}{[\mathrm{CO}]_{\mathrm{ref}}} \tag{5.4}$$

where $\frac{\Delta[\mathrm{OH}]}{[\mathrm{OH}]_{\mathrm{ref}}}$ is the relative difference in the OH concentration obtained with the NZAC SCM with respect to the reference simulation, using all forcings combined. The right hand side of the equation is the summation of the contributions of the individual forcings relative to the reference. The forcings considered are those displayed in Figure 5.11, comprising the kinetics and photolysis effects of O_3 (A_1 and A_1"), H_2O (A_2 or A_3), CH_4 (A_4), and CO (A_5). Temperature was excluded here due to its small and non–linear contribution to OH chemistry as stated in the previous section.

In a forward sense, Equation 5.4 essentially captures the relationship between the single–perturbation experiments (the terms on the right–hand side) and the result of the simulation with all the key variables combined (the term on the left hand side) as displayed in Figure 5.16 C, i.e. it expresses that the OH response is linear to changes in the forcings. An orthogonal fit was applied to the comparison, since it minimizes both the vertical and horizontal distances unlike a simple linear regression. A slope of 1.22 ± 5 % at the 95 % confidence interval, and a high degree of correlation ($r = 0.87$) were obtained for the fit. The deviation from the slope 1 is attributable to non–linearities in the chemistry of the troposphere at Lauder.

In an inverse sense, Equation 5.4 expresses that the coefficients A_1 to A_5 could be determined in a multi–linear regression analysis, using only the all–forcings experiments. However, such a good correspondence was not achieved when the coefficients of each individual variable were retrieved using a multi–linear regression model. This might be attributable to insufficient linear independence between the forcing variables and some non–linearity in the system.

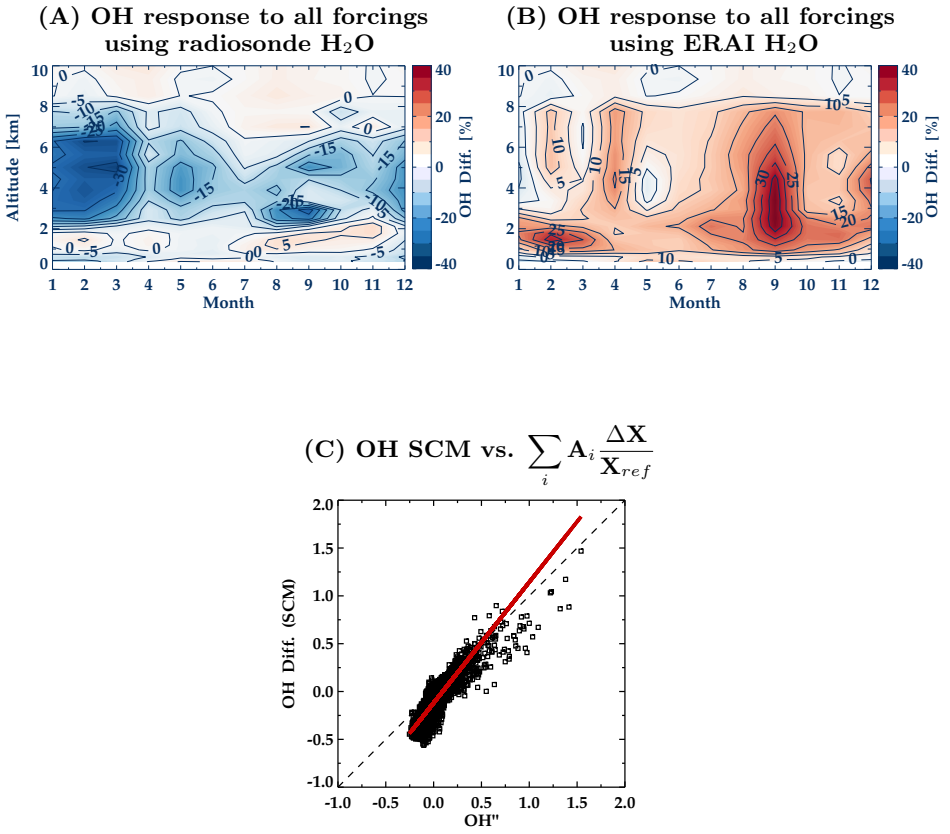

Figure 5.16: *(A) Multi–annual and monthly–mean percentage difference in OH between a simulation with bias–correction applied to all five fields and the reference simulation. Radiosonde H_2O is assumed below 8 km. (B) Multi–annual and monthly–mean percentage difference in OH between a simulation with bias–correction applied to all five fields and the reference simulation. ERAI H_2O is assumed below 8 km. (C) Scatter plot of the response of OH to the combination of all forcings (vertical axis) versus the sum of the OH response to individual forcings (horizontal axis) as expressed by the right hand side of Equation 5.4 (denoted by OH").*

Despite this, the response of OH to changing all forcings simultaneously is basically linear, and is sensitively related to changes in the forcings described in this thesis for a clean environment such as

Lauder. The same analysis considering ERAI and UKCA CCM H_2O was also conducted, and very similar results were obtained (not shown).

5.9 Comparison of modelled OH to observations

The dependence of OH to its sources was also analysed in other studies conducted in clean areas of the SH. Therefore, this section is devoted to illustrating some results, and drawing conclusions on the comparison of the modelled OH by the NZAC SCM under clear–sky conditions with some OH measurements conducted at the Cape Grim Baseline Air Pollution Station (Tasmania) and at the British Antarctic Survey's Halley Research Station (Antarctica), using the FAGE technique. The results obtained from the multiple–perturbation simulation (Section 5.8) are used for this comparison.

The study conducted at the Cape Grim Baseline Air Pollution Station (Tasmania) (Creasey *et al.*, 2003) compared the OH production (assumed to be only due to O_3 photolysis and H_2O) to observed OH over a period of four weeks during austral summer of 1999. The results exhibit a linear relationship between the OH concentration and its production, suggesting that there are no OH sources other than the O_3 photolysis (Reaction R 2.1) followed by the reaction of $O(^1D)$ with H_2O (Reaction R 3.3). This agrees well with the results obtained for Lauder (see previous sections). Furthermore, for the day in which the maximum solar noon OH concentrations occur at Cape Grim (5.5 x 10^6 molec/cm^3), similar values are obtained at Lauder using the NZAC SCM (5.74 x 10^6 molec/cm^3). For other days, up to around 10 – 15 % differences are observed (Figure 5.17).

OH concentrations were also measured in the boundary layer of coastal Antarctica (at the British Antarctic Survey's Halley Research Station) over a six–week period during the austral summer of 2005 (Bloss *et al.*, 2007). In this case, the OH concentration values differ from those of Lauder (by one order of magnitude) with a maximum solar noon level of

7.9 x 10^5 molec/cm^3 compared to the 6.6 x 10^6 molec/cm^3 maximum obtained at Lauder (time series of measurements is not available).

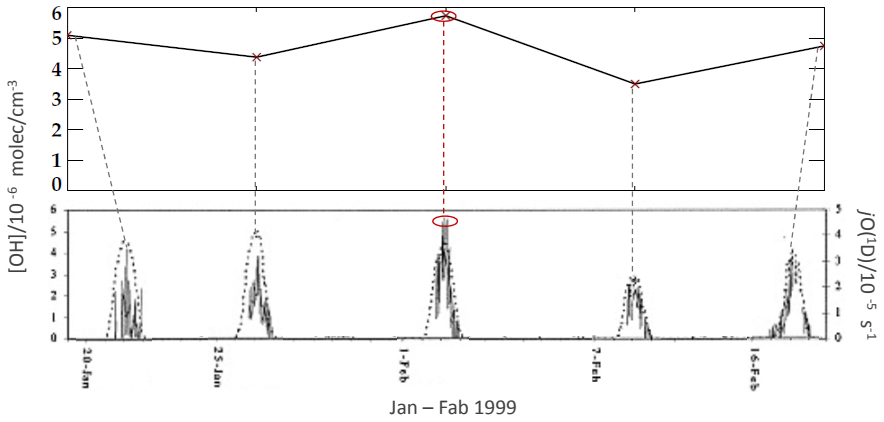

Figure 5.17: *Top: Time series of modelled solar–noon OH at Lauder. Bottom: Time series of OH (solid line) and $jO(^1D)$ (dashed line) measurements at Cape Grim station (Tasmania). The comparison between modelled and measured OH has been conducted for common days between the two data sets (according to the Lauder ozonesonde measurements).*

From the OH measurements conducted in the SH and the results obtained from the NZAC SCM, the atmospheric conditions at Gape Grim station are similar to those at Lauder for clear–sky days. This means that indeed O_3 and H_2O are the major sources of OH at both sites. Small differences found in the OH concentrations for other days are attributable, in principle, to the presence of clouds, and different variations in H_2O and O_3 concentrations between both stations (Figure 5.17). However, larger discrepancies are found between the results obtained from the NZAC SCM at Lauder and the measurements at Halley Research station. These discrepancies might be the result of differences in the atmospheric chemical conditions between both regions, for which the OH chemistry is more affected, i.e. additional molecules, such as HCHO, HONO, and higher

aldehydes, that played a larger role in the production of HO_x compared to Lauder; and other reactants, besides CH_4 and CO, that appeared to have also contributed to the OH loss at this site over that period (Bloss *et al.*, 2007). Furthermore, the larger SZA in the Antarctic austral summer compared to Lauder and the much reduced H_2O content in the Antarctic cold air might have also contributed to smaller OH abundances at Halley Research Station.

The comparisons of modelled OH at Lauder with OH measurements at other sites suggest that OH abundances are highly affected by the atmospheric conditions at the site considered (e.g. small variations in H_2O affect OH concentrations). Therefore, they are not suitable validation tools for the evaluation of the NZAC SCM performance.

5.10 Variability and trends of OH

The last section of Chapter 5 is focused on analysing the variability and trends (if any) of the OH radical at different altitudes of the troposphere. For that, the long time series of the driving forcings (1986 – 2012) was used in order to have as much information as possible regarding the variability and trends of OH at Lauder. Three time series of OH were considered for the analysis: The reference time series of OH, i.e. using UKCA CCM data, the time series of OH obtained from the combined simulation using radiosonde H_2O, and the time series of OH obtained from the combined simulation using ERAI H_2O.

The anomalies of OH for the three series at different altitudes were calculated by subtracting the annual cycle inferred from fitting expression 4.4 to the original series. Then, a one–year moving average filter was applied to the residual in order to reduce high–frequency noise. The resulting anomalies/residuals for OH are depicted in Figure 5.18. A strong interannual variability is observed in the series at all altitudes due to both dynamical [e.g. "El Niño Southern Oscillation (ENSO)"] and chemical

variabilities (e.g. BB events).

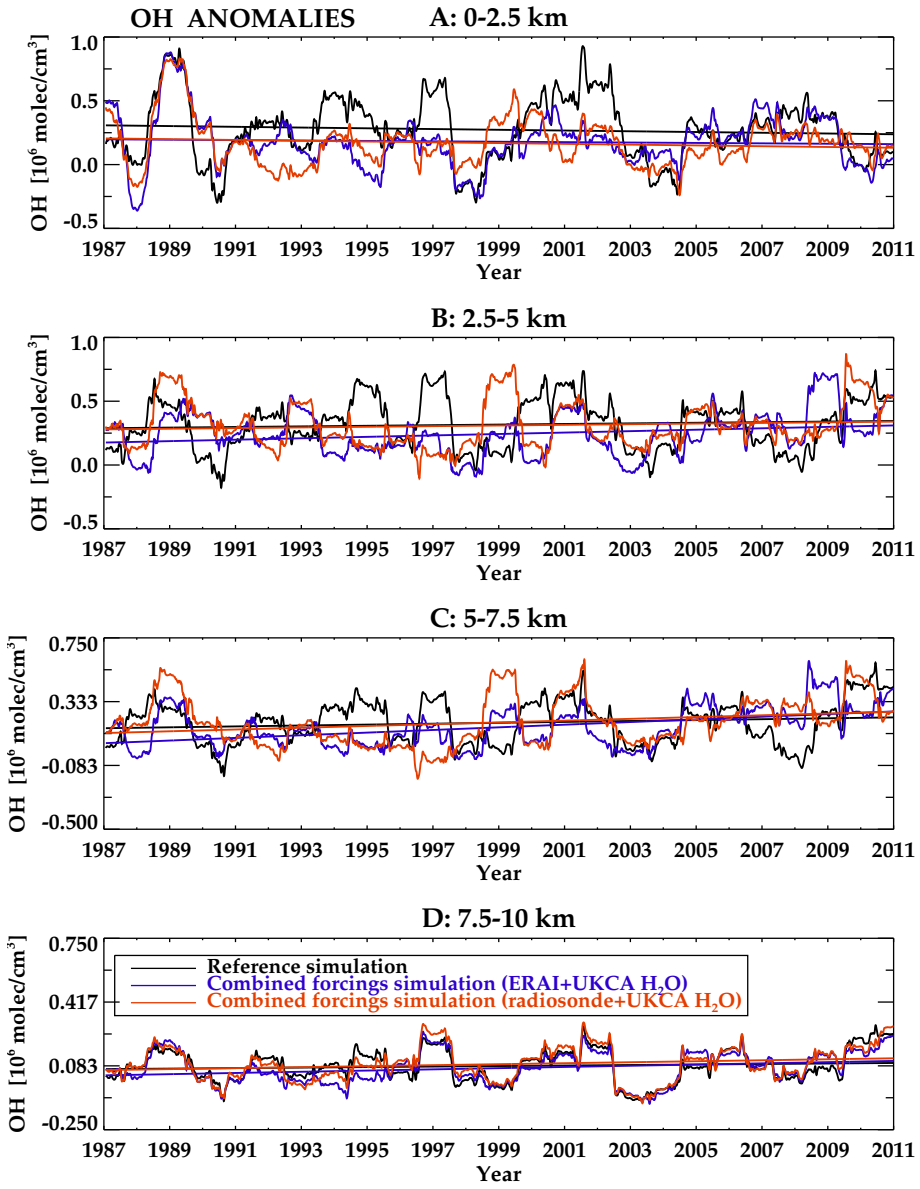

Figure 5.18: *Variability and trends of the OH anomalies at different altitudes: (A) 0 – 2.5 km, (B) 2.5 – 5 km, (C) 5 – 7.5 km, and (D) 7.5 – 10 km. The black solid line is the time series of the reference simulation, the blue solid line stands for the simulation with combined forcings considering ERAI – UKCA CCM H_2O, and the red solid line is the simulation with combined forcings considering radiosonde – UKCA CCM H_2O.*

The reference simulation shows some positive anomalies at given years that might be due to the reasons mentioned above.

Furthermore, trends have been determined at the 95 % confidence interval. To remove autocorrelation, the error calculation of the trend was based on annual–mean OH anomalies. No significant trends were obtained for the 3 simulations, except for the simulation with all forcings combined using the ERAI – UKCA CCM H_2O at 5 – 7.5 km of altitude (Figure 5.19). This simulation indicates a 5.39 ± 2.7 % positive trend at 5 – 7.5 km for OH at the 95 % confidence interval (solid line) for the whole time period, which appears to be caused by increasing ERAI – UKCA CCM H_2O as displayed by Figure 5.19 (dashed line), even though this trend in H_2O is not significant. The annual–mean anomaly of O_3 at 5 – 7.5 km was also compared to OH, but no significant O_3 trend or significant correlation with OH was found. Therefore, the O_3 anomaly is not displayed in Figure 5.19.

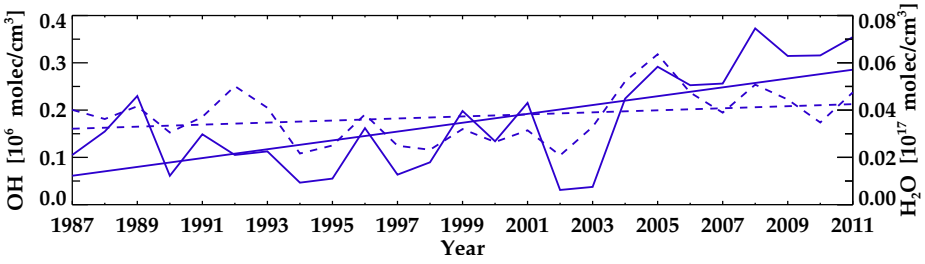

Figure 5.19: *Annual–mean anomaly and trend of OH and ERAI – UKCA CCM H_2O at 5 – 7.5 km of altitude. Solid blue lines are the OH anomaly and trend. Dashed blue lines indicate the H_2O anomaly and trend.*

A conclusion derived from the analysis of the variability and trends of OH is that a long–term trend in OH concentrations is found at Lauder, but only at 5 – 7.5 km, attributed to increasing ERAI H_2O from 2003 to 2011. However, there is evidence of interannual variations at all altitudes. This

result is consistent with that found by Manning *et al.* (2005) from other clean–air sites of the SH, namely Baring Head (New Zealand) and Scott Base (Antarctica) for the period 1989 – 2003.

Chapter 6

Effects of clouds in OH photochemistry

6.1 Introduction

Clouds (water, ice, and mixed clouds) and aerosol particles affect the radiation balance of the Earth, interacting with both shortwave and longwave radiation, and thus affect climate. Therefore, the knowledge of optical, radiative, and microphysical properties of clouds is of great importance to understand the Earth's climate. However, the properties of clouds are generally not well understood. The most important of these include the explanation for the three–dimensional shape of clouds (Evans, 1998; Schreier and Macke, 2001), their vertical and horizontal variability (Rossow, 1989; Cahalan *et al.*, 2001; Platnick, 2001), the influence of aerosols on clouds which can explain their complex contribution to cloud absorption (Stephens and Tsay, 1990), and the characterization of optical properties of ice clouds with a very complex microstructure (Liou, 1992; Yang *et al.*, 2001), the shape of which depends on pressure and temperature (Mason, 1975).

For the purpose of this thesis, the clouds' impact on photolysis is of particular interest. For instance, in overcast situations (i.e. during the presence of dense cloud layers), photolysis rates can be enhanced by as

much as twofold versus the photolysis rates in clear–sky conditions above and in the upper cloud layers (Neu *et al.*, 2007). In the lower part of the clouds and below the cloud base, photolysis rates can be reduced substantially if compared to clear–sky rates, unlike below optically thin clouds where the photolysis rates can be enhanced (Madronich, 1987; Wild *et al.*, 2000; Kylling *et al.*, 2005; Neu *et al.*, 2007).

Likewise, aerosols can influence photolysis rates through three mechanisms. The first, the so–called "direct effect" consists of scattering or absorbing incoming light (Liu *et al.*, 2012). The second mechanism is called the "indirect effect", which alters photolysis rates via clouds. This effect arises from an increase of the cloud albedo via the distribution of the same amount of liquid water content over more, and hence, smaller cloud droplets. This is produced from existing aerosol particles through the process of heterogeneous nucleation (Twomey, 1959; Albretch, 1989), whereby aerosols act as Cloud Condensation Nuclei (CCN) to produce the cloud occurrence. The third mechanism, the so–called "semi–indirect effect", also affects photolysis rates via clouds. It refers to absorption of solar radiation by aerosols leading to a heating of air, which can result in an evaporation of cloud droplets (Chýlek *et al.*, 1996; Hansen *et al.*, 1997). Cloud absorption can also be affected by interstitial aerosol particles, which contribute to the increasing cloud absorption particularly at visible wavelengths (Stephens and Tsay, 1990).

Models have been developed to assess the impact of clouds and aerosols on photolysis rates. Different methods have been employed to analyse the effects of clouds. Early methods include treating clouds as homogeneous reflecting surfaces for different altitudes (London, 1952), and applying scaling factors to the photolysis rates based on vertically averaged cloud cover and the optical depth of clouds above a given level (Chang *et al.*, 1987). More recent methods focus on cloud overlap schemes, like that of Neu *et al.* (2007), which show more realistic photolysis rate values and OH abundances. The cloud overlap scheme by Neu *et al.* (2007), used in FAST–JX, adds additional levels in the algorithm in proportion to optical

density, to solve the radiative transfer problem. Also for each column affected by clouds, a set of random distributions of clouds is generated and the radiative transfer is calculated for every member of the set. The resulting actinic fluxes are then averaged for the photolysis rate calculation. Furthermore, both direct and indirect effects of aerosols are considered in a large number of models, e.g. the global three–dimensional aerosol transport–radiaton model (SPRINTARS) by Takemura *et al.* (2005) and the UKCA CCM. In the NZAC SCM the indirect and semi–indirect effects cannot be directly represented since clouds and temperature are prescribed.

Here, an analysis of the impact of clouds on photolysis rates, and thus the OH abundance at Lauder, is presented. Three sensitivity simulations were run to assess the effects of clouds on photolysis and OH, the results of which are given in the following section. The NZAC SCM was constrained with UKCA CCM output for cloud occurrence and for the rest of the inputs required (i.e. tracers, temperature, and pressure).

6.2 Results and Discussion

This section focuses on describing and discussing the results for OH obtained in the presence of clouds. Implicit in these are the indirect and semi–indirect effects of aerosols as implemented in the UKCA CCM. The aerosol–direct effect is ignored in the version of the UKCA CCM used here, and hence also in the NZAC SCM.

The evaluation of clouds in climate models has long been based on comparisons of observed and simulated climatologies of radiative fluxes, or total and fractional cloud covers. Cloud cover fraction for total cloudiness from the Lauder all–sky camera dataset was compared to that produced by the UKCA CCM. The comparison is performed as monthly means of total cloud cover (TCC) [%] and spans the time frame from September 1999 to December 2013, the period covered by the Lauder all–sky images.

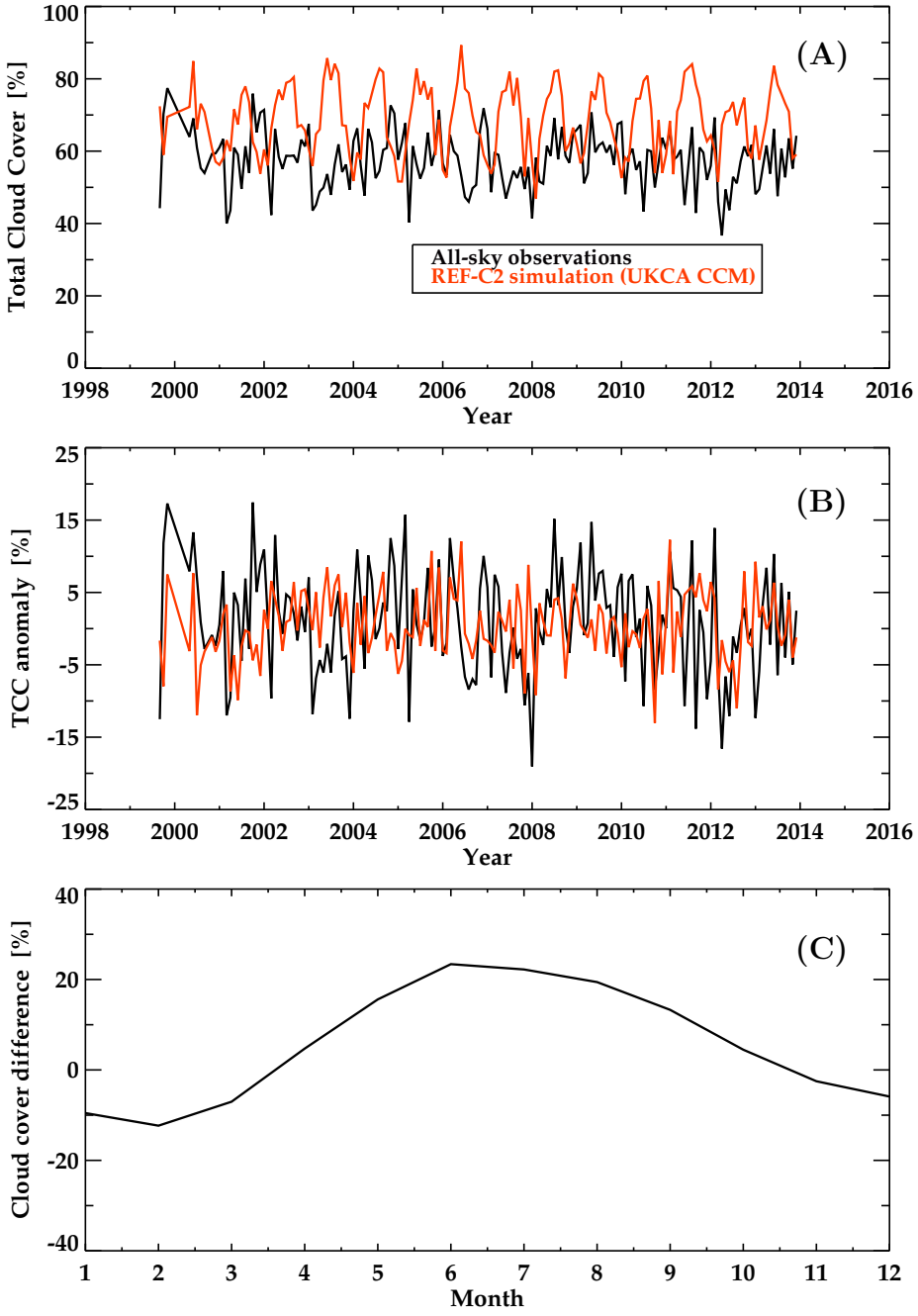

Figure 6.1: *(A) Time series of monthly mean UKCA CCM (red) and observed (black) total cloud covers [%] for the period 1999 – 2013. (B) Time series of montly mean anomalies of UKCA CCM (red) and observed (black) total cloud covers [%] for the period 1999 – 2013. (C) Multi–annual and monthly mean percentage difference in TCC of the UKCA CCM relative to Lauder observations for the period 1999 – 2013. Modelled TCC is the result of the REF–C2 simulation, i.e. it is coupled to an ocean not driven by observed SSTs. TCC from Lauder is obtained continuously from an all–sky camera.*

The annual cycle in the UKCA TCC time series is more pronounced than that of Lauder observations as displayed in Figure 6.1 A. However, the anomalies of TCC (the annual cycles were removed by fitting both time series through Equation 4.4) from both data sets show similar interannual variabilities (Figure 6.1 B). This result indicates that the UKCA CCM REF–C2 simulation must have been driven by aerosol precursor emissions following observations. Figure 6.1 C displays this comparison in terms of multi–annual and monthly mean percentage difference in TCC of the UKCA CCM relative to Lauder observations. The results of this comparison show a $\sim$ 5 – 10 % understimation of TCC by the UKCA CCM in summer, whereas in winter it is overestimated by $\sim$ 20 %.

A global underestimation of TCC by models with respect to satellite measurements has already been pointed out by Zhang *et al.* (2005) and Cesana and Chepfer (2012). However, Figure 6.1 reproduces both scenarios in different seasons, i.e. underestimation and overestimation with respect to observations in summer and winter respectively. This might be due to that models comparison to satellite data focused on zonal mean cloud cover fractions, whereas the comparison conducted here was performed for only one location, Lauder. Additionally, it must be taken into account that the modelled output by the UKCA CCM is the result of a simulation coupled to an ocean not driven by observed SSTs. This may result in differences for cloud cover.

To study the influences of clouds on OH chemistry, three simulations were conducted. OH responses to cloud effects were decomposed into the effects of liquid water and ice clouds (hereafter LWCs and ICs respectively) on OH. The NZAC SCM requires information on liquid water and ice cloud profiles, along with TCC. Given that Lauder solely provides information on TCC, and that the measurements only started in late 1999, cloud occurrence in the NZAC SCM was prescribed with liquid water and ice contents as produced by the UKCA CCM. The period considered for the analysis of the impact of clouds on OH covered the period between 1986 and 2012.

The first simulation was only driven by ICs, whereas LWCs were neglected in the calculations. A second simulation involved prescribing LWCs but without considering ICs. The third and final simulation was run considering the effects of liquid water and ice clouds combined (hereafter LICs). The rest of the parameters required by the NZAC SCM were prescribed using UKCA CCM output data in the three simulations.

Clouds play a critical role in affecting the photolysis rates. As stated in Chapter 5, $j\mathrm{NO_2}$ and $j\mathrm{O(^1D)}$ are two important photolysis rates that control much of tropospheric chemistry. To evaluate the influences of clouds on photolysis rates, the mean annual cycle of $j\mathrm{NO_2}$ and $j\mathrm{O(^1D)}$ obtained from FAST–JX of the NZAC SCM for cloudy conditions are depicted in Figure 6.2 at the surface (panels 1) and at 20 km of altitude (panels 2), along with those obtained from the UKCA CCM[1]. The mean annual cycle of clear–sky observations for $j\mathrm{NO_2}$ and $j\mathrm{O(^1D)}$ (Chapter 5) has been added in the top panels for comparison with the NZAC SCM and UKCA CCM results for $j\mathrm{NO_2}$ and $j\mathrm{O(^1D)}$ under cloudy conditions.

As displayed by Figure 6.2 in panels 1 (top), both surface $j\mathrm{NO_2}$ (1a) and $j\mathrm{O(^1D)}$ (1b) of both models respond to the presence of clouds by substantially decreasing their values by as much as 50 % in overcast conditions, compared to the clear–sky condition. By contrast, at 20 km of altitude [Figure 6.2 panels 2 (bottom)], photolysis rates are mainly affected by the cloud albedo being much larger than that of the Earth's surface, causing an increase in photolysis rates. This effect is substantially larger in $j\mathrm{NO_2}$ (2a) – which seems to be more sensitive to cloud reflection – than in $j\mathrm{O(^1D)}$ (2b), since $j\mathrm{O(^1D)}$ is more affected by $\mathrm{O_3}$ absorption (20 km is in the $\mathrm{O_3}$ layer). These results clearly show the two major impacts that clouds have on photolysis rates: the shielding effect below clouds and the

[1]The LIC simulation is shown in Figure 6.2, since the LWC and IC simulations do not provide further information on $j\mathrm{NO_2}$ and $j\mathrm{O(^1D)}$ compared to the combined simulation. The idea behind the analysis of the cloud effects on $j\mathrm{NO_2}$ and $j\mathrm{O(^1D)}$ relies on the capability of the model to reproduce the photolysis rates below and above clouds.

reflecting effect above them. Therefore, the NZAC SCM is capable of reproducing well the effects of clouds as well as the UKCA CCM. Moreover, the observed $j\mathrm{NO_2}$ and $j\mathrm{O(^1D)}$ confirm that the average and statistics of j–values performed for the two models are correct – by comparing the magnitude of differences in j–values under clear–sky and cloudy conditions.

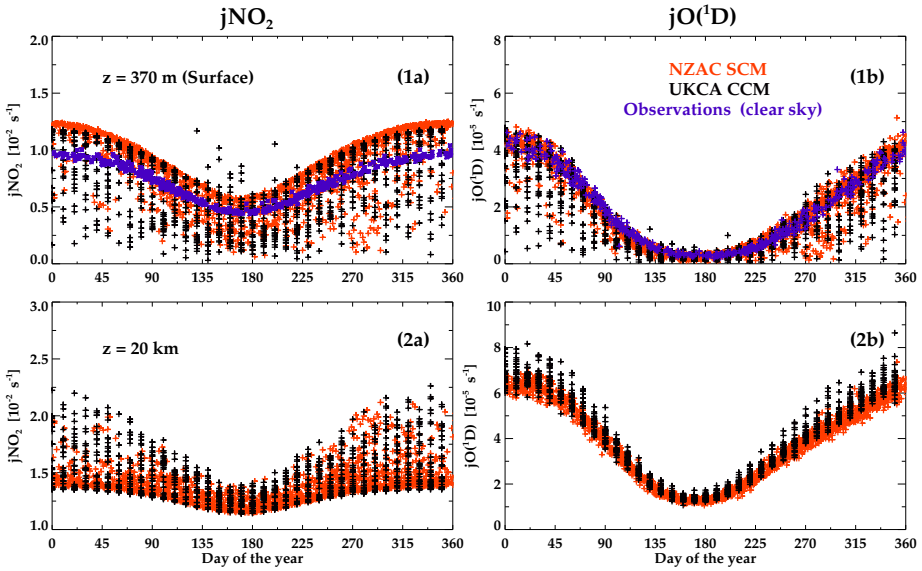

Figure 6.2: *Comparison of the clouds effects on photolysis rates between the UKCA CCM and the NZAC SCM. (1a) and (2a) $j\mathrm{NO_2}$ at the surface and at 20 km of altitude respectively. (2a) and (2b) $j\mathrm{O(^1D)}$ at the surface and at 20 km of altitude respectively. Red crosses stand for the results by the NZAC SCM whereas black crosses stand for those of the UKCA CCM. Blue crosses are the observed clear–sky $j\mathrm{NO_2}$ and $j\mathrm{O(^1D)}$ which have only been added for comparison with the NZAC SCM and UKCA CCM phototlysis rates under cloudy conditions.*

The effects of ICs, LWCs, and LICs on the vertical distribution of photolysis rates and OH are presented in the subsequent sections. Depending on cloud height and type, the enhancement or reduction of j–values can extend throughout the troposphere. This is explored for

$j\mathrm{O}(^1\mathrm{D})$, as it is closely related to OH production (Reactions R 2.1 and R 2.2).

6.2.1 Impact of ICs on $j\mathrm{O}(^1\mathrm{D})$ and OH

As discussed above, clouds have a significant impact on j–values. Certainly, this impact also influences the vertical distribution of OH throughout the troposphere. In this subsection, the responses of $j\mathrm{O}(^1\mathrm{D})$ and OH to the presence of ICs are assessed. Figure 6.3 shows these vertical responses with respect to the clear–sky situation.

Figure 6.3 (1) depicts the vertical and seasonal distribution of ice water content in the troposphere. As ICs are much less optically dense than LWCs, the ice content extends from altitudes of $\sim$ 1 – 2 km to higher altitudes in the troposphere, with most ICs located between 2 to 5 km. Seasonally, ICs peak in austral spring. The percentage differences of the estimated $j\mathrm{O}(^1\mathrm{D})$ relative to the clear–sky case are illustrated in Figure 6.3 2a, reflecting the impact of ICs on $j\mathrm{O}(^1\mathrm{D})$. Figure 6.3 2a also shows that, for an optically thin cloud, $j\mathrm{O}(^1\mathrm{D})$ is mostly enhanced in the cloud upper layers and above. Specifically, the enhancement of $j\mathrm{O}(^1\mathrm{D})$ occurs at 5 – 6 km of altitude and above in autumn and winter, and at lower layers (3 – 4 km) to higher altitudes in spring and summer. The enhancement also reaches a maximum of about 8 % in spring between 6 and 8 km of altitude, and this is consistent with the ice content maximum that occurs in below from 2 to 5 km. However, ICs seem to produce more reduction than enhancement (up to $\sim$ 10 – 15 % in winter at lower altitudes) in $j\mathrm{O}(^1\mathrm{D})$ throughout the troposphere for all seasons except for spring when the maximum of ice water content occurs. For the study shown here, ICs produce a multi–annually and vertically (from the surface up to 10 km of altitude) averaged enhancement and reduction in $j\mathrm{O}(^1\mathrm{D})$ of about 1 % and a 5 % respectively.

In Figure 6.3 2b, the impact of ICs on OH via changing $j\mathrm{O}(^1\mathrm{D})$ is

approximately linear to its influence on $j\mathrm{O}(^1\mathrm{D})$ (Figure 6.3 2a). That is, when ICs are included, the vertical distribution of OH throughout the troposphere is similar to that of $j\mathrm{O}(^1\mathrm{D})$. The maximum reduction in OH is $\sim 10 - 15$ % in winter at lower altitudes in accordance with the maximum reduction in $j\mathrm{O}(^1\mathrm{D})$, relative to the clear–sky condition. Conversely, a maximum enhancement of ~ 8 % occurs in spring between 6 and 8 km of altitude, when the ice water content maximizes (2 – 5 km of altitude). In general, changes in $j\mathrm{O}(^1\mathrm{D})$ and OH concentration have strong seasonal variations, with the maximum reduction occurring in winter close to the surface, and the maximum increase in spring above clouds.

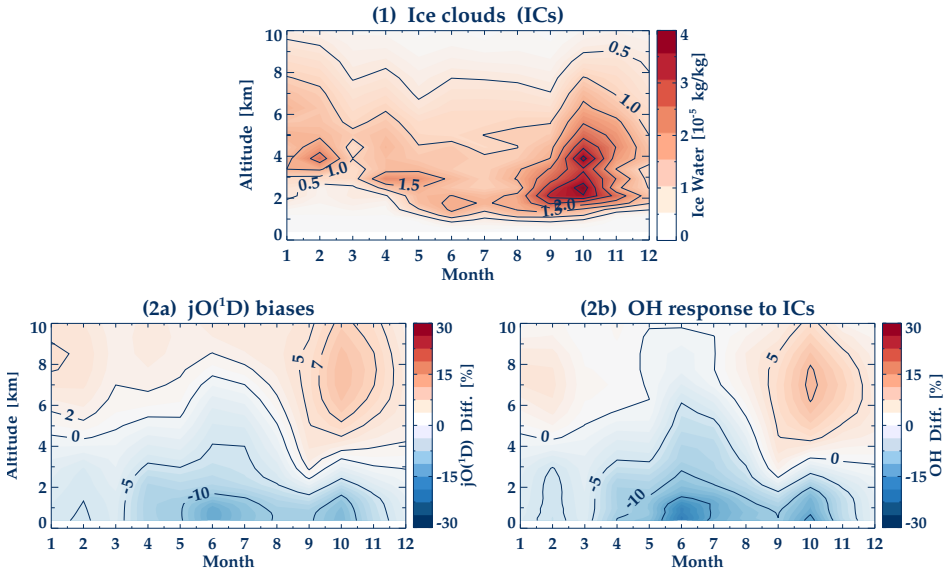

Figure 6.3: *(1) Multi–annual and monthly mean ice content (kg/kg). (2a) Multi–annual and monthly mean response of $j\mathrm{O}(^1\mathrm{D})$ (%) to the presence of ICs relative to the cloud–free reference simulation. (2b) Multi–annual and monthly mean response of OH (%) to the presence of ICs relative to the cloud–free reference simulation.*

This section has reflected the impact of ICs on photolysis rates and OH. Seasonal changes in $j\mathrm{O}(^1\mathrm{D})$ and OH with respect to the clear–sky condition have been analysed for Lauder. It has been shown that ICs

mostly reduce $j\mathrm{O}(^1\mathrm{D})$ below them in the lower troposphere, and to a lesser degree in the middle troposphere. Conversely, it is enhanced in the upper layers and above. Similarly, OH responds to the presence of ICs by reducing (enhancing) its concentrations below (above) them. Figures 6.3 2a and 2b indicate that changes in OH respond approximately linearly to changes in $j\mathrm{O}(^1\mathrm{D})$, i.e. a decrease in $j\mathrm{O}(^1\mathrm{D})$ produces a decrease in the OH abundance and vice versa.

6.2.2 Impact of LWCs on $j\mathrm{O}(^1\mathrm{D})$ and OH

In this subsection, the sensitivity of the impact of LWCs on photolysis and OH is examined. For that, the NZAC SCM was only forced with clouds in the form of liquid water content. ICs were neglected in this calculation. As above, this section is only focused on assessing the changes in OH produced by changes in $j\mathrm{O}(^1\mathrm{D})$ due to the presence of LWCs, since $j\mathrm{O}(^1\mathrm{D})$ (unlike $j\mathrm{NO_2}$) is the most critical parameter for determining OH concentrations at Lauder.

Figure 6.4 (1) displays the vertical and seasonal distribution of liquid water content in the troposphere. LWCs extend from altitudes of $\sim$ 1 to $\sim$ 4 km in the troposphere. They are as much as twice the optical density of ICs. Spring also marks the peak season for liquid water content. Figure 6.4 2a shows that for low optically denser clouds (LWCs) – compared to ICs – $j\mathrm{O}(^1\mathrm{D})$ is enhanced above and throughout much of the cloud and troposphere up to 10 km of altitude. The enhancement in $j\mathrm{O}(^1\mathrm{D})$ is up to 12 % between 2 and 4 km of altitude, coinciding with the spring maximum in liquid water content (1 – 2 km of altitude). Conversely, the reduction in $j\mathrm{O}(^1\mathrm{D})$ with respect to the clear–sky condition is $\sim$ 10 % and is also produced below clouds.

As clearly observed, lower clouds generally produce an enhancement in $j\mathrm{O}(^1\mathrm{D})$ (Figure 6.4 2a), but higher clouds generally produce a reduction in $j\mathrm{O}(^1\mathrm{D})$ in the troposphere (Figure 6.3 2a) (Tang *et al.*, 2003; Tie *et al.*,

2003; Liu *et al.*, 2009). Furthermore, the multi–annually and vertically (from the surface up to 10 km of altitude) averaged enhancement and reduction in $j\mathrm{O}(^1\mathrm{D})$ are about 2 % and 6 % respectively, similar to the response of $j\mathrm{O}(^1\mathrm{D})$ for the ICs condition. This suggests that the cloud vertical distribution has a bigger effect on photolysis, rather than the change in cloud water content. This is in agreement with Tie *et al.* (2003), Liu *et al.* (2006), and Liu *et al.* (2009).

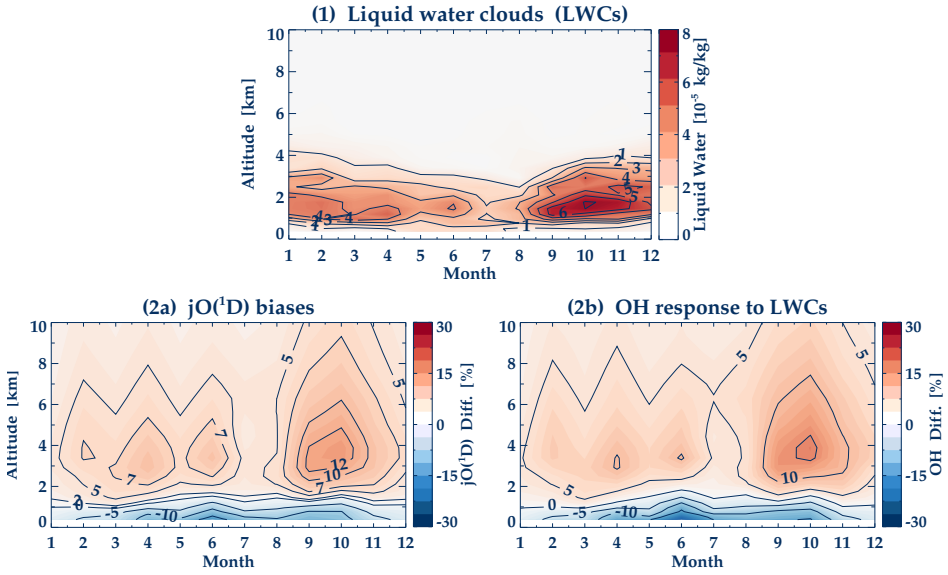

Figure 6.4: *(1) Multi–annual and monthly mean liquid water content (kg/kg). (2a) Multi–annual and monthly mean response of $j\mathrm{O}(^1\mathrm{D})$ (%) to the presence of LWCs relative to the cloud–free reference simulation. (2b) Multi–annual and monthly mean response of OH (%) to the presence of LWCs relative to the cloud–free reference simulation.*

Similarly, Figure 6.4 2b shows that OH responds approximately linearly to changes in $j\mathrm{O}(^1\mathrm{D})$ (Figure 6.4 2a). As for the case of ICs (Subsection 6.2.1), the vertical distribution of OH throughout the troposphere is similar to $j\mathrm{O}(^1\mathrm{D})$. The OH concentration is enhanced by up to 12 % in spring between 2 and 4 km of altitude, similar to the maximum change in

$j\mathrm{O}(^1\mathrm{D})$ and the maximum liquid water content (1 – 2 km of altitude). The maximum reduction in OH is $\sim$ 10 %, in agreement with the maximum relative reduction in $j\mathrm{O}(^1\mathrm{D})$, relative to the clear–sky condition.

This section has focused on assessing the impact of LWCs on photolysis rates and OH. Unlike ICs, clouds in the form of liquid water content mostly enhance $j\mathrm{O}(^1\mathrm{D})$ and OH above them throughout most parts of the troposphere. Conversely, the reduction in $j\mathrm{O}(^1\mathrm{D})$ and OH only occurs in the lowest altitudes of the troposphere (surface – 1 km of altitude). Figures 6.4 2a and 2b indicate that OH responds approximately linearly to changes in $j\mathrm{O}(^1\mathrm{D})$, i.e. a decrease in $j\mathrm{O}(^1\mathrm{D})$ produces a decrease in the OH abundance and vice versa.

6.2.3 Impact of LICs on $j\mathrm{O}(^1\mathrm{D})$ and OH

The combined effects of ICs and LWCs (LICs) on photolysis and OH are explored in this subsection. For this, ice and liquid water contents were prescribed in the NZAC SCM as produced by the UKCA CCM. As for the previous cases, this subsection is devoted to studying the changes in OH produced by changes in $j\mathrm{O}(^1\mathrm{D})$ due to the presence of clouds, in the form of ice and liquid water contents.

The response of $j\mathrm{O}(^1\mathrm{D})$ to differences between cloudy and cloudless conditions is displayed in Figure 6.5 1a. A $\sim$ 0 – 20 % decrease in $j\mathrm{O}(^1\mathrm{D})$ below $\sim$ 2 km of altitude is consistent with the presence of clouds in the forms of ice and liquid water [Figures 6.3 (1) and 6.4 (1)]. As stated in the previous subsections, the optical density of LWCs is twice that of ICs. Therefore, $j\mathrm{O}(^1\mathrm{D})$ is decreased below the transition of ice to liquid clouds at about 2 km of altitude, and increased above this height. Above 2 km of altitude, $j\mathrm{O}(^1\mathrm{D})$ is significantly enhanced with a maximum of 18 % increase in spring, which coincides with the maximum liquid water and ice contents. The response of $j\mathrm{O}(^1\mathrm{D})$ to differences between cloudy and clear–sky conditions responds approximately linearly to the presence of ICs

and LWCs (Figure 6.5 1b), as the result inferred from summing the $jO(^1D)$ responses displayed in Figures 6.3 2a and 6.4 2a.

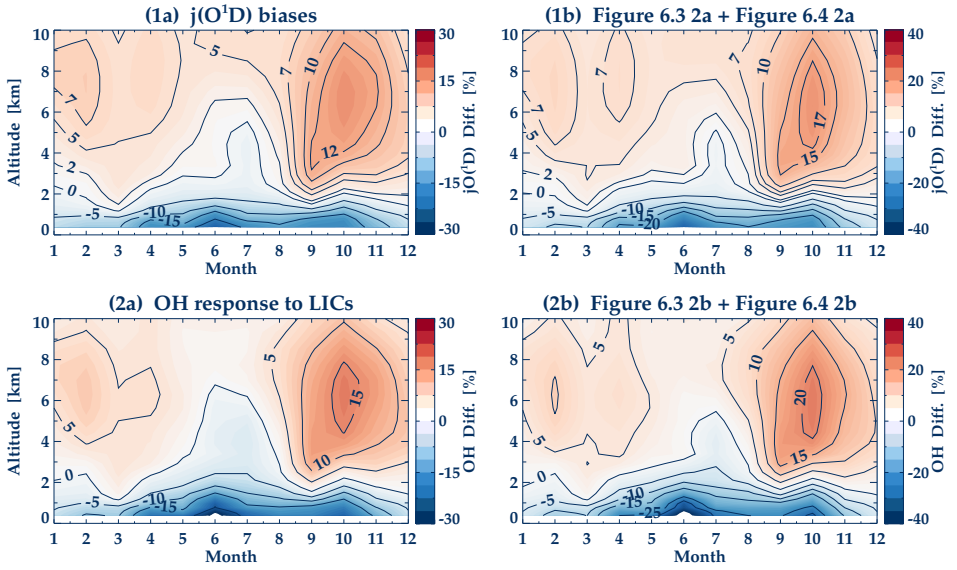

Figure 6.5: *(1a) Multi–annual and monthly mean response of $jO(^1D)$ (%) to the presence of LICs relative to the cloud–free reference simulation. (1b) Sum of Figure 6.3 2a + Figure 6.4 2a. (2a) Multi–annual and monthly mean response of OH (%) to the presence of LICs relative to the cloud–free reference simulation. (2b) Sum of Figure 6.3 2b + Figure 6.4 2b.*

The OH response to the presence of LICs (Figure 6.5 2a) is consistent with the response of $jO(^1D)$ (Figure 6.5 1a and 1b). OH responses are directly proportional to the magnitude of the $jO(^1D)$ differences. Like $jO(^1D)$, OH appears to be more sensitive in the spring and winter seasons. A maximum enhancement of $\sim$ 18 % is clearly seen in spring between 4 and 6 km of altitude, whereas a maximum reduction of $\sim$ 20 % is produced in winter close to the surface. The sensitivity of OH to differences between cloudy and clear–sky conditions responds approximately linearly to the combined effects (ICs and LWCs) (Figure 6.5 2b), as the result inferred

from summing the OH responses displayed in Figures 6.3 2b and 6.4 2b. The small discrepancy observed between Figure 6.5 2a and 2b is more likely due to non–linearities involving OH chemistry, rather than the photolysis effect. The two model runs, considering the effects of ICs and LWCs separately, were useful to study the impact of clouds on OH. From Figure 6.5 2a and 2b, it is inferred that the impact of clouds on OH can be linearly decomposed into the effects of IC and LWC effects.

6.3 Conclusions

This chapter has focused on assessing how photolysis rates [specifically for $j\mathrm{O}(^1\mathrm{D})$] and thus OH, respond in the NZAC SCM when the effects of clouds are included. The NZAC SCM was driven by UKCA CCM output data for clouds and other required inputs. The results presented in this chapter indicate that the NZAC SCM is capable of reproducing the response in photolysis rates and OH due to the presence of clouds in the UKCA CCM. Because of insufficient cloud observations at Lauder (except as for TCC), the aim of the work presented here was not to validate the model for cloud effects but to quantify how clouds, in the model framework, affect photolysis rates and OH with respect to the cloud–free condition.

Three different sensitivity simulations were performed: The first simulation entailed running the NZAC SCM only with ICs. A second simulation was performed by running the NZAC SCM with LWCs. Finally, a third sensitivity simulation was to assess the combined effect of both ICs and LWCs (LICs). In the three simulations, photolysis rates are mainly decreased below clouds and increased above due to reflection off the cloud top (Lefer *et al.*, 2003), as clearly seen in Figures 6.3, 6.4, and 6.5 for $j\mathrm{O}(^1\mathrm{D})$.

The results of the simulation considering only the effects of ICs indicate that photolysis rates are mostly reduced below clouds in the lower

troposphere (up to 10 – 15 %), and to a lesser degree in the middle troposphere. The enhancement in photolysis rates is produced in the cloud upper layers and above reaching a maximum of 8 % in spring. This is consistent with the maximum of ice content. The second simulation, considering the effects of LWCs, produces an inverse response of photolysis rates with respect of ICs. In this case, photolysis rates are mostly enhanced throughout much of the cloud and troposphere. The enhancement is by as much as 12 % and coincides with the maximum of liquid water content that occurs in spring. The reduction in photolysis rates is $\sim$ 10 % and is predominantly produced below clouds. The third simulation was driven by the combined effect of ICs and LWCs (LICs). Since LWCs are twice as optically dense as ICs, the reduction in photolysis rates (0 – 20 %) is produced below the transition of ICs to LWCs at around $\sim$ 2 km of altitude, and the enhancement is produced above that altitude reaching a maximum of $\sim$ 18 % in spring.

Consistent with other studies (Tie *et al.*, 2003; Feng *et al.*, 2004; Liu *et al.*, 2006), the NZAC SCM calculations indicate that clouds have important effects on the chemistry of the OH radical through the modification of photolysis rates. Specifically for each simulation, the calculated OH shows changes (reduction and enhancement) that vary between $\sim$ 0 – 10 % for the case in which only ICs are present, and are proportional to $j\mathrm{O}(^1\mathrm{D})$ changes. Likewise, for the case in which only LWCs are present, OH responds accordingly to $j\mathrm{O}(^1\mathrm{D})$, with changes that vary between 0 – 12 %. When both ICs and LWCs are present (LICs), OH responds proportionally to changes in $j\mathrm{O}(^1\mathrm{D})$. OH is mostly reduced below the transition between ICs and LWCs and enhanced above by as much as 20 % in both cases. Moreover, the sensitivity of OH to differences between cloudy and cloudless conditions responds approximately linearly to the combined effects of liquid water and ice contents.

In this chapter, the impacts of clouds on photolysis rates and OH have been assessed. However, due to insufficient information on cloud observations at Lauder, the NZAC SCM was constrained with UKCA

CCM output data for liquid water and ice contents, and the results compared with cloudless conditions. The results of this analysis show that the NZAC SCM provides a plausible OH response to the presence of clouds corresponding to proportional changes in $j\mathrm{O}(^1\mathrm{D})$, in agreement with previous studies [e.g. Tang *et al.* (2003)]. Moreover, the vertical distribution of clouds has more influence on photolysis and OH, rather than the change in cloud water content. This is consistent with e.g. Tie *et al.* (2003), Liu *et al.* (2006), and Liu *et al.* (2009).

Chapter 7

Summary, conclusions, and outlook

The work presented in this thesis aimed at studying the sensitivity of the OH abundance to CCM biases (of the UKCA CCM) in different variables under clear–sky and alternatively under cloudy conditions. Due to the high reactivity of OH and its high response to model–dependent factors such as cloudiness and humidity, OH is highly variable and difficult to measure. Some *in–situ* measurements of OH do exist (albeit not at Lauder) but they are too sparse (and maybe not representative enough) to be used in a straight forward model validation. Therefore, it remains a challenge to constrain OH correctly in chemistry–chemistry models. To address the problem of modelling OH, a single–column model (NZAC SCM) for Lauder was constructed in which only the fast photochemical processes of the overhead column were incorporated, hence neglecting transport and other physical mechanisms typically found in CCMs. The sensitivity studies conducted in this thesis take into account known variables which play a key role in the OH photochemistry representative of Lauder background conditions. These variables are O_3, H_2O, CH_4, CO, and temperature.

The NZAC SCM adopted here is a simplification of the UKCA CCM, in which only the interactive FAST–JX photolysis scheme and the chemical mechanism incorporated in the UKCA CCM are considered. In

the construction process, profile time series of all the input data were constructed as required by the NZAC SCM. The key variables (O_3, H_2O, CH_4, CO, and temperature) were prescribed using long–term measurements from Lauder and other available data. UKCA CCM output data were used for the remainder of the forcings required by the NZAC SCM. A SSM was developed to provide a plausibility test for the NZAC SCM. Therefore, the performance of the NZAC SCM was assessed by comparing the results of the NZAC SCM with those of the SSM for OH in the troposphere. The steady–state approximation considered the principal reactions involved in the OH photochemistry of clean–air sites such as Lauder. The NZAC SCM compares reasonably well with the SSM, suggesting both that the steady–state assumption adequately describes OH chemistry at Lauder, albeit within limits, and that there are no remaining technical issues in the NZAC SCM. This builds confidence in the NZAC SCM. Some differences between the NZAC SCM and the SSM were not completely reconciled, but they suggest that the inclusion of more reactions in the SSM, i.e. reactions involving NMVOCs, should improve the agreement.

For the sensitivity analyses, variant simulations were produced under clear–sky conditions in which the key variables, individually and combined, were replaced or constrained with observations. A reference simulation was performed, with all forcings taken from the UKCA CCM. The simulations indicate that OH responds approximately linearly to correcting biases in the key variables with respect to the reference, except for temperature. The analysis of the OH response to correcting O_3 biases indicates that the responses of OH were approximately proportional to seasonal changes in O_3 and $j\mathrm{O}(^1\mathrm{D})$ respectively. Thus, changes in the TCO, hence $j\mathrm{O}(^1\mathrm{D})$, translate into OH relative responses that range between 20 % and 50 % of the relative change in $j\mathrm{O}(^1\mathrm{D})$ for the troposphere. Changes in local O_3 through kinetics effects only range from about a null response (at the surface) to around 25 % of the relative change in O_3. For the specific O_3 bias correction applied here, characterizing the Lauder measurements and the UKCA CCM, both effects on OH are generally of similar magnitude.

As for the case of changes in O_3, OH responds approximately linearly to relative changes in H_2O, varying from 50 % of the applied relative H_2O changes at the surface to 5 – 10 % at 10 km of altitude.

Conversely, the loss of OH is dominated by the reactions of OH with CH_4 and CO in clean environments such as Lauder. The impact of CH_4 biases on OH is small since surface CH_4 in the UKCA CCM (and consequently the NZAC SCM reference simulation) is constrained to follow globally averaged observations, unlike O_3 and H_2O. The OH sensitivity to changes in CH_4 is inversely related to changes in CH_4. That is to say, for an enhancement of the CH_4 abundance, the OH amount decreases proportionally by between $\sim$ –17 % of the applied relative CH_4 change (at the surface) to $\sim$ –35 %. Similarly, the sensitivity of OH concentration to changes in CO is always negative (i.e. an increase in CO produces a decrease in OH, and vice versa) (Poppe *et al.*, 1993). The proportional response of OH to changes in CO abundance varies from 30 % (at the surface) to 50 % of the relative change of CO. For the bias correction applied here for CO, the resulting change in OH at Lauder is relatively small compared to bias–correcting O_3 or H_2O. It should be noted that in the analysis of the OH sensitivity to CH_4, the impacts of subsequent changes in CH_4 oxidation products which also affect OH were not addressed. Therefore, a smaller proportionality coefficient for CH_4 than that for CO was obtained. In that sense, the actual OH response to CO may be smaller than that for CH_4 (Naik *et al.*, 2013), hence making OH more sensitive to relative changes in CH_4 than those of CO. This may be different from the NH situation (Spivakovsky *et al.*, 2000).

Changes in climate parameters such as temperature give rise to a complex set of responses in tropospheric chemistry. The assessment of the effects of temperature in OH indicates non–linear seasonal responses to temperature biases. This result is mainly due to the non–linear impact of changing temperature (kinetics effect) on OH rather than photolysis, since most of the reactions rates are temperature dependent (Fuglestvedt *et al.*, 1995). Nevertheless, the impact of temperature changes on OH is very

small, as already reported by O'Connor *et al.* (2009), and corroborated in this thesis.

The results of the simulation considering simultaneous changes in the key forcings indicate that OH responds approximately linearly to all the major forcings that contribute to the oxidising capacity of the atmosphere, except for temperature, of which effects on OH still remain poorly understood. The contribution of each parameter to the OH photochemistry proved difficult to assess by means of a multi–linear regression model due to the insufficient linear independence between the forcing variables and some non–linearity in the system. However, the OH abundance obtained by the simulation run with all forcings combined was compared with the summation of the effects of the individual forcings on OH, resulting in good correspondence of both approaches (with a linear regression slope of 1.2 ± 5 % at the 95 % confidence interval between both OH data sets). The deviation from the slope 1 indicates non–linearities in the chemistry of the troposphere at Lauder.

This study also includes an analysis of the variability and trends of the OH concentration anomalies at different altitudes in the troposphere for the period between 1986 and 2012. A large variability is found, partially reflecting variability of H_2O. Perhaps due to this strong variability of OH, there are no significant trends in the series, except in the simulation with all forcings combined constrained with ERAI – UKCA CCM H_2O at 5 – 7.5 km of altitude. The calculated trend shows a 5.4 ± 2.7 % positive trend at the 95 % confidence interval for the whole time series (1987 – 2011). The trend is mainly caused by increasing H_2O amounts in ERAI between 2003 and 2011. This could be an artefact since ERAI assimilates satellite data which can be subject to discontinuities. In the corresponding simulation constrained with balloon–borne measurements of H_2O, no such significant trend was found. Overall, in almost all cases, OH at Lauder presents no significant trends but it is subject to substantial interannual variations. This is consistent with Manning *et al.* (2005) who assessed OH at other clean–air sites of the SH for the period comprised between 1989

and 2003.

Based on the results of the sensitivity analyses for the cloud–free case, O_3, H_2O, CH_4, and CO are driving the oxidising capacity of the atmosphere in unpolluted regions such as Lauder, where O_3 and H_2O appear to be the dominant factors controlling OH. This suggests that for Lauder, the UKCA CCM biases can be mostly corrected according to the contributions of H_2O and O_3 to OH chemistry. Moreover, at Lauder the UKCA CCM is too moist (by $\sim$ 0 – 50 %); this translates into an overestimation of OH of up to 40 % in the reference simulation. This is in agreement with the likely underestimated global lifetime of CH_4 by the UKCA CCM (Morgenstern *et al.*, 2013; Telford *et al.*, 2013), assuming that the UKCA CCM is also generally too moist in other regions.

In addition, a sensitivity study was performed taking into account the effect of clouds on photolysis and OH. Variant simulations were produced in which different types of clouds were considered in the NZAC SCM simulations. Because of the lack of suitable observations offering cloud profile information, cloud fields were taken from the UKCA CCM. Results indicate that the NZAC SCM produces plausible changes in photolysis rates and OH due to the presence of clouds, decreasing their values below clouds and increasing them above these due to reflection. Three simulations were performed, in which liquid water clouds (LWCs) and ice clouds (ICs) were considered, individually and combined (LICs). The results of the three simulations, together with the cloud–free reference simulation, show that the NZAC SCM provides plausible OH responses to the presence of clouds that are directly proportional to changes in $j\mathrm{O}(^1\mathrm{D})$. In particular, the effects of ICs produce a marked reduction (of up to 10 – 15 %) in $j\mathrm{O}(^1\mathrm{D})$ and OH below clouds in the lower troposphere, and in a lesser degree in the middle troposphere. Conversely, in the presence of LWCs, $j\mathrm{O}(^1\mathrm{D})$ and OH are mostly enhanced throughout much of the cloud and troposphere by as much as 12 %. The simulation with the combined effect of ICs and LWCs produce a reduction in $j\mathrm{O}(^1\mathrm{D})$ and OH (0 – 20 %) below the transition of ICs to LWCs at around 2 km, since LWCs are as

much as twice as optically dense as ICs. An enhancement is produced above this altitude of up to 18 %.

The magnitudes of changes in $jO(^1D)$ and OH are similar when either ICs or LWCs are considered in the NZAC SCM. Their effects add up approximately linearly when both are present in the simulations. However, the impacts of ICs and LWCs differ in their vertical profile on photolysis and OH, because ICs and LWCs are located at different altitudes in the troposphere. For ICs, reductions in photolysis and OH dominate, whereas enhancements in both fields predominate in the case of LWCs. This means that photolysis rates and OH are more sensitive to the vertical distribution of clouds than to the change in cloud optical density. Although the NZAC SCM produces plausible responses of OH to the presence of clouds, the study presented here does not provide a complete validation of the results (only for TCC) due to a lack of suitable observations needed for validation of the cloud fields. This means that the effect of biases in the cloud fields on photolysis and OH at Lauder can not be addressed here.

The results obtained in this thesis regarding the contributions of the key variables to OH chemistry at Lauder are the starting point to this study. Using the NZAC SCM, the study of such contributions can be extended to other clean–air areas of the SH. However, this study is not directly applicable to regions of the NH where tropospheric chemistry is additionally driven by anthropogenic emissions of other species that take part in the chemistry of tropospheric O_3 and hence, OH. In this situation, the applicability of the model would need to be re–assessed. Furthermore, the NZAC SCM does not account for physical mechanisms such as transport which may account for some differences in OH between different CCMs. By using this model we mainly focus on instantaneous changes in the chemistry of the overhead column caused by correcting biases in O_3, H_2O, CO, CH_4, and temperature.

The specific advantage of the NZAC SCM is that it allows the user to straight–forwardly control all impact parameters and to separate long–

from short–lived effects. For a hemisphere–wide generalization of the work in this thesis, CH_4 and CO are straightforwardly constrained using surface and satellite–based observations. For H_2O and temperature, one would need to use re–analyses or satellite products. However, tropospheric O_3 is not straightforward to constrain. While there are global re–analyses of tropospheric O_3 [e.g. Monitoring atmospheric composition and climate (MACC)], they are subject to problems in data–sparse regions. In the absence of a reliable climatology of tropospheric O_3, the model could be rolled out to other stations in the remote SH that launch ozonesondes. For instance, NDACC lists five such stations in addition to Lauder, e.g. Ile de la Reunion and four Antarctic stations.

Having determined the contribution of the major forcings to the chemistry of OH at Lauder under clear–sky conditions, the uncertainty of the clouds impact on photolysis and OH remains a significant problem. The availability of suitable observations to validate the NZAC SCM for cloud cover and profiles is critical, and might result in an improvement in the understanding of the contributions of the major drivers to the budget of OH in cloudy conditions. Note that in this study, the effect of clouds has been quantified separately from the effect of bias–correcting the other forcings, due to the large uncertainty that clouds produce in the chemistry of the atmosphere. This would further complicate the interpretation of the contributions of the major paramaters to OH chemistry.

The NZAC SCM is used to demonstrate the feasibility of validating OH in global models using observations (e.g. ground–based, satellite and aircraft observations). This means that the method used here is a step forward from using tracers like CH_3CCl_3 to study the OH evolution. By using the NZAC SCM, the sensitivity of OH to CCM biases can be quantified, and hence the order of importance in the contributing factors can inform model developers to tackle specific problems regarding OH calculations in CCMs. In a forward sense, not only is the NZAC SCM a suitable tool to advance understanding of OH chemistry, but also having a correct photochemical representation in global models would help improve this (especially regarding the photolysis

rate calculations). For instance, how will climate change impact clouds? And, how will clouds affect photolysis, and hence OH concentrations and trends?

Bibliography

Albretch, B. A., 1989. Aerosols, Cloud Microphysics, and Fractional Cloudiness. *Science* 245 (4923), 1227–1230.

Allen, N. D. C., Abad, G. G., Bernath, P. F., Boone, C. D., 2013. Satellite observations of the global distribution of hydrogen peroxide (H_2O_2) from ACE. *Journal of Quantitative Spectroscopy and Radiative Transfer* 115, 66–77.

Atkinson, R., 2000. Atmospheric chemistry of VOCs and NOx. *Atmospheric Environment* 34 (12–14), 2063–2101.

Balis, D., Zerefos, C., Kourtidis, K., Bais, A., Hofzumahaus, A., Kraus, A., Schmitt, R., Blumthaler, M., Gobbi, G., 2002. Measurements and modeling of photolysis rates during the Photochemical Activity and Ultraviolet Radiation (PAUR) II campaign. *Journal of Geophysical Research–Atmospheres* 107 (D18), 8138.

Bergman, J., Sardeshmukh, P., 2004. Dynamic stabilization of atmospheric single column models. *Journal of Climate* 17 (5), 1004–1021.

Bian, H., Prather, M., 2002. Fast–J2: Accurate simulation of stratospheric photolysis in global chemical models. *Journal of Atmospheric Chemistry* 41 (3), 281–296.

Bloss, W. J., Lee, J. D., Heard, D. E., Salmon, R. A., Bauguitte, S. J. B., Roscoe, H. K., Jones, A. E., 2007. Observations of OH and HO_2 radicals in coastal Antarctica. *Atmospheric Chemistry and Physics* 7 (16), 4171–4185.

Brasseur, G. P., Orlando, J. J., Tyndall, G. S., 1999. Atmospheric Chemistry and Global Change. *Oxford University Press*. Oxford and New York, UK and USA, 654 pp.

Brasseur, G. P., Solomon, S., 1986. Aeronomy of the middle atmosphere. *D. Reidel Publishing Company*, 2nd edition, 452 pp.

Brinksma, E., Ajtic, J., Bergwerff, J., Bodeker, G., Boyd, I., de Haan, J., Hogervorst, W., Hovenier, J., Swart, D., 2002. Five years of observations of ozone profiles over Lauder, New Zealand. *Journal of Geophysical Research–Atmospheres* 107 (D14), 4216.

Brinksma, E., Bergwerff, J., Bodeker, G., Boersma, K., Boyd, I., Connor, B., de Haan, J., Hogervorst, T., Hovenier, J., Parrish, A., Tsou, J., Zawodny, J., Swart, D., 2000. Validation of 3 years of ozone measurements over network for the detection of stratospheric change station Lauder, New Zealand. *Journal of Geophysical Research–Atmospheres* 105 (D13), 17291–17306.

Brown, S. S., Stark, H., Ravishankara, A. R., 2003. Applicability of the steady state approximation to the interpretation of atmospheric observations of NO_3 and N_2O_5. *Journal of Geophysical Research–Atmospheres* 108 (D17), 4539–4549.

Butchart, N., 2014. The Brewer–Dobson circulation. *Reviews of Geophysics* 52 (2), 157–184.

Cahalan, R., Oreopoulos, L., Wen, G., Marshak, A., Tsay, S., DeFelice, T., 2001. Cloud characterization and clear–sky correction from Landsat–7. *Remote Sensing of Environment* 78 (1–2, SI), 83–98.

Cantrell, C. A., Shetter, R. E., Calvert, J. G., Eisele, F. L., Williams, E., Baumann, K., Brune, W. H., Stevens, P. S., Mather, J. H., 1997. Peroxy radicals from photostationary state deviations and steady state calculations during the tropospheric OH photochemistry experiment at Idaho Hill, Colorado, 1993. *Journal of Geophysical Research–Atmospheres* 102 (D5), 6369–6378.

Carver, G., Brown, P., Wild, O., 1997. The ASAD atmospheric chemistry integration package and chemical reaction database. *Computer Physics Communications* 105 (2–3), 197–215.

Cesana, G., Chepfer, H., 2012. How well do climate models simulate cloud vertical structure? a comparison between calipso-goccp satellite observations and CMIP5 models. *Geophysical Research Letters* 39 (20), L20803.

Chahine, M. T., 1992. The hydrological cycle and its influence on climate. *Nature* 359, 373–380.

Chan, L. Y., Chu, K. W., 2007. Halocarbons in the atmosphere of the industrial–related Pearl River Delta region of China. *Journal of Geophysical Research–Atmospheres* 112 (D4), D04305.

Chang, J. S., Brost, R. A., Isaksen, I. S. A., Madronich, S., Middleton, P., Stockwell, W. R., Walcek, C. J., 1987. A three–dimensional Eulerian acid deposition model: Physical concepts and formulation. *Journal of Geophysical Research–Atmospheres* 92 (D12), 14681–14700.

Chapman, S., 1930. On ozone and atomic oxygen in the upper atmosphere. *Philosophical Magazine* 10 (64, 7^{th} series), 369–383.

Chipperfield, M., 1999. Multiannual simulations with a three–dimensional chemical transport model. *Journal of Geophysical Research–Atmospheres* 104 (D1), 1781–1805.

Chýlek, P., Lesins, G. B., Videen, G., Wong, J. G. D., Pinnick, R. G., Ngo, D., Klett, J. D., 1996. Black carbon and absorption of solar radiation by clouds. *Journal of Geophysical Research–Atmospheres* 101 (D18), 23365–23371.

Clemitshaw, K., 2004. A review of instrumentation and measurement techniques for ground–based and airborne field studies of gas–phase tropospheric chemistry. *Critical Reviews in Environmental Science and Technology* 34 (1), 1–108.

Collins, W. J., Bellouin, N., Doutriaux-Boucher, M., Gedney, N., Halloran, P., Hinton, T., Hughes, J., Jones, C. D., Joshi, M., Liddicoat, S., Martin, G., O'Connor, F., Rae, J., Senior, C., Sitch, S., Totterdell, I., Wiltshire, A., Woodward, S., 2011. Development and evaluation of an Earth–System model–HadGEM2. *Geoscientific Model Development* 4 (4), 1051–1075.

Crawford, J., Davis, D., Chen, G., Shetter, R., Mller, M., Barrick, J., Olson, J., 1999. An assessment of cloud effects on photolysis rate coefficients: Comparison of experimental and theoretical values. *Journal of Geophysical Research-Atmospheres* 104 (D5), 5725–5734.

Creasey, D., Evans, G., Heard, D., Lee, J., 2003. Measurements of OH and HO_2 concentrations in the Southern Ocean marine boundary layer. *Journal of Geophysical Research-Atmospheres* 108 (D15), 4475.

Crutzen, P. J., 1970. The influence of nitrogen oxides on the atmospheric ozone content. *Quarterly Journal of the Royal Meteorological Society* 96 (408), 320–325.

Crutzen, P. J., 1973. A discussion of the chemistry of some minor constituents in the stratosphere and troposphere. *Pure and Applied Geophysics* 106–108 (1), 1385–1399.

Cuxart, J., Holtslag, A., Beare, R., Bazile, E., Beljaars, A., Cheng, A., Conangla, L., Ek, M., Freedman, F., Hamdi, R., Kerstein, A., Kitagawa, H., Lenderink, G., Lewellen, D., Mailhot, J., Mauritsen, T., Perov, V., Schayes, G., Steeneveld, G., Svensson, G., Taylor, P., Weng, W., Wunsch, S., Xu, K., 2006. Single–column model intercomparison for a stably stratified atmospheric boundary layer. *Boundary–Layer Meteorology* 118 (2), 273–303.

Davies, T., Cullen, M., Malcolm, A., Mawson, M., Staniforth, A., White, A., Wood, N., 2005. A new dynamical core for the Met Office's global and regional modelling of the atmosphere. *Quarterly Journal of The Royal Meteorological Society* 131 (608, B), 1759–1782.

de Laat, A. T. J., Gloudemans, A. M. S., Schrijver, H., Aben, I., Nagahama, Y., Suzuki, K., Mahieu, E., Jones, N. B., Paton-Walsh, C., Deutscher,

N. M., Griffith, D. W. T., De Maziere, M., Mittermeier, R. L., Fast, H., Notholt, J., Palm, M., Hawat, T., Blumenstock, T., Hase, F., Schneider, M., Rinsland, C., Dzhola, A. V., Grechko, E. I., Poberovskii, A. M., Makarova, M. V., Mellqvist, J., Strandberg, A., Sussmann, R., Borsdorff, T., Rettinger, M., 2010. Validation of five years (2003–2007) of SCIAMACHY CO total column measurements using ground–based spectrometer observations. *Atmospheric Measurement Techniques* 3 (5), 1457–1471.

Dessler, A., 2000. The chemistry and physics of stratospheric ozone. *Academic Press*, London, UK, 214 pp.

Dixon, M., Li, Z., Lean, H., Roberts, N., Ballard, S., 2009. Impact of data assimilation on forecasting convection over the United Kingdom using a high–resolution version of the Met Office Unified Model. *Monthly Weather Review* 137 (5), 1562–1584.

Dobson, G. M. B., 1957. Observers' handbook for the ozone spectrophotometer. *Annuals of the International Geophysical Year* 5 (1), 46–89.

Dusanter, S., Vimal, D., Stevens, P. S., Volkamer, R., Molina, L. T., 2009. Measurements of OH and HO_2 concentrations during the MCMA–2006 field campaign – Part 1: Deployment of the Indiana University laser–induced fluorescence instrument. *Atmospheric Chemistry and Physics* 9 (5), 1665–1685.

Edwards, D., Emmons, L., Gille, J., Chu, A., Attié, J., Giglio, L., Wood, S., Haywood, J., Deeter, M., Massie, S., Ziskin, D., Drummond, J., 2006. Satellite–observed pollution from Southern Hemisphere biomass burning. *Journal of Geophysical Research–Atmospheres* 111 (D14), D14312.

Elliott, W., Gaffen, D., 1991. On the utility of radiosonde humidity archives for climate studies. *Bulletin of the American Meteorological Society* 72, 1507–1520.

Elshorbany, Y. F., Kleffmann, J., Hofzumahaus, A., Kurtenbach, R., Wiesen, P., Brauers, T., Bohn, B., Dorn, H. P., Fuchs, H., Holland,

F., Rohrer, F., Tillmann, R., Wegener, R., Wahner, A., Kanaya, Y., Yoshino, A., Nishida, S., Kajii, Y., Martinez, M., Kubistin, D., Harder, H., Lelieveld, J., Elste, T., Plass-Duelmer, C., Stange, G., Berresheim, H., Schurath, U., 2012. HOx budgets during HOxComp: A case study of HOx chemistry under NOx–limited conditions. *Journal of Geophysical Research–Atmospheres* 117, D03307.

Emmerson, K., Carslaw, N., Carpenter, L., Heard, D., Lee, J., Pilling, M., 2005. Urban atmospheric chemistry during the PUMA campaign 1: Comparison of modelled OH and HO_2 concentrations with measurements. *Journal of Atmospheric Chemistry* 52 (2), 143–164.

Emmerson, K. M., Carslaw, N., Carslaw, D. C., Lee, J. D., McFiggans, G., Bloss, W. J., Gravestock, T., Heard, D. E., Hopkins, J., Ingham, T., Pilling, M. J., Smith, S. C., Jacob, M., Monks, P. S., 2007. Free radical modelling studies during the UK TORCH campaign in summer 2003. *Atmospheric Chemistry and Physics* 7 (1), 167–181.

Evans, K., 1998. The spherical harmonics discrete ordinate method for three–dimensional atmospheric radiative transfer. *Journal of Atmospheric Sciences* 55 (3), 429–446.

Eyring, V., Harris, N., Rex, M., Shepherd, T., Fahey, D., Amanatidis, G., Austin, J., Chipperfield, M., Dameris, M., Forster, P., Gettelman, A., Graf, H., Nagashima, T., Newman, P., Pawson, S., Prather, M., Pyle, J., Salawitch, R., Santer, B., Waugh, D., 2005. A strategy for process–oriented validation of coupled chemistry–climate models. *Bulletin of the American Meteorological Society* 86 (8), 1117–1133.

Farrow, L. A., Graedel, T. E., 1977. Steady state approximations and urban atmospheric chemistry. *The Journal of Physical Chemistry* 81 (25), 2480–2483.

Feng, Y., Penner, J. E., Sillman, S., Liu, X., 2004. Effects of cloud overlap in photochemical models. *Journal of Geophysical Research–Atmospheres* 109 (D4), D04310.

Fishman, J., Fakhruzzaman, K., Cros, B., Nganga, D., 1991. Identification of widespread pollution in the Southern Hemisphere deduced from satellite analyses. *Science* 252, 1693–1696.

Forster, P. M. D. F., 1995. Modeling ultraviolet radiation at the Earth's surface. Part 1: The sensitivity of ultraviolet irradiances to atmospheric changes. *Journal of Applied Meteorology* 34, 2412–2425.

Fuglestvedt, J., Jonson, J., Isaksen, I., 1994. Effects of reductions in stratospheric ozone on tropospheric chemistry through changes in photolysis rates. *Tellus B–Chemical and Physical Meteorology* 46B (3), 172–192.

Fuglestvedt, J., Jonson, J., Wang, W., Isaksen, I., 1995. Responses in tropospheric chemistry to changes in UV fluxes, temperatures and water vapour densities. *Springer Berlin Heidelberg* 32, 145–162.

Goff, J., Gratch, S., 1946. Low–pressure properties of water from –160 to 212 F. *Transactions of the American Society of Heating and Ventilating Engineers* 52, 95–122.

Götz, F. W. P., 1931. Zum Stralungsklima des Spitzbergen Sommers: Stralungs und Ozonmessungen in der Knigsbucht 1929. *Gerlands Beitrage zur Geophys.* 31, 119–154.

Graham, E., Sarazin, M., Beniston, M., Collet, C., Hayoz, M., Neun, M., Casals, P., 2005. Climate–based site selection for a very large telescope using GIS techniques. *Meteorological Applications* 12, 77–81.

Grenfell, J., Savage, N., Harrison, R., Penkett, S., Forberich, O., Comes, F., Clemitshaw, K., Burgess, R., Crdenas, L., Davison, B., McFadyen, G., 1999. Tropospheric box–modelling and analytical studies of the hydroxyl (OH) radical and related species: Comparison with observations. *Journal of Atmospheric Chemistry* 33 (2), 183–214.

Hansen, J., Sato, M., Ruedy, R., 1997. Radiative forcing and climate response. *Journal of Geophysical Research–Atmospheres* 102 (D6), 6831–6864.

Hardiman, S. C., Butchart, N., Osprey, S. M., Gray, L. J., Bushell, A. C., Hinton, T. J., 2010. The climatology of the middle atmosphere in a vertically extended version of the Met Office's Climate Model. part I: Mean state. *Journal of the Atmospheric Sciences* 67 (5), 1509–1525.

Heard, D. E., Pilling, M. J., 2003. Measurement of OH and HO_2 in the troposphere. *Chemical Reviews* 103 (12), 5163–5198.

Hewitt, H. T., Copsey, D., Culverwell, I. D., Harris, C. M., Hill, R. S. R., Keen, A. B., McLaren, A. J., Hunke, E. C., 2011. Design and implementation of the infrastructure of HadGEM3: the next–generation Met Office climate modelling system. *Geoscientific Model Development* 4 (2), 223–253.

Holton, J. R., 2004. An introduction to dynamic meteorology. *Elsevier Academic Press*, 4^{th} edition, 535 pp.

Houghton, J. T., Ding, Y., Griggs, D. J., Noguer, M., Van der Linden, P. J., Dai, X., Maskell, K., Johnson, C. A., 2001. Climate Change 2001: The scientific basis. Contribution of working group 1 to the third assessment report of the intergovernmental panel on climate change. *Cambridge University Press*, Cambridge, UK, 881 pp.

Hua, W., Chen, Z. M., Jie, C. Y., Kondo, Y., Hofzumahaus, A., Takegawa, N., Chang, C. C., Lu, K. D., Miyazaki, Y., Kita, K., Wang, H. L., Zhang, Y. H., Hu, M., 2008. Atmospheric hydrogen peroxide and organic hydroperoxides during PRIDE–PRD'06, China: their concentration, formation mechanism and contribution to secondary aerosols. *Atmospheric Chemistry and Physics* 8 (22), 6755–6773.

Hudson, R., 1979. Minor constituents in the stratosphere and mesosphere. *Reviews of Geophysics* 17 (4), 467–477.

Hurst, D. F., Lambert, A., Read, W. G., Davis, S. M., Rosenlof, K. H., Hall, E. G., Jordan, A. F., Oltmans, S. J., 2014. Validation of Aura Microwave Limb Sounder stratospheric water vapor measurements by the NOAA frost point hygrometer. *Journal of Geophysical Research–Atmospheres* 119 (3).

Hyland, R., Wexler, A., 1983. Formulations for the thermodynamic properties of the saturated phases of H_2O from 173.15 K to 473.15 K. *Transactions of the American Society of Heating and Ventilating Engineers* 89, 500–519.

Johns, T. C., Durman, C. F., Banks, H. T., Roberts, M. J., McLaren, A. J., Ridley, J. K., Senior, C. A., Williams, K. D., Jones, A., Rickard, G. J., Cusack, S., Ingram, W. J., Crucifix, M., Sexton, D. M. H., Joshi, M. M., Dong, B.-W., Spencer, H., Hill, R. S. R., Gregory, J. M., Keen, A. B., Pardaens, A. K., Lowe, J. A., Bodas-Salcedo, A., Stark, S., Searl, Y., 2006. The new hadley centre climate model (HadGEM1): Evaluation of coupled simulations. *Journal of Climate* 19 (7), 1327–1353.

Johnson, B. J., Oltmans, S. J., Vmel, H., Smit, H. G. J., Deshler, T., Krger, C., 2002. Electrochemical concentration cell (ECC) ozonesonde pump efficiency measurements and tests on the sensitivity to ozone of buffered and unbuffered ECC sensor cathode solutions. *Journal of Geophysical Research–Atmospheres* 107 (D19), 4393.

Johnston, H., 1971. Reduction of stratospheric ozone by nitrogen oxide catalysts from supersonic transport exhaust. *Science* 173 (3996), 517–522.

Jones, C. D., Hughes, J. K., Bellouin, N., Hardiman, S. C., Jones, G. S., Knight, J., Liddicoat, S., O'Connor, F. M., Andres, R. J., Bell, C., Boo, K.-O., Bozzo, A., Butchart, N., Cadule, P., Corbin, K. D., Doutriaux-Boucher, M., Friedlingstein, P., Gornall, J., Gray, L., Halloran, P. R., Hurtt, G., Ingram, W. J., Lamarque, J.-F., Law, R. M., Meinshausen, M., Osprey, S., Palin, E. J., Chini, L. P., Raddatz, T., Sanderson, M. G., Sellar, A. A., Schurer, A., Valdes, P., Wood, N., Woodward, S., Yoshioka, M., Zerroukat, M., 2011. The HadGEM2–ES implementation of CMIP5 centennial simulations. *Geoscientific Model Development* 4 (3), 543–570.

Jones, N., Rinsland, C., Liley, J., Rosen, J., 2001. Correlation of aerosol and carbon monoxide at 45°S: Evidence of biomass burning emissions. *Geophysical Research Letters* 28 (4), 709–712.

Joyce, P. L., von Glasow, R., Simpson, W. R., 2014. The fate of NO_x

emissions due to nocturnal oxidation at high latitudes: 1–D simulations and sensitivity experiments. *Atmospheric Chemistry and Physics* 14 (14), 7601–7616.

Kleinman, L. I., Daum, P. H., Lee, J. H., Lee, Y.-N., Nunnermacker, L. J., Springston, S. R., Newman, L., Weinstein-Lloyd, J., Sillman, S., 1997. Dependence of ozone production on NO and hydrocarbons in the troposphere. *Geophysical Research Letters* 24 (18), 2299–2302.

Komhyr, W. D., 1969. Electrochemical concentration cell for gas analysis. *Annual Geophysics* 25, 203–210.

Komhyr, W. D., 1980. Operations handbook – ozone observations with a Dobson spectrophotometer. *World Meteorological Organization.* Report 6, Geneva.

Komhyr, W. D., Grass, R. D., Leonard, R. K., 1989. Dobson spectrophotometer 83: A standard for total ozone measurements, 1962–1987. *Journal of Geophysical Research—Atmospheres* 94 (D7), 9847–9861.

Krol, M. C., Weele, M. V., 1997. Implications of variations in photodissociation rates for global tropospheric chemistry. *Atmospheric Environment* 31 (9), 1257–1273.

Krummel, P., Fraser, P., Steele, L., Derek, N., Rickard, C., Ward, J., Sommerville, N. T., Cleland, S. J., Dunse, B., Langenfelds, R., Baly, S. B., Leist, M., 2014. The AGAGE in situ program for non–CO_2 greenhouse gases at Cape Grim, 2009–2010, in: Baseline Atmospheric Program (Australia), 2009–2010. *Australian Bureau of Meteorology and CSIRO Marine and Atmospheric Research.* Aspendale, Victoria, Australia, 56–70.

Kylling, A., Webb, A., Kift, R., Gobbi, G., Ammannato, L., Barnaba, F., Bais, A., Kazadzis, S., Wendisch, M., Jakel, E., Schmidt, S., Kniffka, A., Thiel, S., Junkermann, W., Blumthaler, M., Silbernagl, R., Schallhart, B., Schmitt, R., Kjeldstad, B., Thorseth, T., Scheirer, R., Mayer, B., 2005. Spectral actinic flux in the lower troposphere: measurement and

1–D simulations for cloudless, broken cloud and overcast situations. *Atmospheric Chemistry and Physics* 5, 1975–1997.

Langenfelds, R., Steele, L., Gregory, R. L., Krummel, P., Spencer, D., Howden, R., 2014. Atmospheric methane, carbon dioxide, hydrogen, carbon monoxide and nitrous oxide from Cape Grim flask air samples analysed by gas chromatography, in: Baseline Atmospheric Program (Australia), 2009–2010. *Australian Bureau of Meteorology and CSIRO Marine and Atmospheric Research*. Aspendale, Victoria, Australia, 45–49.

Lary, D., Pyle, J., 1991. Diffuse radiation, twilight, and photochemistry–I. *Journal of Atmospheric Chemistry* 13 (4), 373–392.

Lefer, B. L., Shetter, R. E., Hall, S. R., Crawford, J. H., Olson, J. R., 2003. Impact of clouds and aerosols on photolysis frequencies and photochemistry during TRACE–P: 1. analysis using radiative transfer and photochemical box models. *Journal of Geophysical Research–Atmospheres* 108 (D21), 8821.

Lelieveld, J., Dentener, F. J., 2000. What controls tropospheric ozone? *Journal of Geophysical Research–Atmospheres* 105 (D3), 3531–3551.

Levy, H., 1971. Normal atmosphere: Large radical and formaldehyde concentrations predicted. *Science* 173 (3992), 141–143.

Liou, K. N., 1992. Radiation and cloud processes in the atmosphere. *Oxford University Press*, Oxford, UK.

Liu, H., Crawford, J. H., Considine, D. B., Platnick, S., Norris, P. M., Duncan, B. N., Pierce, R. B., Chen, G., Yantosca, R. M., 2009. Sensitivity of photolysis frequencies and key tropospheric oxidants in a global model to cloud vertical distributions and optical properties. *Journal of Geophysical Research–Atmospheres* 114 (D10), D10305.

Liu, H., Crawford, J. H., Pierce, R. B., Norris, P., Platnick, S. E., Chen, G., Logan, J. A., Yantosca, R. M., Evans, M. J., Kittaka, C., Feng, Y., Tie, X., 2006. Radiative effect of clouds on tropospheric chemistry

in a global three–dimensional chemical transport model. *Journal of Geophysical Research–Atmospheres* 111 (D20), D20303.

Liu, J., Zheng, Y., Li, Z., Flynn, C., Cribb, M., 2012. Seasonal variations of aerosol optical properties, vertical distribution and associated radiative effects in the Yangtze Delta region of China. *Journal of Geophysical Research–Atmospheres* 117, D00K38.

Liu, S. C., Trainer, M., 1988. Response of the tropospheric ozone and odd hydrogen radicals to column ozone change. *Journal of Atmospheric Chemistry* 6, 221–233.

Logan, J. A., Prather, M. J., Wofsy, S. C., McElroy, M. B., 1981. Tropospheric chemistry: A global perspective. *Journal of Geophysical Research–Oceans* 86 (C8), 7210–7254.

London, J., 1952. The distribution of radiational temperature change in the Northern Hemisphere during March. *Journal of Meteorology* 9, 145–151.

Luers, J., Eskridge, R., 1998. Use of radiosonde temperature data in climate studies. *Journal of Climate* 11 (5), 1002–1019.

Madronich, S., 1987. Photodissociation in the atmosphere: 1. Actinic flux and the effects of ground reflections and clouds. *Journal of Geophysical Research–Atmospheres* 92 (D8), 9740–9752.

Madronich, S., Granier, C., 1992. Impact of recent total changes on tropospheric ozone photodissociation, hydroxyl radicals, and methane trends. *Geophysical Research Letters* 19, 465–467.

Madronich, S., Shao, M., Wilson, S. R., Solomon, K. R., Longstreth, J. D., Tang, X. Y., 2015. Changes in air quality and tropospheric composition due to depletion of stratospheric ozone and interactions with changing climate: implications for human and environmental health. *Photochemical and Photobiological Sciences* 14, 149–169.

Mann, G. W., Carslaw, K. S., Spracklen, D. V., Ridley, D. A., Manktelow, P. T., Chipperfield, M. P., Pickering, S. J., Johnson, C. E.,

2010. Description and evaluation of GLOMAP–mode: a modal global aerosol microphysics model for the UKCA composition–climate model. *Geoscientific Model Development* 3 (2), 519–551.

Manning, M., Lowe, D., Moss, R., Bodeker, G., Allan, W., 2005. Short–term variations in the oxidizing power of the atmosphere. *Nature* 436 (7053), 1001–1004.

Marenco, A., Gouget, H., Nédélec, P., Pagés, J.-P., Karcher, F., 1994. Evidence of a long–term increase in tropospheric ozone from Pic du Midi data series: Consequences: Positive radiative forcing. *Journal of Geophysical Research–Atmospheres* 99 (D8), 16617–16632.

Martin, G. M., Bellouin, N., Collins, W. J., Culverwell, I. D., Halloran, P. R., Hardiman, S. C., Hinton, T. J., Jones, C. D., McDonald, R. E., McLaren, A. J., O'Connor, F. M., Roberts, M. J., Rodriguez, J. M., Woodward, S., Best, M. J., Brooks, M. E., Brown, A. R., Butchart, N., Dearden, C., Derbyshire, S. H., Dharssi, I., Doutriaux-Boucher, M., Edwards, J. M., Falloon, P. D., Gedney, N., Gray, L. J., Hewitt, H. T., Hobson, M., Huddleston, M. R., Hughes, J., Ineson, S., Ingram, W. J., James, P. M., Johns, T. C., Johnson, C. E., Jones, A., Jones, C. P., Joshi, M. M., Keen, A. B., Liddicoat, S., Lock, A. P., Maidens, A. V., Manners, J. C., Milton, S. F., Rae, J. G. L., Ridley, J. K., Sellar, A., Senior, C. A., Totterdell, I. J., Verhoef, A., Vidale, P. L., Wiltshire, A., Team, H. D., 2011. The HadGEM2 family of Met Office Unified Model climate configurations. *Geoscientific Model Development* 4 (3), 723–757.

Martin, G. M., Ringer, M. A., Pope, V. D., Jones, A., Dearden, C., Hinton, T. J., 2006. The physical properties of the atmosphere in the new hadley centre global environmental model (HadGEM1). part I: Model description and global climatology. *Journal of Climate* 19 (7), 1274–1301.

Martínez, M., Perner, D., Hackenthal, E. M., Kulzer, S., Schutz, L., 2000. NO_3 at Helgoland during the NORDEX campaign in October 1996. *Journal of Geophysical Research–Atmospheres* 105 (D18), 22685–22695.

Mason, B. J., 1975. Clouds, rain and rainmaking. *Cambridge University Press*, Cambridge, UK., 198 pp.

Matsumura, Y., Ananthaswamy, H., 2004. Toxic effects of ultraviolet radiation on the skin. *Toxicology and Applied Pharmacology* 195 (3), 298–308.

McKenna, D., Konopka, P., Grooss, J., Gunther, G., Muller, R., Spang, R., Offermann, D., Orsolini, Y., 2002. A new Chemical Lagrangian Model of the Stratosphere (CLaMS) – 1. Formulation of advection and mixing. *Journal of Geophysical Research–Atmospheres* 107 (D16), 4309.

McKenzie, R., Johnston, P., Hofzumahaus, A., Kraus, A., Madronich, S., Cantrell, C., Calvert, J., Shetter, R., 2002. Relationship between photolysis frequencies derived from spectroscopic measurements of actinic fluxes and irradiances during the IPMMI campaign. *Journal of Geophysical Research–Atmospheres* 107 (D5), 4042.

McKenzie, R., Madronich, S., 2003. Surface ultraviolet radiation. *Encyclopedia of Atmospheric Sciences. Elsevier Ltd.*, 2474–2480.

McKenzie, R. L., Liley, J. B., Bjorn, L. O., 2009. UV Radiation: Balancing Risks and Benefits. *Photochemistry and Photobiology* 85 (1), 88–98.

McLinden, C., Olsen, S., Hannegan, B., Wild, O., Prather, M. J., Sundet, J., 2000. Stratospheric ozone in 3–D models: A simple chemistry and the cross–tropopause flux. *Journal of Geophysical Research–Atmospheres* 105 (D11), 14653–14665.

Measures, R. M., 1984. Laser Remote Sensing. Fundamentals and Applications. *John Wiley and Sons*. New York, USA.

Meijer, Y., van der A, R., van Oss, R., Swart, D., Kelder, H., Johnston, P., 2003. Global Ozone Monitoring Experiment ozone profile characterization using interpretation tools and lidar measurements for intercomparison. *Journal of Geophysical Research–Atmospheres* 108 (D23), 4723.

Mihailovic, D., Rao, S., Alapaty, K., Ku, J., Arsenic, I., Lalic, B., 2005. A study on the effects of subgrid–scale representation of land use on the

boundary layer evolution using a 1–D model. *Environmental Modelling and Software* 20 (6), 705–714.

Millar, T. J., Rawlings, J. M. C., Bennett, A., Brown, P. D., Chamley, S. B., 1991. Gas phase reactions and rate coefficients for use in astrochemistry. The UMIST ratefile. *Astronomy and Astrophysics Supplement* 87 (585), 585–619.

Miloshevich, L., Vomel, H., Paukkunen, A., Heymsfield, A., Oltmans, S., 2001. Characterization and correction of relative humidity measurements from vaisala RS80–A radiosondes at cold temperatures. *Journal of Atmospheric and Oceanic Technology* 18 (2), 135–156.

Molina, M., Rowland, F., 1974. Stratospheric sink for chlorofluoromethanes – chlorine atomic-catalysed destruction of ozone. *Nature* 249 (5460), 810–812.

Montzka, S. A., Krol, M., Dlugokencky, E., Hall, B., Jckel, P., Lelieveld, J., 2011. Small Interannual Variability of Global Atmospheric Hydroxyl. *Science* 331 (6013), 67–69.

Moradi, I., Soden, B., Ferraro, R., Arkin, P., Voemel, H., 2013. Assessing the quality of humidity measurements from global operational radiosonde sensors. *Journal of Geophysical Research–Atmospheres* 118 (14), 8040–8053.

Morgenstern, O., Braesicke, P., Hurwitz, M. M., O'Connor, F. M., Bushell, A. C., Johnson, C. E., Pyle, J. A., 2008. The world avoided by the Montreal protocol. *Geophysical Research Letters* 35 (16), L16811.

Morgenstern, O., Braesicke, P., O'Connor, F. M., Bushell, A. C., Johnson, C. E., Osprey, S. M., Pyle, J. A., 2009. Evaluation of the new UKCA climate–composition model – Part 1: The stratosphere. *Geoscientific Model Development* 2 (1), 43–57.

Morgenstern, O., Giorgetta, M. A., Shibata, K., Eyring, V., Waugh, D. W., Shepherd, T. G., Akiyoshi, H., Austin, J., Baumgaertner, A. J. G., Bekki, S., Braesicke, P., Bruehl, C., Chipperfield, M. P., Cugnet, D., Dameris,

M., Dhomse, S., Frith, S. M., Garny, H., Gettelman, A., Hardiman, S. C., Hegglin, M. I., Joeckel, P., Kinnison, D. E., Lamarque, J. F., Mancini, E., Manzini, E., Marchand, M., Michou, M., Nakamura, T., Nielsen, J. E., Olivie, D., Pitari, G., Plummer, D. A., Rozanov, E., Scinocca, J. F., Smale, D., Teyssedre, H., Toohey, M., Tian, W., Yamashita, Y., 2010. Review of the formulation of present–generation stratospheric chemistry–climate models and associated external forcings. *Journal of Geophysical Research–Atmospheres* 115 (D3), D00M02.

Morgenstern, O., Zeng, G., Abraham, N. L., Telford, P. J., Braesicke, P., Pyle, J. A., Hardiman, S. C., O'Connor, F. M., Johnson, C. E., 2013. Impacts of climate change, ozone recovery, and increasing methane on surface ozone and the tropospheric oxidizing capacity. *Journal of Geophysical Research–Atmospheres* 118 (2), 1028–1041.

Naik, V., Voulgarakis, A., Fiore, A. M., Horowitz, L. W., Lamarque, J.-F., Lin, M., Prather, M. J., Young, P. J., Bergmann, D., Cameron-Smith, P. J., Cionni, I., Collins, W. J., Dalsøren, S. B., Doherty, R., Eyring, V., Faluvegi, G., Folberth, G. A., Josse, B., Lee, Y. H., MacKenzie, I. A., Nagashima, T., van Noije, T. P. C., Plummer, D. A., Righi, M., Rumbold, S. T., Skeie, R., Shindell, D. T., Stevenson, D. S., Strode, S., Sudo, K., Szopa, S., Zeng, G., 2013. Preindustrial to present–day changes in tropospheric hydroxyl radical and methane lifetime from the Atmospheric Chemistry and Climate Model Intercomparison Project (ACCMIP). *Atmospheric Chemistry and Physics* 13 (10), 5277–5298.

Nair, P. J., Godin-Beekmann, S., Froidevaux, L., Flynn, L. E., Zawodny, J. M., Russell, III, J. M., Pazmino, A., Ancellet, G., Steinbrecht, W., Claude, H., Leblanc, T., McDermid, S., van Gijsel, J. A. E., Johnson, B., Thomas, A., Hubert, D., Lambert, J. C., Nakane, H., Swart, D. P. J., 2012. Relative drifts and stability of satellite and ground–based stratospheric ozone profiles at NDACC lidar stations. *Atmospheric Measurement Techniques* 5 (6), 1301–1318.

Nejad, L. A. M., 1986. PhD thesis. *University of Manchester*. Manchester, United Kingdom.

Neu, J. L., Prather, M. J., Penner, J. E., 2007. Global atmospheric chemistry: Integrating over fractional cloud cover. *Journal of Geophysical Research–Atmospheres* 112 (D11).

Newell, R. E., 1963. Transfer through the tropopause and within the stratosphere. *Quarterly Journal of the Royal Meteorological Society* 89 (380), 167–204.

Newman, P. A., Nash, E. R., Kawa, S. R., Montzka, S. A., Schauffler, S. M., 2006. When will the Antarctic ozone hole recover? *Geophysical Research Letters* 33 (12), L12814.

O'Connor, F. M., Johnson, C. E., Morgenstern, O., Abraham, N. L., Braesicke, P., Dalvi, M., Folberth, G. A., Sanderson, M. G., Telford, P. J., Voulgarakis, A., Young, P. J., Zeng, G., Collins, W. J., Pyle, J. A., 2014. Evaluation of the new UKCA climate–composition model – Part 2: The troposphere. *Geoscience Model Development* 7 (1), 41–91.

O'Connor, F. M., Johnson, C. E., Morgenstern, O., Collins, W. J., 2009. Interactions between tropospheric chemistry and climate model temperature and humidity biases. *Geophysical Research Letters* 36, L16801.

Oltmans, S., Vomel, H., Hofmann, D., Rosenlof, K., Kley, D., 2000. The increase in stratospheric water vapor from balloonborne, frostpoint hygrometer measurements at Washington, DC, and Boulder, Colorado. *Geophysical Research Letters* 27 (21), 3453–3456.

Oltmans, S. J., Lefohn, A. S., Harris, J. M., Galbally, I., Scheel, H. E., Bodeker, G., Brunke, E., Claude, H., Tarasick, D., Johnson, B. J., Simmonds, P., Shadwick, D., Anlauf, K., Hayden, K., Schmidlin, F., Fujimoto, T., Akagi, K., Meyer, C., Nichol, S., Davies, J., Redondas, A., Cuevas, E., 2006. Long–term changes in tropospheric ozone. *Atmospheric Environment* 40 (17), 3156–3173.

Parrish, A., 1994. Millimeter–wave remote sensing of ozone and trace constituents in the stratosphere. *Proceedings of the IEEE* 82 (12), 1915–1929.

Parrish, A., Connor, B. J., Tsou, J. J., McDermid, I. S., Chu, W. P., 1992. Ground–based microwave monitoring of stratospheric ozone. *Journal of Geophysical Research–Atmospheres* 97 (D2), 2541–2546.

Peixoto, J. P., Oort, A. H., 1992. Chapter 2: Nature of the problem. *Physics of Climate*, AIP, 8–26.

Piot, M., von Glasow, R., 2008. The potential importance of frost flowers, recycling on snow, and open leads for ozone depletion events. *Atmospheric Chemistry and Physics* 8 (9), 2437–2467.

Platnick, S., 2001. Approximations for horizontal photon transport in cloud remote sensing problems. *Journal of Quantitative Spectroscopy and Radiative Transfer* 68 (1), 75–99.

Poppe, D., Wallasch, M., Zimmermann, J., 1993. The dependence of the concentration of OH on its precursors under moderately polluted conditions: A model study. *Journal of Atmospheric Chemistry* 16 (1), 61–78.

Pöschl, U., von Kuhlmann, R., Poisson, N., Crutzen, P. J., 2000. Development and intercomparison of condensed isoprene oxidation mechanisms for global atmospheric modeling. *Journal of Atmospheric Chemistry* 37 (1), 29–52.

Prather, M., Ehhalt, D., Dentener, F., Derwent, R., Dlugokencky, E., Holland, E., Isaksen, I., Katima, J., Kirchhoff, V., Matson, P., Midgley, P., Wang, M., 2001. Atmospheric chemistry and greenhouse gases, in Climate Change 2001: The Scientific Basis. *Cambridge University Press*. Cambridge and New York, UK and USA.

Prinn, R., 2001. Evidence for substantial variations of atmospheric hydroxyl radicals in the past two decades. *Science* 293 (5532), 1048.

Prinn, R., Huang, J., Weiss, R., Cunnold, D., Fraser, P., Simmonds, P., McCulloch, A., Harth, C., Reimann, S., Salameh, P., O'Doherty, S., Wang, R., Porter, L., Miller, B., Krummel, P., 2005. Evidence for

variability of atmospheric hydroxyl radicals over the past quarter century. *Geophysical Research Letters* 32 (7), L07809.

Randall, D., Krueger, S., Bretherton, C., Curry, J., Duynkerke, P., Moncrieff, M., Ryan, B., Starr, D., Miller, M., Rossow, W., Tselioudis, G., Wielicki, B., 2003. Confronting models with data – The GEWEX cloud systems study. *Bulletin of the American Meteorological Society* 84 (4), 455–469.

Rasch, P. J., Boville, B. A., Brasseur, G. P., 1995. A 3–dimensional general–circulation model with coupled chemistry for the middle atmosphere. *Journal of Geophysical Research–Atmospheres* 100 (D5), 9041–9071.

Real, E., Sartelet, K., 2011. Modelling of photolysis rates over Europe: impact on chemical gaseous species and aerosols. *Atmospheric Chemistry and Physics* 11 (4), 1711–1727.

Ren, X., Harder, H., Martinez, M., Lesher, R. L., Oliger, A., Simpas, J. B., Brune, W. H., Schwab, J. J., Demerjian, K. L., He, Y., Zhou, X., Gao, H., 2003. OH and HO_2 chemistry in the urban atmosphere of New York city. *Atmospheric Environment* 37 (26), 3639 –3651.

Rinsland, C., Connor, B., Jones, N., Boyd, I., Matthews, W., Goldman, A., Murcray, F., Murcray, D., David, S., Pougatchev, N., 1996. Comparison of infrared and dobson total ozone columns measured from Lauder, New Zealand. *Geophysical Research Letters* 23 (9), 1025–1028.

Rinsland, C., Jones, N., Connor, B., Logan, J., Pougatchev, N., Goldman, A., Murcray, F., Stephen, T., Pine, A., Zander, R., Mahieu, E., Demoulin, P., 1998. Northern and southern hemisphere ground–based infrared spectroscopic measurements of tropospheric carbon monoxide and ethane. *Journal of Geophysical Research–Atmospheres* 103 (D21), 28197–28217.

Rinsland, C., Jones, N., Connor, B., Wood, S., Goldman, A., Stephen, T., Murcray, F., Chiou, L., Zander, R., Mahieu, E., 2002. Multiyear infrared solar spectroscopic measurements of HCN, CO, C_2H_6,and C_2H_2 tropospheric columns above Lauder, New Zealand (45°S latitude). *Journal of Geophysical Research–Atmospheres* 107 (D14), 4185.

Rodgers, C. D., 1976. Retrieval of atmospheric temperature and composition from remote measurements of thermal radiation. *Reviews of Geophysics* 14 (4), 609–624.

Rossow, W. B., 1989. Measuring cloud properties from space: a review. *Journal of Climate* 2, 201–213.

Saad, K. M., Wunch, D., Toon, G. C., Bernath, P., Boone, C., Connor, B., Deutscher, N. M., Griffith, D. W. T., Kivi, R., Notholt, J., Roehl, C., Schneider, M., Sherlock, V., Wennberg, P. O., 2014. Derivation of tropospheric methane from TCCON CH_4 and HF total column observations. *Atmospheric Measurement Techniques* 7 (9), 2907–2918.

Schmidlin, F. J., Ivanov, A., 1998. Radiosonde relative humidity sensor performance: The WMO intercomparison–Sept 1995. Preprints. *10th Symposium on Meteorological Observations and Instrumentations*. Phoenix, Arizona, United States, 68–71.

Schreier, R., Macke, A., 2001. On the accuracy of the independent column approximation in calculating the downward fluxes in the UVA, UVB, and PAR spectral regions. *Journal of Geophysical Research* 106 (D13), 14301–14312.

Smit, H. G. J., Straeter, W., Johnson, B. J., Oltmans, S. J., Davies, J., Tarasick, D. W., Hoegger, B., Stubi, R., Schmidlin, F. J., Northam, T., Thompson, A. M., Witte, J. C., Boyd, I., Posny, F., 2007. Assessment of the performance of ECC–ozonesondes under quasi–flight conditions in the environmental simulation chamber: Insights from the Juelich Ozone Sonde Intercomparison Experiment (JOSIE). *Journal of Geophysical Research–Atmospheres* 112 (D19), D19306.

Smith, S. C., Lee, J. D., Bloss, W. J., Johnson, G. P., Ingham, T., Heard, D. E., 2006. Concentrations of OH and HO_2 radicals during NAMBLEX: measurements and steady state analysis. *Atmospheric Chemistry and Physics* 6 (5), 1435–1453.

Solomon, K. R., Tang, X., Wilson, S. R., Zanis, P., Bais, A. F., 2003.

Changes in tropospheric composition and air quality due to stratospheric ozone depletion. *Photochemical and Photobiological Sciences* 2, 62–67.

Solomon, S., 1983. Minor constituents in the stratosphere and mesosphere. *Reviews of Geophysics* 21 (2), 276–283.

Spivakovsky, C. M., Logan, J. A., Montzka, S. A., Balkanski, Y. J., Foreman-Fowler, M., Jones, D. B. A., Horowitz, L. W., Fusco, A. C., Brenninkmeijer, C. A. M., Prather, M. J., Wofsy, S. C., McElroy, M. B., 2000. Three–dimensional climatological distribution of tropospheric OH: Update and evaluation. *Journal of Geophysical Research–Atmospheres* 105 (D7), 8931–8980.

Standard Atmosphere, US, 1976. The chemistry and physics of stratospheric ozone. *U. S. Government Printing Office*, Washington D. C., USA, 243 pp.

Stephens, G. L., Tsay, S. C., 1990. On the cloud absorption anomaly. *Quarterly Journal of the Royal Meteorological Society* 116, 671–704.

Stevenson, D., Dentener, F., Schultz, M., Ellingsen, K., van Noije, T., Wild, O., Zeng, G., Amann, M., Atherton, C., Bell, N., Bergmann, D., Bey, I., Butler, T., Cofala, J., Collins, W., Derwent, R., Doherty, R., Drevet, J., Eskes, H., Fiore, A., Gauss, M., Hauglustaine, D., Horowitz, L., Isaksen, I., Krol, M., Lamarque, J., Lawrence, M., Montanaro, V., Muller, J., Pitari, G., Prather, M., Pyle, J., Rast, S., Rodriguez, J., Sanderson, M., Savage, N., Shindell, D., Strahan, S., Sudo, K., Szopa, S., 2006. Multimodel ensemble simulations of present–day and near–future tropospheric ozone. *Journal of Geophysical Research–Atmospheres* 111 (D8), D08301.

Stevenson, D., Johnson, C., Collins, W., Derwent, R., Edwards, J., 2000. Future estimates of tropospheric ozone radiative forcing and methane turnover – the impact of climate change. *Geophysical Research Letters* 27 (14), 2073–2076.

Stolarski, R. S., Cicerone, R. J., 1974. Stratospheric chlorine: a possible sink for ozone. *Canadian Journal of Chemistry* 52 (8), 1610–1615.

Stübi, R., Levrat, G., Hoegger, B., Viatte, P., Staehelin, J., Schmidlin, F. J., 2008. In–flight comparison of Brewer–Mast and electrochemical concentration cell ozonesondes. *Journal of Geophysical Research–Atmospheres* 113 (D13), D13302.

Swart, D. P. J., Spakman, J., Bergwerff, J. B., Brinksma, E. J., Orme, F. T., 1995. RIVM stratospheric ozone lidar for NDSC station Lauder, New Zealand. *NOP report*. RIVM, Bilthoven, The Netherlands (Available at http://www.rivm.nl/lib/Reports/722701002.html), 57 pp.

Swinbank, R., Lahoz, W., O'Neill, A., Douglas, C., Heaps, A., Podd, D., 1998. Middle atmosphere variability in the UK Meteorological Office Unified Model. *Quarterly Journal of The Royal Meteorological Society* 124 (549), 1485–1525.

Swinnerton, J. W., Linnenbom, V. J., Lamontagne, R. A., 1970. The ocean: a natural source of carbon monoxide. *Science* 167, 984–986.

Takemura, T., Nozawa, T., Emori, S., Nakajima, T., Nakajima, T., 2005. Simulation of climate response to aerosol direct and indirect effects with aerosol transport–radiation model. *Journal of Geophysical Research–Atmospheres* 110 (D2), D02202.

Tang, X., Wilson, S. R., Solomon, K. R., Shao, M., Madronich, S., 2011. Changes in air quality and tropospheric composition due to depletion of stratospheric ozone and interactions with climate. *Photochemical and Photobiological Sciences* 10, 280–291.

Tang, Y., Carmichael, G. R., Uno, I., Woo, J.-H., Kurata, G., Lefer, B., Shetter, R. E., Huang, H., Anderson, B. E., Avery, M. A., Clarke, A. D., Blake, D. R., 2003. Impacts of aerosols and clouds on photolysis frequencies and photochemistry during TRACE–P: 2. three-dimensional study using a regional chemical transport model. *Journal of Geophysical Research–Atmospheres* 108 (D21), 8822.

Telford, P. J., Abraham, N. L., Archibald, A. T., Braesicke, P., Dalvi, M., Morgenstern, O., O'Connor, F. M., Richards, N. A. D., Pyle, J. A., 2013.

Implementation of the Fast–JX Photolysis scheme (v6.4) into the UKCA component of the MetUM chemistry–climate model (v7.3). *Geoscientific Model Development* 6 (1), 161–177.

Telford, P. J., Braesicke, P., Morgenstern, O., Pyle, J. A., 2008. Technical note: Description and assessment of a nudged version of the new dynamics Unified Model. *Atmospheric Chemistry and Physics* 8 (6), 1701–1712.

Thompson, A. M., 1984. The effect of clouds on photolysis rates and ozone formation in the unpolluted troposphere. *Journal of Geophysical Research–Atmospheres* 89 (D1), 1341–1349.

Thompson, A. M., 1992. The oxidizing capacity of the Earth's atmosphere: Probable past and future changes. *Science* 256 (5060), 1157–1165.

Thompson, A. M., Stewart, R. W., Owens, M. A., Herwehe, J. A., 1989. Sensitivity of tropospheric oxidants to global chemical and climate change. *Atmospheric Environment* 23 (3), 519–532.

Tie, X., Madronich, S., Walters, S., Zhang, R., Rasch, P., Collins, W., 2003. Effect of clouds on photolysis and oxidants in the troposphere. *Journal of Geophysical Research-Atmospheres* 108 (D20).

Turner, D., Lesht, B., Clough, S., Liljegren, J., Revercomb, H., Tobin, D., 2003. Dry bias and variability in Vaisala RS80–H radiosondes: The ARM experience. *Journal of Atmospheric and Oceanic Technology* 20 (1), 117–132.

Twomey, S., 1959. The nuclei of natural cloud formation part II: The supersaturation in natural clouds and the variation of cloud droplet concentration. *Geofisica pura e applicata* 43 (1), 243–249.

Volz, A., Kley, D., 1988. Evaluation of the Montsouris series of ozone measurements made in the nineteenth century. *Nature* 332, 240–242.

Vömel, H., Diaz, K., 2010. Ozone sonde cell current measurements and implications for observations of near–zero ozone concentrations in the tropical upper troposphere. *Atmospheric Measurement Techniques* 3 (2), 495–505.

Vömel, H., Selkirk, H., Miloshevich, L., Valverde-Canossa, J., Valdes, J., Kyroe, E., Kivi, R., Stolz, W., Peng, G., Diaz, J. A., 2007. Radiation dry bias of the vaisala RS92 humidity sensor. *Journal of Atmospheric and Oceanic Technology* 24 (6), 953–963.

Voulgarakis, A., Savage, N. H., Wild, O., Carver, G. D., Clemitshaw, K. C., Pyle, J. A., 2009. Upgrading photolysis in the p–TOMCAT CTM: model evaluation and assessment of the role of clouds. *Geoscientific Model Development* 2 (1), 59–72.

Vuilleumier, L., Brown, N. J., Harley, R. A., Reynolds, S. D., 2001. Review and improvement of methods for estimating rate of photolysis in photochemical models. *California Air Resources Board and California Environmental Protection Agency*, Sacramento, CA. Contract No. 96–335. LBL Report No. 45869, California, United States.

Vupputuri, R., Higuchi, K., Hengeveld, H., 1995. A 1–D modelling of climatic and chemical effects of greenhouse gases. *Theoretical and Applied Climatology* 52 (3–4), 151–167.

Wang, J., Zhang, L., Dai, A., Immler, F., Sommer, M., Voemel, H., 2013. Radiation Dry Bias Correction of Vaisala RS92 Humidity Data and Its Impacts on Historical Radiosonde Data. *Journal of Atmospheric and Oceanic Technology* 30 (2), 197–214.

Watson, C. E., Fishman, J., Reichle Jr, H. G., 1990. The significance of biomass burning as a source of carbon monoxide and ozone in the Southern Hemisphere tropics: a satellite analysis. *Journal of Geophysical Research–Atmospheres* 95, 16443–16450.

Watts, R. G., 1997. Engineering Response to Global Climate Change: Planning a Research and Development Agenda. *CRC Press*, 512 pp.

Wennberg, P. O., Hanisco, T. F., Jaeglé, L., Jacob, D. J., Hintsa, E. J., Lanzendorf, E. J., Anderson, J. G., Gao, R.-S., Keim, E. R., Donnelly, S. G., del Negro, L. A., Fahey, D. W., McKeen, S. A., Salawitch, R. J., Webster, C. R., May, R. D., Herman, R. L., Proffitt, M. H., Margitan,

J. J., Atlas, E. L., Schauffler, S. M., Flocke, F., McElroy, C. T., Bui, T. P., 1998. Hydrogen radicals, nitrogen radicals, and the production of O_3 in the upper troposphere. *Science* 279 (49), 49–53.

Wild, O., 2007. Modelling the global tropospheric ozone budget: exploring the variability in current models. *Atmospheric Chemistry and Physics* 7 (10), 2643–2660.

Wild, O., Zhu, X., Prather, M., 2000. Fast–J: Accurate simulation of in– and below–cloud photolysis in tropospheric chemical models. *Journal of Atmospheric Chemistry* 37 (3), 245–282.

Yang, P., Gao, B.-C., Baum, B. A., Wiscombe, W. J., Hu, Y. X., Nasiri, S. L., Soulen, P. F., Heymsfield, A. J., McFarquhar, G. M., Miloshevich, L. M., 2001. Sensitivity of cirrus bidirectional reflectance to vertical inhomogenity of ice crystal habits and size distributions for two moderate–resolution imaging spectroradiometer (MODIS) bands. *Journal of Geophysical Research* 106 (D15), 17267–17291.

Zahorowski, W., Chambers, S. D., Henderson-Sellers, A., 2004. Ground based radon–222 observations and their application to atmospheric studies. *Journal of Environmental Radioactivity* 76 (1-2), 3–33.

Zander, R., Demoulin, P., Ehhalt, D. H., Schmidt, U., 1989. Secular increase of the vertical column abundance of methane derived from IR solar spectra recorded at the Jungfraujoch station. *Journal of Geophysical Research–Atmospheres* 94 (D8), 11029–11039.

Zellner, R., 1999. Global Aspects of Atmospheric Chemistry (Topics in Physical Chemistry). v. 6. *Springer Science and Business*. New York, USA, 334 pp.

Zeng, G., Wood, S. W., Morgenstern, O., Jones, N. B., Robinson, J., Smale, D., 2012. Trends and variations in CO, C_2H_6, and HCN in the Southern Hemisphere point to the declining anthropogenic emissions of CO and C_2H_6. *Atmospheric Chemistry and Physics* 12 (16), 7543–7555.

Zhang, M. H., Lin, W. Y., Klein, S. A., Bacmeister, J. T., Bony, S., Cederwall, R. T., Del Genio, A. D., Hack, J. J., Loeb, N. G., Lohmann, U., Minnis, P., Musat, I., Pincus, R., Stier, P., Suarez, M. J., Webb, M. J., Wu, J. B., Xie, S. C., Yao, M.-S., Zhang, J. H., 2005. Comparing clouds and their seasonal variations in 10 atmospheric general circulation models with satellite measurements. *Journal of Geophysical Research–Atmospheres* 110 (D15), D15S02.

Appendix A

NZAC SCM chemical abbreviations

Et = C_2H_5	Ethyl radical
HACET = CH_3COCH_2OH	Hydroxyacetone
ISOP = $CH_2C(CH_3)CHCH_2$	Isoprene
$ISOP_2$ = e.g. $HOCH_2C(OO)CH_3CHCH_2$	Peroxy radical (ISO + OH)
ISON = e.g. $HOCH_2C(NO)CH_3CHCH_2$	Isoprine nitrate (ISO_2 + NO)
MACR = CH_2CCH_3CHO	Methacrolein
$MACRO_2$ = $CH_3COCH(OO)CH_2OH$	Peroxy radical (MACR + OH)
MGLY = CH_3COCHO	Methylglyoxal
MPAN = $CH_2C_2H_3CO_3NO_2$	Methacryloyl peroxynitrate
NALD = $HCHOCONO_2HO_2$	Nitrooxyacetaldehyde
PAN = $CH_3CO_3NO_2$	Peroxy acetyl nitrate
PPAN = e.g. RCO_3NO_2	Other higher peroxy acetyl nitrate
Pr = C_3H_7	Propyl radical

Appendix B

FAST–JX photolysis reactions used in the NZAC SCM

Table B.1: **FAST–JX photolysis reactions**. R1 is the reactant. P1, P2, P3, and P4 are the products.

Table B.1					
Num	R1	P1	P2	P3	P4
1	EtOOH	CH_3CHO	HO_2	OH	
2	H_2O_2	OH	OH		
3	HCHO	HO_2	HO_2	CO	
4	HCHO	H_2	CO		
5	HO_2NO_2	HO_2	NO_2		
6	$HONO_2$	OH	NO_2		
7	CH_3CHO	CH_3OO	HO_2	CO	
8	CH_3CHO	CH_4	CO		
9	CH_3OOH	HO_2	HCHO	OH	
10	N_2O_5	NO_3	NO_2		
11	NO_2	NO	$O(^3P)$		
12	NO_3	NO	O_2		
13	NO_3	NO_2	$O(^3P)$		
14	O_2	$O(^3P)$	$O(^3P)$		
15	O_3	O_2	$O(^1D)$		
16	O_3	O_2	$O(^3P)$		
17	PAN	CH_3CO_3	NO_2		
18	HONO	OH	NO		
19	EtCHO	EtOO	HO_2	CO	
20	$(CH_3)_2CO$	CH_3CO_3	CH_3OO		
21	$(CH_3)_2CO$	CH_3CO_3	CH_3OO		
22	n-PrOOH	EtCHO	HO_2	OH	
23	i-PrOOH	$(CH_3)_2CO$	HO_2	OH	
24	CH_3COCH_2OOH	CH_3CO_3	HCHO	OH	
25	PPAN	$EtCO_3$	NO_2		

Continuation of Table B.1

Num	R1	P1	P2	P3	P4
26	CH_3ONO_2	HO_2	HCHO	NO_2	
27	ISOOH	OH	MACR	HCHO	HO_2
28	ISON	NO_2	MACR	HCHO	HO_2
29	MACR	CH_3CO_3	HCHO	CO	HO_2
30	MPAN	$MACRO_2$	NO_2		
31	MACROOH	OH	HO_2	OH	HO_2
32	MACROOH	HACET	CO	MGLY	HCHO
33	HACET	CH_3CO_3	HCHO	HO_2	
34	MGLY	CH_3CO_3	CO	HO_2	
35	NALD	HCHO	CO	NO_2	HO_2
36	CH_3CO_3H	CH_3OO	OH		
37	BrCl	Br	Cl		
38	BrO	Br	$O(^3P)$		
39	$BrONO_2$	Br	NO_3		
40	$BrONO_2$	BrO	NO_2		
41	O_2	$O(^3P)$	$O(^1D)$		
42	OClO	$O(^3P)$	ClO		
43	NO	N	$O(^3P)$		
44	HOBr	OH	Br		
45	N_2O	N_2	$O(^1D)$		
46	H_2O	OH	H		
47	$ClONO_2$	Cl	NO_3		
48	$ClONO_2$	ClO	NO_2		
49	HCl	H	Cl		
50	HOCl	OH	Cl		
51	Cl_2O_2	2Cl		O_2	
52	$CFCl_3$	3Cl			
53	CF_2Cl_2	2Cl			
54	CH_3Br	Br	H		
55	CH_4	CH_3OO	H		
56	CO_2	CO	$O(^3P)$		
57	HO_2NO_2	OH	NO_3		
58	CH_2Br_2	2Br			
59	$CHBr_3$	3Br			

Appendix C

NZAC SCM chemical mechanism

Table C.1: **NZAC SCM heterogeneous reactions**. R1 and R2 are the reactants, and P1, P2 and P3 are the products.

Table C.1					
Num	R1	R2	P1	P2	P3
1	$ClONO_2$	H_2O	HOCl	$HONO_2$	
2	$ClONO_2$	HCl	2Cl	$HONO_2$	
3	HOCl	HCl	2Cl	H_2O	
4	N_2O_5	H_2O	$HONO_2$	$HONO_2$	
5	N_2O_5	HCl	Cl	NO_2	$HONO_2$

Table C.2: **NZAC SCM bimolecular reactions**. R1 and R2 are the reactants, and P1, P2, P3 and P4 are the products. k_0, α, and β are the parameters in the rate tables described in Chapter 3.

Table C.2									
Num	R1	R2	P1	P2	P3	P4	k_0	α	β
1	HO_2	NO	OH	NO_2			3.60E-12	0.00	-270.00
2	HO_2	NO_3	OH	NO_2	O_2		4.00E-12	0.00	0.00
3	HO_2	O_3	OH	$2O_2$			2.03E-16	4.57	-693.00
4	HO_2	HO_2	H_2O_2	O_2			2.20E-13	0.00	-600.00
5	HO_2	CH_3OO	CH_3OOH	O_2			3.80E-13	0.00	-780.00
6	HO_2	CH_3OO	HCHO	H_2O	O_2		3.80E-13	0.00	-780.00
7	HO_2	EtOO	EtOOH	(O_2)			3.80E-13	0.00	-900.00
8	HO_2	CH_3CO_3	CH_3CO_3H	O_2			2.08E-13	0.00	-980.00
9	HO_2	CH_3CO_3	CH_3CO_2H	O_3			1.04E-13	0.00	-980.00
10	HO_2	CH_3CO_3	OH	CH_3OO		O_2	2.08E-13	0.00	-980.00
11	HO_2	n-PrOO	n-PrOOH	O_2			1.51E-13	0.00	-1300.00
12	HO_2	i-PrOO	i-PrOOH	O_2			1.51E-13	0.00	-1300.00
13	HO_2	$EtCO_3$	O_2	$EtCO_3H$			3.05E-13	0.00	-1040.00
14	HO_2	$EtCO_3$	O_3	$EtCO_2H$			1.25E-13	0.00	-1040.00
15	HO_2	CH_3COCH_2OO	CH_3COCH_2OOH				1.36E-13	0.00	-1250.00
16	CH_3OO	NO	HO_2	HCHO	NO_2		2.95E-12	0.00	-285.00
17	CH_3OO	NO	CH_3ONO_2				2.95E-15	0.00	-285.00
18	CH_3OO	NO_3	HO_2	HCHO	NO_2		1.30E-12	0.00	0.00
19	CH_3OO	CH_3OO	CH_3OH	HCHO			1.03E-13	0.00	-365.00
20	CH_3OO	CH_3OO	$2HO_2$	2HCHO			1.03E-13	0.00	-365.00
21	CH_3OO	CH_3CO_3	HO_2	HCHO	CH_3OO		1.80E-12	0.00	-500.00
22	CH_3OO	CH_3CO_3	CH_3CO_2H	HCHO	O_2		2.00E-13	0.00	-500.00
23	EtOO	NO	CH_3CHO	HO_2	NO_2		2.60E-12	0.00	-380.00
24	EtOO	NO_3	CH_3CHO	HO_2	NO_2		2.30E-12	0.00	0.00
25	EtOO	CH_3CO_3	CH_3CHO	HO_2	CH_3OO		4.40E-13	0.00	-1070.00
26	CH_3CO_3	NO	CH_3OO	CO_2	NO_2		7.50E-12	0.00	-290.00
27	CH_3CO_3	NO_3	CH_3OO	CO_2	NO_2		4.00E-12	0.00	0.00
28	n-PrOO	NO	EtCHO	HO_2	NO_2		2.90E-12	0.00	-350.00
29	n-PrOO	NO_3	EtCHO	HO_2	NO_2		2.50E-12	0.00	0.00

Continuation of Table C.2.									
Num	R1	R2	P1	P2	P3	P4	k_0	α	β
30	i-PrOO	NO	$(CH_3)_2CO$	HO_2	NO_2		2.70E-12	0.00	-360.00
31	i-PrOO	NO_3	$(CH_3)_2CO$	HO_2	NO_2		2.50E-12	0.00	0.00
32	$EtCO_3$	NO	EtOO	CO_2	NO_2		6.70E-12	0.00	-340.00
33	$EtCO_3$	NO_3	EtOO	CO_2	NO_2		4.00E-12	0.00	0.00
34	CH_3COCH_2OO	NO	CH_3CO_3	HCHO	NO_2		2.80E-12	0.00	-300.00
35	CH_3COCH_2OO	NO_3	CH_3CO_3	HCHO	NO_2		2.50E-12	0.00	0.00
36	NO	NO_3	NO_2	NO_2			1.80E-11	0.00	-110.00
37	NO	O_3	NO_2				1.40E-12	0.00	1310.00
38	NO_2	O_3	NO_3				1.40E-13	0.00	2470.00
39	NO_3	HCHO	$HONO_2$	HO_2	CO		2.00E-12	0.00	2440.00
40	NO_3	CH_3CHO	$HONO_2$	CH_3CO_3			1.40E-12	0.00	1860.00
41	NO_3	EtCHO	$HONO_2$	$EtCO_3$			3.46E-12	0.00	1862.00
42	NO_3	$(CH_3)_2CO$	$HONO_2$	CH_3COCH_2OO			3.00E-17	0.00	0.00
43	N_2O_5	H_2O	$HONO_2$	$HONO_2$			2.50E-22	0.00	0.00
44	$O(^3P)$	O_3	O_2	O_2			8.00E-12	0.00	2060.00
45	$O(^1D)$	CH_4	OH	CH_3OO			1.05E-10	0.00	0.00
46	$O(^1D)$	CH_4	HCHO	H_2			7.50E-12	0.00	0.00
47	$O(^1D)$	CH_4	HCHO	HO_2	HO_2		3.45E-11	0.00	0.00
48	$O(^1D)$	H_2O	OH	OH			2.20E-10	0.00	0.00
49	$O(^1D)$	N_2	$O(^3P)$	N_2			2.10E-11	0.00	-115.00
50	$O(^1D)$	O_2	$O(^3P)$	O_2			3.20E-11	0.00	-67.00
51	OH	CH_4	H_2O	CH_3OO			1.85E-12	0.00	1690.00
52	OH	C_2H_6	H_2O	EtOO			6.90E-12	0.00	1000.00
53	OH	C_3H_8	n-PrOO	H_2O			7.60E-12	0.00	585.00
54	OH	C_3H_8	i-PrOO	H_2O			7.60E-12	0.00	585.00
55	OH	CO	H	CO_2			1.44E-13	0.00	0.00
56	OH	EtCHO	H_2O	$EtCO_3$			5.10E-12	0.00	-405.00
57	OH	EtOOH	H_2O	CH_3CHO	OH		8.01E-12	0.00	0.00
58	OH	EtOOH	H_2O	EtOO			1.90E-12	0.00	-190.00
59	OH	H_2	H_2O	H			7.70E-12	0.00	2100.00
60	OH	H_2O_2	H_2O	HO_2			2.90E-12	0.00	160.00
61	OH	HCHO	H_2O	HO_2	CO		5.40E-12	0.00	-135.00

Continuation of Table C.2.

Num	R1	R2	P1	P2	P3	P4	k_0	α	β
62	OH	HO_2	H_2O	O_2			4.80E-11	0.00	-250.00
63	OH	HO_2NO_2	H_2O	NO_2	O_2		1.90E-12	0.00	-270.00
64	OH	$HONO_2$	H_2O	NO_3			1.50E-13	0.00	0.00
65	OH	HONO	H_2O	NO_2			2.50E-12	0.00	-260.00
66	OH	CH_3OOH	H_2O	HCHO	OH		1.02E-12	0.00	-190.00
67	OH	CH_3OOH	H_2O	CH_3OO			1.89E-12	0.00	-190.00
68	OH	CH_3ONO_2	HCHO	NO_2	H_2O		4.00E-13	0.00	845.00
69	OH	$(CH_3)_2CO$	H_2O	CH_3COCH_2OO			8.80E-12	0.00	1320.00
70	OH	$(CH_3)_2CO$	H_2O	CH_3COCH_2OO			1.70E-14	0.00	-420.00
71	OH	CH_3COCH_2OOH	H_2O	CH_3COCH_2OO			1.90E-12	0.00	-190.00
72	OH	CH_3COCH_2OOH	OH	MGLY			8.39E-12	0.00	0.00
73	OH	CH_3CHO	H_2O	CH_3CO_3			4.40E-12	0.00	-365.00
74	OH	NO_3	HO_2	NO_2			2.00E-11	0.00	0.00
75	OH	O_3	HO_2	O_2			1.70E-12	0.00	940.00
76	OH	OH	H_2O	$O(^3P)$			6.31E-14	2.60	-945.00
77	OH	PAN	HCHO	NO_2	H_2O		3.00E-14	0.00	0.00
78	OH	PPAN	CH_3CHO	NO_2	H_2O		1.27E-12	0.00	0.00
79	OH	n-PrOOH	n-PrOO	H_2O			1.90E-12	0.00	-190.00
80	OH	n-PrOOH	EtCHO	H_2O	OH		1.10E-11	0.00	0.00
81	OH	i-PrOOH	i-PrOO	H_2O			1.90E-12	0.00	-190.00
82	OH	i-PrOOH	$(CH_3)_2CO$	OH			1.66E-11	0.00	0.00
83	$O(^3P)$	NO_2	NO	O_2			5.50E-12	0.00	-188.00
84	OH	C_5H_8	$ISOP_2$				2.70E-11	0.00	-390.00
85	O_3	C_5H_8	1.95MACR	1.74HCHO	0.3$MACRO_2$	0.3CH_3CO_3	3.33E-15	0.00	1995.00
86	O_3	C_5H_8	0.24CH_3OO	0.84HCOOH	0.42CO	0.27H_2O_2	3.33E-15	0.00	1995.00
87	O_3	C_5H_8	0.75HO_2	0.75OH			3.33E-15	0.00	1995.00
88	NO_3	C_5H_8	ISON				3.15E-12	0.00	450.00
89	NO	$ISOP_2$	NO_2	MACR	HCHO	HO_2	2.43E-12	0.00	-360.00
90	NO	$ISOP_2$	ISON				1.12E-13	0.00	-360.00
91	HO_2	$ISOP_2$	ISOOH				2.05E-13	0.00	-1300.00
92	$ISOP_2$	$ISOP_2$	MACR	MACR	HCHO	HO_2	2.00E-12	0.00	0.00
93	OH	ISOOH	MACR	OH			1.00E-10	0.00	0.00

Continuation of Table C.2.									
Num	R1	R2	P1	P2	P3	P4	k_0	α	β
94	OH	ISON	HACET	NALD			1.30E-11	0.00	0.00
95	OH	MACR	$MACRO_2$				1.30E-12	0.00	-610.00
96	OH	MACR	$MACRO_2$				4.00E-12	0.00	-380.00
97	O_3	MACR	1.8MGLY	0.9HCOOH	$0.64HO_2$	0.44CO	2.13E-16	0.00	1520.00
98	O_3	MACR	0.38OH	$0.2CH_3CO_3$			2.13E-16	0.00	1520.00
99	O_3	MACR	1.8MGLY	0.9HCOOH	$0.64HO_2$	0.44CO	3.50E-16	0.00	2100.00
100	O_3	MACR	0.38OH	$0.2CH_3CO_3$			3.50E-16	0.00	2100.00
101	NO	$MACRO_2$	$2NO_2$	$0.5CH_3CO_3$	0.5HACET	0.5CO	1.27E-12	0.00	-360.00
102	NO	$MACRO_2$	MGLY	1.5HCHO	$1.5HO_2$		1.27E-12	0.00	-360.00
103	HO_2	$MACRO_2$	MACROOH				1.82E-13	0.00	-1300.00
104	$MACRO_2$	$MACRO_2$	2HACET	2MGLY	HCHO	CO	1.00E-12	0.00	0.00
105	$MACRO_2$	$MACRO_2$	$2HO_2$				1.00E-12	0.00	0.00
106	OH	MPAN	HACET	NO_2			2.90E-11	0.00	0.00
107	OH	MACROOH	$MACRO_2$				3.00E-11	0.00	0.00
108	OH	HACET	MGLY	HO_2			3.00E-12	0.00	0.00
109	OH	MGLY	CH_3CO_3	CO			1.50E-11	0.00	0.00
110	NO_3	MGLY	CH_3CO_3	CO	$HONO_2$		3.46E-12	0.00	1860.00
111	OH	NALD	HCHO	CO	NO_2		4.40E-12	0.00	-365.00
112	OH	CH_3CO_3H	CH_3CO_3				3.70E-12	0.00	0.00
113	OH	CH_3CO_2H	CH_3OO				4.00E-13	0.00	-200.00
114	OH	HCOOH	HO_2				4.50E-13	0.00	0.00
115	Br	Cl_2O_2	BrCl	Cl	O_2		3.00E-12	0.00	0.00
116	Br	O_3	BrO	O_2			1.70E-11	0.00	800.00
117	Br	OClO	BrO	ClO			2.70E-11	0.00	1300.00
118	Br	HCHO	HBr	CO	HO_2		1.70E-11	0.00	800.00
119	Br	HO_2	HBr	O_2			1.40E-11	0.00	590.00
120	BrO	BrO	2Br	O_2			2.40E-12	0.00	-40.00
121	BrO	ClO	Br	OClO			1.60E-12	0.00	-430.00
122	BrO	ClO	Br	Cl	O_2		2.90E-12	0.00	-220.00
123	BrO	ClO	BrCl	O_2			5.80E-13	0.00	-170.00
124	BrO	NO	Br	NO_2			8.70E-12	0.00	-260.00
125	BrO	HO_2	0.979HOBr	$0.979O_2$	0.02HBr	$0.02O_3$	3.37E-12	0.00	-540.00

Continuation of Table C.2.

Num	R1	R2	P1	P2	P3	P4	k_0	α	β
126	Br	CH_3CHO	HBr	CH_3CO_3			1.80E-11	0.00	460.00
127	BrO	OH	Br	HO_2			7.50E-11	0.00	0.00
128	Cl	CH_4	HCl	CH_3OO			6.60E-12	0.00	1240.00
129	Cl	Cl_2O_2	3Cl				1.00E-10	0.00	0.00
130	Cl	$ClONO_2$	2Cl	NO_3			6.50E-12	0.00	-135.00
131	Cl	H_2	HCl	H			3.90E-11	0.00	2310.00
132	Cl	H_2O_2	HCl	HO_2			1.10E-11	0.00	980.00
133	Cl	HCHO	HCl	CO	HO_2		8.20E-11	0.00	34.00
134	Cl	HO_2	HCl	O_2			1.80E-11	0.00	-170.00
135	Cl	HO_2	ClO	OH			4.10E-11	0.00	450.00
136	Cl	HOCl	2Cl	OH			2.50E-12	0.00	130.00
137	Cl	NO_3	ClO	NO_2			2.40E-11	0.00	0.00
138	Cl	O_3	ClO	O_2			2.90E-11	0.00	260.00
139	Cl	OClO	ClO	ClO			3.20E-11	0.00	-170.00
140	ClO	ClO	2Cl	O_2			3.00E-11	0.00	2450.00
141	ClO	ClO	2Cl	O_2			1.00E-12	0.00	1590.00
142	ClO	ClO	Cl	OClO			3.50E-13	0.00	1370.00
143	ClO	HO_2	HOCl	O_2			4.60E-13	0.00	-710.00
144	Cl	EtCHO	HCl	$EtCO_3$			1.30E-10	0.00	0.00
145	ClO	CH_3OO	Cl	HCHO	HO_2		3.30E-12	0.00	115.00
146	ClO	NO	Cl	NO_2			6.20E-12	0.00	-295.00
147	ClO	NO_3	Cl	O_2	NO_2		4.60E-13	0.00	0.00
148	Cl	CH_3CHO	CH_3CO_3	HCl			8.00E-11	0.00	0.00
149	NO_2	NO_3	NO	NO_2	O_2		4.50E-14	0.00	1260.00
150	NO_3	Br	BrO	NO_2			1.60E-11	0.00	0.00
151	$O(^3P)$	BrO	O_2	Br			1.90E-11	0.00	-230.00
152	$O(^3P)$	ClO	Cl	O_2			3.80E-11	0.00	0.00
153	$O(^3P)$	H_2	OH	H			9.00E-18	0.00	0.00
154	$O(^3P)$	H_2O_2	OH	HO_2			1.40E-12	0.00	2000.00
155	$O(^3P)$	HBr	OH	Br			5.80E-12	0.00	1500.00
156	$O(^3P)$	O_2	HCHO	OH	CO	HO_2	3.40E-11	0.00	1600.00
157	$O(^3P)$	HCl	OH	Cl			1.00E-11	0.00	3300.00

Continuation of Table C.2.									
Num	R1	R2	P1	P2	P3	P4	k_0	α	β
158	$O(^3P)$	HO_2	OH	O_2			2.70E-11	0.00	-224.00
159	$O(^3P)$	HOCl	OH	ClO			1.70E-13	0.00	0.00
160	$O(^3P)$	NO_3	O_2	NO_2			1.70E-11	0.00	0.00
161	$O(^3P)$	OClO	O_2	ClO			2.40E-12	0.00	960.00
162	$O(^3P)$	OH	O_2	H			2.40E-11	0.00	-110.00
163	$O(^1D)$	HBr	0.2HBr	$0.2O(^3P)$	0.8OH	0.8Br	1.50E-10	0.00	0.00
164	Cl	CH_3ONO_2	HCHO	NO_2	HCl		1.30E-11	0.00	1200.00
165	$O(^1D)$	CO_2	$O(^3P)$	CO_2			7.40E-11	0.00	-120.00
166	$O(^1D)$	H_2	OH	H			1.10E-10	0.00	0.00
167	$O(^1D)$	HCl	$O(^3P)$	HCl			1.35E-11	0.00	0.00
168	$O(^1D)$	HCl	0.263H	0.263ClO	0.737OH	0.737Cl	1.37E-10	0.00	0.00
169	Cl	$(CH_3)_2CO$	HCl	CH_3COCH_2OO			1.50E-11	0.00	590.00
170	$O(^1D)$	N_2O	$0.39N_2$	$0.39O_2$	1.22NO		1.19E-10	0.00	-20.00
171	Cl	C_3H_8	HCl	n-PrOO			8.26E-11	0.00	90.00
172	$O(^1D)$	O_3	$1.5O_2$	$O(^3P)$			2.40E-10	0.00	0.00
173	Cl	C_3H_8	HCl	i-PrOO			6.02E-11	0.00	-75.00
174	OClO	NO	NO_2	ClO			3.40E-13	0.00	0.00
175	OH	ClO	HO_2	Cl			7.40E-12	0.00	-270.00
176	OH	ClO	HCl	O_2			6.00E-13	0.00	-230.00
177	OH	HBr	H_2O	Br			1.10E-11	0.00	0.00
178	OH	HCl	H_2O	Cl			1.80E-12	0.00	240.00
179	OH	HOCl	ClO	H_2O			3.00E-12	0.00	500.00
180	OH	OClO	HOCl	O_2			4.50E-13	0.00	-800.00
181	$O(^3P)$	$ClONO_2$	ClO	NO_3			2.90E-12	0.00	800.00
182	OH	$ClONO_2$	HOCl	NO_3			1.20E-12	0.00	330.00
183	Cl	CH_3OOH	HCl	CH_3OO			5.70E-11	0.00	0.00
184	$CFCl_3$	$O(^1D)$	2Cl	ClO			2.30E-10	0.00	0.00
185	CF_2Cl_2	$O(^1D)$	Cl	ClO			1.40E-10	0.00	0.00
186	CH_3Br	OH	Br	H_2O			2.35E-12	0.00	1300.00
187	CH_3Br	$O(^1D)$	Br	OH			1.80E-10	0.00	0.00
188	CH_3Br	Cl	Br	HCl			1.70E-11	0.00	1080.00
189	N	O_2	NO	$O(^3P)$			1.50E-11	0.00	3600.00

Continuation of Table C.2.

Num	R1	R2	P1	P2	P3	P4	k_0	α	β
190	N	NO	N_2	$O(^3P)$			2.10E-11	0.00	-100.00
191	N	NO_2	N_2O	$O(^3P)$			5.80E-12	0.00	-220.00
192	H	O_3	OH	O_2			1.40E-10	0.00	470.00
193	H	HO_2	1.38OH	$0.29H_2$	$0.02O(^3P)$	$0.02H_2O$	8.10E-11	0.00	0.00
194	Cl	CH_3OH	HO_2	HCl	HCHO		5.50E-11	0.00	0.00
195	Cl	C_2H_6	HCl	EtOO			7.20E-11	0.00	70.00
196	H	NO_2	OH	NO			4.00E-10	0.00	340.00
197	OH	CH_3OH	HO_2	HCHO			2.85E-12	0.00	345.00
198	$O(^1D)$	CH_2Br_2	2Br	OH			2.70E-10	0.00	0.00
199	OH	CH_2Br_2	2Br	H_2O			2.00E-12	0.00	840.00
200	Cl	CH_2Br_2	2Br	HCl			6.30E-12	0.00	800.00
201	$O(^1D)$	CHBr3	3Br	OH			6.60E-10	0.00	0.00
202	OH	$CHBr_3$	3Br	H_2O			1.35E-12	0.00	600.00
203	Cl	$CHBr_3$	3Br	HCl			4.85E-12	0.00	850.00

End of Table C.2.

Table C.3: **NZAC SCM unimolecular and termolecular reactions**. R1 and R2 are the reactants. P1 and P2 are the products. k_1, α_1, β_1, k_2, α_2, β_2, and f are the parameters in the rate tables described in Chapter 3. A third body (M) would be the R2 and R3 in unimolecular and termolecular reactions respectively.

Table C.3											
Num	R1	R2	P1	P2	f	k_1	α_1	β_1	k_2	α_2	β_2
1	HO_2	HO_2	H_2O_2	O_2	0.0	1.90E-33	0.00	-980.0	0.00E+00	0.00	0.0
2	HO_2	NO_2	HO_2NO_2		0.6	1.80E-31	-3.20	0.0	4.70E-12	0.00	0.0
3	HO_2NO_2		HO_2	NO_2	0.6	4.10E-05	0.00	10650.0	4.80E+15	0.00	11170.0
4	CH_3CO_3	NO_2	PAN		0.3	2.70E-28	-7.10	0.0	1.20E-11	-0.90	0.0
5	PAN		CH_3CO_3	NO_2	0.3	4.90E-03	0.00	12100.0	5.40E+16	0.00	13830.0
6	N_2O_5		NO_2	NO_3	0.3	1.30E-03	-3.50	11000.0	9.70E+14	0.10	11080.0
7	NO_2	NO_3	N_2O_5		0.3	3.60E-30	-4.10	0.0	1.90E-12	0.20	0.0
8	$O(^3P)$	O_2	O_3		0.0	5.70E-34	-2.60	0.0	0.00E+00	0.00	0.0
9	OH	NO	HONO		1420.0	7.40E-31	-2.40	0.0	3.30E-11	-0.30	0.0
10	OH	NO_2	$HONO_2$		0.4	3.30E-30	-3.00	0.0	4.10E-11	0.00	0.0
11	OH	OH	H_2O_2		0.5	6.90E-31	-0.80	0.0	2.60E-11	0.00	0.0
12	EtCO3	NO_2	PPAN		0.3	2.70E-28	-7.10	0.0	1.20E-11	-0.90	0.0
13	PPAN		$EtCO_3$	NO_2	0.4	1.70E-03	0.00	11280.0	8.30E+16	0.00	13940.0
14	$MACRO_2$	NO_2	MPAN		0.3	2.70E-28	-7.10	0.0	1.20E-11	-0.90	0.0
15	MPAN		$MACRO_2$	NO2	0.3	4.90E-03	0.00	12100.0	5.40E+16	0.00	13830.0
16	BrO	NO_2	$BrONO_2$		327.0	4.70E-31	-3.10	0.0	1.40E-11	-1.20	0.0
17	Cl_2O_2		ClO	ClO	0.6	1.00E-06	1.00	8000.0	4.80E+15	0.00	8820.0
18	ClO	ClO	Cl_2O_2		0.6	1.70E-32	-4.00	0.0	5.40E-12	0.00	0.0
19	ClO	NO_2	$ClONO_2$		430.0	1.60E-31	-3.40	0.0	1.50E-11	0.00	0.0
20	NO	NO	NO_2	NO_2	0.0	6.93E-40	0.00	-530.0	0.00E+00	0.00	0.0
21	$O(^3P)$	NO	NO_2		0.6	9.00E-31	-1.50	0.0	3.00E-11	0.00	0.0
22	$O(^3P)$	NO_2	NO_3		0.6	1.30E-31	-1.50	0.0	2.30E-11	0.24	0.0
23	$O(^1D)$	N_2	N_2O		0.0	3.50E-37	-0.60	0.0	0.00E+00	0.00	0.0
24	H	O_2	HO_2		0.6	5.70E-32	-1.60	0.0	7.50E-11	0.00	0.0

Appendix D

Instrumentation and other data sources

Table D.1: Instrumentation and other data sources.

Instrument	**Measurement**	**Usage**	**Period**	**Time resolution**	**Vertical coverage**
Upper/lower radiometers	Actinic fluxes	FAST–JX validation	late 1993 – present	10 min	surface
UVM spectrometer	Erythemally–weighted irradiances	Upper radiometer correction	late 1993 – present	30 min	surface
Eppley UVA radiometer	Erythemally–weighted UVA irradiances	Upper radiometer correction	late 1993 – present	10 min	surface
Yankee UVB radiometer	Erythemally–weighted UVB irradiances	Upper radiometer correction	late 1993 – present	10 min	surface
Ozone sondes	O_3	Construction O_3 profiles	1986 – present	Weekly	0 – $\sim$ 35 km
Lidar	O_3	Comparison O_3 profiles	1994 – present	Weekly (clear–sky)	8 – 50 km
MOPI1	O_3	Construction O_3 profiles	1994 – present	Continuous	20 – 75 km
TEI	O_3	Comparison O_3 ozonesondes	2004 – present	Hourly	Surface
Dobson	O_3	Comparison ozonesondes – MOPI1	1987 – present	clear–sky	TCO

Continuation of Table D.1.

Instrument	Measurement	Usage	Period	Time resolution	Vertical coverage
Radiosondes	H_2O, Pressure Temperature	Construction H_2O profiles	1986 – present	Weekly	0 – $\sim$ 35 km
FTIR	CH_4, CO	Comparison columns	1994 – present CH_4 2001 – present CO	Continuous	Total columns
Radiative transfer model	Erythemally–weighted UVA irradiances	Upper radiometer correction	late 1993 – present	30 min	surface
ERAI	Global H_2O estimates	Construction H_2O profiles	1979 – present	Daily	0 – $\sim$ 10 km
Cape Grim CH_4	CH_4	Construction CH_4 profiles	1984 – present	Daily	surface
UKCA CCM	O_3, H_2O CH_4, CO temperature, pressure	Construction profiles	1980 – present	Monthly	0 – $\sim$ 84 km